

Dissertation

submitted to the

Combined Faculty of Natural Sciences and Mathematics

of Heidelberg University, Germany

for the degree of

Doctor of Natural Sciences

Put forward by

Divya Bharti

born in: Nalanda, India

Oral examination: 18-07-2023

Multi-Sideband Photoelectron Interferometry in Argon and Helium

Referees: Prof. Dr. Thomas Pfeifer

Apl. Prof. Dr. Andreas Wolf

Abstract

This thesis explores the photoionization dynamics in atoms using phase-locked two-color pulses, a high-frequency extreme ultraviolet (XUV) and a low-frequency infrared (IR) pulse, with the focus on extending the understanding of the interaction between the IR field and the outgoing electrons. To achieve this, a multi-sideband RABBITT (reconstruction of attosecond beating by two-photon transitions) technique was developed.

An attosecond-beamline is constructed which includes a femtosecond IR laser, a high-order harmonic generation module for producing XUV pulses, an interferometer, and a reaction microscope. The setup enables angle-differential and coincidence measurements of photoionization and photodissociation processes with attosecond precision in a pump-probe configuration.

The XUV pulse initiates the photoionization process, and the resulting photoelectron interacts with the IR field, exchanging several photons as it escapes the ionic potential. Depending on the combination of XUV and IR photon exchanges, and/or the angular-momentum channels involved, the photoelectrons can reach the same state via different quantum paths. The resulting signal in the photoelectron spectrum is the coherent superposition of all these distinct quantum paths, which oscillates as the temporal delay between the XUV and IR pulses varies, creating an interferogram.

The recorded angle-differential photoelectron interferograms in helium and argon enable the extraction of information on the relative amplitudes and phases of the dipole transition matrix elements associated with the many-order continuum-continuum transitions.

We compare the experimental results with *ab initio* theoretical calculations based on solving the time-dependent Schrödinger equation and use a few-level-model simulation to understand the impact of different parameters on the photoelectron interferogram and the extracted information.

Zusammenfassung

Ziel dieser Arbeit ist es, das Verständnis der Photoionisationsdynamik in Atomen mit Hilfe von Zweifarbenpulsen, einem hochfrequenten extrem ultravioletten (XUV) und einem niederfrequenten infraroten (IR) Puls, zu erweitern mit besonderem Fokus auf die Wechselwirkung zwischen dem IR-Feld und den austretenden Elektronen. Um dies zu erreichen, wurde eine Mehrseitenband-RABBIT-Technik (“reconstruction of attosecond beating by two-photon transitions”) entwickelt.

Zur Durchführung dieser Studie haben wir eine Attosekunden-Strahlführung konstruiert, die einen Femtosekunden-IR-Laser, einen Aufbau zur Erzeugung von Oberwellen hoher Ordnung (die XUV-Pulse), ein Interferometer und ein Reaktionsmikroskop umfasst. Der Aufbau macht es möglich, Winkeldifferenzial- und Koinzidenzmessungen von Photoionisations- und Photodissoziationsprozessen mit Attosekundenpräzision in einer Pump-Probe-Konfiguration durchzuführen.

Der XUV-Puls löst den Photoionisationsprozess aus. Das Photoelektron wechselwirkt mit dem IR-Feld und tauscht mehrere Photonen aus, während es dem Ionenpotential entkommt. Je nach Kombination von XUV- und IR-Photonenaustausch und/oder den beteiligten Drehimpulskanälen können die Photoelektronen dieselbe kinetische Energie über verschiedene Quantenpfade erhalten. Das daraus resultierende Signal im Photoelektronenspektrum ist die kohärente Überlagerung all dieser unterschiedlichen Quantenpfade. Es oszilliert, wenn die zeitliche Verzögerung zwischen den XUV- und IR-Pulsen variiert wird, wodurch ein Interferogramm entsteht.

Die aufgezeichneten winkeldifferentiellen Photoelektronen-Interferogramme in Helium und Argon ermöglichen die Extraktion von Informationen über die relativen Amplituden und Phasen der Dipolübergangsmatrixelemente, die mit den Kontinuum-Kontinuum-Übergängen höherer Ordnung des entweichenden Elektrons im IR-Feld verbunden sind.

Wir vergleichen die experimentellen Ergebnisse mit theoretischen Berechnungen, die auf der Lösung der zeitabhängigen Schrödinger-Gleichung basieren. Zusätzlich verwenden wir eine ”Few-Level-Simulation”, um die Auswirkung verschiedener Parameter auf das Photoelektronen-Interferogramm und die extrahierten Informationen zu verstehen.

Contents

Abstract	v
Zusammenfassung	vi
Contents	vii
1 Introduction	1
2 Theoretical Background	4
2.1 Ultrashort Pulses	4
2.2 Second-order Harmonic Generation (SHG)	5
2.3 High-order Harmonic Generation (HHG)	6
2.4 Photoionization	8
2.5 Photoelectron Interferometry	12
2.5.1 1-SB RABBITT	12
2.5.2 3-SB RABBITT	16
3 Few-Level Model Simulation	19
3.1 1-SB RABBITT	21
3.2 3-SB RABBITT	34
3.3 Summary	44
4 Publications	45
4.1 Publication I: High-repetition rate attosecond beamline for multi-particle coincidence experiments	45
4.2 Publication II: Decomposition of the transition phase in multi-sideband schemes for reconstruction of attosecond beating by interference of two-photon transitions	63
4.3 Publication III: Multisideband interference structures observed via high-order photon-induced continuum-continuum transitions in argon	73
4.3.1 Additional Data on Paper III	82

5	Unpublished Results on Helium	87
5.1	Method	87
5.2	RABBITT Trace Analysis	89
5.2.1	Angle-integrated RABBITT	89
5.2.2	Under-threshold RABBITT	94
5.2.3	Angle-resolved phase measurements	96
5.3	Summary and Outlook	101
6	Discussion and Summary	103
A	Additional information on the Experimental Setup	115
A.1	Laser	115
A.2	Interferometer	116
A.3	Reaction Microscope	118
A.3.1	Data acquisition and signal processing	119
A.3.2	Momentum reconstruction	119
A.3.3	Angular acceptance	120
A.3.4	Resolution	121
	Acknowledgements	123
	Declaration/Erklärung	124

Chapter 1

Introduction

The interaction between light and matter has been a subject of scientific research for centuries. With advancements in laser technology and charged fragment detection systems, our understanding of this interaction has significantly improved.

The past century has witnessed remarkable progress in the development of laser technology, which began in 1960 with the development of the first laser by Theodore Maiman [1]. Since then, lasers have undergone continuous improvement and found applications in numerous fields. Notably, the development of mode-locking and pulse compression techniques has enabled the generation of ultra-short laser pulses in the picosecond and femtosecond regimes [2, 3]. In 2018, Donna Strickland and Gérard Mourou received the Nobel Prize in Physics for their pioneering work on chirped pulse amplification [4], which revolutionized laser technology by making it possible to generate high-intensity femtosecond laser pulses.

The development of high-intensity ultrashort lasers has paved the way for the discovery of high-order harmonic generation (HHG). This process was first experimentally observed in the early 1990s by McPherson [5], and almost simultaneously by Ferray and L'Huillier at CEA-Saclay [6]. HHG occurs due to the highly nonlinear interaction between a medium and a high-intensity laser pulse. This interaction converts the long-wavelength laser pulse into spatially and temporally coherent radiation in the extreme ultraviolet (XUV) and soft X-ray spectral ranges. It was later demonstrated that the XUV radiation emitted in the HHG process by few tens of femtosecond pulses corresponds to a train of attosecond pulses ($1 \text{ as} = 10^{-18} \text{ s}$) [7,8]. By using only a few-cycle pulse to drive the HHG process, it is possible to generate a single attosecond burst lasting less than 50 attoseconds [9]. The emergence of table-top XUV attosecond pulses has transformed the investigation of electron dynamics in matter, which was previously only accessible through the use of large-scale synchrotron facilities, facilitating the growth of attosecond science.

Along with the advancements in light sources, improvements in particle detection and

imaging technologies have been equally crucial for enhancing our ability to measure photoionization dynamics. Compared to the detectors used in the past, such as photographic plates and cloud chambers, modern time-of-flight spectrometers like Magnetic bottles [10], Velocity Map Imaging (VMI) [11], and Reaction Microscope (ReMi) [12] offer significant improvements in target selectivity and energy resolution. The ReMi detector, for example, enables the coincidence detection of charged particles (electrons and ions) and their momentum vectors. This allows for a complete measurement of the energy and momentum of the particles produced in a photoionization process.

Photoionization is a fundamental process that occurs when an atom or a molecule absorbs photons, resulting in the release of electrons. Due to the wave-particle duality of matter, the emitted photoelectron can be described as a wave packet with a specific amplitude and phase. While the amplitude of the electron wave packet can be determined through ionization cross-section measurements, determining the phase often requires the use of interferometric methods. Interference occurs when two or more coherent waves meet at the same point in space and time, generating a density distribution that depends on the relative phases and amplitudes of the contributing waves.

The photoelectron angular distribution (PAD) is a common way to study these interferences, where the yield of emitted electrons varies with the emission angle. This angular distribution is a result of the coherent superposition of all the constituent partial waves of photoelectrons generated during the process of photoionization.

In the context of two-color photoionization processes, an interference pattern can be observed in the photoelectron energy distribution in the spectral domain. This pattern arises as a result of a coherent superposition of continuum states that are created through different ionization pathways.

In this thesis, the RABBITT technique (reconstruction of attosecond beating by interference of two-photon transitions) [13] is utilized. This method involves ionizing a target using an XUV pulse in the presence of a phase-locked IR pulse, and then recording the resulting photoelectron spectrum. By varying the temporal delay between the two pulses, the intensity of the photoelectron signal is modulated, creating an interferogram. Analyzing this interferogram allows for the extraction of the phase of the electron wavepacket (EWP).

Furthermore, RABBITT has found applications in characterizing attosecond pulse trains (APT) generated in the HHG process [7] and studying photoionization and photo-dissociation dynamics across various systems [14–17].

This thesis focuses on investigating the XUV-IR photoionization dynamics in argon and helium, with particular emphasis on detecting continuum-continuum (cc) transitions of photoelectrons using the RABBITT technique. Specifically, the XUV pulse creates an electron wavepacket that propagates in the ionic potential in the presence of the IR pulse.

As the EWP escapes, it accumulates a phase that depends on the form of the long-range potential of the ion and the order of interactions with the IR field. This phase information is then imprinted on the photoelectron interference pattern. The photoelectron spectrum reveals multiple peaks resulting from various orders of continuum-continuum transitions. We investigate the contribution of these many-order continuum-continuum transitions in the XUV-IR delay induced modulation of the photoelectron signal at varying kinetic energies and emission angles.

The thesis is structured as follows:

Chapter 2 provides the necessary theoretical background to establish the important aspects of the thesis. It includes a brief discussion on ultra-short laser pulses, the high-order harmonic generation process, and photo-ionization processes. The chapter also provides a brief discussion on the photo-electron interferometry technique, primarily the standard RABBITT scheme, and its extension to 3-SB RABBITT.

In chapter 3, we use a few-level-model simulation to explain the oscillation in the photoelectron yield and retrieve the phases of the oscillation. We demonstrate how different parameters, specifically the transition amplitude, the phase, the IR intensity, and the XUV-APT spectrum affect the measured result.

In chapter 4, we include the three publications on which this thesis is based. Publication I details the attosecond beamline built at the MPIK in Heidelberg. Publication II delves deeper into the theory of the 3-SB RABBITT setup. Publication III shows the results from the very first 3-SB RABBITT measurements in argon. We explain the angle-integrated oscillation phase and the angle-resolved phases. We also compare the experimental data with theoretical predictions from fully quantum-mechanical, many-electron calculations carried out within the R-matrix (close-coupling) with time dependence (RMT) approach.

In chapter 5, we present unpublished results from 3-SB RABBITT experiments in helium at three IR intensities.

In chapter 6, we summarize the results of this thesis and give an outlook.

Chapter 2

Theoretical Background

This chapter provides the necessary theoretical foundation for understanding the pump-probe photoelectron interferometric method used to study photo-ionization dynamics. An overview of ultra-fast laser pulses, second-order harmonic generation, and high-order harmonic generation is presented, all of which are helpful in understanding the experiment. Next, different mechanisms involved in the photoionization process, such as single- and multi-photon ionization and Above Threshold Ionization (ATI), are introduced to provide a groundwork for further understanding of the underlying physics. Finally, the chapter explores the photoelectron interferometric technique, specifically focusing on the standard 1-SB RABBITT method and its extension to the 3-SB RABBITT technique, which helps understand the analysis of the experimental data.

2.1 Ultrashort Pulses

The generation of ultrashort pulses has led to significant advancements in various scientific fields, including physics, chemistry, biology, materials science, and engineering. These pulses possess an extremely short duration, typically in the femtosecond range, enabling the investigation of ultrafast processes. In this section, we provide an overview of the description, and propagation of ultrashort laser pulses. The influence of the magnetic field component is significantly weaker in light matter interaction compared to the electric field component. Consequently, in the description of many light-matter interaction processes, the magnetic field can often be disregarded. In the time domain, a pulse can be exclusively expressed using the electric field as:

$$\tilde{E}(t) = E(t)e^{i(\omega t + \phi(t))}. \quad (2.1)$$

Here $E(t)$ is the envelope of the field, ω is the carrier frequency, and $\phi(t)$ is a slowly-varying phase. The electric field can also be presented in the spectral domain through its Fourier

transform:

$$\tilde{E}(\omega) = E(\omega)e^{i\phi(\omega)}. \quad (2.2)$$

The spectral phase is often expanded around the central frequency (ω_0) in a Taylor series:

$$\phi(\omega) = \phi(\omega_0) + \phi'_0(\omega - \omega_0) + \frac{1}{2!}\phi''_0(\omega - \omega_0)^2 + \frac{1}{3!}\phi'''_0(\omega - \omega_0)^3 + \dots, \quad (2.3)$$

where

$$\text{GD} : \phi'_0 = \left. \frac{\partial\phi(\omega)}{\partial\omega} \right|_{\omega_0}; \quad \text{GDD} : \phi''_0 = \left. \frac{\partial^2\phi(\omega)}{\partial\omega^2} \right|_{\omega_0}; \quad \text{TOD} : \phi'''_0 = \left. \frac{\partial^3\phi(\omega)}{\partial\omega^3} \right|_{\omega_0}. \quad (2.4)$$

The first term in equation (2.3) is the absolute phase. It is also often called the carrier-envelope phase (CEP) and describes the relative phase difference between the carrier wave and the envelope of the pulse. The CEP becomes important when the pulse is only a few cycles long. In particular, it determines the electric field of the pulse near its peak, which can significantly affect the way the pulse interacts with matter.

The coefficient of the second term is called the group dispersion (GD). Group dispersion results in a translation of the entire pulse in the time domain. The quadratic term in the expansion is called group-delay dispersion (GDD). A positive GDD causes the low-frequency components of the pulse to arrive later than the high-frequency components, resulting in a broadening of the pulse duration. The fourth term in the Taylor expansion, called third-order dispersion (TOD), describes the third-order variation of the group delay with respect to the optical frequency. The presence of TOD makes the pulse asymmetric in time. Generally, the first few terms of the Taylor expansion, up to the TOD, provide a comprehensive description of the dispersion properties of a material or optical system.

2.2 Second-order Harmonic Generation (SHG)

Second-order harmonic generation (SHG) is a coherent nonlinear optical process that involves the interaction of a laser field with a medium to generate a new beam at twice the original frequency. Nonlinear crystals, such as potassium dihydrogen phosphate (KDP), beta-barium borate (BBO), lithium niobate (LiNbO₃), and lithium triborate (LBO), are commonly used for SHG. In our experiment, we used BBO for SHG. For SHG, the nonlinear material must have a non-zero second-order susceptibility, which is the coefficient that relates the polarization of the material to the square of the electric field. When the electric field of the incoming photon is strong enough, it induces a polarization in the material that oscillates at twice the frequency of the electric field. This oscillating polarization then emits a new photon at the second harmonic frequency. The resulting SHG pulse has a shorter duration than the original pulse, since it has a higher frequency. The efficiency of the SHG

process depends on the intensity of the input pulse, the non-linearity of the material, and the phase-matching conditions [18]: $I_{\text{SHG}} \propto |d_{\text{eff}}|^2 L^2 \text{sinc}^2(\frac{\Delta k L}{2}) I_{\text{fundamental}}^2$, where L is the length of the crystal, λ is the wavelength of the fundamental wave, $|d_{\text{eff}}|$ is the magnitude of the effective second-order nonlinear coefficient of the crystal, Δk is the phase mismatch, and $I_{\text{fundamental}}$ is the intensity of the fundamental wave. A thicker crystal can result in higher efficiency, but it also typically leads to a narrower phase-matching bandwidth, which can limit the spectral range of the generated second-harmonic signal.

2.3 High-order Harmonic Generation (HHG)

High-order harmonic generation (HHG) is a highly nonlinear optical process where a strong pulsed laser beam is focused onto a gas jet or solid material, leading to the generation of coherent radiation in the extreme ultraviolet (EUV) and soft X-ray regions.

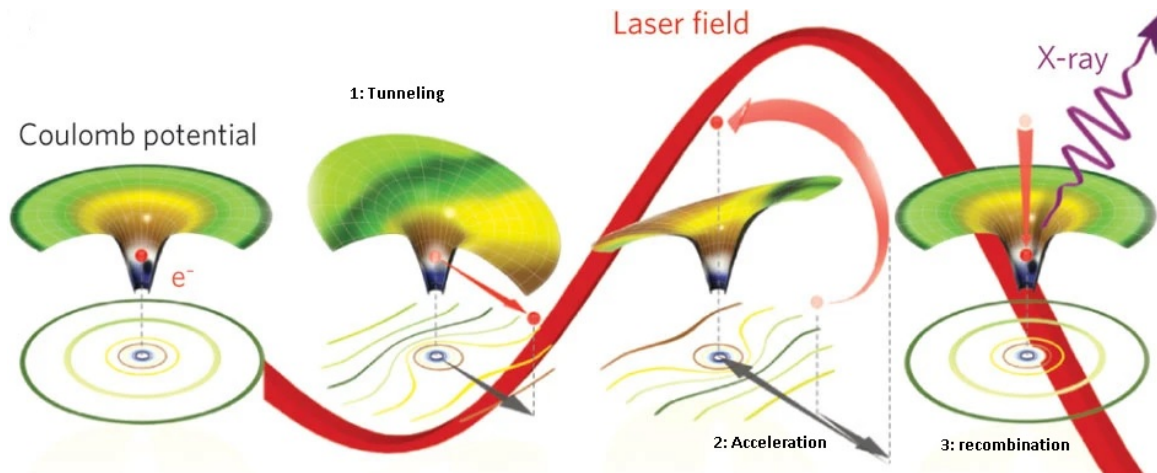


Figure 2.1. Illustration of the three-step model of HHG. Figure taken from [19]

The mechanism of HHG can be understood through the semi-classical three-step model proposed by Corkum [20]. In this model, the laser field is strong enough to significantly distort the electron binding potential within the atom. As shown in the figure 2.1, the process unfolds in three steps: In the first step, the strong electric field of the laser pulse bends the Coulomb potential of the atom, and the electron tunnels out of the lowered potential. Subsequently, in the second step, the electron is accelerated by the electric field of the laser, acquiring kinetic energy in the process. In the third step, when the sign of the laser's electric field changes, the electron is accelerated back towards the parent ion, potentially leading to a recombination event. When the electron recombines with the parent ion, its kinetic energy and the binding energy is converted into a short burst of light.

During each cycle of the laser field, the three-step process occurs twice, resulting in the emission of a pulse every half cycle. If the driving field consists of multiple cycles, the

entire process repeats multiple times, generating a train of pulses. This periodicity in time gives rise to a frequency comb in the spectral domain, where two consecutive peaks of the comb are separated by a distance of 2ω , i.e., twice the frequency of the driving field. In a centro-symmetric generation medium, only odd harmonics are emitted. The bandwidth of each harmonic in the spectra depends on the pulse duration of the driving field. When the driving field is sub-cycle, the process generates a single attosecond pulse with a broad frequency spectrum.

Depending on the time the electron tunnels out of the potential, it may follow different trajectories before recombining with the parent ion. The electron that acquires the largest kinetic energy leaves the atom approximately $0.31/\omega$ after each peak of the laser field and generates photons with a maximum energy (cut-off energy) given by [21]:

$$E_{\Omega} = I_p + 3.17 U_p \quad ; \quad U_p(\text{eV}) = 9.33 I(10^{14}\text{W/cm}^2) \lambda^2(\mu\text{m}^2). \quad (2.5)$$

where I_p is the ionization potential of the atom and U_p is the ponderomotive energy which is determined by the laser wavelength (λ) and intensity (I).

Electrons that tunnels out earlier or later than this time ($0.31/\omega$) will have less kinetic energy upon return, and these trajectories are referred to as long and short trajectories, respectively. The radiation emitted from these electrons is chirped, and the photon energy depends on the time of recombination with the parent ion. Short-trajectory harmonics have a positive chirp, while long-trajectory harmonics have a negative chirp. This means that for short trajectory radiation, the higher the harmonic order, the later is the emission time.

As can be seen from equation 2.3, using atoms with higher ionization potentials, increasing the laser intensity (I), and using longer laser wavelengths can increase the cut-off of the HHG process. However, increasing the intensity is limited by the saturation intensity, beyond which the neutral medium depletes severely, thus resulting in rapid decrease in efficiency. As the wavelength of the laser increases, the electron spends more time in the continuum region before it recombines with the parent ion. This extended time in the continuum region results in increased spatial dispersion of the electron wave packet, leading to a decrease in the recombination efficiency. Consequently, the efficiency of HHG conversion also decreases as the wavelength increases.

Therefore, achieving a balance between generation efficiency and energy cut-off is crucial. Factors such as the laser wavelength and intensity, gas pressure and composition, and laser beam focusing conditions also affect HHG efficiency. Phase-matching is a major challenge in HHG, as the generated EUV and soft X-ray photons are highly susceptible to dispersion in the medium.

In a gaseous medium, the wavevector-mismatch is a function of harmonic order and has

four contributions [22]:

$$\Delta k_q = \Delta k_q^e + \Delta k_q^n + \Delta k_q^g + \Delta k_q^d. \quad (2.6)$$

Here, Δk_q^e and Δk_q^n describe the mismatch due to plasma and neutral gas-dispersion, Δk_q^g is the mismatch due to geometry of the focus, and Δk_q^d is the dipole phase mismatch. The four contributions should be balanced against each other to minimize the overall mismatch. The mismatches Δk_q^n and Δk_q^e have opposite signs and scale linearly with pressure. The pressure can be increased to increase the flux but increasing the pressure too much results in re-absorption of the generated XUV beam. While a high driving intensity is desirable to increase the cutoff, increasing the intensity creates more free electrons, thereby increasing the contribution of plasma dispersion Δk_q^e .

The dipole phase mismatch (Δk_d) is a function of the spatial and temporal intensity distribution of the laser beam. It can be minimized by moving the focus across the gas medium. Since the dipole phase-mismatch depends on the spatial gradient of the laser intensity, it changes sign before and after the focus. The dipole wave-vector mismatch can be countered by the geometrical wave-vector mismatch by keeping the generation point a little behind the focus. In the experiment, therefore, one has to play with the medium length and density, focal condition, pulse duration, and intensity to optimize the conversion efficiency and the cutoff energy.

2.4 Photoionization

Photoionization is the process in which an atom or molecule absorbs a photon of sufficient energy, causing one or more electrons to be ejected from the atom or molecule. Depending on the frequency and intensity of the incident light, as well as the binding energy of the electrons in the system, different mechanisms of photoionization can occur. These are schematically illustrated in Figure 2.2. The most straightforward photoionization process is Single-Photon Ionization (SPI), where the energy of a single photon is greater than the minimum energy required to remove an electron from the system in its ground state:

$$A + \hbar\omega = A^+ + e^-. \quad (2.7)$$

The excess energy from the absorbed photon is mainly transferred to the ejected electron, rather than the recoiling ion, due to the conservation of total momentum and the large mass difference between the ion and electron. As a result, the kinetic energy of the ejected electron can be determined by the equation: $E_{kin}^e = \hbar\omega - I_p$, where $\hbar\omega$ represents the energy of the absorbed photon and I_p is the ground-state ionization potential of the system. In multi-electron systems, electron-electron correlation effects can cause the energy

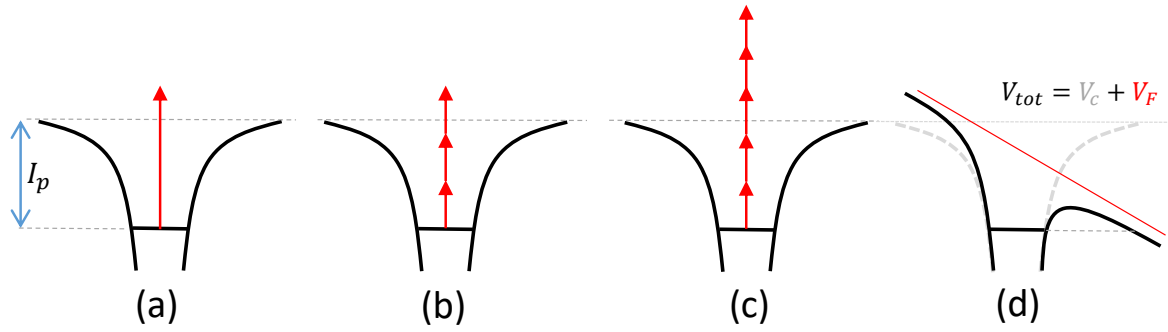


Figure 2.2. Photoionization processes in an atomic system. (a) Single-Photon Ionization (SPI), (b) Multi-Photon Ionization (MPI), (c) Above-Threshold Ionization (ATI), and (d) Tunnel Ionization (TI).

from the absorbed photon to be shared between multiple electrons, leading to simultaneous ionization plus excitation or the removal of additional electrons. Single-photon ionization spectroscopy generally employs XUV (Extreme Ultraviolet) or soft X-ray (SXR) sources.

The rate of single-photon ionization varies linearly with the pulse intensity (I):

$$\Gamma^{(1)} \propto \sigma^{(1)}(\omega) \frac{I(\omega)}{\hbar\omega} \quad (2.8)$$

where $\sigma^{(1)}$ is the single-photon ionization cross section.

When the energy of a single photon is insufficient to ionize the target, the combined energy of several photons can overcome the ionization potential of the system and lead to the ejection of an electron.

$$A + n\hbar\omega = A^+ + e^-; \quad E_{kin}^e = n\hbar\omega - I_p. \quad (2.9)$$

The rate of this process, called multi-photon ionization (MPI), scales as the n th power of the intensity [23]:

$$\Gamma^{(n)} \propto \sigma^{(n)}(\omega) \left(\frac{I(\omega)}{\hbar\omega} \right)^n. \quad (2.10)$$

Here $\sigma^{(n)}$ is the n -photon ionization cross section, and n is the minimum number of photons needed for ionization.

In multi-photon ionization, the atom can even absorb more than the minimum number of the photons required to ionize the atom, leading to photoelectrons with higher kinetic energy. This process is called above-threshold ionization (ATI). ATI can be identified in the kinetic-energy spectrum of the ejected electrons by discrete peaks at intervals of the photon energy:

$$A + (n + s)\hbar\omega = A^+ + e^-; \quad E_{kin}^e = (n + s)\hbar\omega - I_p. \quad (2.11)$$

The ionization rate of ATI is given by [24]:

$$\Gamma^{(n+s)}(I) \propto \sigma^{(n+s)}(\omega) \left(\frac{I(\omega)}{\hbar\omega} \right)^{n+s}. \quad (2.12)$$

When a strong laser pulse interacts with an atom or molecule, the oscillating electric field can temporarily modify the potential barrier that an electron would typically encounter. The effective potential barrier is the sum of the static Coulomb potential of the ion and a time-dependent linear potential due to the laser's electric field. As the laser electric field amplitude oscillates and changes sign, the effective potential oscillates as well, alternately lowering and raising the barrier. If the potential barrier is lowered enough by the laser electric field, the electron can tunnel through the barrier and escape from the atom or molecule. However, this tunneling process must occur within the half period of each laser cycle, because the laser field changes sign every half period. If the electron does not tunnel out within this time frame, the lowered potential barrier will be increased again when the field changes sign, making tunneling less likely during this cycle. In addition, tunneling in cycles is exponentially favored near the peak of the envelope.

While MPI and tunneling ionization both require a strong laser field, the Keldysh parameter (γ) is a useful quantity for distinguishing between these two regimes. This parameter is defined as the ratio of the tunneling time of an electron through a potential barrier to the period of the laser field [25]. It can be expressed as $\gamma = \omega\sqrt{2I_p}/E_0$, where ω is the frequency and E_0 is the maximum amplitude of the laser field. When the Keldysh parameter is much greater than 1, the dominant ionization process is multi-photon ionization, while for values much smaller than 1, tunneling ionization becomes dominant.

For $\gamma \ll 1$, the tunneling rate can be approximated as [26]

$$\Gamma^{tunnel} \propto N \exp\left(-\frac{2(2I_p)^{2/3}}{3E_0}\right), \quad (2.13)$$

where N is a slowly-varying function that depends on the cycle-averaged field intensity.

When the electric field of the laser pulse exceeds the Coulomb field experienced by the electron in the bound state, the electron can freely escape the Coulomb potential of the ion. This process is known as over-the-barrier ionization (OBI).

Laser-assisted photoionization

We now discuss a laser-assisted photoionization process, where a system is ionized in the presence of two synchronized fields: a high-frequency XUV field and a low-frequency IR field. The XUV field generates photoelectrons through single-photon ionization, which contribute to the mainband (M_0) with a kinetic energy given by $E_{kin}^M = \hbar\Omega - I_p$, where I_p is the ionization potential and $\hbar\Omega$ is the energy of the XUV photon. In the presence of residual ion potential, the emitted photoelectron can interact with the IR field, resulting in the formation of sidebands with higher or lower kinetic energy. In the photoelectron spectrum, these sidebands are spaced apart by the energy of the IR photon and their kinetic energy is determined by the number of IR photons exchanged. The kinetic energy of the

n th sideband is thus expressed as $\hbar\Omega \pm n\hbar\omega - I_p$, where n is the net number of IR photons absorbed (+) or emitted (-). The process is illustrated in Figure 2.3. It should be noted that in the absence of intermediate resonances, the likelihood of the IR field being absorbed before the XUV field to generate photoelectrons is much lower than the probability of the XUV photon being absorbed first, followed by the IR photons. Therefore, these transitions are not depicted in Figure 2.3.

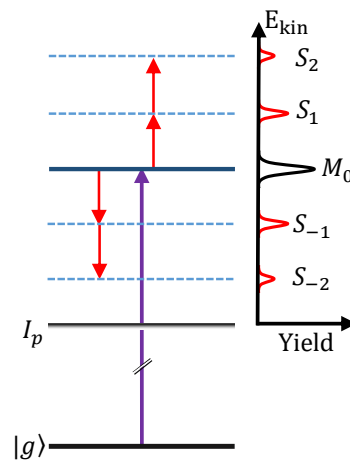


Figure 2.3. XUV-IR photoionization diagram. The XUV photon absorption creates a main peak (M_0) in the photoelectron spectrum (PES) and absorption of IR photons then creates positive sidebands (S_1, S_2, \dots) and emission of IR photons creates negative sidebands (S_{-1}, S_{-2}, \dots).

A common approach to determine the yield of the n -th sideband in XUV-IR two-color photoionization involves treating the one-photon XUV ionization as a first-order perturbation, while the interaction between the photoelectron and the IR field is handled non-perturbatively through the strong-field approximation (SFA) [27, 28]. Under this framework, and if the kinetic energy of the emitted photoelectron is significantly greater than the energy of the IR photon, the population of the n -th sideband can be approximated as

$$S_{\pm n} \propto J_{\pm n}^2(\vec{\alpha}_0 \cdot \vec{k}) |\langle \vec{k} | \vec{r} \cdot \vec{E}_{\text{XUV}} | i \rangle|^2, \quad (2.14)$$

where $\vec{\alpha}_0 = \vec{E}_{\text{IR}}/\omega^2$ and $\langle \vec{k} | \vec{r} \cdot \vec{E}_{\text{XUV}} | i \rangle$ is the dipole transition amplitude in XUV absorption creating a photoelectron with asymptotic momentum \vec{k} .

When the argument of the Bessel function is less than the order n , i.e., $(\vec{\alpha}_0 \cdot \vec{k}) < n$, the population of the n -th sideband in the continuum-continuum transition increases with the final momentum of the photoelectron. In the weak-field limit, one can use perturbation theory to estimate the population of the sidebands. However, estimating the population of higher-order sidebands requires the calculation of higher-order dipole-matrix elements, which is very challenging for $n > 1$.

2.5 Photoelectron Interferometry

Photoelectron interferometry is a versatile and powerful technique used for studying the dynamics of photoionization processes. The first step involves ionizing an atom or molecule with a laser pulse, creating a photoelectron with a specific energy and momentum. A second laser pulse is then used to perturb the photoelectron wavepacket, resulting in an interference pattern. By analyzing this interference pattern, valuable information about the ionization process can be obtained, such as the relative phases and amplitudes of the different ionization pathways, and the lifetimes of the excited states involved.

Two commonly used variants of this technique are RABBITT [7] and attosecond streaking [29]. In both techniques, an XUV pulse is used to initiate the electron dynamics, and an IR pulse is employed to probe the temporal evolution of the electron dynamics by varying the delay between the two pulses. However, the two techniques differ in their pump-pulse characteristics and probe-pulse intensities. In the attosecond streaking method, a single attosecond pulse (SAP) serves as the pump, and a few-cycle IR pulse with high intensity acts as the probe. In contrast, the RABBITT technique uses an attosecond pulse train (APT) as the pump and typically a longer IR pulse with lower intensity.

Since RABBITT was used in the present work, only this technique will now be described in some detail. A separate subsection is devoted to the extension of the standard one-sideband (1-SB) version to a three-sideband (3-SB) mode. 3-SB RABBITT contains additional information that is not accessible through 1-SB RABBITT and was specifically developed for this thesis.

2.5.1 1-SB RABBITT

RABBITT employs a two-color pump-probe scheme, where a superposition of an XUV-APT (pump) and a phase-locked IR pulse (probe) is used to photoionize a target, and the kinetic energy spectrum of the resulting photoelectron is measured as a function of the pump-probe delay. As the delay between the XUV-APT and IR pulse is varied, the photoelectron yield in the recorded spectra oscillates, and these oscillations encode the time delay information in the photoionization process.

The XUV spectrum, generated in the HHG process, typically comprises several odd harmonics of the IR pulse. Consequently, the ionization by the XUV pulse produces photoelectrons with kinetic energies that correspond to these harmonics:

$$E_{kin}(M_{q+1}) = \hbar(q+1)\omega - I_p; \quad q \in \text{even number} \quad (2.15)$$

These photoelectron peaks created directly by the XUV field are known as the main peaks or mainbands (M). They are separated by twice the photon energy of the HHG driving

field. When the photoelectrons created by the XUV pulse interact with the residual ion and the IR probe pulse, the kinetic energy of the photoelectrons can change. This change in energy occurs in steps that are multiples of the energy of the IR photons. As a result, new peaks in the photoelectron spectrum appear at energies in between the main peaks. These peaks are called sidebands (S). Their energies are given by:

$$E_{kin}(S_q) = \hbar(q \pm 1)\omega \mp \hbar\omega - I_p; \quad q \in \text{even number} \quad (2.16)$$

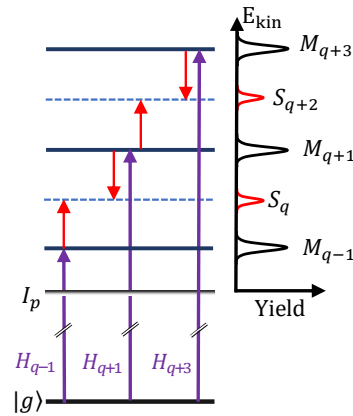


Figure 2.4. Energy diagram showing two sets of quantum paths leading to the formation of sidebands.

Figure 2.4 illustrates two sets of possible quantum paths leading to the same energy states of the respective sidebands. These arise from different combinations of XUV and IR photons. The sideband S_q , for example, can be generated in two distinct pathways: the first path involves the absorption of an XUV photon from the $(q-1)$ th harmonic (H_{q-1}) followed by the absorption of an IR photon, which we refer to as the absorption path ('a'). The second path involves the absorption of the next energetic harmonic H_{q+1} followed by the emission of an IR photon, which we refer to as the emission path ('e'). The sideband signal is formed by adding coherently all the quantum paths that lead to the same energy state. Note that the intensities of the mainbands, which are formed by the absorption of the XUV photons, are slightly weakened due to the redistribution of the flux into the sidebands.

When the IR field is weak, the transition to the SB can be modeled using second-order perturbation theory. The two-photon transition element that corresponds to the absorption of the XUV photon followed by the IR photon can be expressed as:

$$\begin{aligned} \mathcal{A}^{(2)}(\vec{k}_q; \Omega, \omega) &= -i\tilde{E}_\Omega \tilde{E}_\omega \lim_{\epsilon \rightarrow 0^+} \sum_i \frac{\langle \vec{k}_q | z | i \rangle \langle i | z | g \rangle}{\epsilon_g + \Omega - \epsilon_i + i\epsilon} \\ &= \tilde{E}_\Omega \tilde{E}_\omega M^{(2)}(\vec{k}_q; \Omega, \omega). \end{aligned} \quad (2.17)$$

Here ϵ_g is the ground-state energy. The sum/integral include all intermediate states denoted by $|i\rangle$, including the discrete Rydberg states and the ionization continuum. $\tilde{E}_\Omega = E_\Omega e^{i\phi_\Omega}$ and $\tilde{E}_\omega = E_\omega e^{i\omega\tau}$ (for absorption) are the complex electric-field amplitudes of the XUV-pump (Ω) and IR-probe (ω) pulses, respectively. τ is the temporal delay between the XUV and IR pulses. Both fields are polarized in the z direction, which is the chosen quantization axis.

As mentioned above, the sideband signal is formed by adding coherently all the quantum paths that lead to the same energy state:

$$\begin{aligned} S_q(\vec{k}_q, \tau) &\propto \left| \mathcal{A}^{(2,a)}(\vec{k}_q; (q-1)\omega, \omega) + \mathcal{A}^{(2,e)}(\vec{k}_q; (q+1)\omega, -\omega) \right|^2 \\ &\propto |\mathcal{A}^{(2,a)}|^2 + |\mathcal{A}^{(2,e)}|^2 + 2 |\mathcal{A}^{(2,a)}| |\mathcal{A}^{(2,e)}| \cos(\arg(\mathcal{A}^{(2,a)} \mathcal{A}^{(2,e)*})) \\ &\propto |\mathcal{A}^{(2,a)}|^2 + |\mathcal{A}^{(2,e)}|^2 + 2 |\mathcal{A}^{(2,a)}| |\mathcal{A}^{(2,e)}| \cos(2\omega\tau - \Delta\phi_{XUV} - \Delta\phi_{atom}) \end{aligned} \quad (2.18)$$

Here $\Delta\phi_{XUV} = (\phi_{q+1} - \phi_{q-1})$ is the phase difference (atto-chirp) between the harmonic fields $(q+1)$ and $(q-1)$, while $\Delta\phi_{atom} = \arg[M^{(2,a)}M^{*(2,e)}]$ is the phase difference between the dipole transition matrix element constituting the absorption and the emission paths.

Equation 2.18 again states that the yield of the sideband depends on the phase difference between two different paths. This phase difference can be varied by adjusting the temporal delay between the XUV and IR pulses, resulting in a delay-dependent oscillation of the yield. The yield oscillates at twice the IR photon frequency as the delay between the two pulses is varied. One can fit this yield oscillation to a cosine form, $I_0 + I_1 \cos(2\omega\tau - \phi_R)$, and thereby retrieve the phase and the contrast of the oscillation. The extracted phase is referred to as the RABBITT phase (ϕ_R) or simply the oscillation phase in this thesis. It is a composite term, which contains the spectral phase difference of the two harmonics involved in the two distinct paths and the phase difference of the two-photon dipole matrix elements describing the two distinct transition paths:

$$\phi_R = \Delta\phi_{XUV} + \Delta\phi_{atom}. \quad (2.19)$$

It is often convenient to express the phase in terms of the time as: $\tau_R = \frac{\phi_R}{2\omega}$. Hence the RABBITT phase can be written in terms of time as:

$$\tau_R = \Delta\phi_{XUV}/2\omega + \Delta\phi_{atom}/2\omega \quad (2.20)$$

The RABBITT technique was initially utilized to measure the spectral phases of the harmonics, $\Delta\phi_{XUV}$, in order to characterize the XUV-APT generated in the HHG process [7]. Assuming that the atomic phase varies smoothly with energy and that $\Delta\phi_{XUV}$ is much

larger than $\Delta\phi_{atom}$, the retrieved oscillation phase can be approximated as the spectral phase difference between two adjacent harmonics, i.e., $\phi_R \approx \Delta\phi_{XUV}$.

Since its introduction, RABBITT has been widely employed to measure relative photoemission time delays in a variety of systems, including atoms, molecules, and metal surfaces [14, 16, 30–32]. Similar to the concept of group delay in optics, a time delay for an electron wave-packet can be defined by taking the spectral derivative of its phase. In photoionization experiments, the relative photoemission delay between two electron wave-packets can be related to the difference in their spectral phase derivatives. To determine the relative photoemission time delay in two different photoemission processes using the RABBITT technique, the first step is to measure the relative atomic phase difference ($\Delta\phi_{atom}$) corresponding to the two processes. The atomic phase ϕ_{atom} , which is the phase of the two-photon dipole matrix element, can be decomposed into two terms [33]:

$$\phi_{atom} = \eta + \phi^{cc}. \quad (2.21)$$

Here η is called the Wigner phase, which is the phase of the dipole matrix element corresponding to single-photon ionization by the XUV, while ϕ^{cc} is called the continuum-continuum coupling phase (cc-phase). The latter corresponds to a phase change due to the interaction of the photoelectron with the Coulomb field of the residual ion and the IR field.

The concept of time delay in quantum mechanics was first introduced by Eisenbud [34] and later developed further by Wigner and Smith [35, 36] in the context of scattering processes. The EWS (Eisenbud-Wigner-Smith) time delay, also known as the Wigner delay, is defined as the spectral derivative of the scattering phase accumulated by the partial waves of the scattered particle as it passes through a short-range attractive potential. It is interpreted as the difference between the expected time of arrival of a wave packet at a detector in the absence of the potential and the actual time of arrival in the presence of the potential. The time delay can be positive or negative, depending on the energy of the incident particle and the properties of the potential. The photoionization process is considered a half-scattering process, hence in a photoionization measurements the Wigner delay corresponds to the photoionization delay. As mentioned above, it is the spectral derivative of the phase of the single-photon dipole matrix element.

From the RABBITT measurement, one can only get the total oscillation phase ϕ_R . Consequently, in order to measure the atomic phase difference ($\Delta\phi_{atom}$), one needs to first know the group delay of the XUV pulse train. In practice, the XUV group delay is often the dominant part of the total RABBITT phase and cannot be neglected. Therefore, a common approach is to make a relative measurement by comparing two different $\Delta\phi_{atom}$ values, which may correspond to electrons originating from different orbitals [14] or from different species [17].

Furthermore, even in the relative measurement of the atomic phase shift, one needs to know the continuum-continuum phase (ϕ^{cc}) in order to extract the relative Wigner phase from the relative phase of the two-photon matrix element. Numerous theoretical studies have been conducted [33,37,38] to evaluate ϕ^{cc} . It was found that ϕ^{cc} is a universal quantity, since it is mainly determined by the long-range Coulomb potential of the residual ion, rather than the properties of the short-range potential. To estimate the value of ϕ^{cc} , an asymptotic approximation was introduced [33] to derive an analytic expression for ϕ^{cc} . In the asymptotic approximation, ϕ^{cc} is indeed independent of the details of the short range-potential of the ionic species and also independent of the angular momentum of the continuum states involved.

However, angle-resolved RABBITT measurements in helium demonstrated that ϕ^{cc} does depend on the angular momentum of the continuum states [39]. Subsequent studies [40, 41] then showed that while ϕ^{cc} depends on the orbital angular momentum it still remains nearly universal in a sense that it doesn't depend on the species but only on the kinetic energy and the angular momenta. These experimental studies of ϕ^{cc} involved retrieving the amplitude and phase of the constituent partial waves of the electron wave packet (EWP) through a multi-dimensional fitting procedure of the angle-resolved delay-dependent photoelectron yield.

2.5.2 3-SB RABBITT

This thesis employs a novel variation of the standard RABBITT technique, called the three-sideband (3-SB) RABBITT technique, to study the continuum-continuum phase. Unlike previous methods that only probed single continuum-continuum transitions, our new approach allows us to investigate many-order transitions.

To implement the 3-SB RABBITT technique, the separation between the harmonics in the XUV spectra is adjusted. First, a second-harmonic generation of the fundamental laser pulse is performed, and this second harmonic is then used to drive the HHG. This results in an XUV spectrum containing odd harmonics of the second harmonic of the fundamental pulse. Two consecutive peaks in the XUV spectrum are now separated by four times the frequency of the fundamental pulse that is still used as the probe. As a result, photoionization in the superposition of the XUV-APT and the IR fields leads to the formation of three sidebands between two mainbands, as shown in Figure 2.5.

For each sideband, Figure 2.5 shows the two lowest-order transition paths that determine the delay-dependent oscillation in the photoelectron yield. We have omitted the other paths, which might contribute significantly to the yield but do not contribute much to the oscillations. (See publication II [42] for details.) To induce the oscillation in the yields of

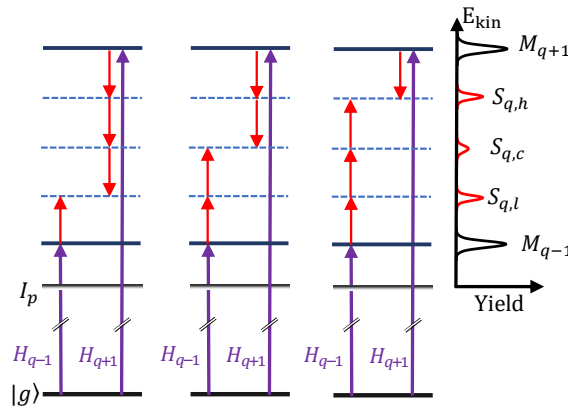


Figure 2.5. Transition diagram showing the formation of mainbands (M) via single photoionization by the harmonics (H) in the XUV pulse and the three sidebands (S : lower, central and higher) formed by the absorption or emission of multiple probe photons.

the sidebands, there must be interference between at least two paths involving distinct harmonics. The oscillations observed in the lower (S_l) and higher sidebands (S_h) are mainly due to the interference between a two-photon path and a four-photon path, whereas the oscillation in the central sideband (S_c) results from the interference between two terms of the same (third) order. The transition amplitudes of each quantum path can be described using lowest-order perturbation theory. To obtain delay-dependent yields of the sidebands, we again consider the coherent sum of two distinct absorption and emission paths. As discussed in detail in Publication II, the relevant formulas are:

$$\begin{aligned}
 S_{q,l}(\vec{k}_l, \tau) &\propto \left| \mathcal{A}^{(2,a)}(\vec{k}_l; (q-1)\omega, \omega) + \mathcal{A}^{(4,e)}(\vec{k}_l; (q+1)\omega, -3\omega) \right|^2 \\
 &\propto \left| \tilde{E}_{q-1} \tilde{E}_\omega M_{q,l}^{(2,a)} + \tilde{E}_{q+1} \tilde{E}_\omega^3 M_{q,l}^{(4,e)} \right|^2 \\
 &\propto I_0^l + I_1^l \cos(4\omega\tau - \Delta\phi_{XUV} - \Delta\phi_{atom}^l + \pi)
 \end{aligned} \tag{2.22}$$

$$\begin{aligned}
 S_{q,c}(\vec{k}_c, \tau) &\propto \left| \mathcal{A}^{(3,a)}(\vec{k}_c; (q-1)\omega, 2\omega) + \mathcal{A}^{(3,e)}(\vec{k}_c; (q+1)\omega, -3\omega) \right|^2 \\
 &\propto \left| \tilde{E}_{q-1} \tilde{E}_\omega^2 M_{q,c}^{(3,a)} + \tilde{E}_{q+1} \tilde{E}_\omega^2 M_{q,c}^{(3,e)} \right|^2 \\
 &\propto I_0^c + I_1^c \cos(4\omega\tau - \Delta\phi_{XUV} - \Delta\phi_{atom}^c)
 \end{aligned} \tag{2.23}$$

$$\begin{aligned}
 S_{q,h}(\vec{k}_h, \tau) &\propto \left| \mathcal{A}^{(4,a)}(\vec{k}_h; (q-1)\omega, 3\omega) + \mathcal{A}^{(2,e)}(\vec{k}_h; (q+1)\omega, -\omega) \right|^2 \\
 &\propto \left| \tilde{E}_{q-1} \tilde{E}_\omega^3 M_{q,h}^{(4,a)} + \tilde{E}_{q+1} \tilde{E}_\omega^* M_{q,h}^{(2,e)} \right|^2 \\
 &\propto I_0^h + I_1^h \cos(4\omega\tau - \Delta\phi_{XUV} - \Delta\phi_{atom}^h + \pi)
 \end{aligned} \tag{2.24}$$

Here, $\Delta\phi_{atom}^{l/c/h}$ is the phase difference between the absorption and emission dipole matrix elements, denoted as $M^{(a)}$ and $M^{(e)}$, respectively. These matrix elements correspond to different orders in the lower, central, and higher sidebands. We see that the oscillations in the yields of all three sidebands occur at the same frequency (4ω) as the delay is varied.

Additionally, the XUV-group delay contribution is the same in all three sidebands, since they are generated by the same pair of harmonics.

The atomic phase information contained in the three sidebands, therefore, can provide insights into the multi-order continuum-continuum interaction. Publication II [42] delves deeper into this topic by utilizing perturbation theory and the asymptotic approximation to study multi-photon continuum-continuum transitions and uncover further details about the atomic phases of the three sidebands. In the 3-SB RABBITT measurements, the oscillation phase (ϕ_R) is expressed in units of time as $\tau_R = \frac{\phi_R}{4\omega}$.

In systems where ionization occurs through a single angular-momentum channel, such as atomic hydrogen and helium, the Wigner phase contribution is the same for all three sidebands, and any discrepancy in the atomic phase among the sidebands originates solely from the continuum-continuum coupling [43]. However, in systems involving multiple angular-momentum channels in the XUV ionization process, like argon, the Wigner phase associated with each channel contributes differently to the atomic phases of the three sidebands [44]. As a result, the RABBITT phase becomes a complex function of the angular-momentum-dependent transition amplitudes and their associated phases. By analyzing the RABBITT phase at different emission angles, one can still extract information about the ratios of the transition amplitudes and the phase differences between different channels, although direct information about the continuum-continuum phase alone is not possible.

Chapter 3

Few-Level Model Simulation

In this chapter, we conduct simulations based on the few-level model (FLM) to explore the phases of oscillation of sidebands and their angle-dependence in both the 1-SB and 3-SB RABBITT schemes. The FLM is a modification of the two-level model, where the system now comprises a ground state and several discrete excited states. The system undergoes excitation by an XUV pulse, which transfers a portion of the population from the ground state to the excited states, and an IR pulse redistributes the population among the excited states. To characterize the system, we assign an amplitude and phase for each dipole transition. We perform RABBITT simulation by varying the XUV and IR temporal delays while monitoring the population of the excited states as a function of the delay. The population of these states oscillates with the delay, and the phases of these oscillations is retrieved for the further analysis.

We begin by defining the time-varying interaction Hamiltonian of the system as $H(t) = H_0 + H'(t)$, where H_0 represents the unperturbed Hamiltonian and $H'(t)$ represents the perturbation induced by the external field. In the length gauge of the dipole approximation, $H'(t)$ can be expressed as $\vec{r} \cdot \vec{E}(t)$, where $\vec{E}(t) = \vec{E}_{\text{XUV}}(t) + \vec{E}_{\text{IR}}(t)$ denotes the total electric field of co-linearly polarized IR and XUV pulses. The time-dependent wavefunction of the system can be expressed as a sum of the eigenstates of the field-free Hamiltonian written as

$$|\Psi(t)\rangle = \sum_j c_j(t) e^{-i\omega_j t} |\phi_j\rangle. \quad (3.1)$$

Here, $c_j(t)$ represents the time-dependent coefficients, ω_j is the energy of the j -th eigenstate denoted as $|\phi_j\rangle$.

We substitute the wavefunction expressed in terms of stationary states (given by equation (3.1)) into the time-dependent Schrödinger equation (TDSE), $i\partial_t |\Psi(t)\rangle = H(t) |\Psi(t)\rangle$, and project it onto $\langle\phi_i|$. This yields a set of differential equations that describe the time evolution of the time-dependent population coefficients.

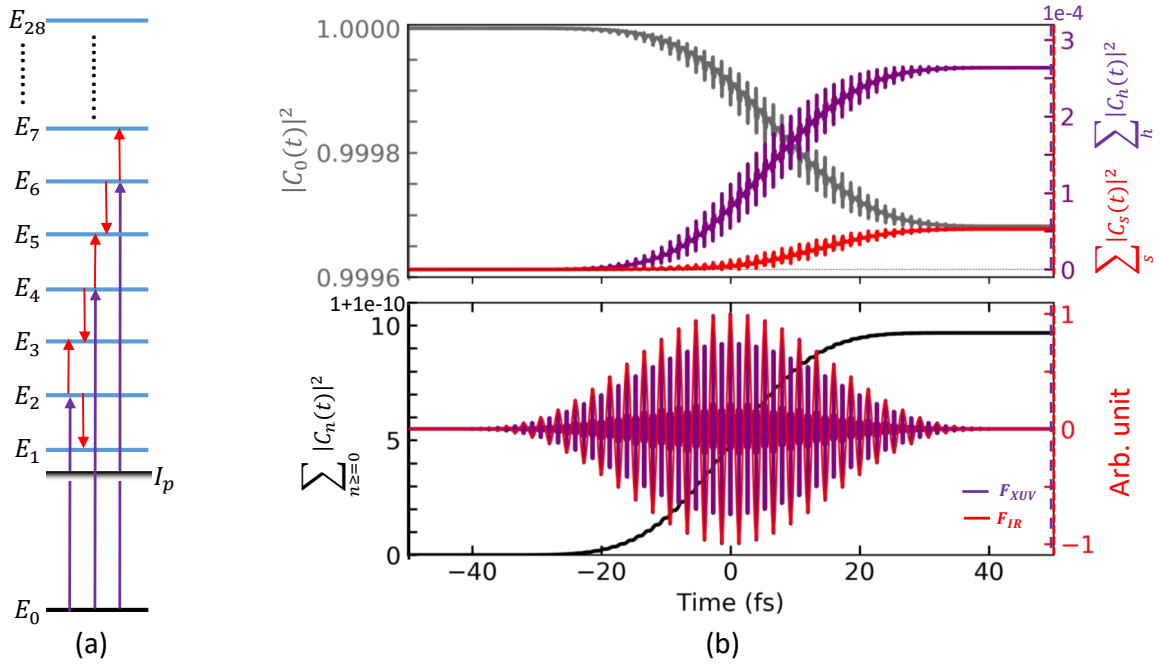


Figure 3.1. Energy levels in the FLM (a). Upper panel of (b) shows temporal variation in population of ground state (grey, left y-axis), states directly connected via XUV pulse (purple, right y-axis) and states coupled by IR pulse (red, right y-axis). Lower panel displays total population change over time (black, left y-axis) and temporal profile of normalized XUV (purple) and IR (red) fields (right y-axis).

$$\frac{d}{dt}c_i(t) = -i \sum_j \mu_{ij} E(t) e^{-i\omega_{ji}t} c_j(t) \quad (3.2)$$

Here, μ_{ij} represents the dipole matrix element for the transition from the j -th to the i -th energy level, and ω_{ji} denotes the energy difference between the two levels. We use the Runge-Kutta method to solve the set of coupled differential equations (3.2) numerically to obtain the time-dependent population coefficients $c_j(t)$.

The model features a system consisting of a finite number of discrete energy levels, as illustrated in Figure 3.1(a). The ground state is assigned an energy of zero ($E_0 = 0$), while the other states have energies higher than the hydrogen atom's ionization potential of 13.6 eV. While we refer to the states above the ionization threshold as continuum states in this chapter, they are actually discrete. We limit our analysis to a few discrete energy states above the ionization threshold that are equally spaced and can be resonantly excited by the pump or probe pulses. The spacing between adjacent levels in the continuum is equal to the energy of a single probe photon (E_{ph}).

We express the dipole matrix elements responsible for coupling the ground state to the

continuum states via a single-photon ionization as

$$\mu_{0,j} = \tilde{\mathcal{D}}(k_j) e^{-i\eta(k_j)}, \quad (3.3)$$

where k_j represents the momentum of the j th state.

We employ the momentum representation of the ground state in atomic hydrogen [45] to determine the amplitude of the dipole transition matrix element:

$$\tilde{\mathcal{D}}(k_j) = \frac{2\sqrt{2}Z^{5/2}}{\pi(k_j^2 + Z^2)^2} \quad (3.4)$$

The phase term η of the dipole matrix element corresponds to the single-photon ionization phase. To express this phase, we use the Coulomb phase shift, which is defined as [45]:

$$\eta(k_j) = \Gamma \left(1 + \ell - i \frac{Z}{k_j} \right); \quad \ell = 1(s \rightarrow p) \quad \& \quad j > 0 \quad (3.5)$$

Here, ℓ represents the angular momentum quantum number of the j th state.

We describe the matrix element responsible for coupling within the continuum as

$$\mu_{i,j} = \frac{k_i + k_j}{2} e^{-i\phi^{cc}(k_i, k_j)}; \quad i, j > 0 \quad (3.6)$$

Here, k_i and k_j are the momenta of the two states, and $\phi^{cc}(k_i, k_j)$ is the phase associated with the coupling. This phase is obtained from the asymptotic approximation, as stated in [33]:

$$\phi^{cc}(k_i, k_j) = \arg \left[\frac{(2k_j)^{iZ/k_j} \Gamma[2 + iZ(1/k_j - 1/k_i)]}{(2k_i)^{iZ/k_i} (k_j - k_i)^{iZ(1/k_j - 1/k_i)}} \right]. \quad (3.7)$$

At the beginning, when the fields are not present, the system is in its ground state with $c_0 = 1$ and $c_i = 0$ for $i > 0$. When the laser field is introduced, the population of the ground state starts to distribute among the states that can be resonantly coupled by the field. The upper panel of Figure 3.1(b) illustrates how the population of the ground state (grey) and all the states that the XUV and IR pulses can resonantly couple evolve over time. Specifically, the purple line represents the total population of all states directly connected by the XUV pulse, while the red line shows the population of all states coupled by IR pulses. In the lower panel, the black line displays the total population of all states, which remains almost constant at 1, thus conserving the norm. Additionally, the temporal profiles of the normalized XUV (purple) and IR (red) fields are shown on the right side.

3.1 1-SB RABBITT

For the 1-SB RABBITT simulation, we used a Fourier-limited Gaussian pulse centered around 800 nm with a temporal duration of 25 fs for the probe pulse and an XUV pulse

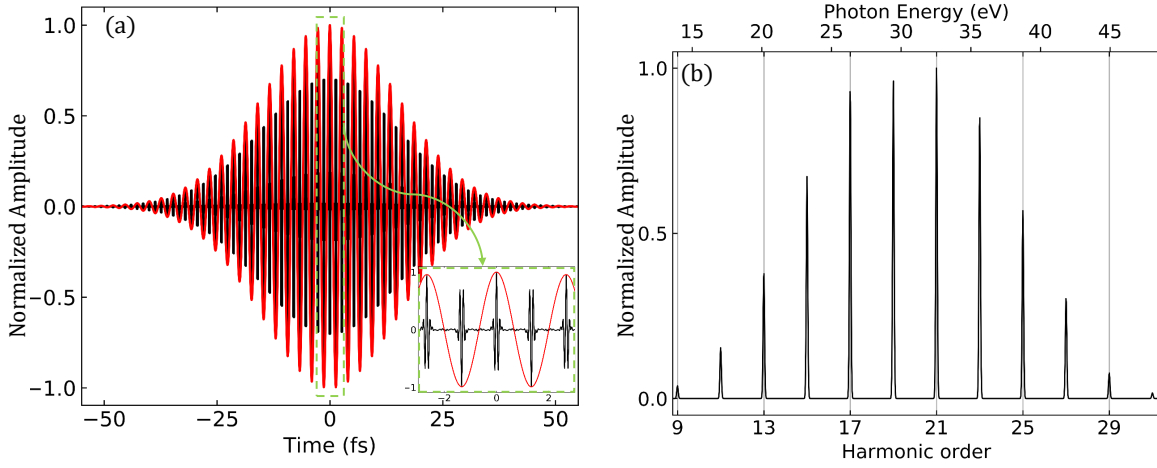


Figure 3.2. Normalized XUV-APT field (black) and the probe field (red) (a) Fourier spectra of the XUV-APT (b).

train of 25 fs. The peak intensity of the XUV pulse was set at 2.38×10^{-8} a.u., while that of the IR pulse was 1.4×10^{-6} a.u. [1 a.u. = 3.51×10^{16} W/cm².] Figure 3.2(a) displays the normalized field amplitudes of the probe pulse (red) and the XUV pulse train (black), with an inset showing two attosecond bursts in each period of the probe pulse. Figure 3.2(b) shows the XUV-spectrum containing 12 odd harmonics of 800 nm ($H_9, H_{11}, \dots, H_{31}$). The strength of each harmonic was chosen arbitrarily.

We varied the temporal delay between the XUV and IR pulses from $\tau = 0$ to $\tau = 2T_0$ in increments of $T_0/20$, solving equation 3.2 at each delay step. The population of all states $|c_i(\tau)|^2$ was then recorded at the end of each calculation.

The results are presented in Figure 3.3, where Figure 3.3(a) depicts the population of the continuum states at the end of calculation when only the XUV pulse is included (black). The red curve represents the population when both pulses are used. It is averaged over all the delay steps. The false colormap in Figure 3.3(b) illustrates the population change of the states as a function of delay (RABBITT trace), with the colormap scale chosen to highlight the yield oscillations in the weaker sidebands. As the temporal delay is varied, the population of both the mainbands and the sidebands undergoes oscillations at twice the frequency of the probe pulse. In addition, the oscillations in the mainbands are out of phase with those in the adjacent sidebands.

To extract the phases of the oscillations, the population of the states is fitted to a cosine functional form given by:

$$|c_q(\tau)|^2 = A^q + B^q \cos(2\omega\tau - \phi_R^q) \quad (3.8)$$

In Figure 3.4(a), the retrieved phase (ϕ_R) of the 2ω oscillation for the mainbands (yellow squares) and sidebands (red circles) at different kinetic energies are shown. To correct for

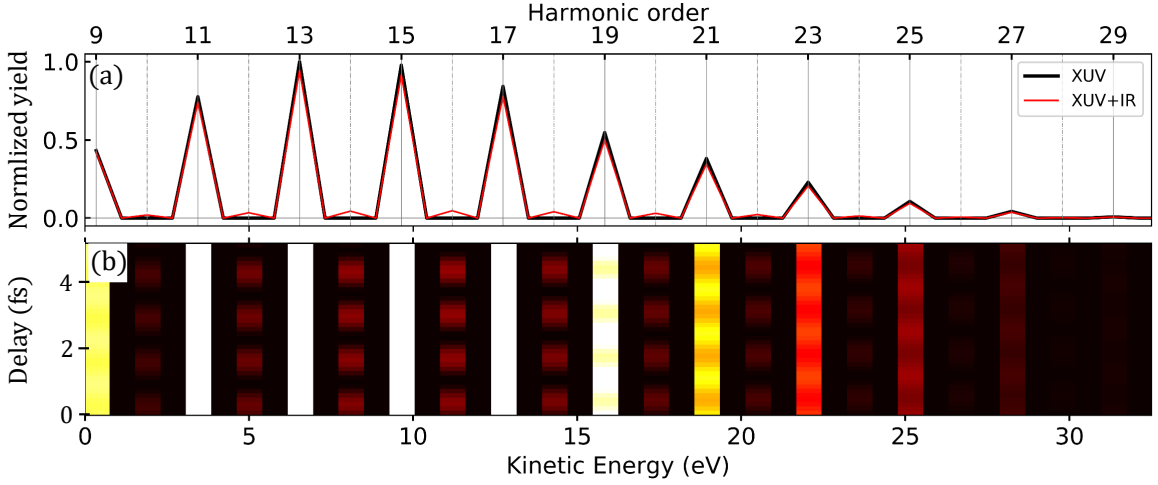


Figure 3.3. Normalized XUV-only PES (black) and the delay-integrated PES in RABBITT scan (red) (a). RABBITT spectrogram (b).

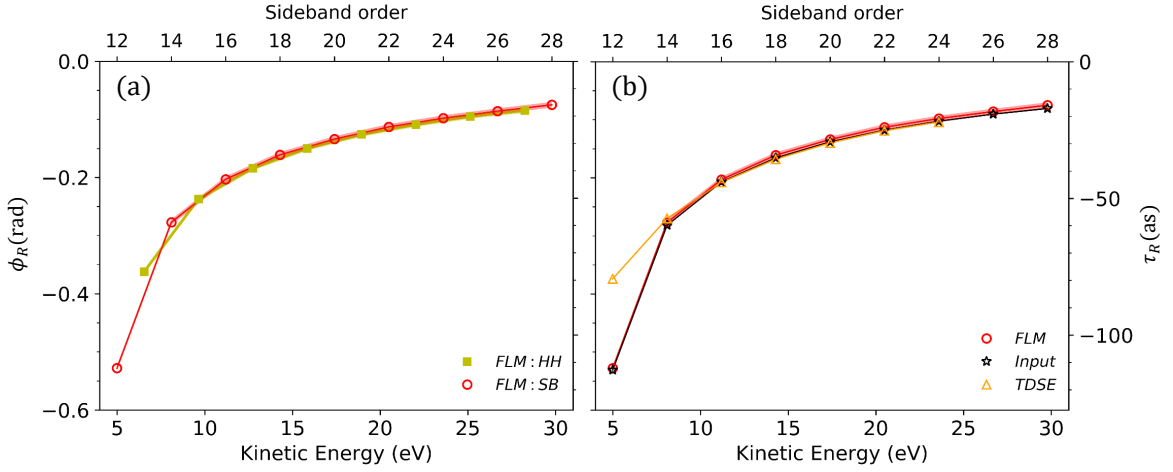


Figure 3.4. The phase retrieved from the oscillation in the sidebands (red circle) and main bands (yellow square) from the FLM RABBITT calculation (a). The phase of the sideband obtained from the RABBITT trace generated in FLM (black star), and TDSE calculation (yellow triangle) and the analytically estimated phase (black star) (b).

the out-of-phase oscillation between the sidebands and mainbands, an additional π phase was subtracted from the mainband before plotting in Figure 3.4(a).

Figure 3.4(b) compares the retrieved phase values (ϕ_R) of the sidebands obtained from the FLM simulation (red circles), TDSE simulation (yellow triangles), and analytical input phase (black stars). The analytical phase is given by

$$\phi_{atom}^{ana}(k_q) = \eta(k_{q+1}) + \phi^{cc}(k_q, k_{q+1}) - \eta(k_{q-1}) - \phi^{cc}(k_q, k_{q-1}) \quad (3.9)$$

The FLM simulation reproduces the analytical phase, which represents the phase difference between the two paths following step-wise transitions.

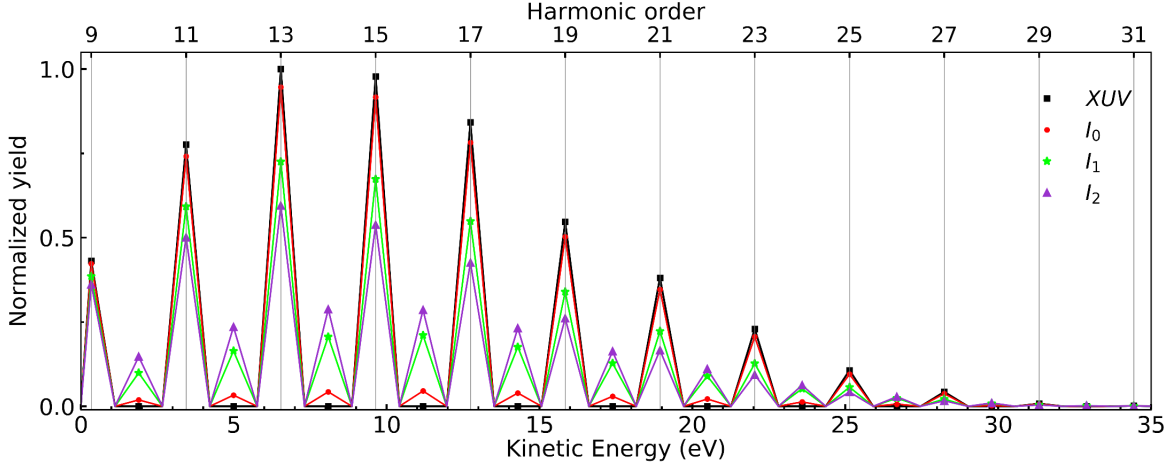


Figure 3.5. XUV-only (black) PES and delay integrated PES in the RABBITT scan at varying probe intensities normalized to the XUV-only PES.

To highlight the impact of IR intensity on oscillation phase, we performed a RABBITT scan using three probe intensities: $I_0 (= 1.4 \times 10^{-6} \text{ a.u.})$, $I_1 = 6I_0$, and $I_2 = 10I_0$. Additionally, a second-order chirp with a value of ($\phi_{\text{xuv}} = 0.01 \text{ fs}^2$) was introduced to the XUV-APT. To simplify the analysis, the Wigner and cc-coupling phases were disabled ($\eta = \phi^{cc} = 0$). Figure 3.5 illustrates the delay-integrated photoelectron spectrum obtained from RABBITT scans performed at three different probe intensities, accompanied by the PES obtained with XUV-only. With an increase in the IR intensity, depletion of the mainbands begins on the high-energy side. At the highest IR intensity, the delay-averaged yield of the sidebands above the 20th band exceeds that of the next mainbands.

Figure 3.6(a) presents the RABBITT spectrogram at probe intensity I_0 , while Figure 3.6(b) exhibits the oscillation in the sideband yield for various IR intensities (I_0 , I_1 , and I_2). Figure 3.6(b) shows the oscillation in the sideband yield for various IR intensities (I_0 , I_1 , and I_2). To maintain consistency in the scale, for each intensity calculation, the sideband yield is first integrated over the entire delay range and then subtracted from the delay-dependent yield to eliminate the background. The resulting signal is then normalized to its maximum value before being plotted in Figure 3.6(b). Figure 3.6(c) presents the Fourier transform of these oscillations. When the IR intensity is at its lowest value, the yield of the sidebands shows purely sinusoidal oscillations, and the Fourier spectrum exhibits only one peak at 2ω . As the IR intensity increases, the oscillations become distorted, and additional peaks at 4ω and 6ω start to emerge. At the highest IR intensity used, the 4ω peak becomes more prominent than the 2ω peak for the highest energy sideband (S_{28}). These results suggest that the contribution of higher-order transitions depends not only on the IR intensity but also on the energy of the sideband. This phenomenon occurs because the coupling in the continuum increases with both the momentum of the photoelectron and the IR intensity.

For arbitrary probe intensity, the delay dependence of the photoelectron signal can then

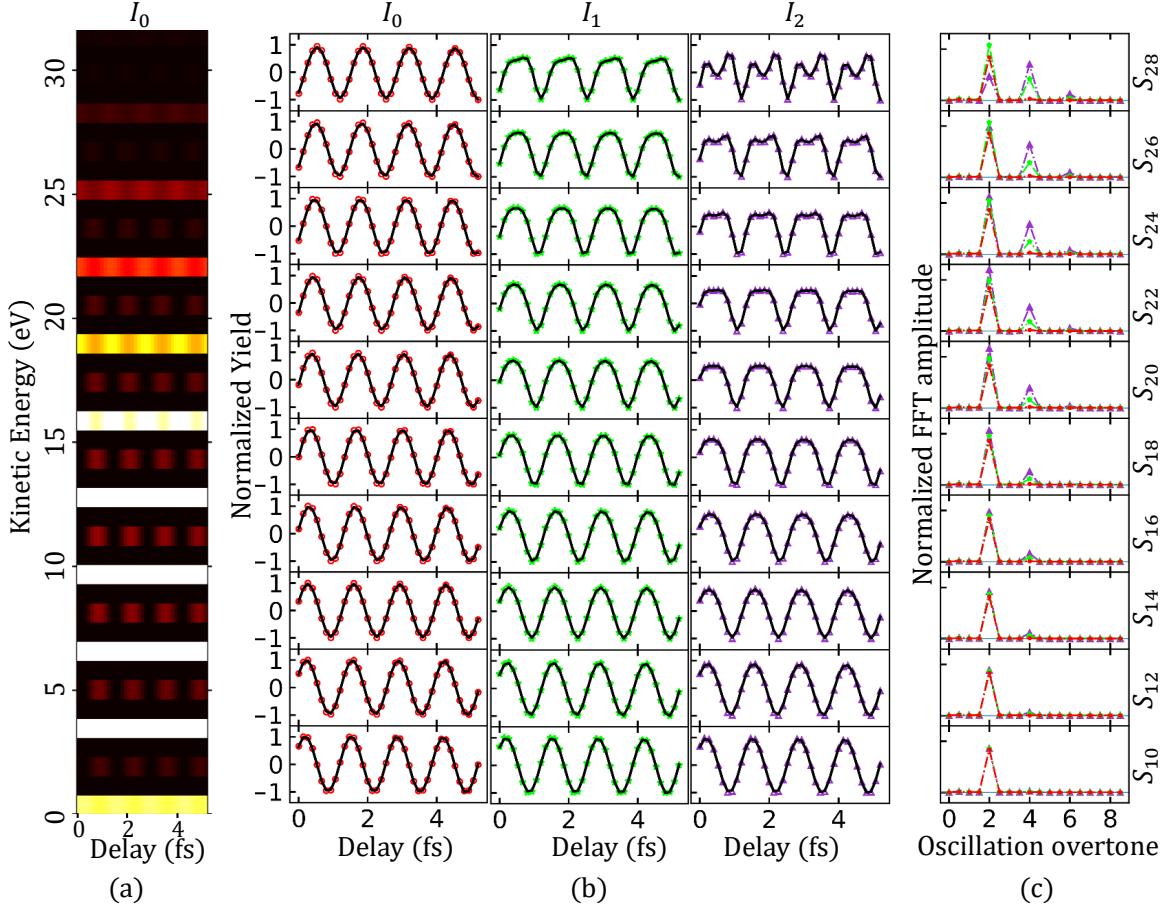


Figure 3.6. RABBITT spectrogram at I_0 (a), the yield line out of the SBs at varying IR intensities (b), and corresponding Fourier spectra (c) shown for I_0 (red dot), I_1 (green star), and I_2 (purple triangle).

be decomposed into the overtones of 2ω :

$$S(\tau) = A + B\cos(2\omega\tau - \phi_R) + B\cos(4\omega\tau - \phi_{2R}) + C\cos(6\omega\tau - \phi_{3R}) + \dots \quad (3.10)$$

In Figure 3.6(b), the red curve shows the delay-dependent yield of the sidebands, while the black curve shows the fit to the functional form $A + B\cos(2\omega\tau - \phi_R) + B\cos(4\omega\tau - \phi_{2R}) + C\cos(6\omega\tau - \phi_{3R})$. For all three applied IR intensities, Fig. 3.7 displays the retrieved phase ϕ_R corresponding to the 2ω oscillation of the yield.

As the IR intensity is increased, we note a significant deviation in the retrieved oscillation phase, with the most substantial deviation being observed in the highest energy sideband. At low intensities, the 2ω oscillation in the q^{th} -SB is dominated by transition scheme (T_A), and the oscillation phase is simply the group delay of the two neighboring harmonics ($\phi_R^q = \phi_{xuv}^{q-1} - \phi_{xuv}^{q+1}$).

As the intensity increases, the likelihood of n th-order interactions increases as I^n , causing higher-order IR photon exchange originating from the distant mainband and ending up to the sideband (S_q) to become more substantial. These higher-order transitions also

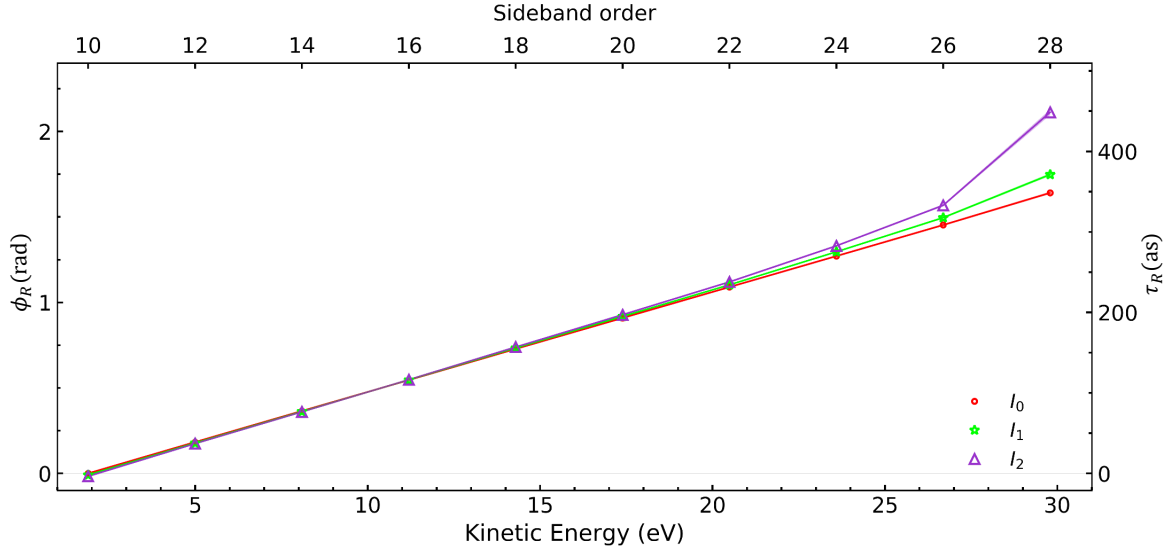


Figure 3.7. Oscillation phase corresponding to 2ω oscillation at probe intensity I_0 (red circle), I_1 (green star), and I_2 (purple triangle).

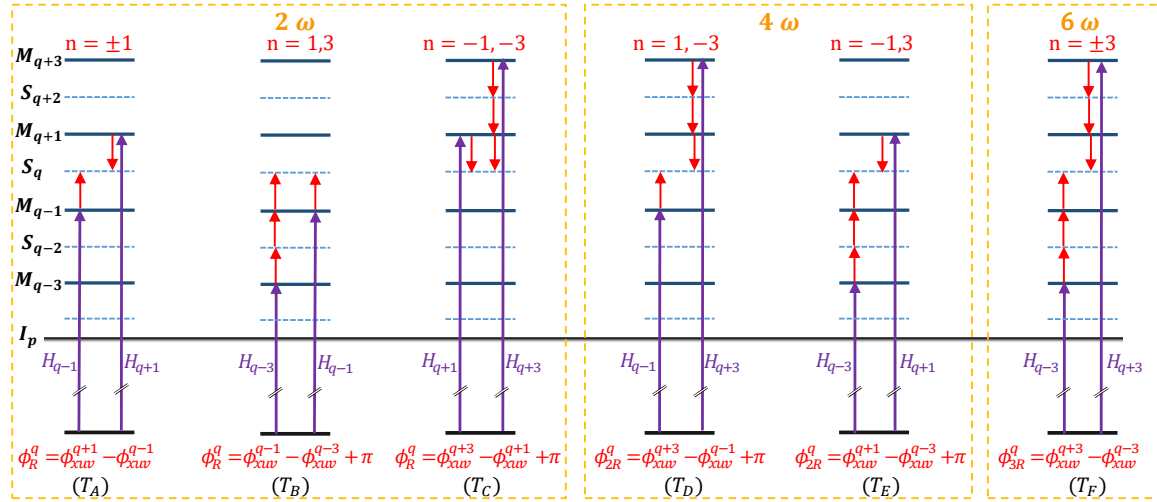


Figure 3.8. Interference schemes that cause delay-dependent oscillations in the sideband yield. T_A , T_B , and T_C lead to oscillations at 2ω , with T_A being dominant at low intensity. T_D and T_E result in oscillations at 4ω , while T_F leads to oscillations at 6ω . The oscillation phases for each interference are also indicated.

contribute to the 2ω oscillation through schemes T_B and T_C .

Schemes T_D and T_E result in yield oscillation at 4ω , and T_F at 6ω . Since every order of interaction adds a $\pi/2$ phase, the oscillation phase (ϕ_R^q) obtained from T_B and T_C has an extra π phase compared to that obtained from T_A . As a result, the relative magnitude of the 2ω oscillation may start to decrease with increasing IR intensity, since the oscillation due to T_B and T_C is opposite to that of T_A . This is why the peak corresponding to 4ω oscillation in Figure 3.6(c) is higher than that of 2ω for S_{28} at the IR intensity I_2 . Furthermore, the interference between transition terms involving different harmonic pairs contains different

oscillation phases, and the resultant phase of 2ω oscillation in the sideband signal is the average of all the ϕ_R^q weighted according to their relative interference amplitude.

The effect of the higher-order terms on the retrieved phase becomes even more significant when the magnitude of the two adjacent main peaks is imbalanced, which occurs in the high-energy region where the magnitude of the mainbands decreases rapidly with energy due to decreasing harmonic strength as well as the decreasing ionization cross section. As a result, the interference of the two lowest-order terms (T_A) involving adjacent mainbands is incomplete, resulting in weaker oscillation, while the oscillation resulting from the interference of higher-order transition paths involving two strong lines, but both from the lower-energy side (T_B), can become stronger, thereby significantly altering the retrieved phase. This is illustrated in Figure 3.7, which shows that the phase varies rapidly with intensity beyond S_{20} , because the harmonics in the XUV spectrum decrease after H_{19} , and the higher-order interference term (T_B) becomes comparable in strength to the lowest-order interference term (T_A).

There are additional transition pathways up to fourth-order that are possible but not shown in Figure 3.8. These pathways involve back and forth transitions between the two continuum states. Since each transition accumulates a phase of $\pi/2$, interference involving these pathways can also contribute to the reduction of oscillation contrast.

Angle-dependence

Up to this point, the energy levels used in the simulation did not incorporate any orbital quantum numbers. To account for the angular dependence in the RABBITT phase, we split each energy level used in the simulation into five degenerate states corresponding to the five

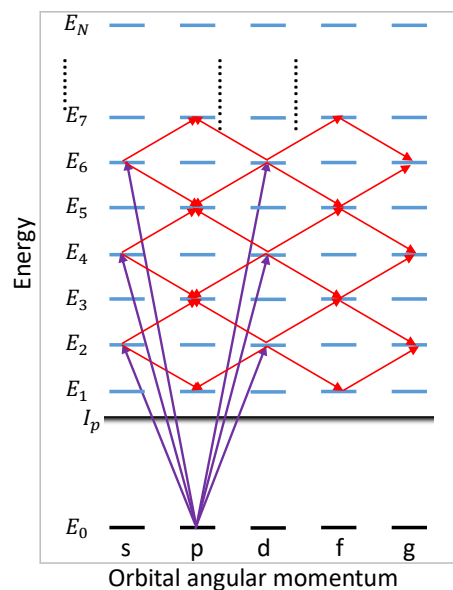


Figure 3.9. Transition scheme between degenerate energy states with different orbital quantum numbers.

angular momentum states ($\ell = 0, 1, 2, 3, 4 : s, p, d, f, g$), as illustrated in Figure 3.9. We ignore the role of magnetic quantum numbers.

Only transitions that satisfy the dipole selection rule of $\Delta\ell = \pm 1$ are allowed. The magnitude and phase of the dipole transition matrix element now depend not only on the kinetic energies but also on the orbital angular momentum of the two states. We used the Fano-propensity rule to assign the magnitudes of these matrix elements, which suggests that the absorption (emission) of a photon in a dipole transition tends to increase (decrease) the angular momentum [41, 46, 47].

We investigate two scenarios: one where the initial state has zero angular momentum in the s -state ($\ell_i = 0$), and the other where the system starts in the p -state ($\ell_i = 1$). In Figure 3.10 (a), the transition amplitudes for absorption from the ground state (s or p) to different angular momentum states of the continuum states are plotted as a function of kinetic energy. The information displayed in Fig.3.10 (a) regarding the $p \rightarrow s$ and $p \rightarrow d$ transitions was obtained from reference [41]. As for the $s \rightarrow p$ transition, its values were generated as

$$A_{abs}^w(s \rightarrow p) = \sqrt{(A_{abs}^w)^2(p \rightarrow d) + (A_{abs}^w)^2(p \rightarrow s)}. \quad (3.11)$$

The single-photon ionization phase for the transition from the initial angular momentum state (ℓ_i) to the final angular momentum state (ℓ) is now expressed as

$$\eta_{\ell, \ell_i}(k) = \eta_{\ell}(k) - \frac{\pi\ell}{2} + \delta_{\ell, \ell_i}(k). \quad (3.12)$$

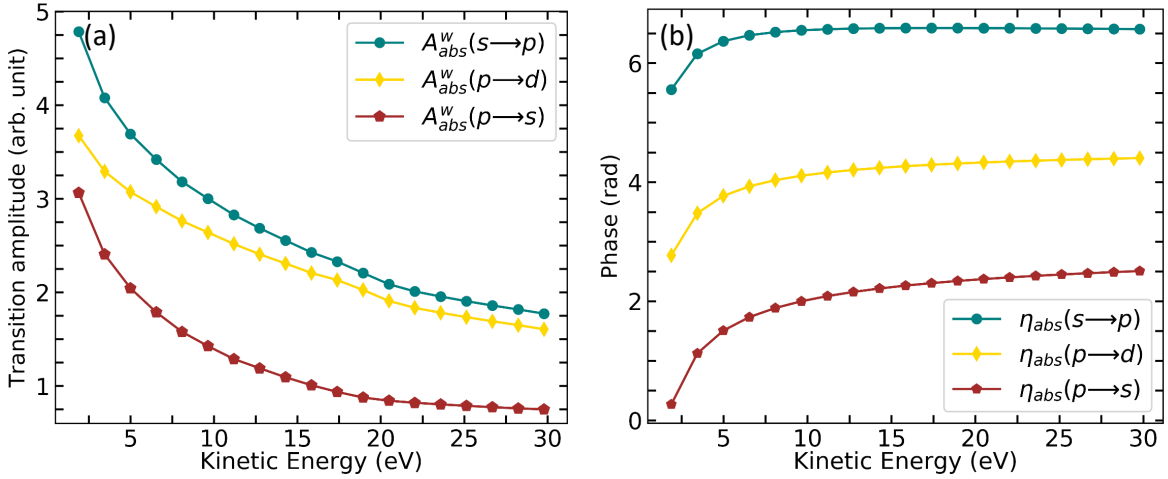


Figure 3.10. Dipole coupling amplitude (relative) (a) and phase (b) for transitions from the ground state to continuum states through different angular-momentum channels.

Figure 3.10(b) presents the kinetic-energy dependence of the phase of the dipole matrix elements, which describe the transition from the ground state to the continuum states through different angular-momentum channels via single-photon absorption. To improve the representation of the single-photon ionization phase, a short-range correction with $\delta_{0,1}(k) =$

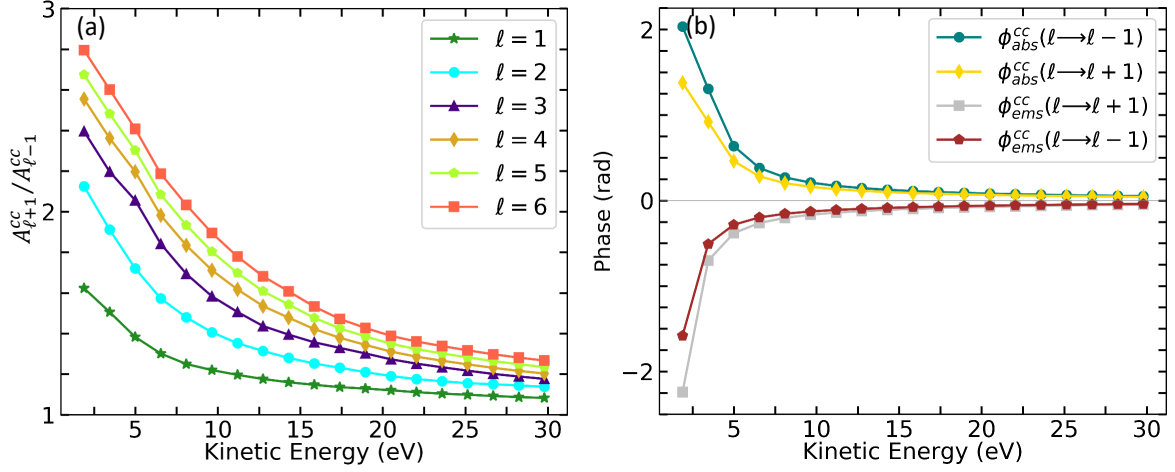


Figure 3.11. Amplitude ratio of transitions with increasing and decreasing orbital angular momentum (a), and the phase of the dipole matrix element corresponding to the increase and decrease of the angular momentum during absorption and emission in the continuum (b), as a function of kinetic energy.

1.2π and $\delta_{2,1}(k) = 0$ [41] was added to the hydrogenic Wigner phase. Additionally, $\delta_{1,0}(k) = 0$ was arbitrarily assigned.

Figure 3.11 (a) presents the ratio of transition amplitudes for increasing and decreasing ℓ states during IR photon absorption in the continuum. The values for $\ell = 1, 2, 3$ were obtained from reference [41], while the values for the remaining ℓ states were artificially generated. Figure 3.11 (b) displays the kinetic energy dependence of the phase of the dipole matrix element corresponding to the increase or decrease of angular momentum during absorption and emission in the continuum.

We utilized the same XUV and IR pulses as those described in the previous section. Both pulses were Fourier-limited and had a duration of 25 fs, as shown in Figure 3.2. The XUV pulse intensity remained unchanged at 2.38×10^{-8} a.u. For the IR pulse, we selected the lowest peak intensity (1.4×10^{-6} a.u.) utilized in the previous section. This allowed us to focus on two-photon transitions for the sidebands while safely ignoring any higher-order contributions.

To incorporate the dependence of the yield and oscillation phase on the electron emission angle, we first multiply the population coefficients $c_{q,\ell}$ of all the angular momentum states of the q th energy state with their corresponding spherical harmonics and then add them coherently:

$$S_q(\tau, \theta) = \left| \sum_{\ell=0}^5 c_{q,\ell}(\tau) Y_{\ell,0}(\theta) \right|^2. \quad (3.13)$$

Here, $S_q(\tau, \theta)$ represents the signal in the q th sideband, $c_{q,\ell}(\tau)$ is the population coefficient

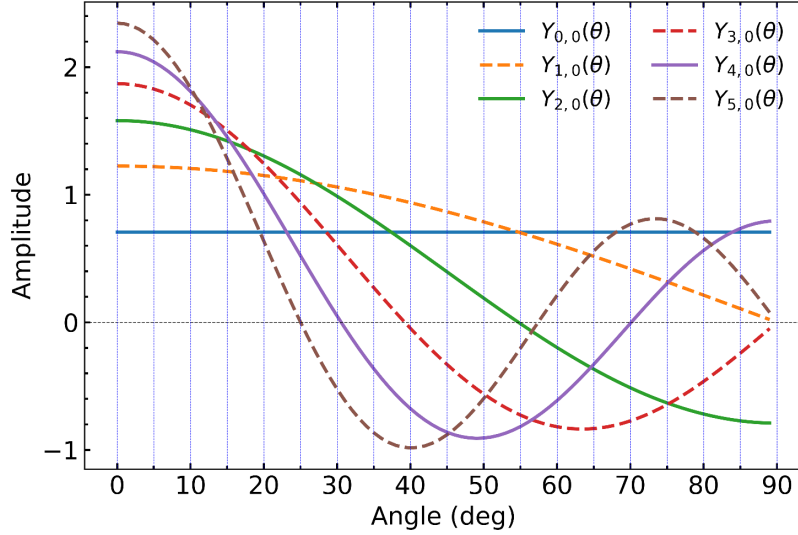


Figure 3.12. First six orthonormalized spherical harmonics as a function of polar angle.

of the ℓ th angular momentum state of the q th sideband at the end of the calculation for the XUV-IR temporal delay τ , $Y_{\ell,0}$ is the spherical harmonic of order ℓ , and θ is the angle between the photoelectron momentum and the polarization of the XUV and IR pulses.

When the ground state is an s -state, a two-photon interaction creates a sideband that occupies both s and d states. Both absorption ($H_{q-1} + \omega$) and emission ($H_{q+1} - \omega$) pathways can lead to population in the s and d states of the sideband. The absorption and emission pathways leading to the same angular momentum state of the sideband interfere with each other ($s - s$ or $d - d$), resulting in a delay-dependent oscillation in the population of that angular momentum state. Similarly, the absorption and emission pathways leading to different final angular momentum states of the sideband also interfere with each other ($s - d$), producing an oscillation in the population that varies with the delay. The phase of the oscillation depends on the angular momentum channels involved in the ionization step and in the cc transition. As the magnitude of the spherical harmonic changes with the polar angle, this also leads to an angle-dependent yield variation in the sideband and a change in the overall oscillation phase of its yield. This can be expressed as:

$$\begin{aligned}
 S_q(\tau, \theta) &= A_0^q(\theta) + Y_{0,0}(\theta)Y_{0,0}(\theta) C_s^{q,a} C_s^{q,e} \cos(2\omega\tau + \phi_R^{s,s}) \\
 &\quad + Y_{2,0}(\theta)Y_{2,0}(\theta) C_d^{q,a} C_d^{q,e} \cos(2\omega\tau + \phi_R^{d,d}) \\
 &\quad + Y_{0,0}(\theta)Y_{2,0}(\theta) \left(C_s^{q,a} C_d^{q,e} (\cos(2\omega\tau + \phi_R^{s,d}) + C_d^{q,a} C_s^{q,e} \cos(2\omega\tau + \phi_R^{d,s})) \right) \\
 &= A_0^q(\theta) + B^q(\theta) \cos(2\omega\tau + \phi_R^q(\theta)).
 \end{aligned} \tag{3.14}$$

Here, $A_0^q(\theta)$ represents all contributions that do not participate in the delay-dependent oscillation. $C_\ell^{q,a/e}$ denotes the transition probability to the ℓ th angular momentum state of the q th sideband via the path involving harmonic ($a : H_{q-1}$) or the harmonic ($e : H_{q+1}$). The

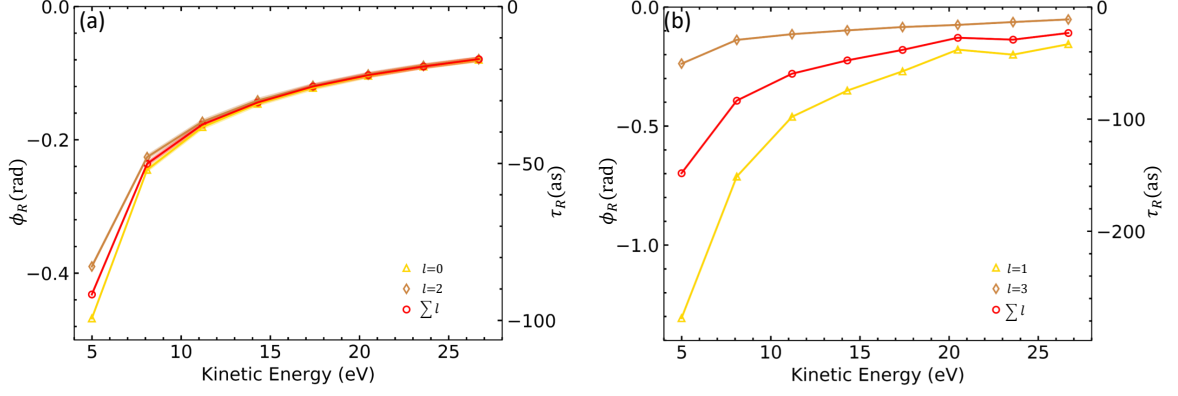


Figure 3.13. RABBITT phase as a function of sideband energy for ground states with (a) $l_i = 0$ and (b) $l_i = 1$. The red circles represent the angle-integrated phase, while the golden stars and brown triangles show the phase from each individual ℓ channel.

phase difference between the two interfering transition paths is denoted by $\phi_R^{\ell',\ell}$, where ℓ and ℓ' represent the final angular momentum states with possible values of 0 or 2.

Since both the single photoionization and the cc-coupling phase vary with the angular momentum, the phase of each distinct transition term depends not only on the final angular momentum states but also on all the intermediate angular momentum states that are encountered in reaching the final state. In the case of angle-integrated measurements, the interference between two different final ℓ states, such as $s - d$ and $d - s$, vanishes. Therefore, the resulting RABBITT phase (ϕ_R) is the weighted average of the RABBITT phases of each individual ℓ state.

Figure 3.13 shows the RABBITT phase obtained from the delay-dependent signal of each individual angular momentum state ($\phi_R^{\ell,\ell}$) of the sidebands, as well as the angle-integrated RABBITT phase (ϕ_R). To retrieve the oscillation phase from each ℓ state of the sideband, we fit the delay-dependent population of each ℓ state to the following functional form:

$$|c_{q,\ell}(\tau)|^2 = A + B \cos(2\omega\tau - \phi_R^{\ell,\ell}). \quad (3.15)$$

When the initial state is an s -state, the only bound-continuum transition possible is through an $s \rightarrow p$ transition. As a result, the Wigner contribution will be the same in all the different RABBITT phases ($\phi_R^{\ell',\ell}$) corresponding to different angular momentum channels, regardless of the cc-transition channels. The difference between $\phi_R^{s,s}$ and $\phi_R^{p,p}$ is thus solely due to the difference in the cc-phase (ϕ^{cc}), which depends on the angular-momentum channels. As the kinetic energy increases, the dependence of ϕ^{cc} on ℓ reduces (c.f. 3.11), resulting in $\phi_R^{s,s}$ and $\phi_R^{p,p}$ becoming more similar.

When the ground state is a p -state, however, the sidebands will consist of a mixture of p and f states. In both the absorption and emission paths, there are two possible distinct channels to reach the p -state of the sideband: $p \rightarrow s \rightarrow p$ or $p \rightarrow d \rightarrow p$. Consequently,

the p -state of the sideband will have a combination of two different Wigner phases: $\eta_{0,1}$ and $\eta_{2,0}$. In contrast, the f -state of the sideband can only be accessed through a single channel $p \rightarrow d \rightarrow f$, and therefore will contain only the Wigner phase $\eta_{2,0}$. The RABBITT phases ($\phi_R^{\ell',\ell}$) that result from the interference between the final angular-momentum states of the absorption and emission paths will have distinct Wigner phase contributions depending on the specific path taken. As the kinetic energy increases, the single-photon transition amplitude decreases, with a faster rate for $p \rightarrow s$ compared to $p \rightarrow d$, as depicted in Figure 3.10. Consequently, at higher kinetic energy, the $p \rightarrow d$ channel dominates the single-photon transition, reducing the contribution of the Wigner phase corresponding to the $p \rightarrow s$ transition ($\eta_{0,1}$). This leads to a decrease in the difference between $\phi_R^{p,p}$ and $\phi_R^{f,f}$, as shown in Figure 3.13(b).

We now present an explanation for the angular variation in the RABBITT phase. It is worth repeating that the oscillation phases arising from the interference of different angular-momentum channels are unique. As Equation 3.14 indicates, the weight of these interference terms is modulated by the associated spherical harmonics, resulting in an angle-dependent overall retrieved phase.

Figure 3.14 illustrates the angle-dependent overall RABBITT phase ($\phi_R(\theta)$), as well as the various RABBITT phases ($\phi_R^{\ell',\ell}$) obtained from considering the possible interferences between transitions ending up in different or the same angular-momentum states of SB_{12} . Figure 3.14 (a) illustrates the case when the system starts in an s -state, while Figure 3.14 (b) represents the case when the system begins in a p -state.

The horizontal lines in panels (a) and (b) correspond to the interference between the absorption and emission paths that end in the same final ℓ state, as indicated by the yellow triangle ($\phi_R^{s,s}$ or $\phi_R^{p,p}$) and the brown diamond ($\phi_R^{d,d}$ or $\phi_R^{f,f}$), respectively. To obtain these lines, the delay-dependent signal from each individual angular-momentum state was isolated using Equation (3.14). The lines with a sharp π -jump represent the interference between the absorption and emission paths ending in different final ℓ states, shown as green squares ($\phi_R^{s,d}$ or $\phi_R^{d,s}$ in (a) and $\phi_R^{p,f}$ or $\phi_R^{f,p}$ in (b)).

To obtain the oscillation phase of the cross-term interference, the first step is to isolate the cross-term interference signal $S'_q(\tau, \theta)$ by subtracting the signal in the individual angular-momentum states from the total angle-dependent signal $S_q(\tau, \theta)$ of the sideband. This can be achieved as:

$$S'_q(\tau, \theta) = \left| \sum_{\ell} c_{q,\ell}(\tau) Y_{\ell,0}(\theta) \right|^2 - |c_{q,\ell_1}(\tau) Y_{\ell_1,0}(\theta)|^2 - |c_{q,\ell_2}(\tau) Y_{\ell_2,0}(\theta)|^2 \quad (3.16)$$

Note that $\ell_1 = 0$ and $\ell_2 = 2$ for an s ground state while $\ell_1 = 1$ and $\ell_2 = 3$ in the case of a ground p -state. We then fit the delay-dependent signal of $S'_q(\tau, \theta)$ again to a cosine form ($A + B \cos(2\omega\tau - \phi_R^{\ell_1,\ell_2})$) and retrieve the phase of the cross-term interference.

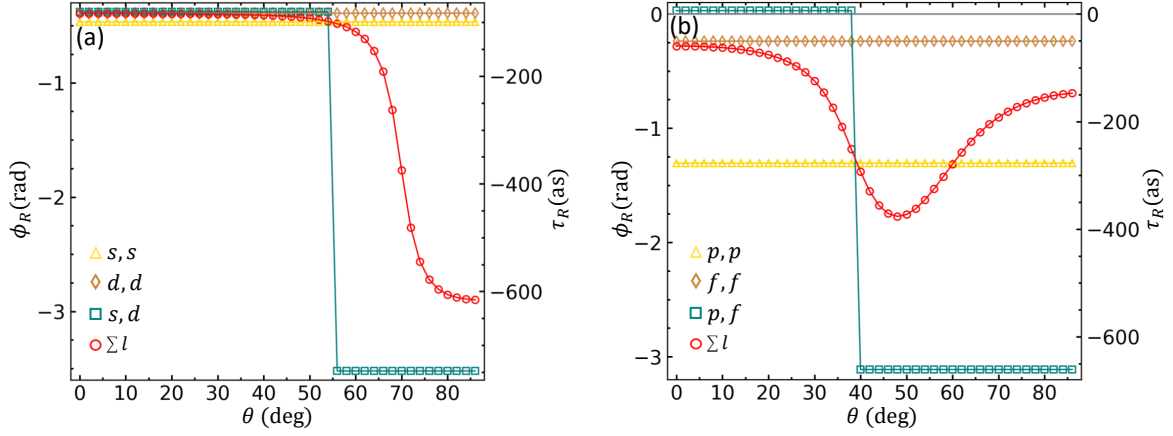


Figure 3.14. ϕ_R retrieved from individual ℓ channels (pink star and golden triangle) and including all the ℓ channels (red circle) in SB_{12} . The system starts in either an s -state (a) or a p -state (b).

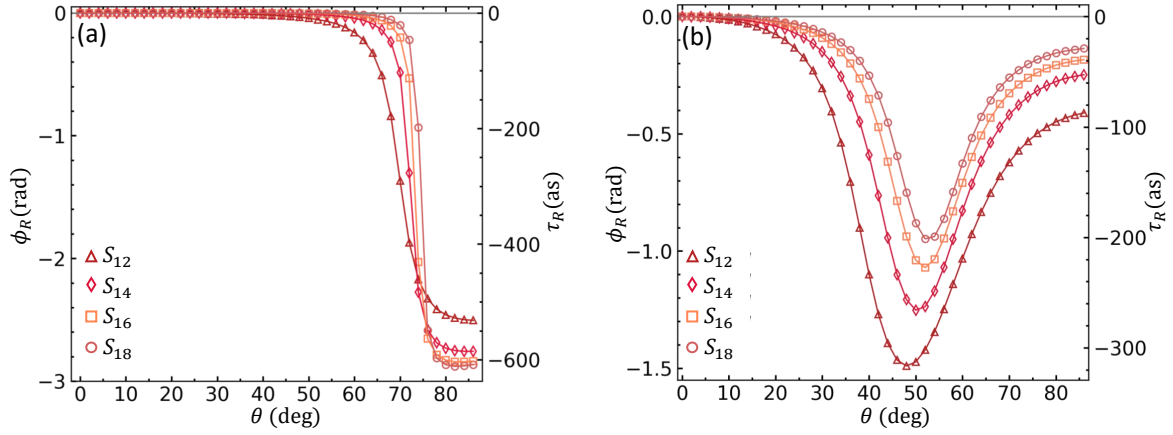


Figure 3.15. Angle-dependence of the RABBITT phase (ϕ_R) for different sidebands in the case of the ground state being an s -state (a) or a p -state (b).

The cross-term oscillation phase in Figure 3.14 (a) exhibits a π -jump due to the sign change in the coefficient $Y_{0,0}(\theta)Y_{2,0}(\theta)$ at 54.7° . In Figure 3.14 (b), on the other hand, the phase jump occurs at 39° due to the sign change in the coefficient $Y_{1,0}(\theta)Y_{3,0}(\theta)$. The angle-resolved RABBITT phase is the average of all these phases, taking into account the transition amplitudes and the amplitudes of the corresponding spherical harmonics, as shown in equation 3.14.

In the vicinity of zero degree, the RABBITT phase ($\phi_R(\theta)$) varies slowly with respect to the angle. As the angle increases, the weight of $Y_{2,0}(\theta)$ decreases, while $Y_{0,0}(\theta)$ remains constant. Consequently, the RABBITT phase $\phi_R(\theta)$ shifts towards $\phi_R^{s,s}$. At $\theta = 54.7^\circ$, $Y_{2,0}$ becomes zero, resulting in the RABBITT phase being the same as the s -channel phase, i.e., $\phi_R(\theta = 54.7^\circ) = \phi_R^{s,s}$. Beyond 54.7° , the RABBITT phase $\phi_R(\theta)$ continues to decrease with increasing θ , following the phase of the cross term, thereby indicating a significant

weight of this term. This behavior is attributed to the propensity rule, where photon emission primarily creates an electron in the s -state, while photon absorption creates a predominantly d -state photoelectron. As a result, the interference between the two terms has a higher weight compared to the terms with identical final ℓ state.

Figure 3.14 (b) illustrates the scenario where the initial state is a p -state. The phase difference among the three interfering terms in this case is much larger than that in the $\ell_i = 0$ case, resulting in a more significant variation in $\phi_R(\theta)$ even before the appearance of an angular node. At $\theta = 39^\circ$, $Y_{3,0}$ vanishes, causing the RABBITT phase to match the p -channel phase. Around 39° , the cross-term undergoes a π jump, causing $\phi_R(\theta)$ to shift towards the negative cross-term phase. The magnitude of the spherical harmonics ($|Y_{1,0}Y_{3,0}|$) peaks near 57° and declines thereafter. Moreover, the cross-term is not as pronounced in this case. Although the absorption process favors transitions to the f -state over the p -state due to the propensity rule, there are two ways to reach the p -state, and only one way to reach the f -state, making the overall transition amplitude to the p -state comparable to that of the f -state, even for absorption. Therefore, at larger angles, the contribution of the cross-terms decreases faster than that from same-channel interference, resulting in $\phi_R(\theta)$ moving towards the weighted average of $\phi_R^{p,p}$ and $\phi_R^{f,f}$.

Figure 3.15 displays the angle-dependent RABBITT phase for different sideband orders. In both cases, where (a) $\ell_i = 0$ and (b) $\ell_i = 1$, the variation of ϕ_R with angle becomes flatter as the sideband order increases. This is because the difference in $\phi_R^{\ell',\ell}$ corresponding to different angular-momentum states decreases with increasing kinetic energy. Additionally, the angle at which the phase varies significantly shifts to higher values, indicating that the ratio of the magnitudes of the cross-channel interference to the same-channel interference decreases with kinetic energy.

3.2 3-SB RABBITT

To simulate 3-SB RABBITT, the XUV-APT is modified such that the frequency peaks in its spectrum are separated by four times the fundamental frequency.

The XUV spectrum is now composed of nine odd harmonics of the second harmonic of the probe frequency, namely H_5, H_7, \dots, H_{21} , as shown in Figure 3.16 (a). The spectral height of the harmonics is chosen arbitrarily. Figure 3.16 (b) displays the temporal profiles of the Fourier-limited 25-fs XUV field (in black) and the probe field (in red), along with four attosecond bursts every optical cycle of the probe pulse in the inset. The intensity of the XUV-APT is retained at $I_{\text{XUV}} = 2.38 \times 10^{-8}$ a.u., similar to the previous case.

The numerical approach used in the 1-SB RABBITT simulation is also applied in the 3-SB RABBITT simulation. The coupling strength and phases remain the same. To start

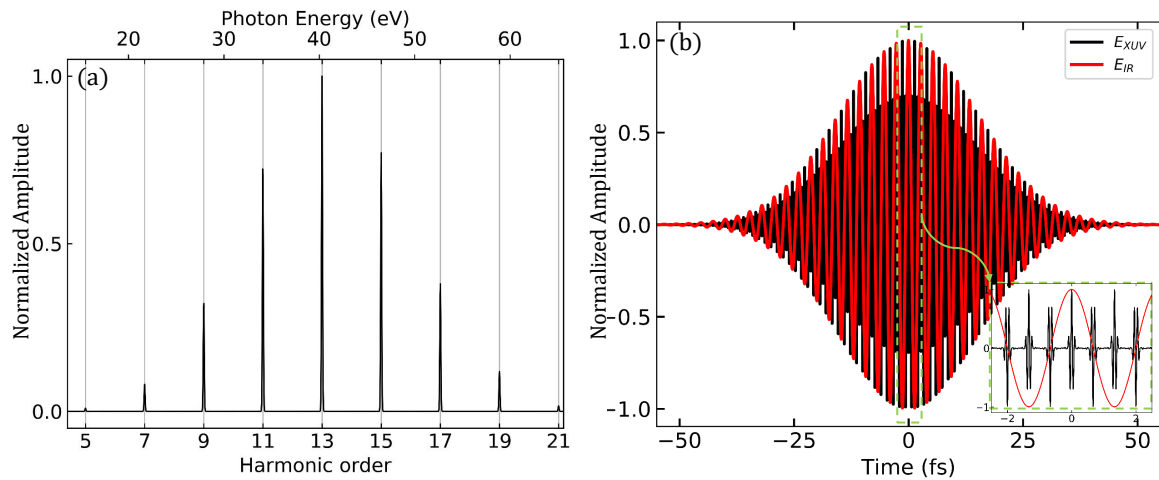


Figure 3.16. Spectral profile of the XUV pulse (a) and the temporal profiles of the XUV (black) and IR (red) fields (b).

with, we present the FLM simulation of the 3-SB RABBITT without any ℓ -degeneracy. The simulation result with a probe intensity of $I_{IR} = 5 \times 10^{-6}$ a.u. is shown in Figure 3.17. The upper panel displays the PES generated by the XUV-APT (black) only, and the PES averaged over the entire delay scan (red). The lower panel shows the 3-SB RABBITT spectrogram on the colormap. The colorplot scale range is selected to clearly exhibit the oscillations in the higher and lower sidebands.

As the delay between the XUV and IR pulses is scanned, we observe oscillations in the signals of both the sidebands and the mainbands. The dominant frequency of these oscillations is 4ω , and the signal can be represented as $A + B \cos(4\omega\tau - \phi_R)$ as a function of delay.

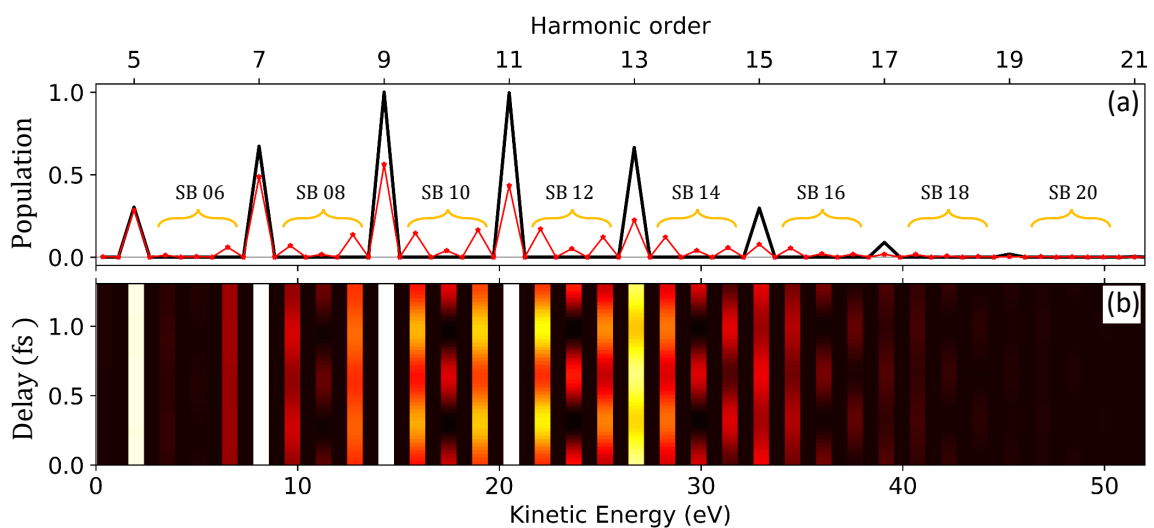


Figure 3.17. (a) 3-SB RABBITT trace; (b) XUV-only PES (black) and delay-integrated PES (red) in the RABBITT scan.

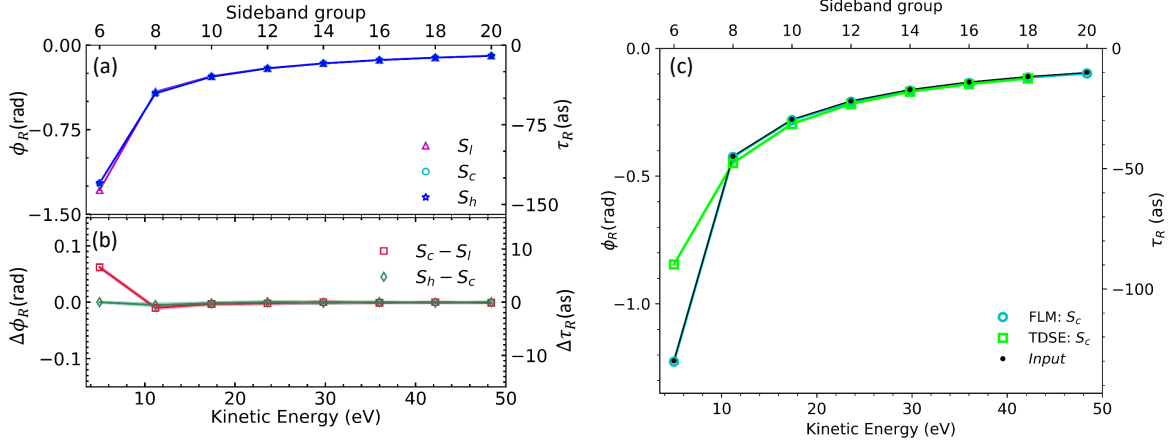


Figure 3.18. RABBITT phase of three sidebands vs. kinetic energy of the central sideband. (a) Relative phase difference (b). The input phase (black dot), phase retrieved from the FLM simulation (blue circle), and the phase retrieved from the TDSE simulation in atomic hydrogen (green square) for the central sideband (S_c) (c).

Due to the increase in coupling strength between neighboring states with increasing kinetic energy, the sideband oscillations are more noticeable at higher energies compared to those near threshold. We extracted the oscillation phases in the yield of all three sidebands and removed the extra π -phase from the lower and higher sidebands. The resulting phases are plotted as a function of the kinetic energy of the central sideband in the upper panel of Figure 3.18 (a). In Figure 3.18 (b), we plot the phase differences between the lower and higher sidebands relative to the central sideband. We observe that the phases in all three sidebands are almost identical, with a minor difference in the lower sideband of the 6th SB group. Figure 3.18 (c) compares the analytical or input phase (represented by a black dot), the retrieved oscillation phase from the FLM 3-SB RABBITT simulation (shown as a cyan circle), and the ϕ_R obtained from a TDSE simulation of 3-SB RABBITT in atomic hydrogen (as described in paper II, [42]).

The analytical (or input) phase is obtained by considering step-wise transitions and accumulating the phase contributions from each photon interaction. For the three sidebands, the analytical phases can be calculated using the following equations:

$$\begin{aligned} \phi_{atom}^{ana}(k_{l,q}) = & (\eta(k_{q+1}) + \phi^{cc}(k_{h,q}, k_{q+1}) + \phi^{cc}(k_{c,q}, k_{h,q}) + \phi^{cc}(k_{l,q}, k_{c,q})) \\ & - (\eta(k_{q-1}) + \phi^{cc}(k_{l,q}, k_{q-1})). \end{aligned} \quad (3.17a)$$

$$\begin{aligned} \phi_{atom}^{ana}(k_{c,q}) = & (\eta(k_{q+1}) + \phi^{cc}(k_{h,q}, k_{q+1}) + \phi^{cc}(k_{c,q}, k_{h,q})) \\ & - (\eta(k_{q-1}) + \phi^{cc}(k_{l,q}, k_{q-1}) + \phi^{cc}(k_{c,q}, k_{l,q})). \end{aligned} \quad (3.17b)$$

$$\begin{aligned} \phi_{atom}^{ana}(k_{h,q}) = & (\eta(k_{q+1}) + \phi^{cc}(k_{h,q}, k_{q+1})) \\ & - (\eta(k_{q-1}) + \phi^{cc}(k_{l,q}, k_{q-1}) + \phi^{cc}(k_{c,q}, k_{l,q}) + \phi^{cc}(k_{h,q}, k_{c,q})). \end{aligned} \quad (3.17c)$$

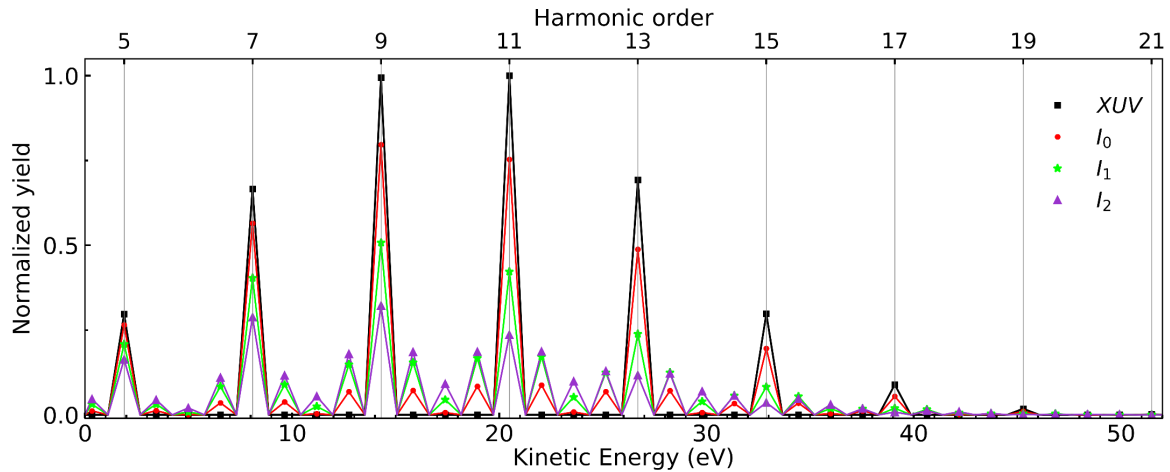


Figure 3.19. XUV-only (black) PES and delay integrated PES in the RABBITT scan at varying probe intensity intensities normalized to the XUV-only PES.

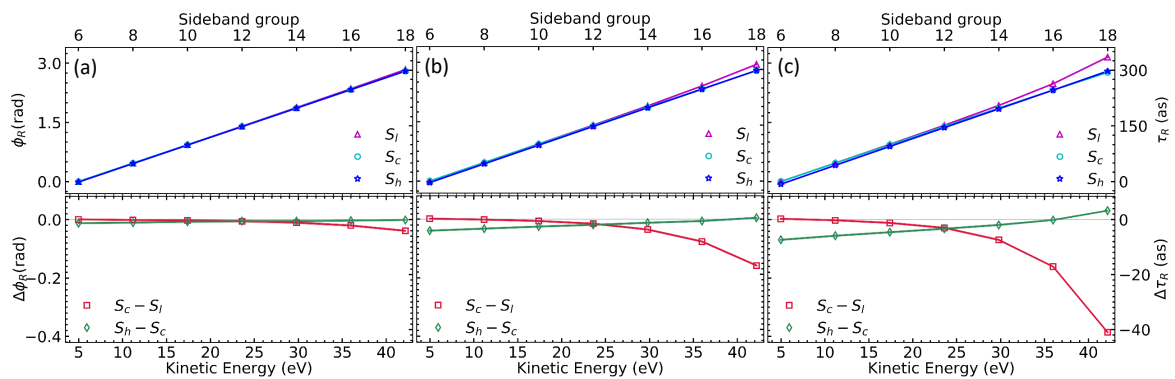


Figure 3.20. Retrieved RABBITT phases of the three sidebands (upper panel) and the relative phase difference within the group (lower panel) at IR intensity $I_0 = 3 \times 10^{-6}$ a.u. (a), $I_1 = 2 I_0$ (b), and $I_2 = 3.33 I_0$ (c).

Here, $k_{q\pm 1}$ represents the momentum of the $q \pm 1$ mainband, and $k_{l/c/h,q}$ represents the momentum in the lower/central/higher sideband of the q th group. It is important to note that $\phi^{cc}(k_a, k_b) \approx -\phi^{cc}(k_b, k_a)$, as verified by Equation 3.7. Consequently, the analytically estimated oscillation phase in the lower, higher, and central sidebands is the same. Since the FLM simulation also follows step-wise transitions, the phase retrieved from the three sidebands also yields the same result (cf. Fig. 3.18). However, very close to threshold, $\phi^{cc}(k_a, k_b) \neq -\phi^{cc}(k_b, k_a)$, which leads to a slight deviation in the phase of the lower sideband of the 6th sideband group (cf. Fig. 3.18b). It is worth mentioning that the equations in 3.17 assume that only two transition paths dominate the yield oscillations, which holds true only for a weak IR field.

We now investigate the effect of increasing the IR intensity on the phases of the three sidebands. To highlight the effect, we add a group delay dispersion of 0.015 fs^2 to the spectrum of the XUV-APT and turn off the atomic phases for simplification. Figure 3.19

displays the delay-integrated PES from the 3-SB RABBITT scan at three different IR intensities, $I_0 = 3 \times 10^{-6}$ a.u. (a), $I_1 = 6 \times 10^{-6}$ a.u. (b), and $I_2 = 10 \times 10^{-6}$ (c). Figure 3.20 shows the retrieved ϕ_R from all three SBs at increasing IR intensities. At the lowest IR intensity, I_0 , the three sidebands have nearly identical phases due to the negligible influence from higher-order terms. However, increasing the IR intensity leads to deviations, mainly observed in S_h near threshold and S_l at higher kinetic energy regions. These deviations are partly due to the specific spectral profile of the XUV pulse, which affects the contribution of higher-order transitions differently in the lower and higher energy regions.

Let's first examine the lowest energy group, SB_6 . The 9th mainband has a much stronger signal than the 5th mainband, and we also know that the cc-coupling strength increases with energy (c.f. Sec. LAP). As a result, the oscillation amplitude arising from the interference of ($M_9 - 5\omega$ and $M_7 - \omega$) cannot be neglected compared to the oscillation amplitude from the interference of ($M_5 + 3\omega$ and $M_7 - \omega$). The two interference terms will have different phases, and the resulting phase is a weighted average of the two. As the IR intensity increases, the overall 4ω oscillation phase retrieved from the higher sideband of group SB_6 changes due to the increasing contribution from higher-order terms. On the high-energy side, the harmonic strength decreases with energy, making the effect of higher-order terms more prominent in the lower sideband. For instance, in sideband group 18 (SB_{18}), the 15th mainband signal is much stronger than that in the 19th mainband, making the oscillation amplitude from the interference of ($M_{15} + 5\omega$ and $M_{17} + \omega$) non-negligible compared to the oscillation amplitude from the interference of ($M_{17} + \omega$ and $M_{19} - 3\omega$). This changes the phase of the lower sideband.

Angle-dependence

Up until now, the oscillation phase obtained from the FLM simulation of 3-SB RABBITT does not account for angle-dependence due to the absence of angular momentum states. To introduce angle-dependence, we modify the simulation by dividing each energy level into eight degenerate ℓ states. We then follow the same procedure as in the angle-dependent FLM simulation of 1-SB RABBITT to extract the angle-dependence of the oscillation phase. It is important to remember that the dipole selection rule allows only transitions that result in a change in the orbital quantum number by one, denoted as $\Delta\ell = \pm 1$. We incorporate the propensity rule for transitions to different ℓ states and make the Wigner (η) and cc-coupling phase dependent on the ℓ -states, as illustrated in Fig. 3.10 and 3.11. Two cases are considered, one where the ground state is an s -state, and the other where it is a p -state.

The transition diagram in Figure 3.21 depicts the various ℓ channels involved in transitions from (a) s -state and (b) p -state. Only the lowest-order paths necessary for generating

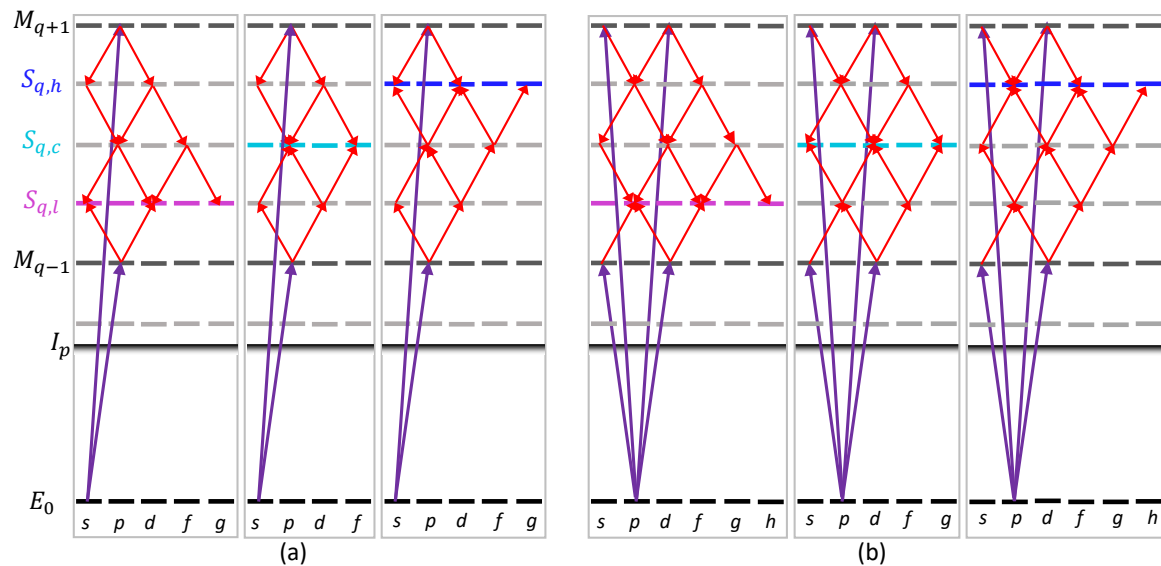


Figure 3.21. Transition diagram for 3SB-RABBITT through various angular-momentum channels for the system starting in $\ell_i = 0$ (a) and $\ell_i = 1$ (b).

oscillations in the yield of sidebands are displayed. Specifically, for the lower sideband, the diagram shows second-order absorption paths ($H_{q-1} + 1\omega$) and fourth-order emission paths ($H_{q+1} - 3\omega$). Similarly, for the higher sideband, the diagram displays fourth-order absorption paths ($H_{q-1} + 3\omega$) and second-order emission path ($H_{q+1} - \omega$). Finally, for the central sideband, the diagram illustrates third-order absorption paths ($H_{q-1} + 2\omega$) and emission paths of the same order ($H_{q+1} - 2\omega$). For the angle-resolved FLM simulation, we employed Fourier-limited XUV and IR pulses, each with a duration of 25 fs (FWHM), as illustrated in Figure 3.16. Similar to the previous section, the intensity of the XUV pulse was fixed at 2.38×10^{-8} a.u. For the IR pulse, we specifically opted for the lowest peak intensity used in the previous section, which was 3×10^{-6} a.u. This choice allows us to confidently disregard any higher-order contributions not depicted in Figure 3.21.

Upon examining Figure 3.21 (a), we observe that when the system is initially in an s -state, the three-photon transition to the central sideband ($S_{q,c}$) leads to the population of p and f angular states through both absorption and emission pathways. On the other hand, the two-photon transition to $S_{q,l}$ ($S_{q,h}$) populates s and d states while the four-photon transition to $S_{q,l}$ ($S_{q,h}$) populates s , d , and g states. The angle-integrated phase ϕ_R in the three sidebands is the weighted average of the oscillation phases retrieved from each final ℓ state. Since there is no interfering partner for the g state, it does not contribute in the angle-integrated calculation of ϕ_R .

Likewise, when the ground state is a p -state (Fig. 3.21 b), the central sideband is a mixture of s , d , and g states that are populated by both absorption and emission paths. The angle-integrated ϕ_R of the central sideband is the weighted average of the oscillation phase in each of the three angular states. In the lower and higher sidebands, a four-photon

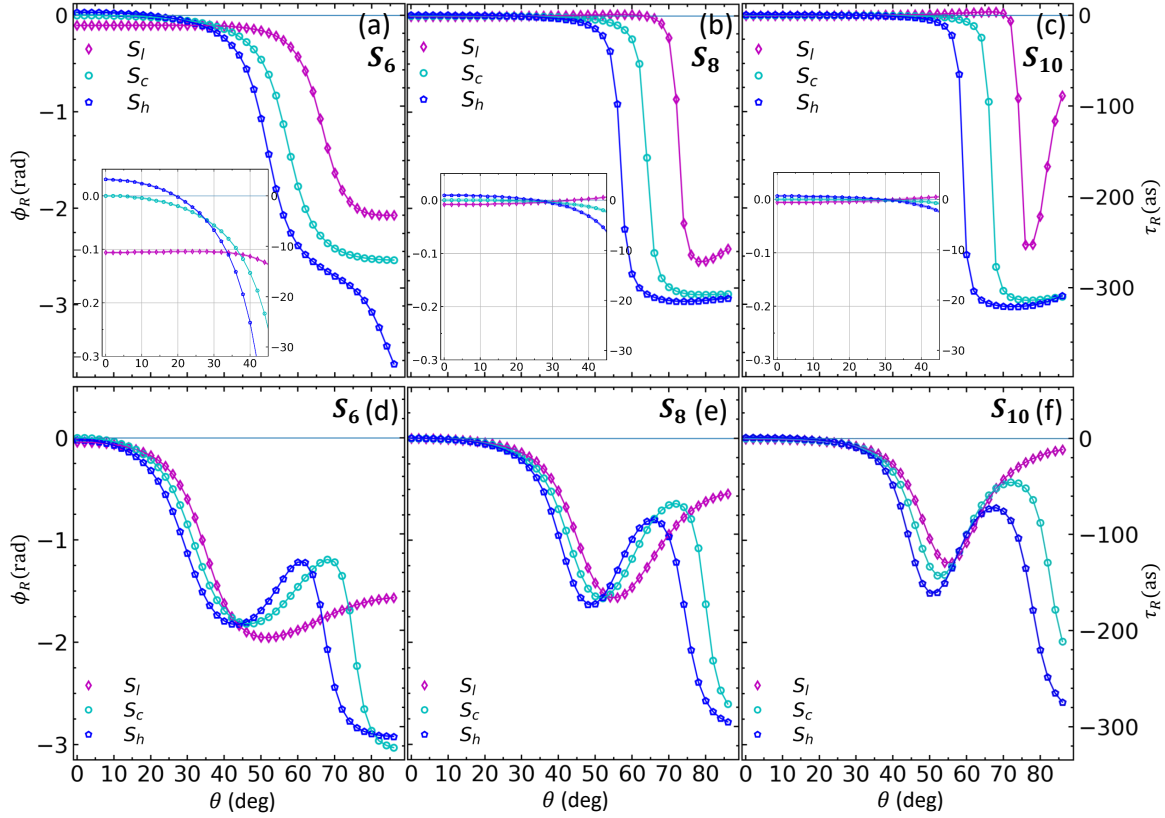


Figure 3.22. Angle-dependent RABBITT phases for three sidebands of groups 8, 10, and 12 with $\ell_i = 0$ (a-c) and $\ell_i = 1$ (d-f).

transition from the p state creates an h state. However, since this state cannot be reached via the two-photon path, it does not contribute to the angle-integrated ϕ_R .

In Figure 3.22, we observe the dependence of the retrieved ϕ_R on the photoelectron emission angle for all three SBs of groups 8, 10, and 12, depicted in panels (a), (b), and (c) for when the system starts in an s -state, and in panels (d), (e), and (f) for when it begins in a p -state. The insets in panels (a), (b), and (c) reveal that as we progress to higher kinetic energies, from group 6 to group 10, the phase difference within each group decreases. Additionally, the variation in phase with angle becomes flatter, and the π jump appears more abrupt as the kinetic energy increases. These observations can be attributed to the decreasing disparity in the cc-coupling phases among different ℓ states at higher kinetic energies, resulting in a reduced discrepancy in the oscillation phases $\phi_R^{\ell',\ell}$ that arise from the interference between different channels.

In order to shed some light on the angle-dependent behavior of the RABBITT phases of the three sidebands, we adopt a similar approach as in the case of one-sideband RABBITT. We first isolate the signal from each angular momentum state and subsequently retrieve the oscillation phase based on equation 3.15. We then separate the cross-term interference signal using equations 3.16 and retrieve the associated oscillation phase.

Let's focus on one specific group of sidebands, namely S_8 , and analyze the angle-

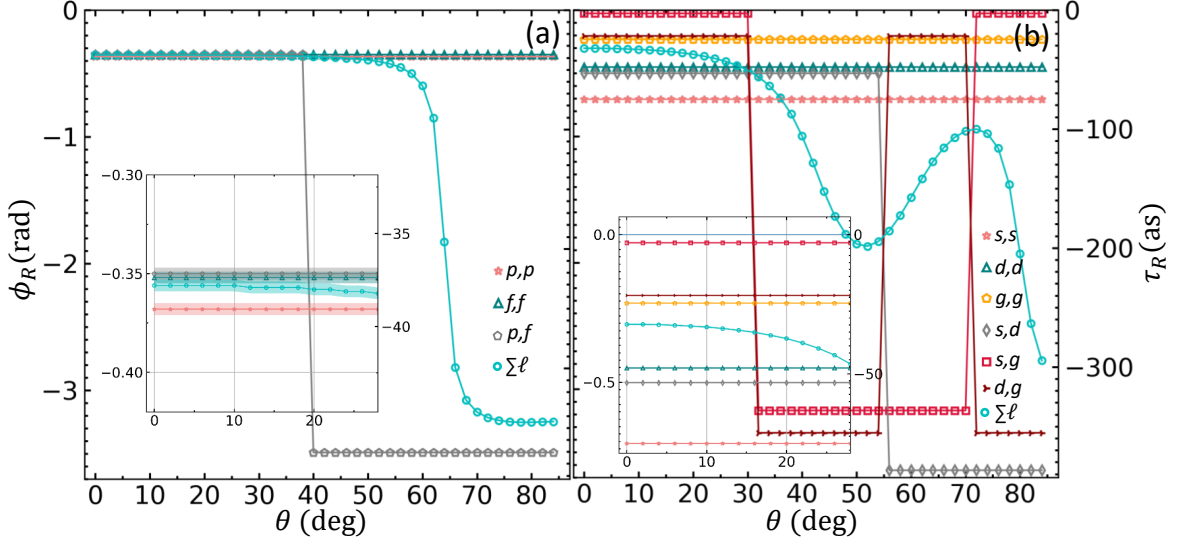


Figure 3.23. Oscillation phases ($\phi_R^{\ell',\ell}$) retrieved from the same-channel and cross-channel interferences, as well as the overall angle-dependent phase considering all ℓ -states in the central sideband for systems starting with $\ell_i = 0$ (a) and $\ell_i = 1$ (b).

dependence of the oscillation phase in more detail. In Figure 3.23, the oscillation phases ($\phi_R^{\ell',\ell}$) retrieved from the same-channel and cross-channel interferences, as well as the overall angle-dependent phase considering all ℓ -states in the central sideband for systems starting in an s - or a p -state, are illustrated. When the system begins in an s -state with $\ell_i = 0$, the central sideband has only one cross-channel interference, $p - f$, and its phase undergoes a discrete π jump at 39° , which corresponds to the node in $Y_{3,0}$. For $\ell_i = 0$, the differences in $\phi_R^{\ell',\ell}$ resulting from the interference between different possible angular momentum states (ℓ', ℓ) are very small. As a result, the overall RABBITT phase shows a small gradual change with angle until it reaches the nodes of the spherical harmonics, where it experiences a sudden π jump. The subsequent change in the angle-dependence after the node in the f -wave relies on the relative weights and phases of the three interference terms. The overall angle-dependent behavior of the RABBITT phase for the central sideband reveals that beyond an emission angle of 65° , the weight of the cross-term ($p - f$) exceeds the combined weight of the same-channel interference, resulting in a decrease in the overall angle-dependent phase. Figure 3.23(b) depicts the angle-dependence of the central sideband for $\ell_i = 1$. In this case, the differences in $\phi_R^{\ell',\ell}$ are relatively large compared to the $\ell_i = 0$ scenario. Consequently, the overall RABBITT phase demonstrates a more pronounced variation with angle even before encountering the π jump at the node positions of the spherical harmonics. It is observed that the angle-dependent phase undergoes rapid changes that align with the nodes of the $Y_{2,0}Y_{4,0}$ term. This behavior indicates a strong weight of the $d - g$ interference term in shaping the angle-dependent phase.

Next, we examine the lower and higher sidebands for the case where the system starts

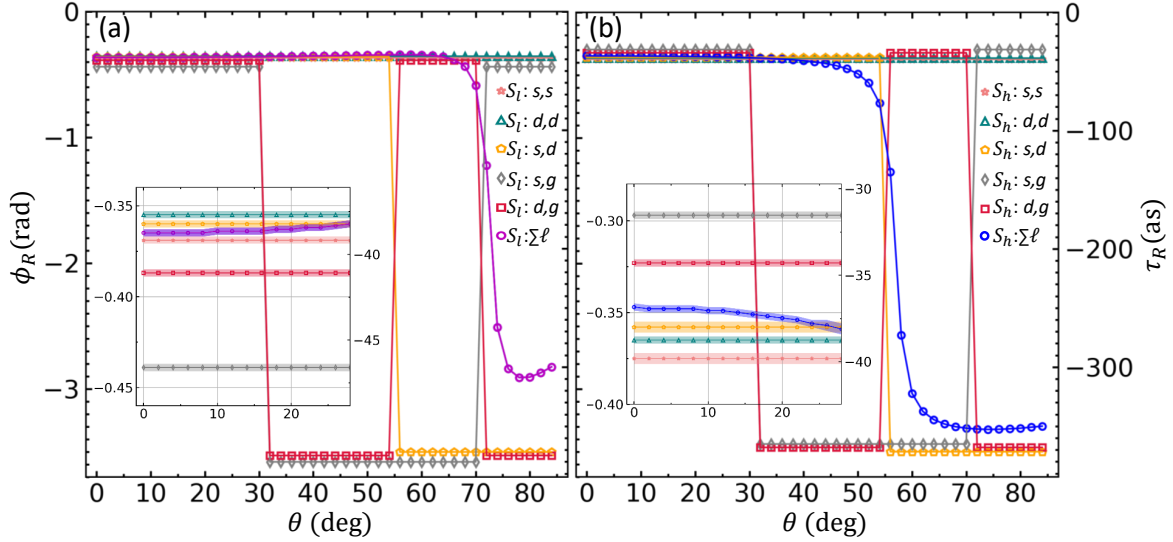


Figure 3.24. Oscillation phases ($\phi_R^{\ell,\ell}$) retrieved from same-channel and cross-channel interferences, and overall angle-dependent phase ($\phi_R(\theta)$) in the lower (a) and higher (b) sidebands for an initial $\ell_i = 0$ state.

in an s state. As shown in Figure 3.24(a), the oscillation phase $\phi_R(\theta)$ exhibits only a slight variation with angle until it reaches 70° . The oscillation phase corresponding to the $d - g$ interference undergoes three discrete π jumps, but $\phi_R(\theta)$ remains almost constant at the first two jumps. Furthermore, $\phi_R(\theta)$ does not change significantly when the phase of the $s - g$ interference term undergoes the first jump. These observations suggest that the transition amplitude to the g state is relatively weak compared to the s and d transition amplitudes. This preference for the s and d states over the g state aligns with the propensity rule. Furthermore, the transition probability to the g state is relatively weak due to the fact that emitting three probe photons offers only one possible way to reach the g state, while there are two ways to reach the s state and three ways to reach the d state. Compared to the same-channel interference, the interference between s and d does not generate a very strong oscillation. Therefore, we do not immediately observe a change in the oscillation phase $\phi_R(\theta)$ following the node in $Y_{2,0}(\theta)$. Instead, the change in $\phi_R(\theta)$ is only noticeable after 70° when the combined amplitudes of the cross-channel interferences of $s - d$ and $d - g$ become stronger than the amplitude of rest of the terms.

Looking at the higher sideband in Figure 3.24 (b), we observe that the angle-dependent phase follows the node of $Y_{2,0}(\theta)$ and drops significantly after 54° , indicating a large amplitude in the d -state for one of the paths. In spite of the propensity rule favoring the population of the g -state via the four-photon transition over the d -state, the fact that there are three ways to reach the d -state and only one way to reach the g -state in the four-photon transition results in the net d -state transition amplitude dominating the g -state transition amplitude. Moreover, the emission path favors the population of the s -state over the d -state due to the

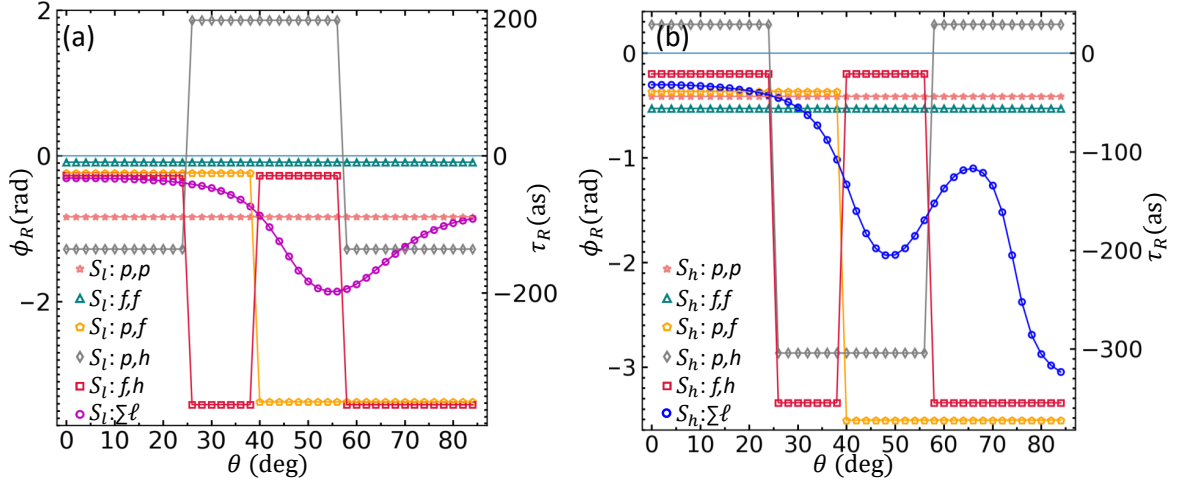


Figure 3.25. Oscillation phases ($\phi_R^{\ell',\ell}$) retrieved from same-channel and cross-channel interferences, and overall angle-dependent phase ($\phi_R(\theta)$) in the lower (a) and higher (b) sidebands of group 8 for initial $\ell_i = 1$ state.

propensity rule, thereby leading to a strong interference amplitude in the $s - d$ channel.

Now we examine the angle-dependence of the RABBITT phase for the lower and higher sidebands when the system initially starts in a p state. Figure 3.25(a) displays the oscillation phases ($\phi_R^{\ell',\ell}$) retrieved from both same-channel and cross-channel interferences, as well as the overall angle-dependent phase considering all ℓ -states in the lower sideband. We observe that the overall angle-dependent oscillation phase $\phi_R(\theta)$ follows the angular variation of the product of the spherical harmonics $Y_{1,0}Y_{3,0}$. Around 39° , where $Y_{3,0}$ has a node, $\phi_R(\theta)$ becomes nearly equal to $\phi_R^{p,p}$. After that it starts to decrease, following the phase of the $p - f$ interference term. As the magnitude of $Y_{1,0}Y_{3,0}$ decreases after 57° , the total RABBITT phase is dominated by the same channel interference terms ($p - p$ and $f - f$). Furthermore, since the propensity rule disfavors the transition to the h -state, the contribution of any cross term involving the h -state is negligible.

For the higher sideband shown in Figure 3.25(b), the RABBITT phase ($\phi_R(\theta)$) initially starts above the $p - p$, $f - f$, and $p - f$ interference terms. This indicates that the weight of the cross term involving the h state is not negligible near zero degrees. This is due to the propensity rule favoring the transition that increases the angular momenta during absorption. The RABBITT phase starts to vary early following the first node in $Y_{5,0}$ at 23° and reaches its first minimum around 50° . It then begins to increase following the phase of the $f - h$ interference term. Beyond 66° , $\phi_R(\theta)$ starts to go down again due to increased angle-dependent weights of $p - f$ and $f - h$.

We also notice that when the system starts in the p state, the change in $\phi_R(\theta)$ occurs much more gradually, instead of exhibiting sharp jumps after the nodes in the spherical harmonics. This is because of the relatively large difference in the oscillation phase of the individual interference terms, causing the RABBITT phase to vary significantly with angle

even before reaching the nodes. Furthermore, since there is no single strong cross term that can counter the strength of the weight of the rest of the interference amplitudes, there is no jump of π , but only small variations instead.

3.3 Summary

3-SB RABBITT involves multiple transitions in the continuum, and the retrieved phase depends on several factors. FLM simulation allows us to examine the impact of various parameters individually. The transitions in the FLM occur stepwise. At each transition, two types of phases are acquired: the spectral phase of the laser pulse and a dipole transition phase. The retrieved phase from the oscillation of the population is the phase difference of the two paths. We discovered that the retrieved phase varies as the IR intensity is increased, with higher-order contributions containing the different spectral phase of the harmonics, and higher-order transition phases mixing in the retrieved phases of oscillation. The deviation in the retrieved phase depends on the relative strength of two adjoining mainbands, which is determined by the spectral amplitude of the harmonics and the ionization cross-section. When the two adjoining mainbands have very different amplitudes, interference between the transition paths involving these two nearest bands will be incomplete, resulting in small oscillations. However, higher-order transition paths involving distant but strong mainbands may compete with the lowest-order path and produce comparable oscillation amplitudes. We observed that the FLM simulation for 3-SB RABBITT yields the same phase in all three sidebands at the lowest applied intensity, due to the stepwise nature of the FLM. We also found that choosing the Wigner phase and the cc-coupling phase depend on the angular momentum of the states causes the population of the different angular momentum states of the same energy to oscillate with different phases, thus resulting in the overall oscillation phase of the sideband depending on the emission angle. Although the angle-dependent oscillation phases of the three sidebands behave differently, the FLM simulation still predicts the angle-integrated phase to be the same across all three sidebands within any given group.

A relatively small difference in the cc-coupling phase for different ℓ channels results in a small variation in the angle-dependent oscillation phase $\phi_R(\theta)$. However, when the interference between the absorption and emission paths ending up in different angular momentum states becomes strong, this may result in a sharp change in $\phi_R(\theta)$ at the angular position where the spherical harmonics corresponding to these two ℓ states have nodes.

Overall, the FLM has been instrumental in visualizing the behavior of RABBITT phases as a function of intensity, emission angle, and other parameters like angular momentum dependent Wigner and cc-phases.

Chapter 4

Publications

This chapter contains the three publications on which the thesis is based. Before inserting the original publication, a brief description of the work is provided.

4.1 Publication I: High-repetition rate attosecond beam-line for multi-particle coincidence experiments

This paper outlines the experimental arrangement used to perform the measurements discussed in this thesis and related publications. The experimental setup consists of a femtosecond CPA laser, a non-linear pulse compression system, a high-order harmonic generation unit, a Mach-Zehnder interferometer, and a reaction microscope. The attached paper provides a summary of the design and capabilities of the system for investigating photoionization dynamics on the attosecond time scale. The paper primarily focuses on the conventional 1-SB RABBITT setup, followed by a description of the modification required for the 3-SB setup.

In addition, the appendix of this thesis provides further details on the laser system, interferometer, data acquisition process, and the technique used to reconstruct the momenta and energies of charged particles, as well as the momentum resolution and angular acceptance of the reaction microscope.



High-repetition rate attosecond beamline for multi-particle coincidence experiments

HEMKUMAR SRINIVAS,^{1,3} FARSHAD SHOBEIRY,^{1,4} DIVYA BHARTI,¹
THOMAS PFEIFER,^{1,2,5} ROBERT MOSHAMMER,^{1,6} AND ANNE
HARTH^{1,7}

¹Max-Planck Institut für Kernphysik, Saupfercheckweg 1, Heidelberg 69117, Germany

²Center for Quantum Dynamics, Ruprecht-Karls-Universität Heidelberg, 69120 Heidelberg, Germany

³hemkumar@mpi-hd.mpg.de

⁴shobeiry@mpi-hd.mpg.de

⁵thomas.pfeifer@mpi-hd.mpg.de

⁶r.moshammer@mpi-hd.mpg.de

⁷anne.harth@mpi-hd.mpg.de

Abstract: In this paper, a 3-dimensional photoelectron/ion momentum spectrometer (reaction microscope) combined with a table-top attosecond beamline based on a high-repetition rate (49 kHz) laser source is presented. The beamline is designed to achieve a temporal stability below 50 attoseconds. Results from measurements on systems like molecular hydrogen and argon dimers demonstrate the capabilities of this setup in observing the attosecond dynamics in 3D while covering the full solid angle for ionization processes having low cross-sections.

© 2022 Optica Publishing Group under the terms of the [Optica Open Access Publishing Agreement](#)

1. Introduction

Photoionization studies on atoms and molecules have been revolutionized since the first measurement involving the generation and characterization of attosecond pulses two decades ago [1]. Attosecond pulses have since then been instrumental in observing the ultrafast electron dynamics in atoms and molecules. Although they were initially limited to atomic systems in the gas phase only, attosecond pulses now aid the understanding of dynamics in systems of increasing size and complexity such as liquids [2] and solids [3].

XUV attosecond pulses are created through the process of high-harmonic generation (HHG) [4] from femtosecond IR pulses. This has been studied extensively with a variety of HHG targets over the years [5], in order to obtain photon energies up to 100 eV or more. In parallel, femtosecond laser systems have also undergone sophistication in terms of pulse energies and wavelength tunability. Most schemes utilize Ti:Sapphire laser oscillators or amplifiers as the starting point. These systems deliver the necessary pulse energy for HHG but they are typically limited to repetition rates of only a few kHz.

To successfully perform either single- or multi-coincidence photoelectron/ion spectroscopy of atomic or molecular targets, generic Ti:Sapphire systems fall short considering that many processes of interest have moderate cross-sections (≈ 10 kBarn). This often results in measurements lasting several days to obtain a statistically significant number of data points. To drastically shorten the data acquisition time, novel laser systems providing pulses at repetition rates of 100 kHz or more have been developed in the recent years [6–9], which have been used for HHG. These include fiber-based amplifiers e.g. [6], nonlinear post-compression of thin-disk lasers [7] or OPCPA based systems such as the one described in [9], used to perform pump-probe experiments in [10]. With pulse energies comparable to those from Ti:Sapphire systems, these fiber-based systems are ideally suited for multi-coincidence momentum spectroscopy. Using a 3-dimensional photoelectron/ion momentum spectrometer (reaction microscope or REMI [11]) along with

attosecond pulses allows to temporally resolve combined electron and nuclear dynamics, by means of kinematically complete measurements on their natural time scale.

Attosecond beamlines with high-repetition-rates for photoelectron spectroscopy exist and have been reported in [10,12–15], with Ref. [10] even demonstrating the ability to perform coincidence measurements. XUV attosecond beamlines (based on Ti:Sapphire systems) combined with a REMI exist as well and have been reported in [16], [17] and [18]. All these systems lack either the ability to study processes with low cross-sections due to their repetition-rate (latter case) or from providing complete momentum information for both ions and electrons (former case).

Although Ref. [10] presents ion-electron coincidence measurements with a high-repetition rate laser, their effusive target limits the ability to perform ion momentum spectroscopy. In our setup, we have a target that is cold ($<5\text{K}$ in the jet direction and $\approx 100\text{ mK}$ in the perpendicular direction) and dilute, which provides us with excellent resolution for ion momentum spectroscopy. This is seen in the results presented in Sec. 4.1, showing joint energy distributions obtained from ion and electron momenta. We therefore present kinematically complete measurements using a high-repetition rate attosecond source in combination with a REMI.

The generated XUV attosecond pulses reach photon energies up to 40 eV. The beamline comprising an interferometer is used to perform XUV-IR pump-probe measurements on noble gases and molecules. Results from RABBITT [1] measurements on argon and H_2 demonstrate the capabilities of the setup. In addition, we present an upgrade to the system with the goal to perform multi-color pump-probe measurements, demonstrating the high stability of the attosecond beamline.

2. Experimental setup

This section describes the experimental setup in detail (shown in Fig. 1). It consists of four main parts: the driving laser, the HHG source with the interferometer, a focusing element and the reaction microscope (REMI). The section ends with a description of the active phase-stabilization of the interferometer.

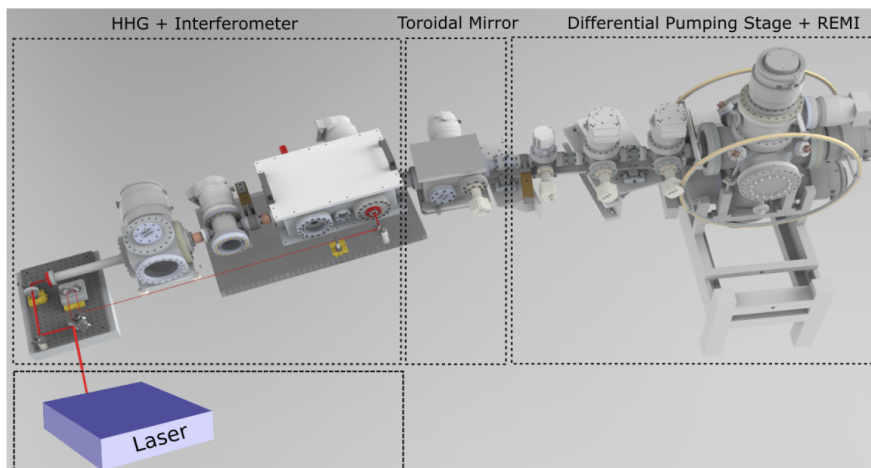


Fig. 1. The constituent parts of the attosecond beamline: The CPA laser, the XUV-IR interferometer and the HHG chamber, toroidal mirror chamber and the differential pumping stages connected to the reaction microscope (REMI).

2.1. Driving laser

A commercial laser from AFS (ActiveFiber Systems GmbH, Jena) is the front-end of the attosecond beamline. The laser system comprises a fiber-based Chirped Pulse Amplifier (CPA) [19] which works on the coherent combination of several phase-locked individual amplifiers as explained in Refs. [20–22]. The CPA delivers pulses with a duration of approximately 250 fs (sech² fit), 2 mJ pulse energy. To reduce the pulse duration, the pulses are coupled into an argon gas (2 bars) filled hollow-core fiber (HCF) [23]. The spectrally broadened pulses are temporally compressed to approximately 40 fs using chirped mirrors, with a pulse energy of 1 mJ. For further pulse compression, the output of the first HCF can be coupled into a second HCF, bringing the pulse duration down to approximately 8 fs. All the experiments presented in this paper were performed with 40 fs pulses. These pulses are steered to an interferometer for XUV-IR pump-probe experiments. The laser has variable repetition rates - 49 kHz, 75 kHz and 147 kHz. The pulse energy is unaffected by choice of the repetition rate and all experimental results presented here were obtained using a repetition rate of 49 kHz. This repetition rate was chosen to ensure that all the ions of interest have a time-of-flight that would be less than the time between two consecutive IR pulses, thereby simplifying the data acquisition. Moreover, the count rate of the ions/electrons was sufficient to acquire a statistically significant number of events for the various ionization processes.

2.2. Interferometer

The Mach-Zehnder arrangement is shown in Fig. 2. The incoming beam, 10 mm in diameter is split into two parts using a mirror with a 3.5 mm central hole (HMBS in Fig. 2). This results in a splitting of the beam into fractions of 85/15 (reflection/transmission). The beam path through the HHG chamber (reflected part) forms the pump (or ionizing) arm of the interferometer while the rest forms the probe arm.

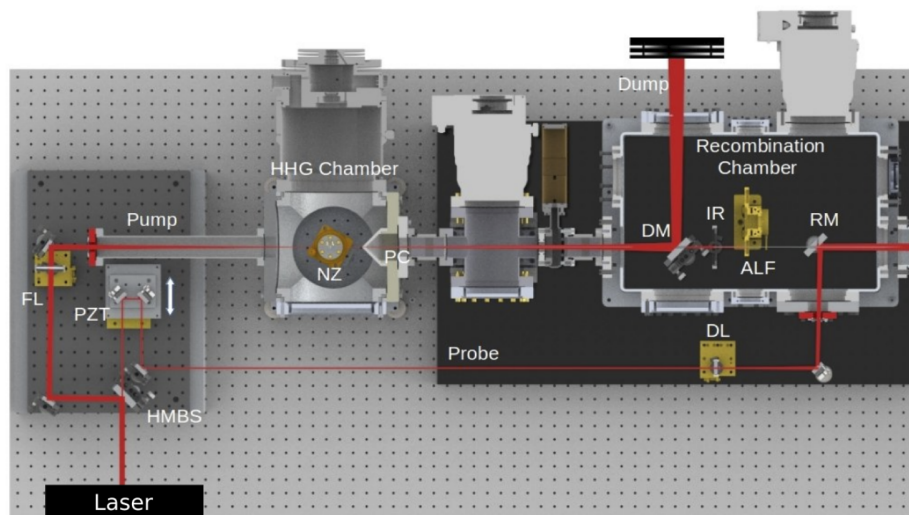


Fig. 2. Schematic drawing of the interferometer including the HHG and recombination chambers. Legend: HMBS - holey mirror beam splitter, FL - focusing lens, NZ - gas nozzle, PC - differential pumping cone, DM - dump mirror, IR - iris, ALF - aluminium filter, RM - recombination mirror, PZT - piezo stage, DL - diverging lens.

The transmitted beam is reflected by a retro-reflector mounted on a piezoelectric translation stage, before it is diverged using a lens of focal length $f = -25$ mm in order to match the

divergence of the XUV beam in the pump arm. The piezoelectric stage for delay control offers a step-resolution of 5 nm. The IR and XUV beams are collinearly merged by a recombination mirror (RM) which is again a mirror with a central hole (3.5 mm diameter).

2.2.1. High-harmonic generation

The reflected intense annular beam is focused with a lens of 50 cm focal length to a spot size of approximately $100\ \mu\text{m}$, right below the exit of a gas nozzle. The gas nozzle is mounted in a vacuum chamber and XUV radiation is generated through the process of HHG [4]. With a backing pressure of 700 mbar before the nozzle, the chamber pressure reaches about 9×10^{-3} mbar. The hole diameter of the cylindrical nozzle is $150\ \mu\text{m}$.

The generated XUV radiation co-propagates with the annular driving IR radiation. The IR radiation is removed through several steps. First, after a distance of 50 cm from the HHG target, the XUV radiation that is located in the center of the IR beam is spatially separated with the help of an additional holey mirror (DM in Fig. 2). The intense IR beam is reflected by the holey mirror and guided to a beam dump outside the vacuum chamber in order to reduce the heat load inside the chamber. In addition, the beam transmitted through the holey mirror passes through an iris which cuts down the remaining IR radiation that might still surround the XUV beam. The iris is not actively cooled since the residual IR cut out by the iris does not cause any significant heating. Finally, an aluminium filter with about 200 nm thickness then filters out any remaining IR radiation along with the lowest order harmonics from the XUV beam. Using this annular beam method protects the aluminium filters from damage due to heating by the residual IR radiation that co-propagates with the XUV.

2.3. Toroidal mirror

The XUV-pump and IR-probe beams are together focused using a toroidal mirror (TM) (Fig. 3) onto a supersonic gas target inside the reaction microscope (REMI). The TM is designed in a way that it images both, the XUV source point and the virtual IR focus inside the REMI. The mirror has a B_4C coating (30 nm thickness) on top of an aluminum layer (30 nm), which at a grazing incidence angle of 8° is designed for high reflectivity of the XUV and IR wavelengths around 1030 nm. The total distance between the HHG source point and the gas-jet is 2.6 m. Under normal operating conditions, the pressure inside the mirror-chamber is in the order of 10^{-7} mbar.

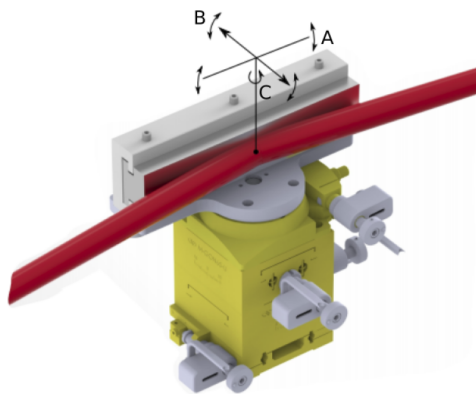


Fig. 3. Schematic of the toroidal mirror mounted on four different stages. The lowest is a translation stage moving the whole mirror on the sagittal plane. Two goniometers in between are used to rotate the mirror along the Pitch and Roll axes (Axes A and B respectively in the figure). The upper-most stage rotates the mirror around the Yaw axis (Axis C). Figure adapted from [24].

2.4. Differential pumping stages and reaction microscope

The toroidal mirror chamber is followed by a differential pumping stage since the REMI requires to be operated at a pressure of 10^{-10} mbar or below. The differential pumping stages create a smooth pressure gradient between the mirror chamber and the REMI from 10^{-8} mbar to 10^{-11} mbar.

The reaction microscope ([11,25]) employs a supersonic gas-jet for target delivery and it can detect ions and electrons in coincidence (see Fig. 4). The gas jet is 1 mm in diameter at the focus of the XUV and IR. The target is internally cooled by supersonic expansion to a few Kelvins, thereby leading to a very narrow momentum distribution of the gas particles. This is achieved by taking a gas reservoir at room temperature (≈ 300 K) with a backing pressure of a few bars and allowing it to undergo expansion through a 30 micron diameter nozzle (technical details from Ref. [24]) into a chamber with a few millibars of pressure. This leads to the formation of a gas-jet which afterwards passes through two skimmers with diameters of $150 \mu\text{m}$ and $200 \mu\text{m}$. The distance between the nozzle and the reaction volume is 115 mm, while the nozzle-skimmer distance is about 7 mm.

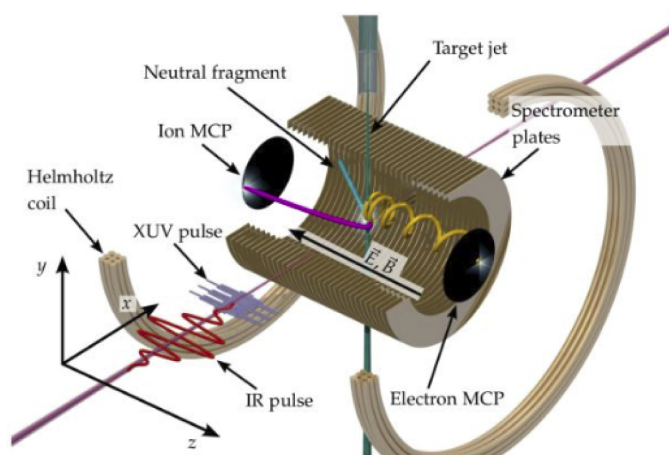


Fig. 4. Schematic of the reaction microscope. Figure taken from [26].

Electrons and ions created in the center of the REMI by the interaction of XUV and IR beams with the gas-jet are guided to their respective MicroChannel Plate (MCP) detectors using co-axial homogenous electric and magnetic fields. The electric field used for accelerating the charged particles is between 3 - 12 V/cm and the magnetic field applied is between 4 and 10 Gauss, thereby providing a 4π acceptance for electrons with kinetic energies up to 22 eV and ions with kinetic energies up to 3 eV.

Along with the MCP detectors, Delay-line Anodes [27] provide the position of the electron and ion hits. The detection system therefore provides the time of flight of the charged particles and their respective hit positions on the detector. This enables a complete reconstruction of the momentum components (see [11]) of all charged fragments detected in coincidence.

In order to avoid false hits due to scattered light in the REMI that causes secondary electron emission, the XUV and the IR beams are dumped onto a slightly bent tubular extension at the end of the REMI.

2.5. Stability of the beamline

The beamline requires a high level of stability to measure photoionization time delays in the order of a few tens of attoseconds. Particularly, the temporal jitter while performing delay scans should be less than about 100 attoseconds [28]. Additionally, interferometric drifts need to be minimized and compensated to perform measurements lasting several hours for targets with low ionization cross-sections. These requirements call for having an active-stabilization system with closed-loop control to reduce both the long-term drifts and short-term jitter. To achieve this, the interferometer is extended as shown in Fig. 5.

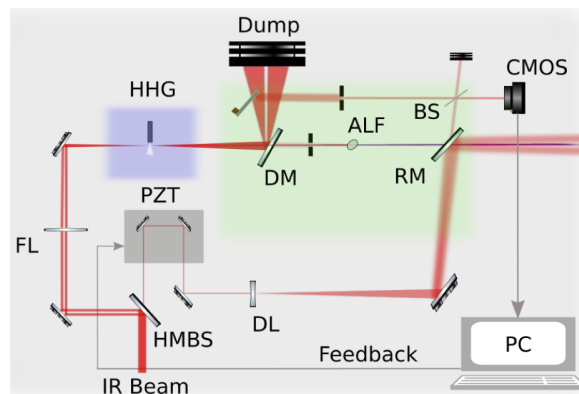


Fig. 5. Schematic drawing of the interferometer with drift stabilization. The extended part of the interferometer is in the region shaded green. Legend : HMBS - hole-mirror beam splitter, FL - focusing lens, HHG - HHG chamber, DM - dump mirror, ALF - aluminium filter, BS - beam splitter, PZT - piezo stage, DL - diverging lens, RM - recombination mirror, CMOS - camera.

A small portion of the pump IR beam that is reflected to the beam dump by the mirror DM, is picked up using a rectangular mirror and guided on to a beam splitter. Likewise, a part of the probe IR beam is guided through a hole in the recombination mirror (RM). By adjusting the spatial overlap of the beams, interference fringes are obtained on the camera which has an exposure time of 1/20th of a second. A narrow section of the image having the best fringe contrast is chosen and cropped. Integrating the cropped image along one axis gives the projection in the form of a sine wave. Figure 6 is a stack of the sine waves from images acquired every 10th of a second, over 1 hour. The phase of this sine wave is obtained using methods from Fourier Transform Interferometry [29,30]. At the beginning of the experiment, a reference image is captured and the phases of the fringes during the experiment is compared every 1/10th of a second to this reference. If a phase shift is registered, an error signal proportional to the phase shift is generated in order to move the piezo stage to compensate the drift. This is conceptually the same as the method presented in Ref. [31].

Figure 6 shows the phase drift when the interferometer is free-running as well as when the interferometer is locked to one particular setpoint phase with the active stabilization. The phase of the free-running interferometer drifts by about $\frac{\pi}{4}$ radians after 60 min. Assuming no variation of the laser's central frequency and using the relation $\phi = \omega_{IR}\tau$ (ω_{IR} - IR frequency, τ - time), this corresponds to about 400 attoseconds temporal drift. With active stabilization, the drift is negligible and only a short-term phase jitter of 0.03π radians (≈ 50 attoseconds (RMS)) is observed (Fig. 6).

While performing pump-probe delay scans the setpoint phase is incremented in regular intervals and the piezo stage is moved accordingly. With an increase in the pump-probe delay, the contrast

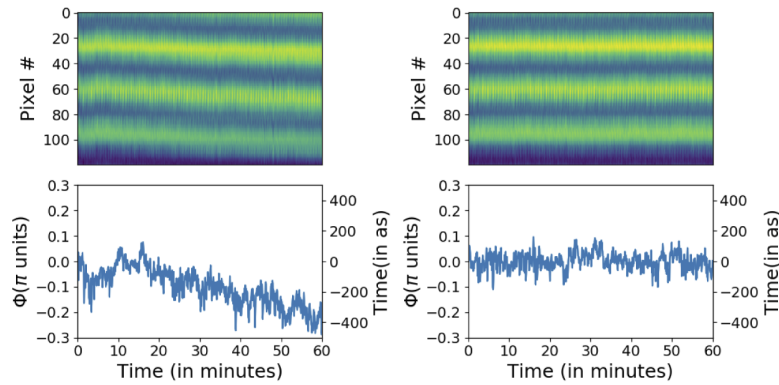


Fig. 6. Top: Interference fringes of the free-running interferometer (left) and the stabilized interferometer (right) over a timeframe of 1 hr. Bottom: Corresponding phase and time delay shifts of the fringes over 1 hr.

of the interference fringes gradually reduces and the fringes vanish for delays more than the FWHM of the pulse. To counter this, a band-pass filter is placed in front of the camera which lets only a narrow band of frequencies. As a result, the interference fringes are visible for a much longer delay range (100s of femtoseconds).

As seen in Fig. 7, a delay scan from 0 to 8.5 femtoseconds (5π shift in phase) also has only a short-term jitter below 50 attoseconds (RMS). The phases from the interference fringes shown here therefore are a part of an 'in-loop' measurement and may not completely mirror the phase shifts of the XUV-IR interferometer, since the actual interferometer has two additional components (ie. the recombination mirror and the toroidal mirror). The stability of the actual interferometer can be seen in the 'out-of-loop' measurements explained in Sec. 4.2. The in-loop and out-of-loop measurements together indicate that XUV-IR pump-probe experiments can be performed with a sub-50 attoseconds stability.

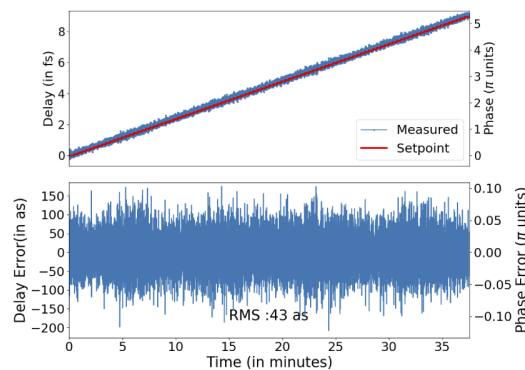


Fig. 7. Top: Measured phases of the interference fringes along with their respective setpoint phases, Bottom: Errors in relative delay throughout the delay scan.

The slow drifts which typically occur over a few hours are very efficiently corrected by this method. The arrangement presented here is comparable to the one presented in [13] and demonstrates the ability to stabilize the interferometer without the need of an additional co-propagating CW laser for interferometric feedback, as reported in Refs. [10,12,31].

The primary temporal information in the experiments presented here is imprinted in amplitude oscillations of the photoelectron spectrum, with a time period of 1.7 femtoseconds (Sections 3,4). With interferometer drifts in the order of a few hundred attoseconds per hour, temporal information is lost when data is taken over a few hours, due to smearing out of the oscillations. Without the active stabilization, the dataset would require corrections to the phase after every 10 minutes to account for the drift. With the stabilized interferometer, data recorded even over a few hours do not need any further corrections.

Limitations manifest when a dataset is acquired over very long durations (>12 hrs). This can be seen with the measurements performed on argon (described in Sec. 4.2). While analyzing the delay-dependent photoelectron spectrum, a drift of 300 attoseconds was observed over 12 hours. This might be caused by a combination of factors such as instabilities in the laser performance (i.e. laser power and beam pointing instabilities), along with the inability to completely eliminate the effects of thermalization. For such long measurements, the dataset would need a correction, but only after 6-8 hours. The stabilization is also a vital element for measurements with oscillation periods less than 1 femtosecond (presented in Section 5.).

3. Characterization of the XUV pulses

3.1. XUV photon flux and spectrum

The XUV photons are generated in the HHG chamber as described in the previous section. The pulse duration of ≈ 40 fs (≈ 12 cycles) of the fundamental IR field results in an XUV Attosecond Pulse Train (APT). The pulse energy is 0.75 mJ. An estimation of the photon flux and spectral shape of the XUV radiation after it has passed through the aluminium filter, on the target inside the REMI is possible using the photoelectron spectrum. The XUV spectrum is obtained by adding the ionization energy (I_p) of the target gas to the kinetic energies of the photoelectrons and by correcting for variations in ionization over the photon energies. Such a reconstructed photon spectrum for the XUV ionization of argon is shown in Fig. 8.

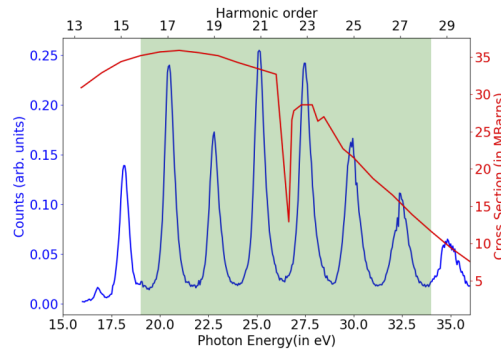


Fig. 8. Reconstructed XUV spectrum (after the Al filter) from the photoelectron spectrum of argon ($I_p = 15.8\text{eV}$). Cross section obtained from Ref. [33]. The area shaded green represents the harmonics chosen for the attosecond pulse train reconstruction.

For calculating the photon flux of the XUV radiation, the following formula is used:

$$\phi = \frac{R}{Ln\sigma\eta}. \quad (1)$$

The factors to be taken into account are: the photoionization rate R (3 kHz), the target density ($n = 10^{11}$ atoms/cm³) of the gas inside the REMI, the interaction length $L = 1$ mm, the detection efficiency ($\eta \approx 40\%$) and the average ionization cross-section ($\sigma \approx 25$ Megabarn). With these

values for photon energies between 15-35 eV plugged into Eq. (1), we obtain an XUV photon flux in the order of 10^{11} photons/s which corresponds to $\approx 10^7$ photons/pulse. This value is comparable to the numbers reported in recent publications on HHG with a high-repetition-rate laser [12,32].

3.2. Attosecond pulse train

The average duration of the pulses in the APT is estimated using the RABBITT method [34]. This method is based on photoionization of atoms or molecules using an APT. The frequency spectrum of an APT has a comb like structure, also called the harmonics. Thus, when an APT ionizes an atom, it results in discrete peaks in the photoelectron spectrum. The spacing between each peak is twice the IR frequency ($2\omega_{IR}$). Adding a phase locked IR field which also spatially and temporally overlaps with the XUV field, leads to the formation of sideband peaks (Fig. 9) in between the harmonics. The amplitude of these sideband peaks varies as a function of the time delay between XUV and IR pulses and are also called sideband oscillations. These sideband oscillations are the key feature of every RABBITT spectrogram.

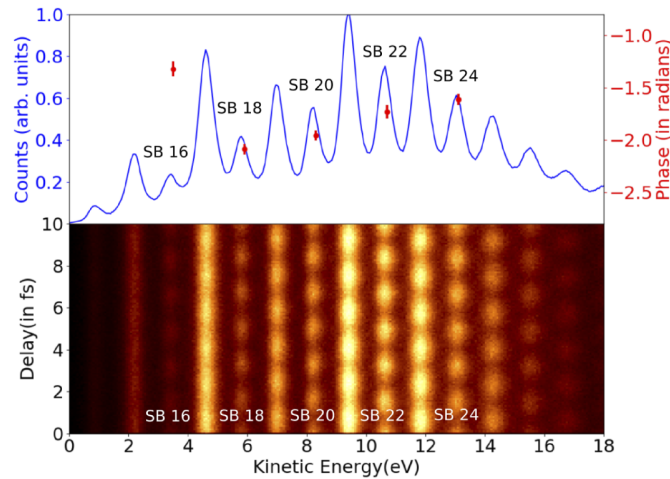


Fig. 9. Top: Photoelectron Spectrum from the ionization of argon with XUV+IR, integrated over all delays. Bottom: Experimental RABBITT trace from the ionization of argon. The red dots in the top part are the sideband oscillation phases.

A cosine function of the form: $I_{sb} = A \cos(2\omega_{IR}\tau + \Delta\phi)$ is fitted to each individual sideband oscillation. The phase term $\Delta\phi$ is approximated to be $\Delta\phi = \Delta\phi_{XUV} + \Delta\phi_A$ [35]. $\Delta\phi_{XUV}$ stands for the spectral group delay of the XUV pulses and $\Delta\phi_A$ is the atomic phase, which contains information about the atomic potential and the interaction between the IR laser pulse and the quasi-free electron in the continuum. Since $\Delta\phi_A \ll \Delta\phi_{XUV}$ [35], in this case, the atomic phase can be neglected and thus $\Delta\phi \approx \Delta\phi_{XUV}$.

Figure 9 shows a RABBITT trace that was measured by ionizing argon as a target gas in the REMI. The phases for sidebands 16 to 24 are also plotted in Fig. 9. From the phase difference between each sideband, the spectral phase of the APT is obtained.

The spectral amplitude of the APT is taken from the reconstructed XUV spectrum (Fig. 8). Knowing the spectral phases and the spectral amplitude of the APT, the structure of the attosecond pulses in time is reconstructed with the inverse Fourier transform. With this method, we obtain an average pulse duration for the XUV pulses in the APT as 410 ± 30 attoseconds. In comparison, the Fourier limited pulses in the APT would have a duration of 305 attoseconds (Fig. 10).

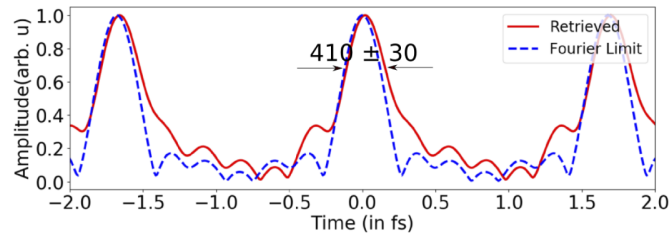


Fig. 10. Reconstructed XUV pulses from the attosecond pulse train. The Fourier Limited pulses have a duration of 305 attoseconds while the retrieved pulses have a duration of 410 ± 30 attoseconds.

4. Multi-particle coincidence RABBITT measurements

Using the coincidence detection capabilities of the REMI, the various ionization channels in atomic/molecular photoionization can be studied through XUV-IR pump-probe experiments. Two examples of attosecond time resolved experiments - the photodissociation of the hydrogen molecule and the photoionization of argon dimers - are presented here.

4.1. RABBITT with H_2

Photoionization of molecules such as H_2 often reveal intriguing aspects of molecular dynamics and corresponding experimental datasets serve as platforms to test the latest theories. Through RABBITT measurements on such systems, it is possible to observe the coupling of electron-nuclear dynamics with attosecond precision, by studying dissociation processes [36]. The cross-section for the dissociation of H_2 is 2 orders of magnitude lower than direct ionization, as seen in Fig. 11, where the Time-of-flight spectrum for ionization by the APT and IR field is shown. The electrons are mainly from the direct ionization. Even with a high-repetition rate laser, the data must therefore be acquired over at least a few hours to obtain a significant number of events from the dissociation channel.

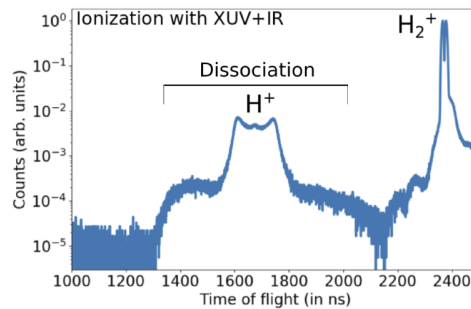


Fig. 11. Time of flight (TOF) spectrum for the ionization of H_2 by the APT + IR. The ratio of ionization yields from direct ionization to the dissociation channel ($\frac{N(H^+)}{N(H_2^+)}$) is approximately 0.06. Figure adapted from [24].

Using the ion and electron momenta provided by the REMI, high quality 2-dimensional joint energy distributions (e.g. Figure 12) can be obtained. In such a distribution, the ion Kinetic Energy Release (KER) [37] in molecular dissociation is plotted against the respective electron kinetic energy. With the help of joint energy distributions, the dissociation pathways can be identified.

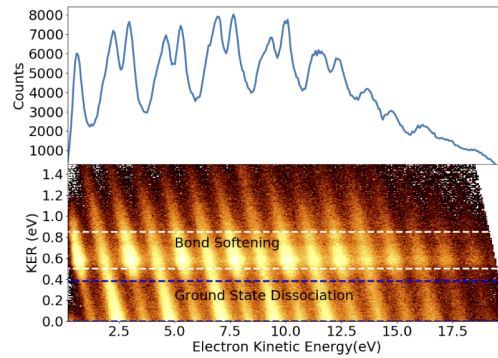


Fig. 12. Bottom: A two dimensional joint-energy distribution of the KER vs electron kinetic energy for the dissociation of hydrogen in the presence of XUV and IR integrated over all delays. Top: Electron kinetic energy spectrum obtained by integrating over all KERs. Figure adapted from [24].

The joint energy distribution obtained by performing an XUV-IR pump-probe measurement on the H_2 molecule and integrating over all delays is shown in Fig. 12. By choosing narrow KER windows, electrons emerging from various dissociation channels are obtained. For each dissociation channel, plotting the electron kinetic energy as a function of time-delay gives the respective RABBITT spectrogram. Two such KER windows are shown in Fig. 12, corresponding to the *Ground state dissociation* and the *Bond Softening* channels. Ground state dissociation occurs when the molecule dissociates directly upon absorption of one XUV photon, while bond softening occurs when an IR photon couples the ground state of the molecular ion to the first excited state of that molecular ion after ionization by XUV [38]. The RABBITT spectrograms for these channels are shown in Fig. 13. Without being able to map the electron kinetic energies to their KERs, the total photoelectron spectrum would contain a mix of signals from all dissociation channels, due to which temporal dynamics cannot be reliably extracted.

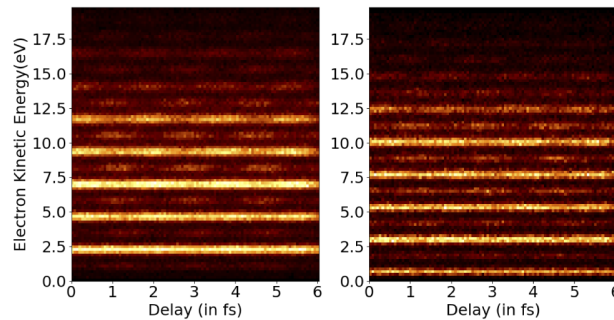


Fig. 13. RABBITT trace for electrons from: Left - the ground state dissociation channel (KER = 0 to 0.38 eV in Fig. 12), Right - the bond softening region (KER = 0.5 to 0.85 eV in Fig. 12). Figures adapted from [24].

The KER distribution for ground state dissociation exhibits a maximum at zero and a tail towards larger KERs. For bond softening, the KER exhibits a broad peak with a maximum around 0.6 eV. Where both the KER distributions overlap, there is an interference between the two channels. This interference leads to an asymmetric electron emission with respect to the proton [39,40]. A detailed analysis of the sideband oscillations for the two channels along with the 3-dimensional momentum distribution of the fragments reveals that this asymmetric

electron emission can be controlled on a sub-femtosecond timescale by varying the XUV-IR delay. This finding is also validated by a theoretical model. The results of this experiment are discussed in detail in a separate publication [41]. This experiment is extremely challenging with a conventional laser system (Rep.-rate <10 kHz) as such a multi-particle coincidence measurement would require a long acquisition time, in the order of a few days.

We note that for this measurement, the stabilization was not used. This was because the interferometer drift stabilization was still being developed while this measurement was performed and was hence not installed in the beamline. The signal to noise ratio was sufficient enough to resolve oscillations in a short time window of approximately 10 minutes, demonstrating good short-term passive stability. However, owing to long-term drifts, the dataset was later corrected in blocks of 10 minutes. The acquisition time for this dataset was around 15 hours.

4.2. RABBITT on argon

A RABBITT measurement was performed with the active stabilization on, to study the time resolved photoionization of argon dimers. While performing RABBITT on argon, a significant number of data points are also obtained from the ionization of argon dimers since the supersonic gas jet has a small but noticeable contribution of dimers. The fraction of coincidences detected from the argon dimer is only about 1% of the coincidences detected from the ionization of atomic argon (Fig. 14).

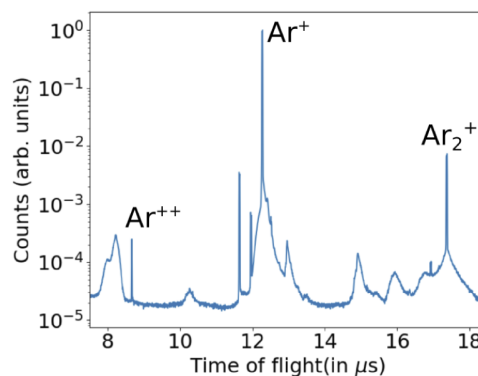


Fig. 14. Time of flight spectrum of the ions for ionization with the APT and IR. The ratio of dimers ionized with respect to atomic argon is around 1%.

To eliminate false coincidences, the ion detection rate for the ionization of atomic argon was maintained at less than one-tenth of the laser's repetition rate. With the Ar⁺ ions being detected at a rate of 3 kHz, the dimer ions were detected at about 30 Hz. To obtain a statistically significant number of data points, the measurement was run over 12 hours, performing multiple delay scans. The measurements on argon are also the "out-of-loop" measurements to quantify the interferometer stability. Although stabilization was on, a small amount of drift was observed upon analyzing the RABBITT trace of atomic argon. This is because the phase shift in the interference fringes does not completely mirror the drift in the real interferometer as explained in Sec. 2.5.

The actual drift of the interferometer is obtained by analyzing the phase shift of one sideband with time. For example, the data taken over 1 hour is divided into four parts and the phase of the sideband is estimated for each RABBITT trace (Fig. 15). Keeping the sideband phase from the first part of the measurement as a reference, the phase shifts over one hour can be found. The mean drift over 1 hour obtained by this method gives a value less than 50 attoseconds. Along with the information from analyzing the interference fringes in Sec. 2.5, this clearly indicates that the XUV-IR pump-probe measurements are performed with a sub-50 attosecond stability.

For the long term stability, the entire dataset over 12 hours was divided into 1 hour slices and the procedure above was repeated, the phase shift of the sideband was around 300 attoseconds ($\approx 0.2\pi$ radians phase shift) over 12 hours. This is because the drift is cumulative and cannot be fully eliminated by the feedback loop. The oscillation contrast in the RABBITT trace is however not significantly affected. The dataset hence did not necessarily require a drift correction, since the oscillation contrast is sufficient to retrieve the phases. The phases retrieved from the sideband oscillations for electrons in coincidence with Ar^+ and Ar_2^+ respectively, are shown in Fig. 16.

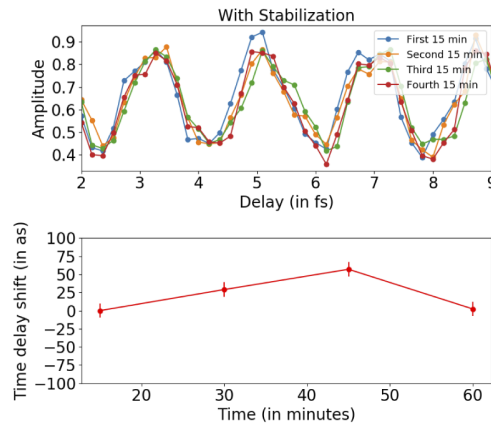


Fig. 15. Top : Projection of the sideband oscillations from a RABBITT measurement on atomic argon, tracked over 1 hour. Bottom: Phase shift of the sideband oscillations over one hour, obtained with the cosine fit described in Sec. 3.2.

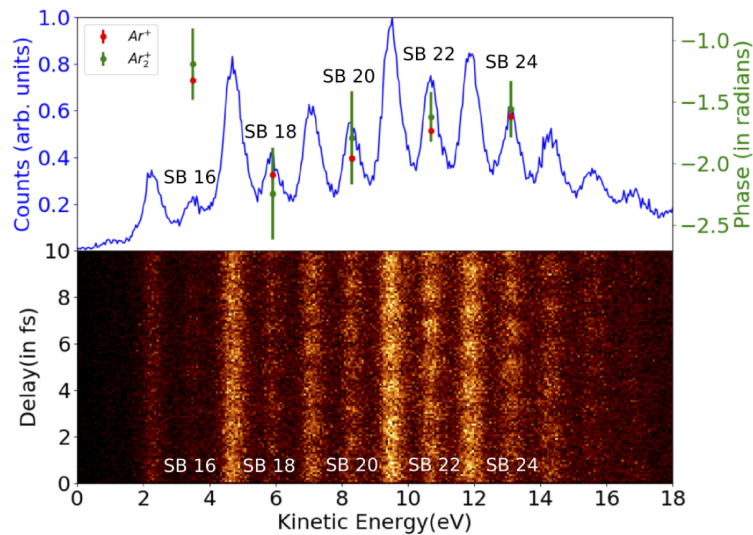


Fig. 16. Top: Photoelectron spectrum integrated over all delays. Bottom: Experimental RABBITT trace for the photoionization of argon dimers. The green dots in the top part are the measured sideband oscillation phases for the dimers and the red dots are the phases from Fig. 9.

The phases measured in the case of dimers show negligible difference to that of atomic argon. The reason for this could be the weak Van der Waals potential that binds the argon atoms in the

dimer. The electron wavepacket exiting such a loosely bound system experiences a phase shift that is mostly from the Coulomb potential of one of the atoms. Hence, the phases resemble the case of atomic argon. Further measurements with longer acquisition times are necessary for an accurate comparison as well as a deeper understanding of how a Van der Waals potential influences photoionization delays.

However, this experiment demonstrates the ability of the setup to reliably perform coincidence measurements over several hours or even days and also opens up the possibility of observing even the dissociation of argon dimers, such as in Interatomic Coulomb Decay [42]. The fraction of dissociated argon dimers is typically 10^{-4} times that of atomic argon, thereby requiring the experiment to be run for at least 48 hours, which is feasible with this system.

5. Towards multi-sideband RABBITT measurements

The photoelectron spectra in conventional RABBITT contain only one sideband in between the two adjacent high-harmonic bands. The sideband is formed by a two-photon transition process where the XUV photon causes a bound-continuum transition and the IR probe photon drives a transition within the continuum. Changing the ratio of the HHG-driving pulse frequency and the probe pulse frequency allows the number of sidebands between the two high-harmonic bands in the photoelectron spectrum to vary. The interfering quantum paths lead to the intensity modulation of the sidebands in the delay scan, involving different numbers of transitions in the continuum [43,44]. This opens an opportunity to study multi-photon transitions within the continuum.

In Ref. [43], a new multi-sideband RABBITT scheme has been proposed, that involves using the second harmonic ($\lambda = 515 \text{ nm}$) of the laser frequency to generate the APT while keeping the fundamental IR beam ($\lambda = 1030 \text{ nm}$) as the probe. Since subsequent harmonics are now separated by four times the IR photon energy, the RABBITT spectrum contains three sidebands instead of one. The modulation frequency for these sidebands is twice that of conventional RABBITT (thus $4\omega_{IR}$ and $\tau_{SB} = 850 \text{ as}$). It is now essential to have a sub-50 attoseconds interferometer stability. We discuss here the two main modifications done to the setup to study 3-Sideband RABBITT, as shown in Fig. 17.

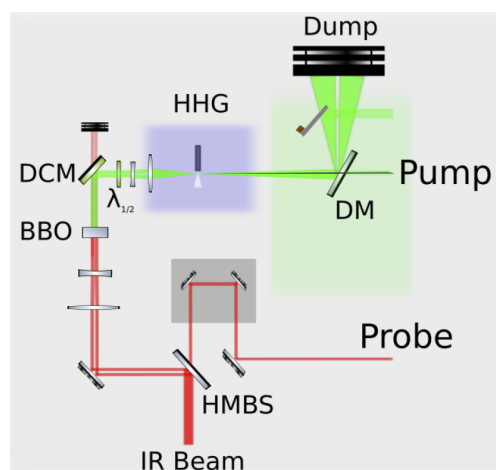


Fig. 17. Modified experimental setup for the Multi-Sideband RABBITT measurements.
Note: DCM- dichroic mirror.

First, a telescope is placed in the pump arm to reduce the beam diameter to approximately 4mm. The collimated beam then goes through a BBO crystal, followed by a dichroic mirror

to separate the fundamental and its second harmonic. A half-wave plate is placed after this in order to match the polarization of the second harmonic pump with the fundamental probe. The collimated second harmonic beam is expanded and focused on the HHG target.

Second, in order to operate the drift stabilization with this setup, interference fringes need to be generated on the CMOS camera. Owing to two different wavelengths of the pump and probe beams, an additional BBO is used to convert the probe IR beam transmitted through the recombination mirror (RM in Fig. 5), into its second harmonic. A half-wave plate is placed after this BBO as well to match the polarizations. Using the drift stabilization system, the interferometric jitter in this case also is less than 50 as, and the $4\omega_{IR}$ oscillations in the 3-sideband RABBITT spectrogram are well resolved. Without stabilizing the interferometer, the oscillations are not visible, indicating that a very good stability is achieved in the former case. Figure 18 shows one of the first experimental RABBITT traces measured with this configuration. The $4\omega_{IR}$ oscillations are clearly visible not only in the center sideband, but also in the upper and lower ones with a good signal to noise ratio. Further analysis of the retrieved sideband phases along with other results of this experiment will be published elsewhere.

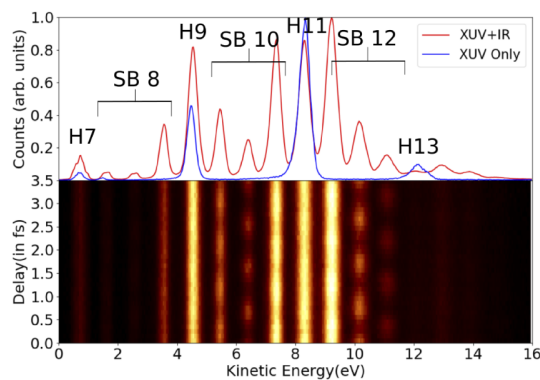


Fig. 18. Bottom: Experimental trace from a 3-Sideband RABBITT measurement on argon, Top: Photoelectron spectrum integrated over all delays.

6. Conclusion

The successful combination of a REMI with a high-repetition rate laser for attosecond pump-probe experiments is presented here. To demonstrate the capabilities of the setup, measurements have been performed with molecular hydrogen and argon dimers on the attosecond timescale. Both measurements lasted at least 12 hours, confirming the required stability for coincidence experiments. The experimental setup has been further modified for performing Multi-Sideband RABBITT measurements. Additionally, work is being carried out to extend the XUV cut-off in order to obtain photons with an energy higher than 50 eV, which would be crucial for studying processes such as single-photon double ionization in noble gases. This system provides a robust tool for performing new and highly demanding experiments that require high-stability, a high-repetition rate attosecond source and a kinematically complete detection scheme allowing data acquisition over days.

Funding. Deutsche Forschungsgemeinschaft (DFG-SPP-1840-HA-8399/2-1).

Acknowledgments. The authors would like to thank Sivarama Krishnan for valuable inputs while preparing the manuscript.

Disclosures. The authors declare no conflicts of interest.

Data availability. Data underlying the results presented in this paper are not publicly available at this time but may be obtained from the authors upon reasonable request.

References

1. P. M. Paul, E. S. Toma, P. Breger, G. Mullot, F. Augé, P. Balcou, H. G. Muller, and P. Agostini, "Observation of a train of attosecond pulses from high harmonic generation," *Science* **292**(5522), 1689–1692 (2001).
2. I. Jordan, M. Huppert, D. Rattenbacher, M. Peper, D. Jelovina, C. Perry, A. von Conta, A. Schild, and H. J. Wörner, "Attosecond spectroscopy of liquid water," *Science* **369**(6506), 974–979 (2020).
3. M. Ossiander, J. Riemensberger, S. Neppl, M. Mittermair, M. Schäffer, A. Duensing, M. S. Wagner, R. Heider, M. Wurzer, M. Gerl, M. Schnitzenbaumer, J. V. Barth, F. Libisch, C. Lemell, J. Burgdörfer, P. Feulner, and R. Kienberger, "Absolute timing of the photoelectric effect," *Nature* **561**(7723), 374–377 (2018).
4. X. F. Li, A. L'Huillier, M. Ferray, L. A. Lompré, and G. Mainfray, "Multiple-harmonic generation in rare gases at high laser intensity," *Phys. Rev. A* **39**(11), 5751–5761 (1989).
5. M. Reduzzi, P. Carpeggiani, S. Kühn, F. Calegari, M. Nisoli, S. Stagira, C. Vozzi, P. Dombi, S. Kahaly, P. Tzallas, D. Charalambidis, K. Varju, K. Osvay, and G. Sansone, "Advances in high-order harmonic generation sources for time-resolved investigations," *J. Electron Spectrosc. Relat. Phenom.* **204**, 257–268 (2015). Gas phase spectroscopic and dynamical studies at Free-Electron Lasers and other short wavelength sources.
6. J. Limpert, F. Roser, D. N. Schimpf, E. Seise, T. Eidam, S. Hadrlich, J. Rothhardt, C. J. Misas, and A. Tünnermann, "High repetition rate gigawatt peak power fiber laser systems: Challenges, design, and experiment," *IEEE J. Sel. Top. Quantum Electron.* **15**(1), 159–169 (2009).
7. J. Fischer, J. Drs, F. Labaye, N. Modsching, V. J. Wittwer, and T. Südmeyer, "Intra-oscillator high harmonic generation in a thin-disk laser operating in the 100-fs regime," *Opt. Express* **29**(4), 5833–5839 (2021).
8. M. Kretschmar, J. Tuemmler, B. Schütte, A. Hoffmann, B. Senftleben, M. Mero, M. Sauppe, D. Rupp, M. J. J. Vrakking, I. Will, and T. Nagy, "Thin-disk laser-pumped opcpa system delivering 4.4 tw few-cycle pulses," *Opt. Express* **28**(23), 34574–34585 (2020).
9. A. Harth, C. Guo, Y.-C. Cheng, A. Losquin, M. Miranda, S. Mikaelsson, C. M. Heyl, O. Prochnow, J. Ahrens, U. Morgner, A. L'Huillier, and C. L. Arnold, "Compact 200 kHz HHG source driven by a few-cycle OPCPA," *J. Opt.* **20**(1), 014007 (2018).
10. S. Mikaelsson, J. Vogelsang, C. Guo, I. Sytcevic, A.-L. Viotti, F. Langer, Y.-C. Cheng, S. Nandi, W. Jin, A. Olofsson, R. Weissenbilder, J. Mauritsson, A. L'Huillier, M. Gisselbrecht, and C. L. Arnold, "A high-repetition rate attosecond light source for time-resolved coincidence spectroscopy," *Nanophotonics* **10**(1), 117–128 (2020).
11. R. Moshhammer, D. Fischer, and H. Kollmus, *Recoil-Ion Momentum Spectroscopy and "Reaction Microscopes"* (Springer Berlin Heidelberg, Berlin, Heidelberg, 2003), pp. 33–58.
12. P. Ye, T. Cszizmadia, L. G. Oldal, H. N. Gopalakrishna, M. Füle, Z. Filus, B. Nagyllés, Z. Divéki, T. Grósz, M. Dumergue, P. Jójárt, I. Seres, Z. Bengery, V. Zuba, Z. Várallyay, B. Major, F. Frassetto, M. Devetta, G. D. Lucarelli, M. Lucchini, B. Moio, S. Stagira, C. Vozzi, L. Poletto, M. Nisoli, D. Charalambidis, S. Kahaly, A. Zaïr, and K. Varjú, "Attosecond pulse generation at ELI-ALPS 100 kHz repetition rate beamline," *J. Phys. B: At., Mol. Opt. Phys.* **53**(15), 154004 (2020).
13. M. Osolodkov, F. J. Furch, F. Schell, P. Šušnjar, F. Cavalcante, C. S. Menoni, C. P. Schulz, T. Witting, and M. J. J. Vrakking, "Generation and characterisation of few-pulse attosecond pulse trains at 100 kHz repetition rate," *J. Phys. B: At., Mol. Opt. Phys.* **53**(19), 194003 (2020).
14. D. Hammerland, P. Zhang, S. Kühn, P. Jojart, I. Seres, V. Zuba, Z. Várallyay, D. Charalambidis, K. Osvay, T. T. Luu, and H. J. Wörner, "Reconstruction of attosecond pulses in the presence of interfering dressing fields using a 100 kHz laser system at ELI-ALPS," *J. Phys. B: At., Mol. Opt. Phys.* **52**(23), 23LT01 (2019).
15. T. Witting, M. Osolodkov, F. Schell, F. Morales, S. Patchkovskii, P. Šušnjar, F. H. M. Cavalcante, C. S. Menoni, C. P. Schulz, F. J. Furch, and M. J. J. Vrakking, "Generation and characterization of isolated attosecond pulses at 100 khz repetition rate," *Optica* **9**(2), 145–151 (2022).
16. M. Sabbar, S. Heuser, R. Boge, M. Lucchini, L. Gallmann, C. Cirelli, and U. Keller, "Combining attosecond xuv pulses with coincidence spectroscopy," *Rev. Sci. Instrum.* **85**(10), 103113 (2014).
17. H. Ahmadi, S. Kellerer, D. Ertel, M. Moiola, M. Reduzzi, P. K. Maroju, A. Jäger, R. N. Shah, J. Lutz, F. Frassetto, L. Poletto, F. Bragheri, R. Osellame, T. Pfeifer, C. D. Schröter, R. Moshhammer, and G. Sansone, "Collinear setup for delay control in two-color attosecond measurements," *JPhys Photonics* **2**(2), 024006 (2020).
18. O. Guyétand, M. Gisselbrecht, A. Huetz, P. Agostini, B. Carré, P. Breger, O. Gobert, D. Garzella, J.-F. Hergott, O. Tcherbakoff, H. Merdji, M. Bougeard, H. Rottke, M. Böttcher, Z. Ansari, P. Antoine, and L. F. DiMauro, "Complete momentum analysis of multi-photon photo-double ionization of xenon by XUV and infrared photons," *J. Phys. B: At., Mol. Opt. Phys.* **41**(6), 065601 (2008).
19. D. Strickland and G. Mourou, "Compression of amplified chirped optical pulses," *Opt. Commun.* **56**(3), 219–221 (1985).
20. M. Müller, M. Kienel, A. Klenke, T. Gottschall, E. Shestae, M. Plötner, J. Limpert, and A. Tünnermann, "1 kw 1 mj eight-channel ultrafast fiber laser," *Opt. Lett.* **41**(15), 3439–3442 (2016).
21. J. Limpert, A. Klenke, M. Kienel, S. Breitkopf, T. Eidam, S. Hadrlich, C. Jauregui, and A. Tünnermann, "Performance scaling of ultrafast laser systems by coherent addition of femtosecond pulses," *IEEE J. Sel. Top. Quantum Electron.* **20**(5), 268–277 (2014).







22. S. Hädrich, A. Klenke, A. Hoffmann, T. Eidam, T. Gottschall, J. Rothhardt, J. Limpert, and A. Tünnermann, "Nonlinear compression to sub-30-fs, 0.5 mJ pulses at 135 W of average power," *Opt. Lett.* **38**(19), 3866–3869 (2013).
23. S. Hädrich, M. Kienel, M. Müller, A. Klenke, J. Rothhardt, R. Klas, T. Gottschall, T. Eidam, A. Drozdy, P. Jójárt, Z. Várallyay, E. Cormier, K. Osvay, A. Tünnermann, and J. Limpert, "Energetic sub-2-cycle laser with 216 W average power," *Opt. Lett.* **41**(18), 4332–4335 (2016).
24. F. Shobeiry, Ph.D. thesis, Universität Heidelberg (2021).
25. J. Ullrich, R. Moshhammer, R. Dörner, O. Jagutzki, V. Mergel, H. Schmidt-Böcking, and L. Spielberger, "Recoil-ion momentum spectroscopy," *J. Phys. B: At., Mol. Opt. Phys.* **30**(13), 2917–2974 (1997).
26. P. Coerlin, Ph.D. thesis, Universität Heidelberg (2015).
27. M. Lampton, O. Siegmund, and R. Raffanti, "Delay line anodes for microchannel-plate spectrometers," *Rev. Sci. Instrum.* **58**(12), 2298–2305 (1987).
28. M. Isinger, D. Busto, S. Mikaelsson, S. Zhong, C. Guo, P. Salières, C. L. Arnold, A. L'Huillier, and M. Gisselbrecht, "Accuracy and precision of the rabbit technique," *Philos. Trans. R. Soc., A* **377**(2145), 20170475 (2019).
29. M. Takeda, H. Ina, and S. Kobayashi, "Fourier-transform method of fringe-pattern analysis for computer-based topography and interferometry," *J. Opt. Soc. Am.* **72**(1), 156–160 (1982).
30. K. H. Womack, "Interferometric Phase Measurement Using Spatial Synchronous Detection," in *Precision Surface Metrology*, vol. 0429 J. C. Wyant, ed., International Society for Optics and Photonics (SPIE, 1983), pp. 8–15.
31. M. Chini, H. Mashiko, H. Wang, S. Chen, C. Yun, S. Scott, S. Gilbertson, and Z. Chang, "Delay control in attosecond pump-probe experiments," *Opt. Express* **17**(24), 21459–21464 (2009).
32. S. Hädrich, J. Rothhardt, M. Krebs, S. Demmler, A. Klenke, A. Tünnermann, and J. Limpert, "Single-pass high harmonic generation at high repetition rate and photon flux," *J. Phys. B: At., Mol. Opt. Phys.* **49**(17), 172002 (2016).
33. J. Samson and W. Stolte, "Precision measurements of the total photoionization cross-sections of He, Ne, Ar, Kr, and Xe," *J. Electron Spectrosc. Relat. Phenom.* **123**(2-3), 265–276 (2002). Determination of cross-sections and momentum profiles of atoms, molecules and condensed matter.
34. H. G. Müller, "Reconstruction of attosecond harmonic beating by interference of two-photon transitions," *Appl. Phys. B* **74**(S1), s17–s21 (2002).
35. J. Dahlström, D. Guénot, K. Klünder, M. Gisselbrecht, J. Mauritsson, A. L'Huillier, A. Maquet, and R. Taïeb, "Theory of attosecond delays in laser-assisted photoionization," *Chem. Phys.* **414**, 53–64 (2013). Attosecond spectroscopy.
36. L. Cattaneo, J. Vos, R. Y. Bello, A. Palacios, S. Heuser, L. Pedrelli, M. Lucchini, C. Cirelli, F. Martín, and U. Keller, "Attosecond coupled electron and nuclear dynamics in dissociative ionization of H₂," *Nat. Phys.* **14**(7), 733–738 (2018).
37. E. Illenberger and J. Momigny, *Energy Balance in the Dissociation Processes of Molecular Ions* (Steinkopff, Heidelberg, 1992), pp. 141–169.
38. P. H. Bucksbaum, A. Zavriyev, H. G. Müller, and D. W. Schumacher, "Softening of the H₂⁺ molecular bond in intense laser fields," *Phys. Rev. Lett.* **64**(16), 1883–1886 (1990).
39. W. Vanroose, F. Martín, T. N. Rescigno, and C. W. McCurdy, "Complete photo-induced breakup of the H₂ molecule as a probe of molecular electron correlation," *Science* **310**(5755), 1787–1789 (2005).
40. A. Fischer, A. Sperl, P. Cörlin, M. Schönwald, H. Rietz, A. Palacios, A. González-Castrillo, F. Martín, T. Pfeifer, J. Ullrich, A. Senfleben, and R. Moshhammer, "Electron localization involving doubly excited states in broadband extreme ultraviolet ionization of H₂," *Phys. Rev. Lett.* **110**(21), 213002 (2013).
41. F. Shobeiry, P. Fross, H. Srinivas, T. Pfeifer, R. Moshhammer, and A. Harth, "Sub-femtosecond optical control of entangled states," arXiv:2110.06668 [quant-ph] (2021).
42. L. S. Cederbaum, J. Zobeley, and F. Tarantelli, "Giant intermolecular decay and fragmentation of clusters," *Phys. Rev. Lett.* **79**(24), 4778–4781 (1997).
43. A. Harth, N. Douguet, K. Bartschat, R. Moshhammer, and T. Pfeifer, "Extracting phase information on continuum-continuum couplings," *Phys. Rev. A* **99**(2), 023410 (2019).
44. D. Bharti, D. Atri-Schuller, G. Menning, K. R. Hamilton, R. Moshhammer, T. Pfeifer, N. Douguet, K. Bartschat, and A. Harth, "Decomposition of the transition phase in multi-sideband schemes for reconstruction of attosecond beating by interference of two-photon transitions," *Phys. Rev. A* **103**(2), 022834 (2021).

4.2 Publication II: Decomposition of the transition phase in multi-sideband schemes for reconstruction of attosecond beating by interference of two-photon transitions

This paper discusses the adaptation of the RABBITT technique to the 3-SB RABBITT scheme and examines the information that can be obtained through this method. The phase information contained within the oscillation of the sideband yield encodes details about the multi-order interaction of photoelectrons in the continuum. In order to interpret the measurable phase, we begin by revisiting the commonly used “asymptotic approximation” for extracting phase information from 1-SB RABBITT measurements. This approximation is rooted in perturbative theory and involves approximating the intermediate and final states of the photoelectron with the asymptotic form of the scattering wave. As a result, the measured phase can be split into two components: a Wigner phase associated with a single-photon ionization process, and a continuum-continuum phase (ϕ^{cc}) linked to additional single-photon transitions that occur in the continuum [33]. We expand upon this approximation to accommodate scenarios where there are multiple transitions in the continuum, and demonstrate that the final phase of the electron wavepacket can still be decomposed into a single-photon ionization phase and a sequence of continuum-continuum coupling phases corresponding to each transition.

An *ab initio* calculation of a 3-SB RABBITT scheme in atomic hydrogen is performed by solving the time-dependent Schrödinger equation. The phases of the yield oscillations of the sidebands are analyzed and compared with the analytical phase obtained using the decomposition approximation. The approximation predicts that the phase of the three sidebands between consecutive harmonics should be identical. While qualitatively correct, deviations from this prediction are observed in the simulation. These deviations are attributed to the dependence of the continuum-continuum coupling phase on the orbital angular momenta involved.

Decomposition of the transition phase in multi-sideband schemes for reconstruction of attosecond beating by interference of two-photon transitions

Divya Bharti ¹, David Atri-Schuller ², Gavin Menning ², Kathryn R. Hamilton ², Robert Moshhammer,¹ Thomas Pfeifer,¹ Nicolas Douguet,³ Klaus Bartschat ² and Anne Harth ^{1,*}

¹Max-Planck-Institute for Nuclear Physics, D-69117 Heidelberg, Germany

²Department of Physics and Astronomy, Drake University, Des Moines, Iowa 50311, USA

³Department of Physics, Kennesaw State University, Marietta, Georgia 30060, USA



(Received 25 November 2020; accepted 2 February 2021; published 26 February 2021)

Reconstruction of attosecond beating by interference of two-photon transitions (RABBITT) is a technique that can be used to determine the phases of atomic transition elements in photoionization processes. In the traditional RABBITT scheme, the so-called asymptotic approximation considers the measured phase as a sum of the Wigner phase linked to a single-photon ionization process and the continuum-continuum phase associated with further single-photon transitions in the continuum. In this paper, we extend the asymptotic approximation to multi-sideband RABBITT schemes. The predictions from this approximation are then compared with results obtained by an *ab initio* calculation based on solving the time-dependent Schrödinger equation for atomic hydrogen.

DOI: [10.1103/PhysRevA.103.022834](https://doi.org/10.1103/PhysRevA.103.022834)

I. INTRODUCTION

The reconstruction of attosecond beating by interference of two-photon transitions (RABBITT) technique was originally introduced for the temporal characterization of attosecond pulse trains (APTs) produced via high-order harmonic generation (HHG) [1]. The utility of this technique was later extended to measure the relative photoionization time delay from different valence shells in argon [2]. Nowadays, RABBITT is extensively employed to study the attosecond dynamics in atoms [2–5], molecules [6,7], and solids [8–10].

RABBITT is a pump-probe interferometric technique, in which an extreme ultraviolet (XUV) APT ionizes a target gas in the presence of a time-delayed near-infrared (NIR) pulse, and the kinetic-energy spectra of the photoelectrons are recorded as a function of the varied relative delay. Without the NIR probe photon, the photoelectron spectrum consists of discrete peaks (here also termed “harmonics”) corresponding to the high-order harmonic peaks in the XUV spectrum. The presence of the probe field leads to the appearance of sidebands as additional peaks between the discrete harmonic peaks. In the traditional RABBITT scheme, only one sideband is formed between two consecutive harmonic peaks. This requires a minimum of one bound-continuum (bc) transition and one continuum-continuum (cc) transition. For RABBITT, two paths leading to the same sideband interfere. As the time

delay (τ) between the pump and probe pulse is varied, the sideband signal is periodically modulated. The phase of this delay-dependent modulation is written as

$$\Delta\phi = \Delta\phi_{\text{XUV}} + \Delta\phi_{\text{atom}}, \quad (1)$$

where $\Delta\phi_{\text{XUV}}$ is the phase related to the average group delay of the XUV pulses. In many cases, the atomic phase $\Delta\phi_{\text{atom}}$ can be conveniently split into two contributions:

$$\Delta\phi_{\text{atom}} = \Delta\eta + \Delta\phi^{cc}. \quad (2)$$

The Wigner-like phase shift $\Delta\eta$ originates from XUV-driven bc-transition processes, while the cc-transition phase $\Delta\phi^{cc}$ is associated with additional absorption and emission of a probe photon by the photoelectron. This relation is well accepted and was derived by Dahlström *et al.* [11] using the “asymptotic approximation,” in which the asymptotic form of the scattering wave function is used to calculate the two-photon ionization amplitude. In this approximation, ϕ^{cc} becomes universal, as it depends on the charge of the residual ion, the photoelectron’s kinetic energy, and the probe frequency, but not on the details of the atomic system. Dahlström *et al.* [11] formulated an analytical expression of ϕ^{cc} , which is additionally independent of the angular momentum ℓ .

However, the actual ϕ^{cc} does depend on the angular momenta [11–13], and this dependence becomes significant close to the ionization threshold. Since the ℓ dependence of ϕ^{cc} decreases with increasing photoelectron energy, we will generally neglect it in the discussion below, except for pointing out occasions where this dependence may become important.

For the one-sideband (1-SB) RABBITT setup, the probe-field intensity is usually kept low to avoid significant contributions from multiple cc transitions. Increasing this intensity leads to the formation of higher-order sidebands, which then may overlap with the harmonic bands [14]. Lately,

* anne.harth@mpi-hd.mpg.de

Published by the American Physical Society under the terms of the [Creative Commons Attribution 4.0 International](https://creativecommons.org/licenses/by/4.0/) license. Further distribution of this work must maintain attribution to the author(s) and the published article’s title, journal citation, and DOI. Open access publication funded by the Max Planck Society.

other forms of RABBITT schemes comprising more than one sideband between two consequent harmonic photoelectron peaks were also proposed and realized. For example, a two-sideband (2-SB) RABBITT configuration was used in an attosecond-pulse shaping measurement [15], and an experimental technique for a three-sideband (3-SB) RABBITT scheme was proposed to extract the cc-related phase *separately* by cancelling contributions from the Wigner phase [16].

In all these other schemes, multiple cc transitions are involved. However, a similar description and interpretation like Eq. (2) for multiphoton continuum transitions is by no means obvious. In this paper, we introduce a decomposition approximation by extending the asymptotic approximation to higher-order matrix elements as mentioned by Dahlström *et al.* [17].

This decomposition approximation leads to the interpretation that the final RABBITT phase is built up from the phases of stepwise transitions of the photoelectron, i.e., first the XUV-induced bc transition, and then subsequent cc transitions, each involving a single IR photon.

This paper is structured as follows. In Sec. II, we outline the basic equations on which the paper is built. This is followed by Sec. III, where we first discuss the well-known 1-SB case before we introduce the decomposition approximation, which is then formally applied to the 3-SB case. Details of our derivation are given in the Appendix. Section IV provides a brief summary of the *ab initio* numerical calculations, against which the predictions of the decomposition approximation are tested and discussed in Sec. V. We finish with a summary and an outlook regarding potential consequences for future experiments.

II. GENERAL FORMULATION

The RABBITT technique is based on the interference of different quantum paths leading to the same final energy. All equations in the present paper are written in the nonrelativistic single-active electron (SAE) picture, assuming that the initial bound electron has orbital angular momentum $\ell_i = 0$ (often omitted in the notation below) and considering linearly polarized electric fields. Unless indicated otherwise, atomic units are used.

In the framework of time-dependent perturbation theory, the general expression of the transition amplitude describing a quantum path from an initial state $|i\rangle$ to a final state $|\vec{k}_N\rangle$ with asymptotic momentum \vec{k}_N , upon absorption of one XUV-pump photon (Ω) and $(N - 1)$ IR-probe photons (ω), is given by the N th-order matrix element [18]

$$M_P^{(N)}(\vec{k}_N) = -i\tilde{E}_\Omega\tilde{E}_\omega^{N-1}\langle\vec{k}_N|z\prod_{n=0}^{N-2}[G^+(\epsilon_i + \Omega + n\omega)z]|i\rangle, \quad (3)$$

where G^+ is the retarded resolvent of the free-field Hamiltonian, ϵ_i is the initial state energy, z is the electric dipole operator, and P specifies the path by which the final state is reached.

By projecting the final continuum states for the photoelectron on a partial-wave basis, the matrix elements corresponding to the different angular momentum channels can be

disentangled as

$$M_P^{(N)}(\vec{k}_N) = \tilde{E}_\Omega\tilde{E}_\omega^{N-1}\sum_{\ell_N}\mathcal{M}_{P,\ell_N}^{(N)}(k_N)Y_{\ell_N,0}(\hat{k}_N). \quad (4)$$

The sum over ℓ_N represents the possible orbital angular momenta in the final state, and $Y_{\ell_N,0}$ are spherical harmonics. Furthermore, $\tilde{E}_\Omega = E_\Omega e^{i\phi_\Omega}$ and $\tilde{E}_\omega = E_\omega e^{i\omega\tau}$ (for absorption) are the complex electric-field amplitudes of the XUV-pump (Ω) and NIR-probe (ω) pulses, respectively.

Although much effort has been put into estimating multiphoton transition matrix elements [19,20], it remains challenging to accurately calculate the phases of multiphoton transition elements for a general target other than atomic hydrogen, even for $N = 2$. Hence, finding a suitable approximation seems highly desirable.

III. DECOMPOSITION OF THE RABBITT PHASE

We start this section by applying the asymptotic approximation to a hydrogenic system to simplify the second-order matrix element $M^{(N=2)}$. We then extend the ideas behind the asymptotic approximation to higher-order matrix elements to arrive at a decomposition relation (see the Appendix for details) and subsequently apply it to the 3-SB RABBITT case.

A. 1-SB RABBITT

Figure 1(a) shows the energy-level diagram and transition pathways involved in a traditional (second-harmonic) 1-SB RABBITT scheme. To explain the appearance of the sideband S , one needs to consider only two paths, A and B, which can both be described by second-order electric dipole transitions. Path A corresponds to the absorption of one XUV photon of energy $\Omega_{q+1} = (q + 1)2\omega$ from the harmonic H_{q+1} and emission of one probe (2ω) photon, while path B corresponds to the absorption of an XUV photon of energy $\Omega_{q-1} = (q - 1)2\omega$ from the lower harmonic H_{q-1} and the absorption of a probe photon. Both paths lead to the same final continuum state $|f\rangle$ with asymptotic photoelectron momentum k_f , thus resulting in the sideband S . Using the notation of Eq. (4), the two-photon transition amplitudes for paths A and B are expressed as

$$M_A^{(2,e)}(\vec{k}_f) = \tilde{E}_{2\omega}^*\tilde{E}_{q+1}\sum_{\ell}\mathcal{M}_{A,\ell}^{(2,e)}(k_f)Y_{\ell,0}(\hat{k}_f), \quad (5)$$

$$M_B^{(2,a)}(\vec{k}_f) = \tilde{E}_{2\omega}\tilde{E}_{q-1}\sum_{\ell}\mathcal{M}_{B,\ell}^{(2,a)}(k_f)Y_{\ell,0}(\hat{k}_f). \quad (6)$$

The superscript e (a) indicates the pathway where a probe photon (2ω) is emitted (absorbed). $\ell (= \ell_f)$ is the angular momentum of the final state ($|f\rangle$).

The angle-resolved sideband signal is formed as the coherent sum of all the quantum paths leading to the same final momentum state:

$$S(\tau, \vec{k}_f) \propto |M_A^{(2,e)}(\vec{k}_f) + M_B^{(2,a)}(\vec{k}_f)|^2. \quad (7)$$

The phase difference between the absorption and emission paths is varied by changing the time delay (τ) between the pump and the probe pulses. This results in an oscillation of the sideband signal as a function of the relative pulse delay. In

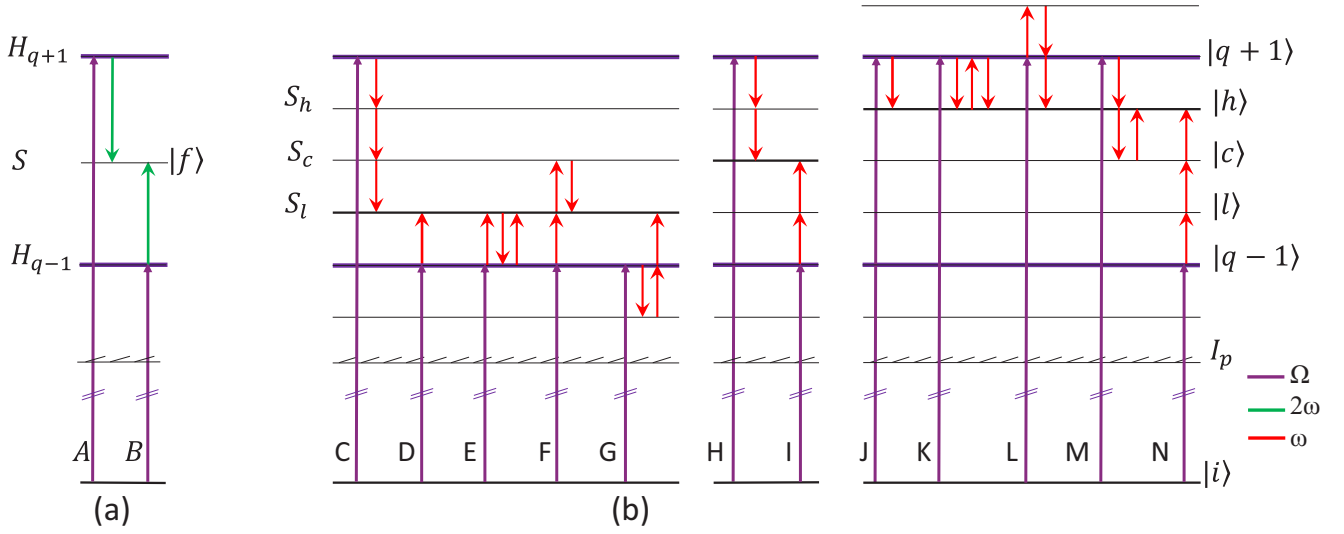


FIG. 1. Energy-level schemes in (a) traditional RABBITT and (b) 3-SB RABBITT. Photoionization by an XUV APT results in the appearance of harmonic peaks H_{q-1} and H_{q+1} (with q being an even integer) in the photoelectron spectrum. The XUV spectrum (Ω) contains only odd harmonics of the 2ω pulse. Exchange of NIR probe photons of frequency 2ω or ω leads to the development of (a) a single sideband or (b) three sidebands, respectively. Interference among the multiple quantum paths leading to final states with the same energy gives rise to periodic oscillations in the sideband signal as a function of delay between pump and probe. Only the lowest-order paths required to explain the oscillations in the signal are shown. Paths in which the probe photon is absorbed before the pump photon are ignored.

the following, we discuss only angle-integrated cases, which results in Eq. (7) becoming an incoherent sum of partial-wave contributions, i.e.,

$$S(\tau, k_f) \propto \sum_{\ell} |\tilde{E}_{q+1} \tilde{E}_{2\omega}^* \mathcal{M}_{A,\ell}^{(2,e)}(k_f) + \tilde{E}_{q-1} \tilde{E}_{2\omega} \mathcal{M}_{B,\ell}^{(2,a)}(k_f)|^2 \propto I_0 + I_1 \cos(4\omega\tau - \Delta\phi_{\text{XUV}} - \Delta\phi_{\text{atom}}), \quad (8)$$

where $\Delta\phi_{\text{XUV}} = (\phi_{q+1} - \phi_{q-1})$ is the phase difference between the harmonic fields ($q+1$) and ($q-1$), while

$$\Delta\phi_{\text{atom}} = \arg \left[\sum_{\ell} \mathcal{M}_{A,\ell}^{(2,e)} \mathcal{M}_{B,\ell}^{*(2,a)} \right] \quad (9)$$

is the atomic phase.

The atomic phase contains the combined effect of the ionizing XUV pump and the NIR probe. It is not obvious whether the two contributions can be separated to recover the pure (Wigner-only) photoionization delay. For the 1-SB RABBITT scheme, Dahlström *et al.* [11] showed that the atomic phase can be split into a single-photon ionization phase (η) and the measurement-induced cc-transition phase (ϕ^{cc}) when using the asymptotic approximation. They also derived an analytical expression for ϕ^{cc} corresponding to the single-photon free-free transition of the photoelectron in the vicinity of the parent ion:

$$\phi_{k,\kappa}^{cc} = \arg \left[\frac{(2\kappa)^{iZ/\kappa} \Gamma[2 + iZ(1/\kappa - 1/k)] + \gamma(k, \kappa)}{(2k)^{iZ/k} (\kappa - k)^{iZ(1/\kappa - 1/k)}} \right]. \quad (10)$$

Here κ is the wave number of the initial state in the continuum while k is the wave number of the final photoelectron momentum after the exchange of an NIR photon, Z is the remaining charge on the parent ion, and γ denotes a long-range amplitude correction. Details can be found in Ref. [11].

It can be verified that $\phi_{k,\kappa}^{cc} = -\phi_{\kappa,k}^{cc}$; i.e., the absolute cc phase for absorption and emission between two given energy levels is identical.

Using the asymptotic approximation, the phase of the two-photon ionization amplitudes for any particular transition channel can be expanded as [11]

$$\arg[\mathcal{M}_{A,\ell}^{(2,e)}] \approx -\frac{\ell_{q+1}\pi}{2} + \eta_{\ell_{q+1}} + \phi_{f,q+1}^{cc}, \quad (11)$$

$$\arg[\mathcal{M}_{B,\ell}^{(2,a)}] \approx -\frac{\ell_{q-1}\pi}{2} + \eta_{\ell_{q-1}} + \phi_{f,q-1}^{cc}. \quad (12)$$

The Wigner-like phase η depends on the angular momentum (ℓ_{q+1} or ℓ_{q-1}) and the energy (ϵ_{q+1} or ϵ_{q-1}) of the intermediate state reached upon the XUV absorption, while ϕ^{cc} depends only on the energy of the two states involved in the free-free transitions. In special cases, where only one angular momentum channel ($\ell_{q+1} = \ell_{q-1} = \lambda$) is significant in the bc transition, the atomic phase shift can be written as

$$\Delta\phi_{\text{atom}} = \arg \left[\sum_{\ell} \mathcal{M}_{A,\ell}^{(2,e)} \mathcal{M}_{B,\ell}^{*(2,a)} \right] \approx \Delta\eta_{\lambda} + \Delta\phi^{cc} \quad (13)$$

with $\Delta\eta_{\lambda} = \eta_{\lambda}(\epsilon_{q+1}) - \eta_{\lambda}(\epsilon_{q-1})$ and $\Delta\phi^{cc} = \phi_{f,q+1}^{cc} - \phi_{f,q-1}^{cc}$ denoting the Wigner and cc phase differences, respectively.

Equation (13) is the same as Eq. (2) and is broadly used to measure the Wigner delay in various systems. We emphasize, however, that ϕ^{cc} here does not depend on the different angular momenta involved in the cc transitions, and the bc-transition step contains only one dominant angular momentum channel. In cases where several angular momentum channels are involved in the bc transition or ϕ^{cc} depends on the angular momenta of the final states, the phase extracted from RABBITT experiments depends on the detection angle

of the observed electron. The atomic phase $\Delta\phi_{\text{atom}}$ measured in angle-integrated RABBITT schemes then becomes the weighted average of the Wigner and cc phases of each contributing channel.

B. Decomposition approximation

For RABBITT schemes involving more than two photon transitions ($N > 2$), the calculation of the necessary matrix elements becomes an increasingly formidable task. To get around this difficulty, we apply the ideas of the asymptotic approximation to estimate the phases of the higher-order matrix elements. Details of our derivation are provided in the Appendix. This allows us to decompose the phase of higher-order matrix elements into a sum of the phases generated by several subsequent single-photon transitions:

$$\arg[\mathcal{M}_{P,\ell}^{(N)}] \approx \frac{(N-2)\pi}{2} - \frac{\lambda\pi}{2} + \eta_\lambda + \phi_{k_2,k_1}^{cc} + \phi_{k_3,k_2}^{cc} + \dots + \phi_{k_{N-2},k_{N-1}}^{cc} + \phi_{k_N,k_{N-1}}^{cc}. \quad (14)$$

The decomposition approximation can be interpreted as a stepwise buildup of the final phase, starting with promotion from the initial bound state to a continuum state by the XUV and followed by $N - 1$ transitions within the continuum states driven by the NIR. We emphasize that this approximation requires that we only have one bc channel (λ) and ϕ^{cc} does not depend on ℓ .

C. 3-SB RABBITT

As an example, we now apply the decomposition approximation to the 3-SB RABBITT case. In this scheme, the consecutive harmonic peaks in the photoelectron spectrum are separated by four times the probe photon energy (ω). Figure 1(b) shows the 3-SB RABBITT scheme and the dominant transition paths, up to fourth order, that are involved in the formation of three sidebands. The population of the center sideband S_c requires the absorption of an XUV pump photon (Ω) and the exchange of at least two probe photons. There are two dominant paths (H and I) leading to S_c , which can both be described using third-order matrix elements.

On the other hand, to explain the oscillations of the lower sideband S_l and the higher sideband S_h , one needs to consider fourth-order dipole transitions, since at least one such high-order process has to be involved (e.g., path C for S_l and path N for S_h). Altogether, there are five transition terms involved: one second-order and four fourth-order terms. Interference among the paths D to G, or similarly J to M, however, does not result in delay-dependent oscillations. Furthermore, the relation $\phi_{k,\kappa}^{cc} = -\phi_{\kappa,k}^{cc}$, along with the decomposition approximation, implies that the phases from back and forth transitions between the same two energy levels will cancel out. Hence, apart from a trivial additional π shift, the phases in all fourth-order absorption paths (E, F, and G) would be the same as in the second-order absorption path (D). Similarly, there would be no phase difference between the paths J, K, L, and M. Within this approximation, therefore, we can ignore the higher-order paths E to G and K to M, as they will only change

the amplitude but not the phase of the oscillation. This results in the following equations:

$$S_l(\tau, k_l) \propto \sum_\ell |\tilde{E}_{q+1}\tilde{E}_\omega^* \mathcal{M}_{C,\ell}^{(4,e)}(k_l) + \tilde{E}_{q-1}\tilde{E}_\omega \mathcal{M}_{D,\ell}^{(2,a)}(k_l)|^2 = I_0^l + I_1^l \cos(4\omega\tau - \Delta\phi_{\text{XUV}} - \Delta\phi_{\text{atom}}^l), \quad (15)$$

$$S_c(\tau, k_c) \propto \sum_\ell |\tilde{E}_{q+1}\tilde{E}_\omega^* \mathcal{M}_{H,\ell}^{(3,e)}(k_c) + \tilde{E}_{q-1}\tilde{E}_\omega^2 \mathcal{M}_{I,\ell}^{(3,a)}(k_c)|^2 = I_0^c + I_1^c \cos(4\omega\tau - \Delta\phi_{\text{XUV}} - \Delta\phi_{\text{atom}}^c), \quad (16)$$

$$S_h(\tau, k_h) \propto \sum_\ell |\tilde{E}_{q+1}\tilde{E}_\omega^* \mathcal{M}_{J,\ell}^{(2,e)}(k_h) + \tilde{E}_{q-1}\tilde{E}_\omega^3 \mathcal{M}_{N,\ell}^{(4,a)}(k_h)|^2 = I_0^h + I_1^h \cos(4\omega\tau - \Delta\phi_{\text{XUV}} - \Delta\phi_{\text{atom}}^h). \quad (17)$$

By applying the decomposition approximation to the various atomic phase contributions in the above equations, and again assuming that there is only one partial wave (λ) created in the XUV ionization process, these phases can be written as

$$\Delta\phi_{\text{atom}}^l = \arg\left[\sum_\ell \mathcal{M}_{C,\ell}^{(4,e)} \mathcal{M}_{D,\ell}^{*(2,a)}\right] \approx \Delta\eta_\lambda + \phi_{h,q+1}^{cc} + \phi_{c,h}^{cc} + \phi_{l,c}^{cc} - \phi_{l,q-1}^{cc} + \pi, \quad (18)$$

$$\Delta\phi_{\text{atom}}^c = \arg\left[\sum_\ell \mathcal{M}_{H,\ell}^{(3,e)} \mathcal{M}_{I,\ell}^{*(3,a)}\right] \approx \Delta\eta_\lambda + \phi_{h,q+1}^{cc} + \phi_{c,h}^{cc} - \phi_{c,l}^{cc} - \phi_{l,q-1}^{cc}, \quad (19)$$

$$\Delta\phi_{\text{atom}}^h = \arg\left[\sum_\ell \mathcal{M}_{J,\ell}^{(2,e)} \mathcal{M}_{N,\ell}^{*(4,a)}\right] \approx \Delta\eta_\lambda + \phi_{h,q+1}^{cc} - \phi_{h,c}^{cc} - \phi_{c,l}^{cc} - \phi_{l,q-1}^{cc} - \pi. \quad (20)$$

Inserting the relation $\phi_{k,\kappa}^{cc} = -\phi_{\kappa,k}^{cc}$ into Eqs. (18)–(20), we see that the atomic phases in all three sidebands are the same, except for an additional phase of π due to the fact that the higher and lower sidebands are created, respectively, by interference of two- and four-photon transitions, while the center sideband is created by two three-photon transitions. Note, however, that the final kinetic energies of the photoelectrons in the three sidebands are different.

IV. NUMERICAL CALCULATIONS

In order to test the validity of the decomposition approximation, we performed *ab initio* calculations on atomic hydrogen to examine the delay-dependent variation in the sideband signals for the 3-SB RABBITT scheme. We chose a pump pulse containing eight odd harmonics (5, 7, 9, . . . , 19) of the generating 400-nm pulse. The pulse duration of each single harmonic (E_{q-1}) is 20 fs and the peak intensity is 10^9 W/cm². All harmonics are in phase, i.e., $\Delta\phi_{\text{XUV}} = 0$. The center wavelength of the probe pulse is 800 nm, the pulse duration is also 20 fs, and the peak intensity is 10^{11} W/cm².

The calculations were performed with a further improved version of the computer code described by Douguet *et al.* [21]. We performed extensive checks to ensure convergence of the predictions with the number of partial waves included, independence of the results from both the radial and the time

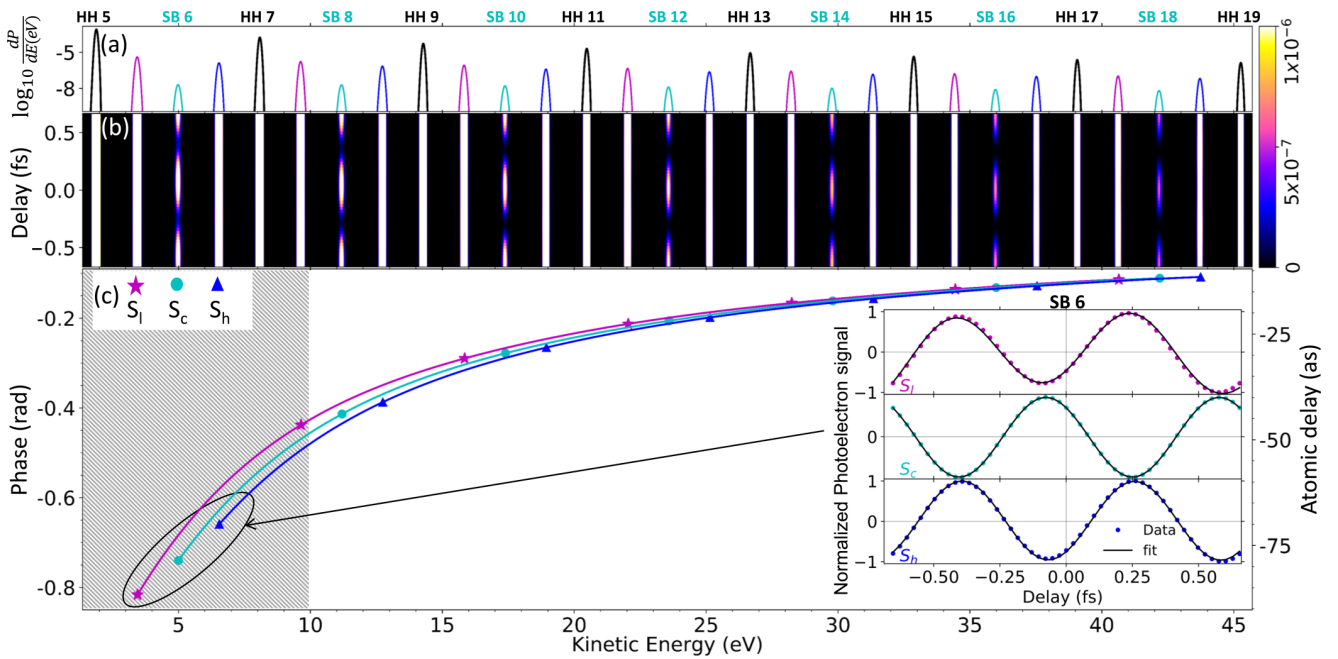


FIG. 2. (a) Photoelectron spectrum at maximum overlap between pump and probe ($\tau = 0$). (b) Contour plot of a 3-SB RABBITT spectrum. (c) Retrieved phases from the sideband oscillations. Inset: Fit of a cosine function (black line) to the photoelectron signals (dots) shown for the sixth sideband group order. After retrieving the sideband phases (procedure demonstrated in the inset), the additional π shift was removed from S_l and S_h in (c) for clarity of presentation. $\Delta\phi_{XUV} = 0$ in this case. The conversion from phase (left axis) to time (right axis) is $\text{time} = \text{phase}/(4\omega)$.

steps in the discretization, and excellent agreement between the results obtained in either the length or the velocity form of the electric dipole operator. Given these rigorous tests, we are confident that the numerical predictions are highly accurate for this nonrelativistic one-electron problem and hence can be used to draw reliable conclusions about the validity (or the lack thereof) of the approximations outlined above.

V. RESULTS AND DISCUSSION

Figure 2(a) exhibits the photoelectron spectrum at zero time delay ($\tau = 0$) on a base-10 logarithmic scale. The pump-probe delay-resolved RABBITT scan is shown in Fig. 2(b). Since the color bar was set to make the intensity oscillations in the center sideband (S_c) visible, the other sideband oscillations are saturated with this setting. The inset in Fig. 2(c) shows the normalized data and the fits of the oscillatory part for the three sidebands in the lowest SB group. Note that the phase of the center sideband is π out of phase as shown by Eq. (19). All the phases were retrieved from the data set shown in Fig. 2(b). For the data analysis, the sideband signals were integrated over an energy window of 0.25 eV around the peaks. A constant component was subtracted from the integrated sideband signals and then renormalized. To retrieve the phase information, the data were then fit to a function containing a cosine term and a quadratic term to account for the decay of the signal with the delay (see the inset in Fig. 2). To simplify the comparison, the additional π phases in S_l and S_h were removed.

As expected, the contrast of the oscillation is best in the center sideband, because both pathways, H and I, contribute

to its population at the same (third) order. Since the modulations in the lower and higher sidebands originate from the interference of second-order and fourth-order transition terms, the depth of the corresponding oscillations is shallow before renormalization. In Fig. 2(c), the phases of the sidebands at their respective kinetic energies are plotted.

Figure 3 shows the phase of the center sideband and the corresponding analytical phase, as expressed in Eq. (19). The

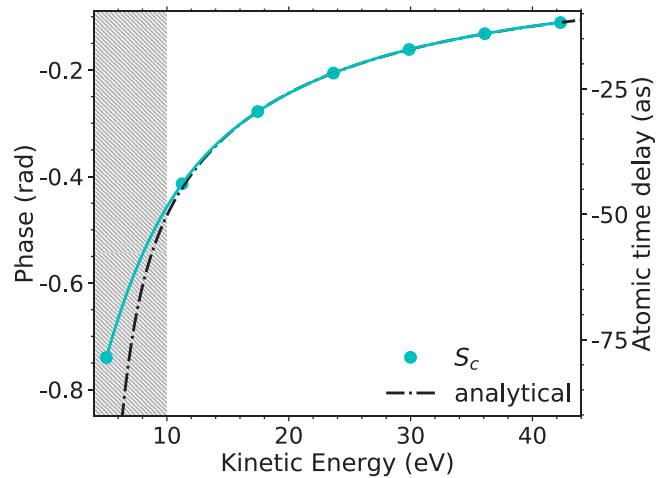


FIG. 3. Phase of the S_c sideband (solid circles) extracted from the time-dependent Schrödinger equation calculation (see Fig. 2) and the corresponding analytical phase (dot-dashed line) estimated from Eq. (19). The difference above 12 eV between the two curves corresponds to a time delay smaller than 0.01 as.

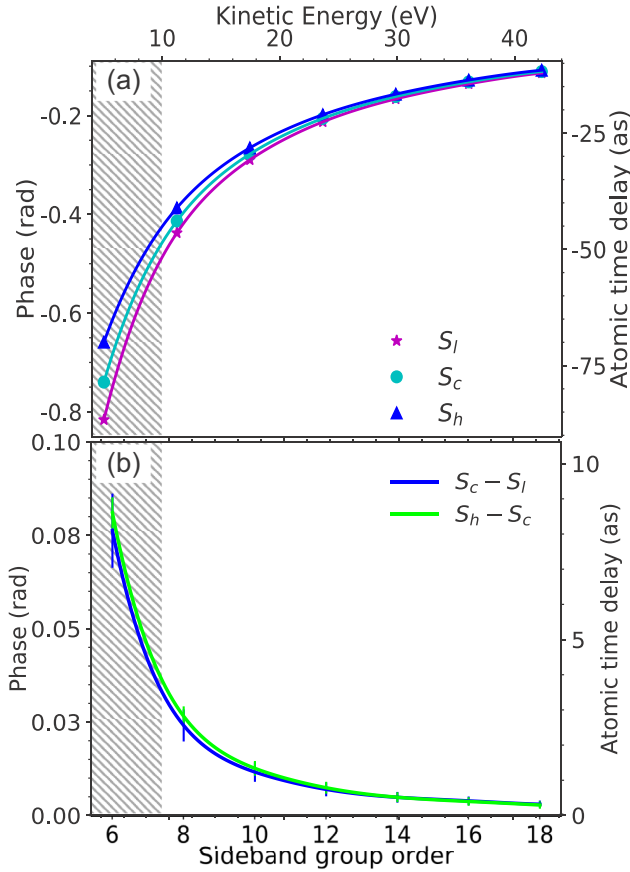


FIG. 4. (a) Phases of three sidebands, S_c (dots), S_l (stars), and S_h (triangles), over the sideband group order. (b) Difference in the phases of nearby sidebands with respect to the center sideband. The error bar corresponds to the fitting error. The kinetic energy on the top horizontal axis corresponds to the kinetic energy of the center sideband.

single-photon ionization phase η_λ for a hydrogenic system is simply the Coulomb phase:

$$\eta_\lambda(\kappa, Z) = \arg \left[\Gamma \left(\lambda + 1 - i \frac{Z}{\kappa} \right) \right]. \quad (21)$$

Here, κ is the momentum of the released photoelectron, while λ is the orbital angular momentum quantum number. In the case of atomic hydrogen, there is only one transition channel available by XUV ionization, which is $s \rightarrow p$, i.e., $\lambda = 1$. The single-photon cc-phase contributions ϕ^{cc} for each transition are calculated using Eq. (10). For more details, see Ref. [11]. By inserting the expressions for η and ϕ^{cc} into Eq. (19), the analytical phase associated with the center sideband S_c is obtained.

The agreement between the two curves is remarkable for photoelectrons with a kinetic energy above 10 eV. Near threshold, however, the curves diverge. It should be mentioned that the analytical formula for ϕ^{cc} breaks down at low kinetic energies. Nevertheless, the good agreement between the analytical phases and the phase retrieved from the numerical calculation indicates that the decomposition approximation

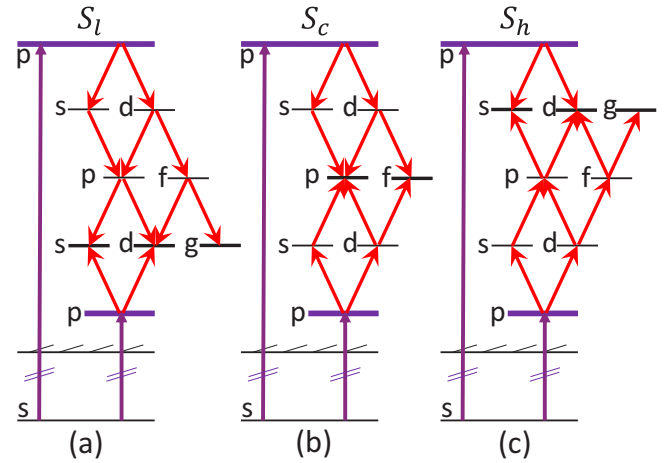


FIG. 5. Angular-momentum-resolved quantum paths leading to (a) the lower sideband, (b) the center sideband, and (c) the higher sideband. The angular momentum state g does not contribute to the delay-dependent modulation of the angle-integrated sideband intensity. Only the dominant paths from Fig. 1 are shown.

works very well for the *center sideband* in a 3-SB RABBITT scheme.

Figure 2(c) is plotted again in Fig. 4(a), but now over the same sideband group order. We immediately see that the phases in the neighboring sidebands are not identical, but the difference between the phases obtained from the three sidebands steadily decreases with increasing kinetic energy. The phase difference between S_h and S_l in the same sideband group corresponds to a time delay of less than 6 as slightly above a photoelectron energy of 10 eV, but reduces to less than 2 as beyond 20 eV.

The fact that the phases in the three sidebands (Fig. 4) are not exactly the same could indicate that the decomposition approximation is not valid. However, we know from Fig. 3 that the approximation works well for the center sideband. Therefore, we now discuss the possible origins of the discrepancy, which is clearly visible for the S_h and S_l sidebands.

As mentioned in the Introduction, it has been shown that the actual ϕ^{cc} depends on the angular momentum of the states involved in the transitions [11–13]. In that case, back-and-forth transitions between two energy levels in the continuum do not cancel out the cc phases, i.e., $\phi_{k,\kappa}^{cc}(\ell_k) \neq -\phi_{\kappa,k}^{cc}(\ell_\kappa)$, because there might be different channels involved in the two processes. As a consequence, the second-order absorption path (D) and the previously neglected fourth-order paths (E, F, and G) may not have the same phase. Similarly, the dependence of ϕ^{cc} on the angular momentum may result in a phase difference between the paths J, K, L, and M even when the decomposition approximation holds.

The angular momentum dependence of ϕ^{cc} may also manifest itself when one considers only the dominant paths contributing to the modulation of all sidebands (see Fig. 5). If an electron with $\ell = 0$ starts in the ground state, the final wave function of the center sideband photoelectron after interaction with three photons will contain orbital angular quantum numbers $\ell = 1$ and $\ell = 3$. On the other hand, the lower (higher) sideband includes quantum numbers $\ell = 0, 2, 4$ in

the emission (absorption) path, and $\ell = 0, 2$ in the absorption (emission) path. Keeping this in mind, all the ϕ^{cc} corresponding to the same energy levels could be different, and hence the phases in the intermediate sidebands may not be the same.

We conclude that the phase difference between the three sidebands comes most likely from the neglected ℓ dependence of ϕ^{cc} while the applied decomposition approximation is reasonable. The good agreement between the ℓ -independent analytical phase and the retrieved phases from the time-dependent Schrödinger equation calculation for the S_c (cf. Fig. 4) can be explained by considering the fact that both the emission and absorption paths are of the same order and contain the same set of possible partial waves (p and f). As hinted in Refs. [11, 12] for 1-SB RABBITT calculations on He and H, the absolute phase difference between distinct partial waves for the absorption paths is the same as for the emission paths. Hence the difference between the two paths nullifies the effect of the ℓ dependence. This is not true for the lower and higher sidebands, where the dominant interfering paths are of different orders.

However, while the angular-momentum dependence is particularly prominent for low kinetic energies of the photoelectron, it becomes increasingly negligible with growing kinetic energy [13]. This parallels our observation of improved agreement between the phases of all three sidebands in our 3-SB RABBITT scheme. Consequently, for sufficiently large photoelectron energies, where the angular momentum dependence of ϕ^{cc} is small, our calculations support the decomposition approximation to interpret the measured atomic phase in multi-sideband RABBITT schemes as stepwise one-photon transitions.

VI. SUMMARY AND OUTLOOK

We studied the formation of sidebands and their oscillations in the 3-SB RABBITT scheme. The phases retrieved from the oscillation of the three sidebands contain the phases of higher-order dipole matrix elements, which are difficult to interpret. A decomposition approximation was attempted to simplify the phase extraction of the higher-order matrix elements as the sum of the phases of sequential one-photon transitions. The decomposition approximation along with the assumption that ϕ^{cc} is independent of the orbital angular momenta involved predicts that the phases extracted from all sidebands between two consecutive harmonics are the same.

In order to check these assumptions, we performed *ab initio* calculations for atomic hydrogen. While the phases in all sideband groups are not identical, the difference decreases with increasing kinetic energy. This difference is attributed to the dependence of ϕ^{cc} on the angular momentum and the involvement of different ℓ channels in the three sidebands. We, therefore, conclude that while the decomposition approximation is an appropriate assumption when describing a multi-sideband RABBITT scheme, the dependence of ϕ^{cc} on the orbital angular momenta cannot be neglected for low-energy sidebands.

Multi-sideband RABBITT provides an opportunity to probe deeper into the continuum of the ionic species. The present benchmark studies are important for a planned exper-

iment using an argon target, which is experimentally much more suitable than atomic hydrogen. We already started numerical calculations for this system and presented preliminary results at a recent conference [22]. Note, however, that having the XUV APT ionize the electron from the $3p$ bound orbital leads to continuum s and d waves, thereby further complicating the interpretation of the RABBITT phase. Work is currently in progress to address these issues.

In summary, we believe that multi-SB RABBITT opens up a frontier in the study of transition phases in photoionization processes. Since many more questions remain, we hope that the present paper will stimulate further work in this area.

ACKNOWLEDGMENTS

This work was supported by the Deutsche Forschungsgemeinschaft under DFG-SPP-1840-HA-8399/2-1 and by the U.S. National Science Foundation under Grants No. OAC-1834740 and No. PHY-1803844 (D.A.S., G.M., K.R.H., K.B.) and No. PHY-2012078 (N.D.), as well as the XSEDE supercomputer allocation Grant No. PHY-090031. The calculations were carried out on Stampede2 and Frontera at the Texas Advanced Computing Center in Austin, Bridges at the Pittsburgh Supercomputing Center, and Comet at the San Diego Supercomputer Center.

APPENDIX

In this Appendix, we derive Eq. (14) by generalizing the asymptotic approximation for the two-photon matrix element introduced by Dahlström *et al.* [11]. In order to set the stage and introduce our shorthand notation for the often lengthy expressions, we first repeat the key ideas of the above paper and then apply them to the third- and higher-order matrix elements.

We begin by explicitly writing Eq. (3) as

$$\begin{aligned} M^{(N)}(\vec{k}_N; \Omega, \omega) &= -i\tilde{E}_\Omega \tilde{E}_\omega^{N-1} \lim_{\epsilon \rightarrow 0^+} \int d^3\vec{k}'_{N-1} \cdots \int d^3\vec{k}'_2 \\ &\times \int d^3\vec{k}'_1 \frac{\langle \vec{k}_N | z | \vec{k}'_{N-1} \rangle \cdots \langle \vec{k}'_2 | z | \vec{k}'_1 \rangle \langle \vec{k}'_1 | z | i \rangle}{(\epsilon_{N-1} - \epsilon'_{N-1} + i\epsilon) \cdots (\epsilon_1 - \epsilon'_1 + i\epsilon)}. \end{aligned} \quad (\text{A1})$$

Here ϵ_i is the initial state energy and $\epsilon_i + \Omega + n\omega = \epsilon_{n+1}$. As in Ref. [11], we neglect all contributions from bound states, since they are expected to be small if the photon energy for the bc transition is sufficiently high.

The final and intermediate continuum states are decomposed into partial waves as

$$\varphi_{\vec{k}}(\vec{r}) = (8\pi)^{3/2} \sum_{\ell, m} i^\ell e^{-i\eta_\ell(k)} Y_{\ell, m}^*(\hat{k}) Y_{\ell, m}(\hat{r}) R_{k, \ell}(r), \quad (\text{A2})$$

where $\eta_\ell(k)$ denotes the scattering phases, $Y_{\ell, m}$ the spherical harmonics, and $R_{k, \ell}$ are the radial parts. Splitting the initial state into its radial and angular parts according to

$$\varphi_{n_i, \ell_i, m_i}(\vec{r}) = Y_{\ell_i, m_i}(\hat{r}) R_{n_i, \ell_i}(r), \quad (\text{A3})$$

using $z = \sqrt{\frac{4\pi}{3}} r Y_{1,0}(\hat{r})$, and inserting Eqs. (A2) and (A3) into Eq. (A1) yields for $N = 2$

$$\begin{aligned} M^{(2)}(\vec{k}_2; \Omega, \omega) &= -i \frac{4\pi}{3} (8\pi)^{3/2} \tilde{E}_\Omega \tilde{E}_\omega \\ &\times \sum_{\ell_2, m_2} (-i)^{\ell_2} e^{i\eta_2} Y_{\ell_2, m_2}(\hat{k}_2) \\ &\times \sum_{\ell_1, m_1} \langle Y_{\ell_2, m_2} | Y_{1,0} | Y_{\ell_1, m_1} \rangle \langle Y_{\ell_1, m_1} | Y_{1,0} | Y_{\ell_i, m_i} \rangle \\ &\times T_{\ell_2, \ell_1, \ell_i}^{(2)}(k_2; \Omega, \omega) \\ &= \tilde{E}_\Omega \tilde{E}_\omega \sum_{\ell_2} \mathcal{M}_{\ell_2, m_2}^{(2)}(k_2) Y_{\ell_2}(\hat{k}_2). \end{aligned} \quad (\text{A4})$$

This defines $\mathcal{M}_{\ell_2, m_2}^{(2)}(k_2)$ and simplifies to Eq. (4) of the main text for $\ell_i = m_i = 0$ and linearly polarized light ($m_2 = 0$).

Defining the first-order radial matrix element

$$T_{\ell_1, \ell_i}^{(1)}(k'_1; \Omega) = \langle R_{k'_1, \ell_1} | r | R_{n_i, \ell_i} \rangle \quad (\text{A5})$$

allows us to write the second-order element as

$$\begin{aligned} T_{\ell_2, \ell_1, \ell_i}^{(2)}(k_2; \Omega, \omega) \\ = \lim_{\varepsilon \rightarrow 0^+} \int_0^\infty d\varepsilon'_1 \frac{\langle R_{k_2, \ell_2} | r | R_{k'_1, \ell_1} \rangle T_{\ell_1, \ell_i}^{(1)}(k'_1; \Omega)}{\varepsilon_i + \Omega - \varepsilon'_1 + i\varepsilon}. \end{aligned} \quad (\text{A6})$$

The first-order perturbed wave function [11] is defined as

$$\begin{aligned} |\rho_{k_1, \ell_1}\rangle &= \lim_{\varepsilon \rightarrow 0^+} \int_0^\infty d\varepsilon'_1 \frac{T_{\ell_1, \ell_i}^{(1)}(k'_1; \Omega) |R_{k'_1, \ell_1}\rangle}{\varepsilon_1 - \varepsilon'_1 + i\varepsilon} \\ &= \mathcal{P} \int_0^\infty d\varepsilon'_1 \frac{T_{\ell_1, \ell_i}^{(1)}(k'_1; \Omega) |R_{k'_1, \ell_1}\rangle}{\varepsilon_1 - \varepsilon'_1} \\ &\quad - i\pi T_{\ell_1, \ell_i}^{(1)}(k_1; \Omega) |R_{k_1, \ell_1}\rangle, \end{aligned} \quad (\text{A7})$$

where \mathcal{P} denotes the principal value.

The key in deriving an analytic expression for the contribution to the phase of the matrix element is to replace the radial functions of the intermediate and final continuum states by their asymptotic form

$$\lim_{r \rightarrow \infty} R_{k, \ell}(r) \approx \frac{N_k}{r} \sin(kr + \phi_{k, \ell}(r)). \quad (\text{A8})$$

Here $N_k \approx \sqrt{2/\pi k} (1 - Z/(2rk^2))$ is the amplitude of the asymptotic wave for a long-range potential ($-Z/r$), and the asymptotic phase is $\phi_{k, \ell}(r) = (Z/k) \ln(2kr) + \eta_\ell(k) - \pi\ell/2$. Using the same steps and approximations as outlined in Ref. [11], this leads to the approximate form

$$\lim_{r \rightarrow \infty} \rho_1(r) \approx -\frac{\pi N_1}{r} T^{(1)}(k_1) e^{i(k_1 r + \phi_1(r))} \quad (\text{A9})$$

for the perturbed wave function after further compressing the notation by defining $R_{k_n, \ell_n} \equiv R_n$, $|\rho_{k_1, \ell_1}\rangle \equiv |\rho_1\rangle$, $N_{k_n} \equiv N_n$, $\phi_{k_n, \ell_n}(r) \equiv \phi_n(r)$, $T_{\ell_1, \ell_i}^{(1)}(k_1; \Omega) \equiv T^{(1)}(k_1)$, and $\eta_{\ell_n}(k_n) \equiv \eta_n$.

The second-order matrix element then becomes

$$\begin{aligned} T_2^{(2)}(k_2) &= \langle R_2 | r | \rho_1 \rangle \\ &\approx \frac{T^{(1)}(k_1)}{i\sqrt{k_1 k_2}} \int_0^\infty dr \left(r - \frac{1}{2} \left(\frac{1}{k_1^2} + \frac{1}{k_2^2} \right) \right) \\ &\quad \times \sin(k_2 r + \phi_2(r)) e^{i(k_1 r + \phi_1(r))}. \end{aligned} \quad (\text{A10})$$

After writing the sin term in exponential form, dropping the fast-oscillating term containing $k_1 + k_2$ while keeping the term with $k_1 - k_2$, and introducing the substitution variable $-i(k_1 - k_2)r$, one obtains a Γ function with complex argument. Using this function, we find

$$\begin{aligned} T_2^{(2)}(k_2) &\approx \frac{T^{(1)}(k_1)}{\sqrt{k_1 k_2}} \frac{e^{-Z(1/k_1 - 1/k_2)\pi/2}}{(k_1 - k_2)^2} i^{\ell_2 - \ell_1 + 1} e^{i(\eta_1 - \eta_2)} \\ &\times \frac{(2k_1)^{iZ/k_1} (\Gamma[2 + iZ(1/k_1 - 1/k_2)] + \gamma(k_2, k_1))}{(2k_2)^{iZ/k_2} (k_1 - k_2)^{iZ(1/k_1 - 1/k_2)}} \end{aligned} \quad (\text{A11})$$

with $\gamma(k_2, k_1) = \frac{iZ(k_1 - k_2)}{2} \left(\frac{1}{k_1^2} + \frac{1}{k_2^2} \right) \Gamma[1 + iZ(1/k_1 - 1/k_2)]$ accounting for the effect of the long-range potential [11]. The phase of the radial matrix element is

$$\arg[T_{\ell_2, \ell_1, \ell_i}^{(2)}(k_2)] = \frac{\pi}{2} (\ell_2 - \ell_1 + 1) + (\eta_1 - \eta_2) + \phi_{2,1}^{cc}, \quad (\text{A12})$$

where

$$\begin{aligned} \phi_{2,1}^{cc} &\equiv \phi_{k_2, k_1}^{cc} \\ &= \arg \left[\frac{(2k_1)^{iZ/k_1} (\Gamma[2 + iZ(1/k_1 - 1/k_2)] + \gamma(k_2, k_1))}{(2k_2)^{iZ/k_2} (k_1 - k_2)^{iZ(1/k_1 - 1/k_2)}} \right], \end{aligned} \quad (\text{A13})$$

and we have used that $T_{\ell_1, \ell_i}^{(1)}(k_1)$ is real. Substituting Eq. (A11) back into Eq. (A4), the phase of the matrix element for the transition path $\ell_i \rightarrow \ell_1 \rightarrow \ell_2$ is

$$\begin{aligned} \arg[\mathcal{M}_{\ell_2, \ell_1, \ell_i}^{(2)}(k_2)] &\approx \frac{-\pi}{2} - \frac{\pi \ell_2}{2} + \eta_2 + \frac{\pi}{2} (\ell_2 - \ell_1 + 1) \\ &\quad + \eta_1 - \eta_2 + \phi_{2,1}^{cc} + T_{\ell_1, \ell_i}^{(1)}(k_1) \\ &= -\frac{\pi \ell_1}{2} + \eta_1 + \phi_{2,1}^{cc}. \end{aligned} \quad (\text{A14})$$

Note the cancellations in this formula, particularly the contributions from both i^{ℓ_2} and η_2 . As will be seen below, these cancellations are a general pattern when we move to higher-order matrix elements.

Our approximation for the higher-order matrix elements is based on the above formalism. Starting with the third-order element, the equivalent of Eq. (A4) is

$$\begin{aligned} M^{(3)}(\vec{k}_3; \Omega, \omega) \\ = -i \left(\frac{4\pi}{3} \right)^{3/2} (8\pi)^{3/2} \tilde{E}_\Omega \tilde{E}_\omega^2 \\ \times \sum_{\ell_3} (-i)^{\ell_3} e^{i\eta_3} Y_{\ell_3}(\hat{k}_3) \\ \times \sum_{\ell_2, \ell_1} \langle Y_{\ell_3} | Y_{1,0} | Y_{\ell_2} \rangle \langle Y_{\ell_2} | Y_{1,0} | Y_{\ell_1} \rangle \langle Y_{\ell_1} | Y_{1,0} | Y_{\ell_i} \rangle \\ \times T_{\ell_3, \ell_2, \ell_1, \ell_i}^{(3)}(k_3; \Omega, \omega) \\ = \tilde{E}_\Omega \tilde{E}_\omega^2 \sum_{\ell_3} \mathcal{M}_{\ell_3}^{(3)}(k_3) Y_{\ell_3}(\hat{k}_3). \end{aligned} \quad (\text{A15})$$

Here

$$T_{\ell_3, \ell_2, \ell_1, \ell_i}^{(3)}(k_3; \Omega, \omega) = \langle R_3 | r | \rho_2 \rangle \quad (\text{A16})$$

with the second-order perturbed wave function

$$|\rho_2\rangle = \int_0^\infty d\epsilon'_2 \frac{|R'_2\rangle \langle R'_2| r | \rho_1 \rangle}{(\epsilon_2 - \epsilon'_2 + i\varepsilon)}. \quad (\text{A17})$$

In the asymptotic approximation, we obtain

$$\rho_2(r) \approx -\frac{\pi N_2}{r} T^{(2)}(k_2) e^{i(k_2 r + \phi_2(r))} \quad (\text{A18})$$

and, consequently,

$$\begin{aligned} T_3^{(3)}(k_3) &\approx \frac{T^{(2)}(k_2)}{\sqrt{k_2 k_3}} \frac{e^{-Z(1/k_2 - 1/k_3)\pi/2}}{(k_2 - k_3)^2} i^{\ell_3 - \ell_2 + 1} e^{i(\eta_2 - \eta_3)} \\ &\times \frac{(2k_2)^{iZ/k_2} (\Gamma[2 + iZ(1/k_2 - 1/k_3)] + \gamma(k_3, k_2))}{(2k_3)^{iZ/k_3} (k_2 - k_3)^{iZ(1/k_2 - 1/k_3)}}. \end{aligned} \quad (\text{A19})$$

Looking at the phases,

$$\begin{aligned} \arg[T_{\ell_3, \ell_2, \ell_1, \ell_i}^{(3)}(k_3)] &= \frac{\pi}{2}(\ell_3 - \ell_2 + 1) + (\eta_2 - \eta_3) + \phi_{3,2}^{cc} + \arg[T^{(2)}(k_2)] \\ &= \frac{\pi}{2}(\ell_3 - \ell_1 + 2) + (\eta_1 - \eta_3) + \phi_{3,2}^{cc} + \phi_{2,1}^{cc}, \end{aligned} \quad (\text{A20})$$

and, therefore, since the above radial matrix element is independent of the intermediate angular momentum ℓ_2 , we obtain that

$$\begin{aligned} \arg[\mathcal{M}_{\ell_3, \ell_2, \ell_1, \ell_i}^{(3)}(k_3)] &= \frac{-\pi}{2} - \frac{\pi \ell_3}{2} + \eta_3 + \arg[T^{(3)}(k_3)] \\ &= \frac{\pi}{2} - \frac{\pi \ell_1}{2} + \eta_1 + \phi_{3,2}^{cc} + \phi_{2,1}^{cc}. \end{aligned} \quad (\text{A21})$$

By repeating the procedure, i.e., straightforward induction, the phase of the N th-order matrix element can be written as

$$\begin{aligned} \arg[\mathcal{M}_{\ell_N, \ell_1}^{(N)}(k_N)] &= \frac{(N-2)\pi}{2} - \frac{\pi \ell_1}{2} + \eta_{\ell_1} \\ &+ \phi_{2,k_1}^{cc} + \phi_{k_3, k_2}^{cc} + \dots + \phi_{k_N, k_{N-1}}^{cc}. \end{aligned} \quad (\text{A22})$$

The analytical form of $\arg[\mathcal{M}_{\ell_N, \ell_1}^{(N)}(k_N)]$ only depends on the angular momenta of the first intermediate state after the XUV step.

-
- [1] P. M. Paul, E. S. Toma, P. Breger, G. Mullot, F. Augé, P. Balcou, H. G. Muller, and P. Agostini, *Science* **292**, 1689 (2001).
- [2] K. Klünder, J. M. Dahlström, M. Gisselbrecht, T. Fordell, M. Swoboda, D. Guénot, P. Johnsson, J. Caillat, J. Mauritsson, A. Maquet, R. Taïeb, and A. L'Huillier, *Phys. Rev. Lett.* **106**, 143002 (2011).
- [3] M. Isinger, R. J. Squibb, D. Busto, S. Zhong, A. Harth, D. Kroon, S. Nandi, C. L. Arnold, M. Miranda, J. M. Dahlström, E. Lindroth, R. Feifel, M. Gisselbrecht, and A. L'Huillier, *Science* **358**, 893 (2017).
- [4] D. Guénot, K. Klünder, C. L. Arnold, D. Kroon, J. M. Dahlström, M. Miranda, T. Fordell, M. Gisselbrecht, P. Johnsson, J. Mauritsson, E. Lindroth, A. Maquet, R. Taïeb, A. L'Huillier, and A. S. Kheifets, *Phys. Rev. A* **85**, 053424 (2012).
- [5] A. W. Bray, F. Naseem, and A. S. Kheifets, *Phys. Rev. A* **97**, 063404 (2018).
- [6] W. Boutu, S. Haessler, H. Merdji, P. Breger, G. Waters, M. Stankiewicz, L. J. Frasinski, R. Taïeb, J. Caillat, A. Maquet, P. Monchicourt, B. Carre, and P. Salieres, *Nat. Phys.* **4**, 545 (2008).
- [7] S. Haessler, J. Caillat, W. Boutu, C. Giovanetti-Teixeira, T. Ruchon, T. Auguste, Z. Diveki, P. Breger, A. Maquet, B. Carré, R. Taïeb, and P. Salieres, *Nat. Phys.* **6**, 200 (2010).
- [8] R. Locher, L. Castiglioni, M. Lucchini, M. Greif, L. Gallmann, J. Osterwalder, M. Hengsberger, and U. Keller, *Optica* **2**, 405 (2015).
- [9] M. Lucchini, L. Castiglioni, L. Kasmi, P. Kliuiev, A. Ludwig, M. Greif, J. Osterwalder, M. Hengsberger, L. Gallmann, and U. Keller, *Phys. Rev. Lett.* **115**, 137401 (2015).
- [10] M. J. Ambrosio and U. Thumm, *Phys. Rev. A* **94**, 063424 (2016).
- [11] J. Dahlström, D. Guénot, K. Klünder, M. Gisselbrecht, J. Mauritsson, A. L'Huillier, A. Maquet, and R. Taïeb, *Chem. Phys.* **414**, 53 (2013).
- [12] I. A. Ivanov, J. M. Dahlström, E. Lindroth, and A. S. Kheifets, [arXiv:1605.04539](https://arxiv.org/abs/1605.04539).
- [13] J. Fuchs, N. Douguet, S. Donsa, F. Martin, J. Burgdörfer, L. Argenti, L. Cattaneo, and U. Keller, *Optica* **7**, 154 (2020).
- [14] M. Swoboda, J. M. Dahlström, T. Ruchon, P. Johnsson, J. Mauritsson, A. L'Huillier, and K. J. Schafer, *Laser Phys.* **19**, 1591 (2009).
- [15] P. K. Marojuet *et al.*, *Nature* **578**, 386 (2020).
- [16] A. Harth, N. Douguet, K. Bartschat, R. Moshhammer, and T. Pfeifer, *Phys. Rev. A* **99**, 023410 (2019).
- [17] J. M. Dahlström, A. L'Huillier, and A. Maquet, *J. Phys. B: At. Mol. Opt. Phys.* **45**, 183001 (2012).
- [18] F. H. M. Faisal, *Theory of Multiphoton Processes*, Physics of Atoms and Molecules (Springer-Verlag, Berlin, 1987).
- [19] P. Lambropoulos, in *Advances in Atomic and Molecular Physics*, edited by D. R. Bates and B. Bederson (Academic Press, 1976), Vol. 12, pp. 87–164.
- [20] L. A. A. Nikolopoulos, *Phys. Rev. A* **73**, 043408 (2006).
- [21] N. Douguet, A. N. Grum-Grzhimailo, E. V. Gryzlova, E. I. Staroselskaya, J. Venzke, and K. Bartschat, *Phys. Rev. A* **93**, 033402 (2016).
- [22] K. R. Hamilton, T. Pauly, K. Bartschat, N. Douguet, D. Bharti, and A. Harth, Conference: 51st Annual Meeting of the Division of Atomic, Molecular, and Optical Physics of the American Physical Society, Contribution: K01.00048, June 2020.

4.3 Publication III: Multisideband interference structures observed via high-order photon-induced continuum-continuum transitions in argon




This publication presents the outcomes of the 3-SB RABBITT measurements conducted in argon. The XUV-APT is generated using high-harmonic generation in neon gas. Six main photoelectron peaks were detected, which corresponded to the six odd harmonics of 515 nm above the ionization threshold. As a result, five sets of sidebands were observed.

We find that the RABBITT phases of the three sidebands obtained from angle-integrated measurements become increasingly similar as the photoelectron energy increases. However, some exceptions are observed in the sideband group closest to threshold and also in the highest energy group. The former are likely due to the coupling to the discrete Rydberg spectrum while the latter are caused by the presence of higher-order processes.

In argon, XUV single-photon ionization produces photo electrons in two intermediate orbital angular momentum states, $\lambda = 0, 2$, which then interact with the dressing field to create sidebands with different possible angular momenta. The distinct Wigner and continuum-continuum coupling phases associated with individual angular momentum channels result in variations in the angle-dependence of the RABBITT phases of the three sidebands. To qualitatively explain this dependence, we utilize a propensity rule to extract information about the dominant angular momenta involved in forming the sidebands.

At the end of the chapter, we provide additional data that were not included in the paper. We also showcase predictions obtained from a simulation utilizing the R-matrix (close-coupling) with time-dependence (RMT) approach, demonstrating the impact of Fano resonances on the phase of the three sidebands within a group.

Multisideband interference structures observed via high-order photon-induced continuum-continuum transitions in argon

D. Bharti ^{1,*}, H. Srinivas,¹ F. Shobeiry,¹ K. R. Hamilton ^{2,3}, R. Moshhammer,¹ T. Pfeifer,¹ K. Bartschat ², and A. Harth^{1,4,*}

¹Max-Planck-Institute for Nuclear Physics, D-69117 Heidelberg, Germany

²Department of Physics and Astronomy, Drake University, Des Moines, Iowa 50311, USA

³Department of Physics, University of Colorado Denver, Denver, Colorado 80217, USA

⁴Department of Optics and Mechatronics, Hochschule Aalen, D-73430 Aalen, Germany



(Received 18 October 2022; accepted 19 January 2023; published 6 February 2023)

We report a joint experimental and theoretical study of a three-sideband (3-SB) modification of the reconstruction of attosecond beating by interference of two-photon transitions (RABBIT) setup. The 3-SB RABBIT scheme makes it possible to investigate phases resulting from interference between transitions of different orders in the continuum. Furthermore, the strength of this method is its ability to focus on the atomic phases only, independent of a chirp in the harmonics, by comparing the RABBIT phases extracted from specific SB groups formed by two adjacent harmonics. We verify earlier predictions that the phases and the corresponding time delays in the three SBs extracted from angle-integrated measurements become similar with increasing photoelectron energy. A variation in the angle dependence of the RABBIT phases in the three SBs results from the distinct Wigner and continuum-continuum coupling phases associated with the individual angular-momentum channels. A qualitative explanation of this dependence is attempted by invoking a propensity rule. Comparison between the experimental data and predictions from an R matrix (close-coupling) with time dependence calculation shows qualitative agreement in most of the observed trends.

DOI: [10.1103/PhysRevA.107.022801](https://doi.org/10.1103/PhysRevA.107.022801)

I. INTRODUCTION

The reconstruction of attosecond beating by interference of two-photon transitions (RABBIT) is a widely employed technique to measure attosecond time delays in photoionization processes [1–3]. The extraction of time information from the RABBIT measurements usually involves retrieving atomic phases encoded in the delay-dependent modulation of the sideband (SB) yield. These SBs are traditionally formed in the photoelectron spectrum by the interaction of two photons (one pump, one probe) with the target. Spectral harmonics from an attosecond pulse train (the pump photons) form discrete photoelectron signal peaks. The presence of a time-delayed infrared field (the probe photon) then creates a signal between these main peaks that oscillates with the time delay. The so-retrieved atomic phase ($\Delta\phi^{\text{at}}$) from the RABBIT measurement can be separated into a single-photon ionization contribution ($\Delta\eta$, Wigner phase [4]) and a continuum-continuum (cc) coupling phase ($\Delta\phi^{\text{cc}}$) by applying an asymptotic approximation [5–7].

Variations of the RABBIT scheme, such as 0-SB, 1-SB, and 2-SB, have been utilized to study dipole transition phases

and attosecond pulse shaping [8–10]. As the name suggests, in a 3-SB RABBIT scheme, three SBs are formed between two consecutive main photoelectron peaks [11,12]. The delay-dependent oscillation in the photoelectron signal of these three SBs requires more than one transition in the continuum, i.e., the absorption or emission of several probe photons. For a hydrogenic system, we recently [12] extended the asymptotic approximation to a decomposition scheme, which expands the phase of the N th-order dipole matrix element $\mathcal{M}^{(N)}$, describing the absorption of an ionizing extreme ultraviolet (XUV) photon followed by $N-1$ infrared (IR) photon exchanges in the continuum, into a sum of the Wigner phase and $N-1$ cc phases.

For atomic hydrogen, where numerical calculations with high accuracy can be carried out by solving the time-dependent Schrödinger equation (TDSE) directly, we verified that the decomposition approximation explains the RABBIT phases in all three SBs qualitatively [12]. As expected, its accuracy improves with increasing energy of the emitted photoelectron. On the other hand, assuming $\Delta\phi^{\text{cc}}$ to be independent of the orbital angular momenta of the continuum states leads to deviations from the analytical prediction, particularly in the lower and the higher SB of the triplet at low kinetic energies.

Even though starting with a $3p$ electron still limits the information that can be extracted due to the combined effect of at least two Wigner and the cc phases, we decided to perform the present proof-of-principle study on argon due to its experimental advantages, including a significantly lower ionization potential than helium, which may be a viable alternative to atomic hydrogen due to its quasi-one-electron character, as

*bharti@mpi-hd.mpg.de; anne.harth@hs-aalen.de

Published by the American Physical Society under the terms of the [Creative Commons Attribution 4.0 International](https://creativecommons.org/licenses/by/4.0/) license. Further distribution of this work must maintain attribution to the author(s) and the published article's title, journal citation, and DOI. Open access publication funded by the Max Planck Society.

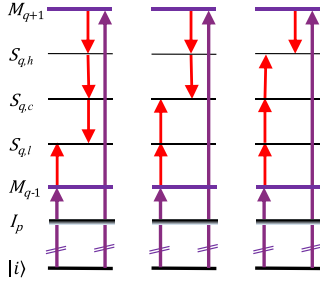


FIG. 1. 3-SB RABBIT scheme. M_{q-1} and M_{q+1} label the main photoelectron peaks created directly by the odd harmonics (H_{q-1} and H_{q+1}) of the frequency-doubled fundamental probe frequency in the XUV pulse, while $S_{q,l}$, $S_{q,c}$, and $S_{q,h}$ are the lower, central, and higher SBs, respectively. These SBs are formed by emission or absorption of probe photons by the quasi-free photoelectrons. $|i\rangle$ denotes the initial state and I_p is the ionization potential.

long as one of the electrons remains in the $1s$ orbital, i.e., away from doubly-excited resonance states. In argon, the intermediate orbital angular momentum after the XUV step is $\lambda=0$ or 2 , while $\lambda=1$ in helium. For the latter target, as for atomic hydrogen, the dependence on the Wigner phase would drop out, and the 3-SB setup would provide direct access to the phase associated with higher-order cc transitions [11,12]. Nevertheless, a significant strength of our current setup already lies in the fact that the results within each group are *independent of any chirp* in the XUV pulse, because the XUV harmonic pair is common to all three SBs.

This paper is organized as follows. We begin with a brief review of the basic idea behind the 3-SB setup in Sec. II. This is followed by a description of the experimental apparatus in Sec. III and the accompanying theoretical R matrix (close-coupling) with time dependence (RMT) approach in Sec. IV. In Sec. V, we first show angle-integrated data (Sec. V A) before focusing on the angle dependence of the RABBIT phases in the three SBs of each individual group in Sec. V B. We finish with a summary and an outlook in Sec. VI.

II. THE 3-SB SCHEME

In this section, we briefly review the 3-SB scheme introduced in Ref. [11] and the analytical treatment presented in Ref. [12] as applied to the 3-SB RABBIT experiment.

Figure 1 illustrates only the two most dominant transition paths for each SB contributing to the oscillation in their respective yields. The lowest-order transition dominates the yield, but its modulation requires interference between at least two distinct paths leading to the same energy. This involves two different XUV harmonics that are aided by absorption or emission of near-infrared (NIR) photons. For the lower (l) and higher (h) SBs, S_l and S_h , the most important interfering paths are of second (one harmonic and one NIR) and fourth (one harmonic and three NIR) order, which results in a weak modulation of the yield. The lowest-order terms contributing to the buildup of the central (c) SB, S_c , are both of third order (one harmonic and two NIR). Consequently, interference between them exhibits the delay-dependent oscillation most clearly.

Mathematically, the angle-integrated yield in the three SBs, considering only two prominent transition paths, can be written as

$$\begin{aligned} S_{q,l} &\propto \sum_{\ell,m} |(\tilde{E}_{q+1}\tilde{E}_\omega^* \mathcal{M}_{\ell,m}^{(4,e)}(k_{l,q}) + \tilde{E}_{q-1}\tilde{E}_\omega \mathcal{M}_{\ell,m}^{(2,a)}(k_{l,q}))|^2 \\ &= I_0^l + \sum_{\ell,m} I_{\ell,m}^l \cos(4\omega\tau - \Delta\phi_\Omega^q - \Delta\phi_{\ell,m}^{l,\text{at}}) \\ &= I_0^l + I_1^l \cos(4\omega\tau - \phi_R^l + \pi); \end{aligned} \quad (1a)$$

$$\begin{aligned} S_{q,c} &\propto \sum_{\ell,m} |(\tilde{E}_{q+1}\tilde{E}_\omega^* \mathcal{M}_{\ell,m}^{(3,e)}(k_{c,q}) + \tilde{E}_{q-1}\tilde{E}_\omega^2 \mathcal{M}_{\ell,m}^{(3,a)}(k_{c,q}))|^2 \\ &= I_0^c + \sum_{\ell,m} I_{\ell,m}^c \cos(4\omega\tau - \Delta\phi_\Omega^q - \Delta\phi_{\ell,m}^{c,\text{at}}) \\ &= I_0^c + I_1^c \cos(4\omega\tau - \phi_R^c); \end{aligned} \quad (1b)$$

$$\begin{aligned} S_{q,h} &\propto \sum_{\ell,m} |(\tilde{E}_{q+1}\tilde{E}_\omega^* \mathcal{M}_{\ell,m}^{(2,e)}(k_{h,q}) + \tilde{E}_{q-1}\tilde{E}_\omega^3 \mathcal{M}_{\ell,m}^{(4,a)}(k_{h,q}))|^2 \\ &= I_0^h + \sum_{\ell,m} I_{\ell,m}^h \cos(4\omega\tau - \Delta\phi_\Omega^q - \Delta\phi_{\ell,m}^{h,\text{at}}) \\ &= I_0^h + I_1^h \cos(4\omega\tau - \phi_R^h + \pi). \end{aligned} \quad (1c)$$

Here q labels the SB group, while $k_{l,q}$, $k_{c,q}$, and $k_{h,q}$ denote the final linear momenta of the ejected electron in the lower, central, and higher sidebands in each group. The subscript ℓ denotes one of generally several allowed orbital angular momenta of the ejected electron in the final state and m labels the magnetic quantum number, which can be 0 or ± 1 for the electron starting in the $3p$ subshell. Note that m is a conserved quantity for all orders n of the transition matrix element $\mathcal{M}_{\ell,m}^{(n)}$ due to our use of linearly polarized light.

Furthermore, $\tilde{E}_\Omega = E_\Omega e^{i\phi_\Omega}$ and $\tilde{E}_\omega = E_\omega e^{i\omega\tau}$ (for absorption) are the complex electric-field amplitudes of the colinearly polarized XUV-pump (Ω) and NIR-probe (ω) pulses, respectively. $\Delta\phi_{\ell,m}^{\text{at}} = \arg[\mathcal{M}_{\ell,m}^{(a)} \mathcal{M}_{\ell,m}^{*(e)}]$ is the phase difference between the two matrix elements and $a(e)$ denotes the pathway involving absorption (emission) of the probe photons. Finally, $\Delta\phi_\Omega^q$ is the spectral phase difference (XUV chirp) of two neighboring harmonics.

As seen from Eqs. (1), the yield of each SB is separated into an average part I_0 and another term I_1 that oscillates at 4ω with the delay. As discussed in Ref. [12], every dipole transition also adds a phase of $\pi/2$. Since the two dominant interfering terms in S_l and S_h are of different orders (second and fourth), this leads to an additional π phase in S_l and S_h relative to S_c , where both interfering terms are of the same (third) order.

The RABBIT phase (ϕ_R) includes the spectral phase difference of the two harmonics and the channel-resolved atomic phases weighted according to their transition amplitudes. It is a complex inverse trigonometric function involving many parameters and hence is best determined by fitting the signal to the known analytic form given above. Since the three SBs involve the same pair of harmonics, the contribution of the XUV group delay (i.e., the chirp) to the oscillation phase is the same in all three SBs. This is a key advantage of the 3-SB method, since it removes the influence of the XUV chirp

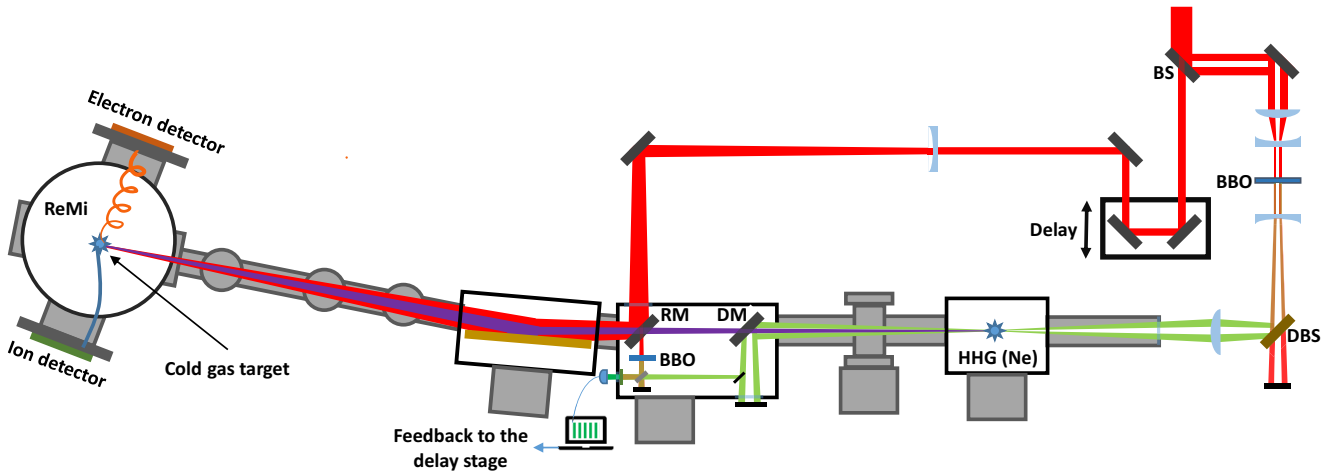


FIG. 2. Experimental setup. A holey mirror (BS) splits the linearly polarized laser beam between the two arms of the interferometer. In the pump arm, the HHG process is driven by the second harmonic of the laser beam. The generated XUV and the fundamental probe beam are recombined and focused onto a supersonic gas jet of argon. The interferometer is stabilized by tracking the movement of the fringes from the pump and the probe beams.

when we compare the phases of the three SBs only within a particular group.

III. EXPERIMENTAL SETUP

Figure 2 shows the schematic design of our 3-SB RABBIT experimental setup. A commercial fiber-based laser delivers pulses with a duration of approximately 50 fs [full width at half maximum (FWHM)] at a 49 kHz repetition rate with a pulse energy of 1.2 mJ and a center wavelength of 1030 nm. This pulse is split into two parts using a holey mirror (BS) that reflects $\sim 85\%$ of the incoming beam into the pump arm, while the rest passes through the hole into the probe arm. The beam size of the reflected donut beam in the pump arm is reduced by a pair of lenses and passed through a 0.5-mm-thick Beta Barium Borate (BBO) crystal to double its frequency.

The conversion efficiency for the second-harmonic generation (SHG) by the BBO crystal is 25%–30%. A dichroic beam-splitter (DBS) filters out the fundamental beam, and a lens with a focal length of 12 cm focuses the second harmonic beam inside a vacuum chamber to a focal spot of 30–40 μm on a jet of neon gas, which results in an XUV frequency comb through high-harmonic generation (HHG). The gas nozzle has a diameter of 100 μm and is operated at a backing pressure of 1.2 bar with a chamber pressure of 5×10^{-3} mbar. The generated XUV beam is spatially separated from the annular second harmonic with the help of an additional holey dumping mirror (DM). The residual second harmonic passed through the dumping mirror is weak and does not generate any visible sidebands. The beam in the probe arm goes through a retro-reflector mounted on a piezoelectric-translation stage that offers a step-resolution of 5 nm with closed-loop position control. Another holey mirror (RM) recombines the NIR (probe) and XUV (pump) beams, which are then focused inside a reaction microscope (ReMi) on a cold gas jet of argon. The ReMi enables coincident detection and the reconstruction of the three-dimensional momenta of the ions and electrons created during the photoionization process [13]. The interfer-

ometer was actively stabilized [14] to achieve a stability of ~ 40 as over a data acquisition time of 7 h. The stability of the interferometer was critical for the successful realization of the 3-SB scheme since the oscillation period was just 850 as.

IV. THEORETICAL APPROACH

In the theoretical part of this study, we employ the general R matrix with time dependence (RMT) method [15] to generate theoretical predictions for comparison with our experimental data. In order to calculate the necessary time-independent basis functions and dipole matrix elements, we set up the two-state nonrelativistic model introduced by Burke and Taylor [16] to treat the steady-state standard photoionization process. In this model, multiconfiguration expansions for the initial $(3s^23p^6)^1S$ bound state and the two coupled final ionic states $(3s^23p^5)^2P$ and $(3s3p^6)^2S$ were employed. We checked that the photoionization cross sections at the photon energies corresponding to the various HHG lines was reproduced properly (in agreement with Burke and Taylor [16] as well as experiments [17,18]) by our RMT model.

The probe-pulse duration was chosen as about twice the length of the XUV pulse. We emphasize that the present calculation was meant as a supplement to the current experiment, with the hope of providing additional qualitative insights rather than quantitative agreement, which would require much more detailed information about the actual pulses than what was available. We purposely employed significantly lower NIR peak intensities (10^{11} W/cm 2) than in the experiment ($\sim 6 \times 10^{11}$ W/cm 2). This reduced the number of partial waves needed to obtain converged results, diminished potential distortions, and thus made it easier to interpret the spectra.

Specifically, we performed calculations for 11 delays in multiples of 0.05 NIR periods. For each delay, we needed about 5 h on 23 nodes using all 56 available cores per node on the Frontera supercomputer hosted at the Texas Advanced Computing Center (TACC) [19].

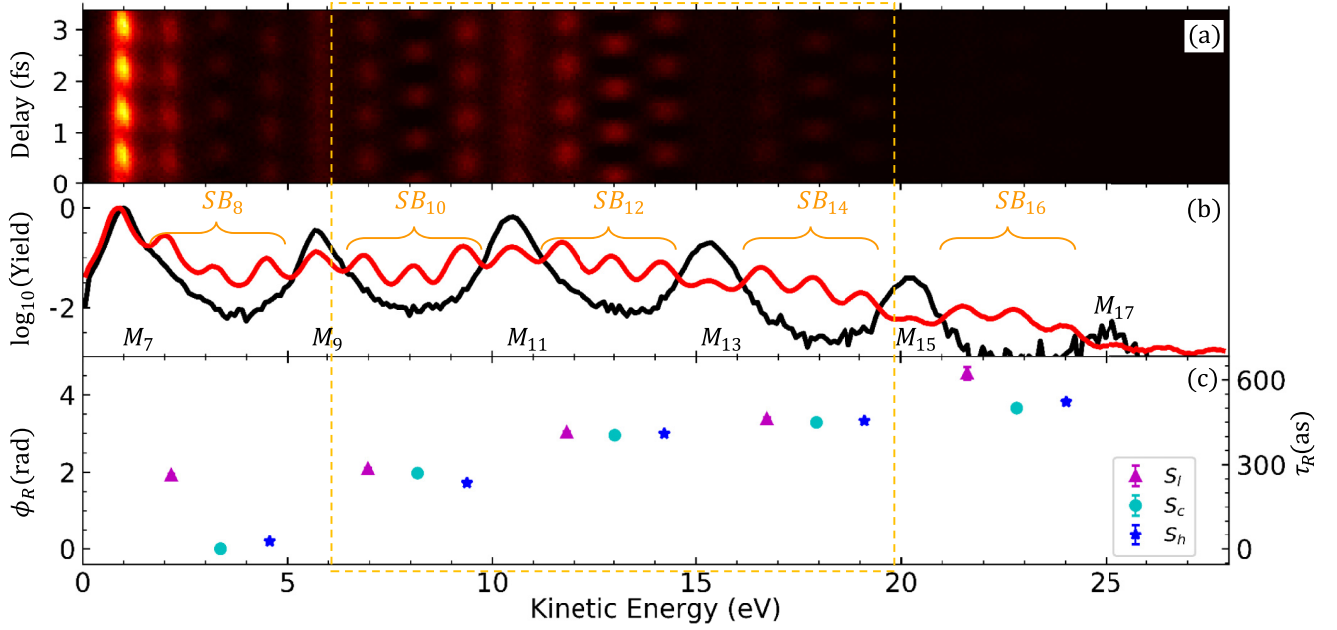


FIG. 3. (a) 3-SB RABBIT trace, (b) normalized photoelectron spectra generated with the XUV pulse only (dark) and during the RABBIT measurement integrated over the delays (lighter), and (c) RABBIT phases extracted from all three sidebands. Note that the π phase difference between S_c and (S_i, S_h), which is clearly seen in the position of the maxima in (a), has been removed for better visibility in (c). The error bars from the fitting procedure are generally smaller than the symbol size and hence hardly visible. The dashed box from about 6 eV to 21 eV indicates the sideband groups that we concentrate on for the angle-differential cases.

V. RESULTS AND DISCUSSION

Below we present our results. We start with the angle-integrated setup in Sec. VA before going into further detail with angle-resolved measurements and calculations in Sec. VB.

A. Angle-integrated RABBIT phases

Figure 3 exhibits the results of our 3-SB RABBIT experiment after integrating the signal over all photoelectron emission angles. To highlight the oscillations, the RABBIT trace in Fig. 3(a) is plotted after subtracting the average delay-integrated signal. The delay-integrated photoelectron spectra (normalized to 1 at the highest peak) are plotted in Fig. 3(b). Due to the high NIR intensity, some of the main bands are depleted substantially and appear weaker than the SBs in their vicinity. The angle-integrated photoelectron spectrum is integrated over a spectral window of 0.7 eV around the peak of the SBs.

The RABBIT phase (ϕ_R) is extracted by fitting a cosine function [cf. Eqs. (1)] to these delay-dependent oscillating signals of the sidebands, as seen in Fig. 4. Due to the large data set available and the excellent stability of the interferometer, the phase retrieval generally resulted in error bars smaller than the symbol size in Fig. 3(c). This gives us confidence in the results obtained from our extraction procedure. The numerical values obtained for the various SB groups, as well as the contrast ratio

$$\gamma \equiv \frac{\max[\text{SB}(\tau)] - \min[\text{SB}(\tau)]}{\max[\text{SB}(\tau)] + \min[\text{SB}(\tau)]} \quad (2)$$

are listed in Table I. As expected, the highest contrast is found for the center sideband, due to the same (third) order of transitions involved.

We note that there are several autoionizing resonances with principal configuration $3s3p^6nl$ in the SB_{12} range of photoelectron kinetic energies, which converge towards the $(3s3p^6)^2S$ threshold of the first excited state of Ar^+ around 13.5 eV [20]. Early measurements of the $(3s3p^6np)^1P^o$ resonances were reported by Madden *et al.* [21]. They were also seen by Burke and Taylor [16] in their photoionization work, and further resonances with other configurations, which can be reached by charged-particle or multiphoton impact, were discussed by Bartschat and Burke [22]. More recently, the

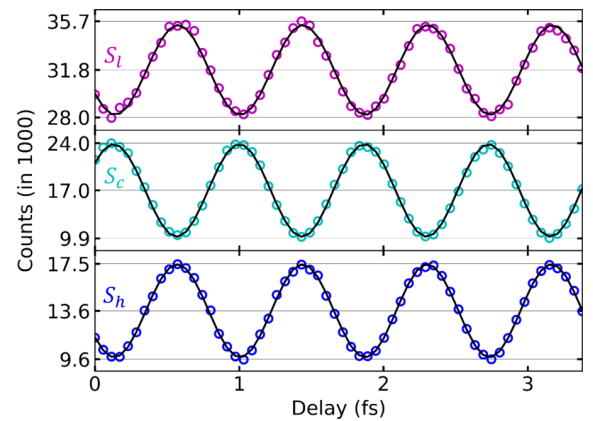


FIG. 4. The delay-dependent photoelectron signal (dots) of the three sidebands in the SB_{12} group and fits to a cosine function (lines).

TABLE I. RABBIT phase extracted from the fitting procedure and the contrast γ of the oscillation.

	SB_8		SB_{10}		SB_{12}		SB_{14}		SB_{16}	
	ϕ_R	γ	ϕ_R	γ	ϕ_R	γ	ϕ_R	γ	ϕ_R	γ
S_l :	1.93 ± 0.03	0.07	2.09 ± 0.02	0.11	3.03 ± 0.02	0.11	3.38 ± 0.03	0.09	4.56 ± 0.10	0.04
S_c :	0.00 ± 0.02	0.15	1.98 ± 0.01	0.36	2.96 ± 0.01	0.41	3.29 ± 0.01	0.38	3.66 ± 0.02	0.24
S_h :	0.19 ± 0.02	0.09	1.73 ± 0.02	0.10	3.00 ± 0.01	0.28	3.33 ± 0.01	0.32	3.82 ± 0.05	0.15

effect of these resonances on the RABBIT phase in 1-SB setups was reported by Kotur *et al.* [23] and Cirelli *et al.* [24].

Since we used the coupled-state description of Burke and Taylor [16], we saw resonance effects in test calculations, but only with appropriate frequencies and sufficiently long pulses, for which the resonance widths could be well resolved. Note that these features are very sensitive to small fluctuations in the frequency and bandwidth of the APT during the XUV generation process. Therefore, these structures were not seen in the three experimental data points presented in the SB_{12} region. We hope to generate additional data with tunable high-order harmonic frequencies in the future. This will make it possible to investigate the resonance phenomena in more detail.

As predicted by our generalized decomposition approximation [cf. Eqs. (1)], the lower and the higher SBs oscillate by π out of phase with the central SB. The retrieved RABBIT phases ϕ_R are plotted in Fig. 3(c) after removing the extra π from S_l and S_h to simplify the comparison. The time-delay axis on the right side of this panel was created via the conversion $\tau_R = \phi_R/(4\omega)$.

Five SB groups are clearly identifiable in Fig. 3(c). While there are some irregularities in SB_8 and SB_{16} , especially with the phase extracted from S_l , groups SB_{10} , SB_{12} , and SB_{14} show the expected trend: The RABBIT phases of the three SBs in each group are similar, although a small difference remains visible in SB_{10} . That difference, however, essentially vanishes in SB_{12} and SB_{14} .

The irregularity seen in the SB_8 group is due to a significant contribution of another fourth-order transition in the absorption path of the lowest SB S_l , which involves a transition from M_7 down to the Rydberg states and back up to S_l . The Rydberg states enhance the strength of this transition and add a resonance phase that leads to a significant deviation in the RABBIT phase of S_l compared to the other members of the SB_8 group. Furthermore, due to the low cutoff of the XUV spectrum based on HHG and the decreasing photoionization cross section of argon with increasing photon energy, the strength of the M_{17} peak is very weak compared to the rest of the lower main peaks. As a result, higher-order transitions involving lower main bands also play a significant role in the oscillation of S_l in the SB_{16} group, which again affects the extracted phase.

B. Angle-differential RABBIT phases

We now further increase the level of detail by investigating angle-dependent RABBIT phases, which is possible due to the angle-resolving capability of the reaction microscope. For the reasons given above regarding the additional complexities

associated with the SB_8 and SB_{16} groups, we concentrate the remaining discussion on SB_{10} , SB_{12} , and SB_{14} .

Figures 5(a)–5(c) show the RABBIT phases extracted within these groups as a function of the photoelectron emission angle, which is defined relative to the (linear) laser polarization vector. The photoelectron signal is integrated over an angular window of 10° for each data point. The angle-resolved RABBIT phases are shifted to fix the starting phase of the central sideband in each group to zero. According to both our experiment and the calculation [Figs. 5(d)–5(f)], the phase of S_h exhibits a stronger angular dependence compared to that of S_c and S_l . With increasing photoelectron energy, the differences diminish in both experiment and theory, with theory predicting almost no angle dependence in the range of SB_{14} plotted.

To explain the angle dependence in the RABBIT phase, we need to consider the interference among all the angular-momentum channels of the sidebands accessed through the absorption and emission paths. We write the signal in compressed form as

$$\begin{aligned}
 S_q(\tau, \theta) &\propto \sum_{\ell, \ell', m} \alpha_{\ell, m}^a \alpha_{\ell', m}^e Y_{\ell, m}(\theta) Y_{\ell', m}^*(\theta) \\
 &\quad \times \cos(4\omega\tau - \Delta\phi_{\Omega}^q - \Delta\phi_{\ell\ell', m}^{\text{at}}) \\
 &\propto I_1(\theta) \cos[4\omega\tau - \phi_R(\theta)]. \quad (3)
 \end{aligned}$$

Here α^a and α^e are the transition amplitudes involving the various fields and matrix elements, while $\ell(\ell')$ denotes the angular-momentum channels accessed through the absorption (emission) paths.

The dissimilarity in the RABBIT phases $[\phi_R(\theta)]$ of the three SBs can be explained by considering a propensity rule for the transition amplitudes and the dependence of both the Wigner and ϕ^{cc} phases on the orbital angular momenta. It is well known that the Wigner phase depends on the angular momentum channel. The cc phase has also been shown to depend slightly on whether there is an increase or decrease in the angular momentum, while it appears to remain independent of the target species [25,26]. Therefore, the atomic phases ($\Delta\phi_{\ell\ell', m}^{\text{at}}$) arising from the interference between various ℓ channels in the emission and absorption paths are also expected to differ. Similar to bound-continuum transitions [27], absorption (emission) within the continuum favors an increase (decrease) in the angular momentum of the outgoing photoelectron, especially for low kinetic energies [26,28–31]. The higher SB (S_h) of the group involves the absorption of three probe photons ($H_{q-1} + 3\omega$) that, according to the propensity rule, predominantly populate higher angular-momentum states. Along the other path ($H_{q+1} - 1\omega$) leading

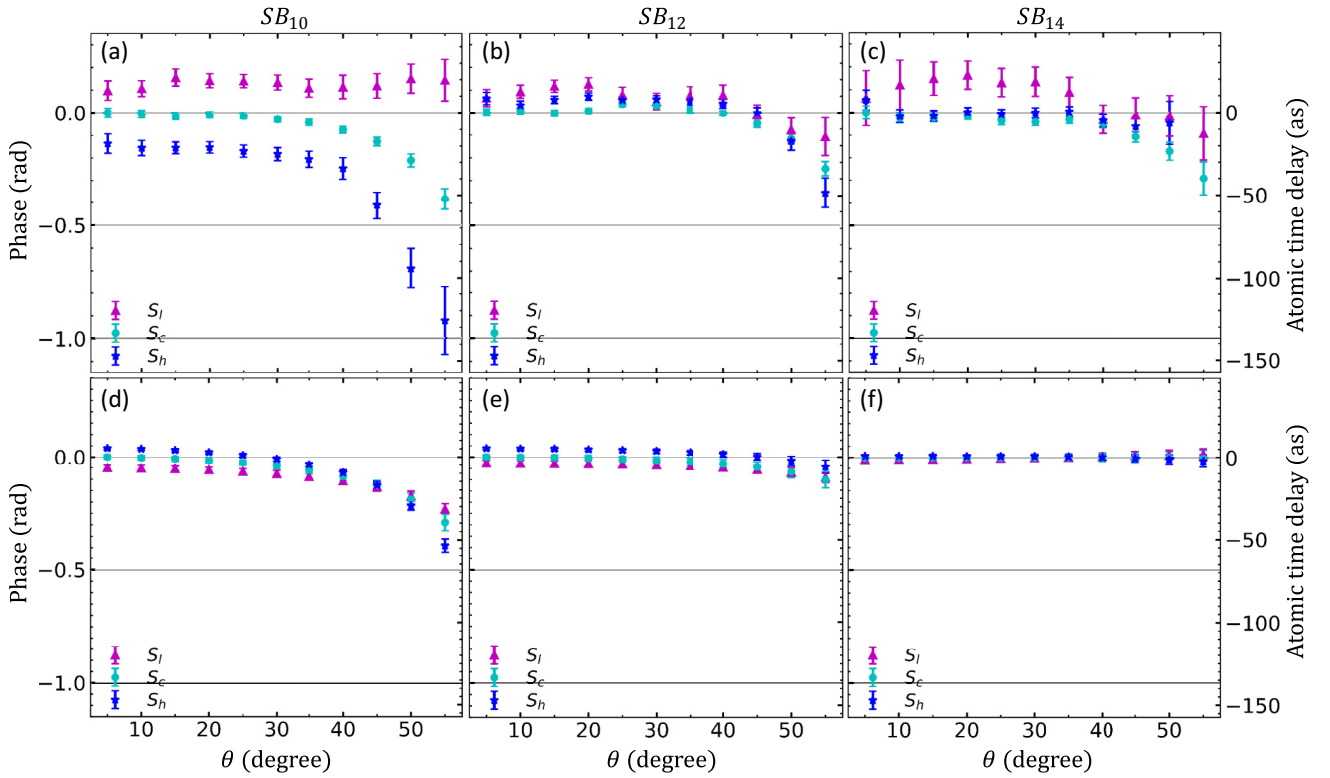


FIG. 5. Top row: Angle-dependent RABBIT phases extracted from the measurements in group (a) SB_{10} , (b) SB_{12} , and (c) SB_{14} . Bottom row: Corresponding RMT predictions.

to S_h , the emission of one probe photon mainly creates lower angular-momentum states. For S_l , emission of three probe photons ($H_{q+1} - 3\omega$) primarily leads to the population of lower angular-momentum states. Even though the absorption path ($H_{q-1} + 1\omega$) to S_l also favors an increase in the photoelectron's angular momentum, the possible values reached by the absorption of a single probe photon remain relatively small.

The interplay of the propensity rule for transition amplitudes to each ℓ channel and the angle-dependent amplitudes of the coupled spherical harmonics determine the angular variation of ϕ_R in the three SBs. In cross-channel interference, $\ell \neq \ell'$, the angle-dependent spherical harmonics undergo a sign change across their angular nodes, thus resulting in a phase jump by π . If the relative magnitude of these cross-channel interferences is significant compared to that of the same-channel interference terms, $\ell = \ell'$, this can lead to a rapid variation in the angle dependence of ϕ_R in the vicinity of the nodes [29]. Depending on the value of $\Delta\phi_{\ell\ell',m}^{\text{at}}$ relative to the average $\Delta\phi^{\text{at}}$ of the interference terms, the additional π jump at the nodes in $Y_{\ell,m}$ and/or $Y_{\ell',m}$ can drive the angle-dependent curve downward or upward.

With increasing ℓ value, the position of the first node in the associated Legendre polynomial of the spherical harmonic moves to smaller angles. Due to the propensity rule, the weight of the cross-channel interference term containing large ℓ values is most significant in the higher sideband. This results in a relatively early onset of the descent in the angle-dependent RABBIT phase in the higher sideband. In the lower

sideband, the amplitude of the cross-channel interference term containing large ℓ values is not very strong; hence, the π jump across the node does not produce a substantial change in the overall retrieved phase. With increasing kinetic energy, for both the absorption or emission of the probe photons, the transition amplitudes for increasing and decreasing angular momentum tend to become similar [29]. Hence, the contribution of cross-channel interference containing large ℓ values decreases with increasing kinetic energy. Thus the π jumps at the nodes of the corresponding spherical harmonics do not change the retrieved phase significantly.

Since the retrieved angle-integrated RABBIT phase is the weighted average of all the channel-resolved RABBIT phases and the weights of these channels in the S_l , S_c , and S_h SBs are different, the angle-integrated RABBIT phase in the three SBs also turns out different. Also, owing to the propensity rule, the unequal transition probabilities of reaching the various angular-momentum states of the SBs in absorption and emission of the probe photons may cause incomplete interference in the individual ℓ channels, thereby reducing the overall oscillation contrast in the angle-integrated photoelectron signal.

Finally, we notice that the scale of the variations in the angle-dependence of the RABBIT phase depicted in Fig. 5 is smaller in the calculation than in our experiment. Also, the positions of S_l and S_h relative to S_c appear to be switched. In addition to always possible shortcomings in the theoretical model (as sophisticated as it might be) and unknown potential systematic errors in the experiment, the differences in the probe intensities and the pulse details, in general, are likely

responsible for at least some of the discrepancies seen here. We hope to be able to investigate this in more detail in the future by performing additional calculations with different intensities and more time delays.

VI. SUMMARY AND OUTLOOK

In summary, we carried out a proof-of-principle 3-SB RABBIT experiment in argon. In contrast to more popular single-SB studies, our technique enables us to focus on the photon-induced transition phases without distortion from a possibly unknown or experimentally drifting XUV chirp. While we confirmed earlier predictions that the angle-integrated RABBIT phases extracted within a SB group become increasingly similar, we enhanced the analyzing power of the setup significantly by resolving the emission angle with a reaction microscope. By doing so, we could identify which of the three sideband phases within a group is most sensitive to a change in the detection angle.

Our experimental efforts were accompanied by numerical calculations performed with the nonperturbative all-electron R matrix with time dependence method. There is some qualitative agreement between experiment and theory regarding the general trends observed, but significant differences remain in the details. Given the remaining limitations and challenges faced in the present study, especially concerning the details of the pulse and the argon target, the remaining deviations between experiment and theory in the quantitative values of the phases are not too surprising. We hope to address these issues in future improvements of the setup.

As the next step, we plan to repeat this experiment with helium, where the contribution of the Wigner phase for an $s \rightarrow p$ transition remains the same in all three sidebands.

Any differences in the phases within the group then clearly indicate the influence of ϕ^{cc} . This switch of targets will require extending the harmonic cutoff, which is by no means trivial in our scheme, as the cutoff in the HHG process decreases with the driving frequency. Using helium instead of argon also has the advantage of theory likely being more reliable due to the simplicity of the target. On the other hand, heavier quasi-two-electron targets with an $(ns^2)^1S$ outer-shell configuration (unfortunately, these are metals that would need to be vaporized rather than inert gases) would provide a larger short-range modification of the relevant interaction potential and therefore may be more suitable to investigate whether ϕ^{cc} is indeed nearly universal.

Undoubtedly, many open questions will need to be answered before the effects of the additional continuum-continuum transitions in single- and multi-SB RABBIT setups are fully understood. It would be interesting to analyze whether the SB phases always converge to each other with increasing energy, whether or not they cross in a predictable way with increasing emission angle, and how the behavior depends on the target investigated. While we cannot answer these questions at the present time, we hope that other groups will see the work reported in this paper as a worthwhile inspiration to carry out further studies in this field.

ACKNOWLEDGMENTS

The experimental part of this work was supported by the DFG-QUTIF program under Project No. HA 8399/2-1 and IMPRS-QD. K.R.H. and K.B. acknowledge funding from the NSF through Grants No. PHY-1803844 and No. PHY-2110023, respectively, as well as the Frontera Pathways allocation PHY-20028.

-
- [1] P. M. Paul, E. S. Toma, P. Breger, G. Mullot, F. Augé, P. Balcou, H. G. Muller, and P. Agostini, *Science* **292**, 1689 (2001).
 - [2] H. G. Muller, *Appl. Phys. B* **74**, s17 (2002).
 - [3] K. Klünder, J. M. Dahlström, M. Gisselbrecht, T. Fordell, M. Swoboda, D. Guénot, P. Johnsson, J. Caillat, J. Mauritsson, A. Maquet, R. Taieb, and A. L'Huillier, *Phys. Rev. Lett.* **106**, 143002 (2011).
 - [4] E. P. Wigner, *Phys. Rev.* **98**, 145 (1955).
 - [5] J. M. Dahlström, A. L'Huillier, and A. Maquet, *J. Phys. B: At. Mol. Opt. Phys.* **45**, 183001 (2012).
 - [6] J. M. Dahlström and E. Lindroth, *J. Phys. B: At. Mol. Opt. Phys.* **47**, 124012 (2014).
 - [7] R. Pazourek, S. Nagele, and J. Burgdörfer, *Rev. Mod. Phys.* **87**, 765 (2015).
 - [8] V. Loriot, A. Marciniak, G. Karras, B. Schindler, G. Renois-Predelus, I. Compagnon, B. Concina, R. Brédy, G. Celep, C. Bordas, E. Constant, and F. Lépine, *J. Opt.* **19**, 114003 (2017).
 - [9] S. D. López, S. Donsa, S. Nagele, D. G. Arbó, and J. Burgdörfer, *Phys. Rev. A* **104**, 043113 (2021).
 - [10] P. K. Maroju, C. Grazioli, M. Di Fraia, M. Moioli, D. Ertel, H. Ahmadi, O. Plekan, P. Finetti, E. Allaria, L. Giannessi *et al.*, *Nature (London)* **578**, 386 (2020).
 - [11] A. Harth, N. Douguet, K. Bartschat, R. Moshhammer, and T. Pfeifer, *Phys. Rev. A* **99**, 023410 (2019).
 - [12] D. Bharti, D. Atri-Schuller, G. Menning, K. R. Hamilton, R. Moshhammer, T. Pfeifer, N. Douguet, K. Bartschat, and A. Harth, *Phys. Rev. A* **103**, 022834 (2021).
 - [13] J. Ullrich, R. Moshhammer, A. Dorn, R. Dörner, L. P. H. Schmidt, and H. Schmidt-Böcking, *Rep. Prog. Phys.* **66**, 1463 (2003).
 - [14] H. Srinivas, F. Shobeiry, D. Bharti, T. Pfeifer, R. Moshhammer, and A. Harth, *Opt. Express* **30**, 13630 (2022).
 - [15] A. C. Brown, G. S. Armstrong, J. Benda, D. D. Clarke, J. Wragg, K. R. Hamilton, Z. Mašín, J. D. Gorfinkiel, and H. W. van der Hart, *Comput. Phys. Commun.* **250**, 107062 (2020).
 - [16] P. G. Burke and K. T. Taylor, *J. Phys. B: At. Mol. Phys.* **8**, 2620 (1975).
 - [17] G. Marr and J. West, *At. Data Nucl. Data Tables* **18**, 497 (1976).
 - [18] J. Samson and W. Stolte, *J. Electron Spectrosc. Relat. Phenom.* **123**, 265 (2002).
 - [19] <https://www.tacc.utexas.edu/systems/frontera>
 - [20] A. Kramida, Yu. Ralchenko, J. Reader, and NIST ASD Team, NIST Atomic Spectra Database (ver. 5.10) [Online]. Available: <http://physics.nist.gov/asd> National Institute of Standards and Technology, Gaithersburg, MD (2022).
 - [21] R. P. Madden, D. L. Ederer, and K. Codling, *Phys. Rev.* **177**, 136 (1969).

- [22] K. Bartschat and P. G. Burke, *J. Phys. B: At. Mol. Opt. Phys.* **21**, 2969 (1988).
- [23] M. Kotur, D. Guénot, Á. Jiménez-Galán, D. Kroon, E. W. Larsen, M. Louisy, S. Bengtsson, M. Miranda, J. Mauritsson, C. L. Arnold, S. E. Canton, M. Gisselbrecht, T. Carette, J. M. Dahlström, E. Lindroth, A. Maquet, L. Argenti, F. Martín, and A. L'Huillier, *Nat. Commun.* **7**, 10566 (2016).
- [24] C. Cirelli, C. Marante, S. Heuser, C. L. M. Petersson, Á. J. Galán, L. Argenti, S. Zhong, D. Busto, M. Isinger, S. Nandi, S. Maclot, L. Rading, P. Johnsson, M. Gisselbrecht, M. Lucchini, L. Gallmann, J. M. Dahlström, E. Lindroth, A. L'Huillier, F. Martín *et al.*, *Nat. Commun.* **9**, 955 (2018).
- [25] J. Fuchs, N. Douguet, S. Donsa, F. Martin, J. Burgdörfer, L. Argenti, L. Cattaneo, and U. Keller, *Optica* **7**, 154 (2020).
- [26] J. Peschel, D. Busto, M. Plach, M. Bertolino, M. Hoflund, S. Maclot, J. Vinbladh, H. Wikmark, F. Zapata, E. Lindroth, M. Gisselbrecht, J. M. Dahlström, A. L'Huillier, and P. Eng-Johnsson, *Nat. Commun.* **13**, 5205 (2022).
- [27] U. Fano, *Phys. Rev. A* **32**, 617 (1985).
- [28] M. Bertolino, D. Busto, F. Zapata, and J. M. Dahlström, *J. Phys. B: At. Mol. Opt. Phys.* **53**, 144002 (2020).
- [29] D. Busto, J. Vinbladh, S. Zhong, M. Isinger, S. Nandi, S. Maclot, P. Johnsson, M. Gisselbrecht, A. L'Huillier, E. Lindroth, and J. M. Dahlström, *Phys. Rev. Lett.* **123**, 133201 (2019).
- [30] A. S. Kheifets, *Phys. Rev. A* **105**, 013114 (2022).
- [31] D. I. R. Boll, L. Martini, and O. A. Fojón, *Phys. Rev. A* **106**, 023116 (2022).

4.3.1 Additional Data on Paper III

Sideband group 8

In the paper, it is mentioned that the significant disparity in the RABBITT phase observed in the lower sideband of group 8 is attributed to the enhanced contribution of a four-photon path, represented as P_C in figure 4.1. To further support this interpretation, additional experimental data is presented in this section.

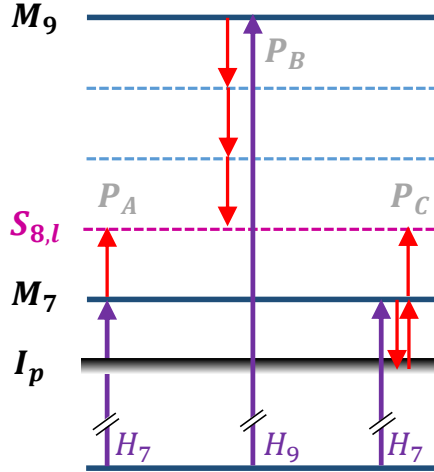


Figure 4.1. Energy-level diagram depicting the three main pathways, P_A , P_B , and P_C , which contribute to the generation of the lower sideband in group 8.

This path (P_C) involves the emission and absorption of IR photons that connect the lower sidebands with Rydberg states near the ionization threshold. The interference between P_B and P_C leads to yield oscillations at the same frequency 4ω as the interference between P_A and P_B , but with an extra π -phase due to the different number of photons involved. Moreover, the oscillation phase arising from the interference between P_B and P_C also includes a resonance phase that varies rapidly with the photoelectron energy. The overall RABBITT phase is a weighted average of the two interference terms. The amplitude of P_C is significantly enhanced due to resonances with Rydberg states, making it comparable to the two-photon path P_A . This leads to a significant deviation in the angle-integrated RABBITT phase of the lower sideband compared to that of the other sidebands in the group.

Obtained through the analysis of experimental data, Figure 4.2 presents the phase variation across the peak of the main band (M_7) and the three sidebands of group 8. Each subplot depicts the normalized yield, represented by a black solid line, and the retrieved phases, indicated by dots. The normalization is performed relative to the highest value observed in the full photoelectron spectrum (PES).

To obtain the phase variation as a function of energy, the angle-integrated photoelectron yields were binned into an energy window of 0.28 eV with an interval of 0.07 eV across

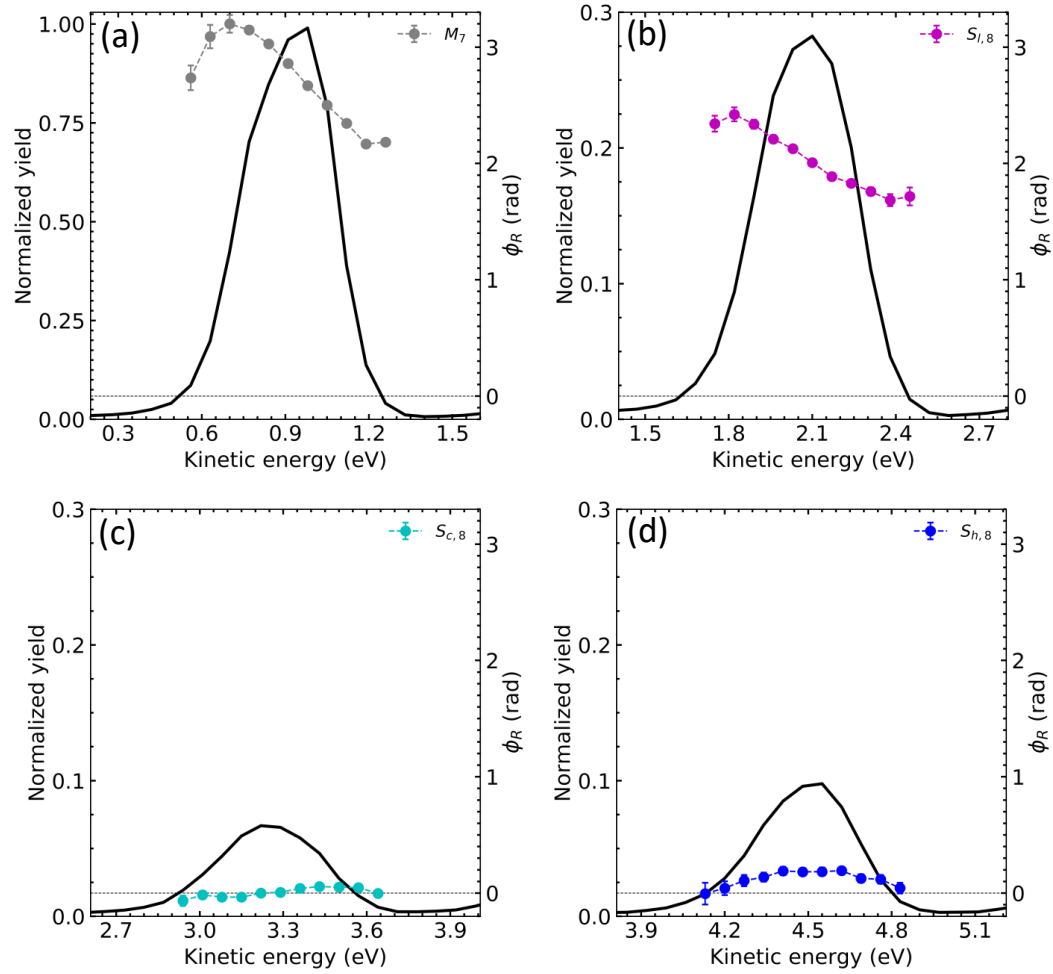


Figure 4.2. The energy-dependent RABBITT phase is shown in (a) for the main band M_7 , (b) for the lower sideband $S_{l,8}$, (c) for the central sideband $S_{c,8}$, and (d) for the higher sideband $S_{h,8}$. The black line represents the yield, and the dots represent the phase.

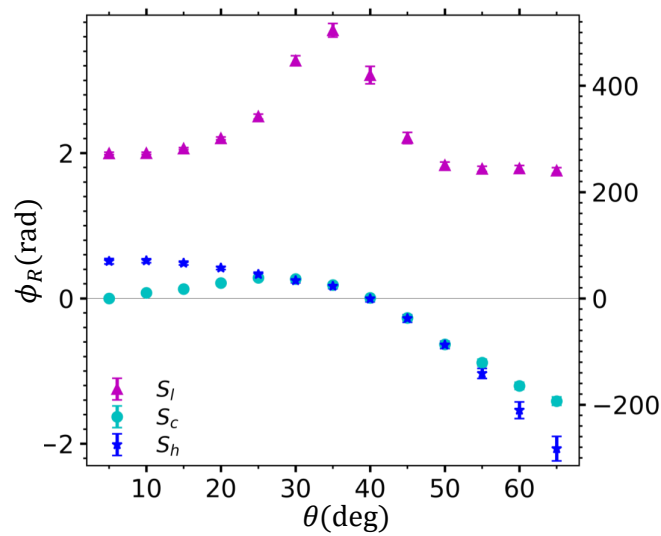


Figure 4.3. Angle-dependence of the RABBITT phase in group 8.

the photoelectron peak. Subsequently, the delay-dependent photoelectron counts in each energy bin were fitted to a cosine function to retrieve the oscillation phase.

To generate the angle-dependence plot of the RABBITT phase for the three sidebands shown in Figure 4.3, the electron yield was divided into angle-differential datasets. This division involved integrating the photoelectron yield over 10-degree angular windows at 5-degree intervals, where the emission angle was measured relative to the polarization plane of the laser field. Next, the photoelectron spectra from each angle-differential dataset were integrated over a 0.7 eV energy window centered around the peak of each sideband. The resulting angle-differential delay-dependent signals from each sideband were then fitted to a cosine function, enabling the extraction of the corresponding phase values.

As can be observed from Figure 4.2, the slope of the phase variation with energy is the largest in the M_7 main band, followed by the $S_{i,8}$ sideband. On the other hand, the phase variation with energy in the central and higher sidebands is negligible. As mentioned earlier in this section, the energy dependence of the RABBITT phase arises from the involvement of transition pathways that include Rydberg states. In the case of the main band (M_7), this type of transition can be attributed to a minimum third-order process. Consequently, it has a significant influence on the phase variation with energy. In the case of the lower sideband, the corresponding transition is of fourth order, resulting in a detectable yet weaker influence on the phase variation. The central sideband, involving a transition path with Rydberg states, is at least fifth-order, leading to a negligible impact on the phase. Similarly, in the higher sideband, this type of transition plays no significant role in determining the phase. This also provides an explanation for the distinct behavior of the angle-dependent phase observed in the lower sideband when compared to the phase dependence of the other two sidebands within group 8, as depicted in Figure 4.3.

Impact of Autoionizing Resonances

An autoionizing state is an excited state of an atom or molecule where an inner shell electron is promoted to an energy level located above the ionization threshold. These states are unstable and rapidly decay through the interaction between the bound-excited and continuum electron states in the system, known as configuration interaction. This results in the release of the excess energy as a free electron. This interference between the ionization amplitudes of the direct and autoionization processes leads to an asymmetric line shape in the photoionization cross section, known as the Fano profile, which depends on the energy and width of the autoionizing state and the strength of the coupling between the autoionizing and direct ionization channels [46].

Autoionizing states have been studied via different techniques, including ion mass spectroscopy, transient spectroscopy, and photoelectron interferometry [48–51]. The spectral

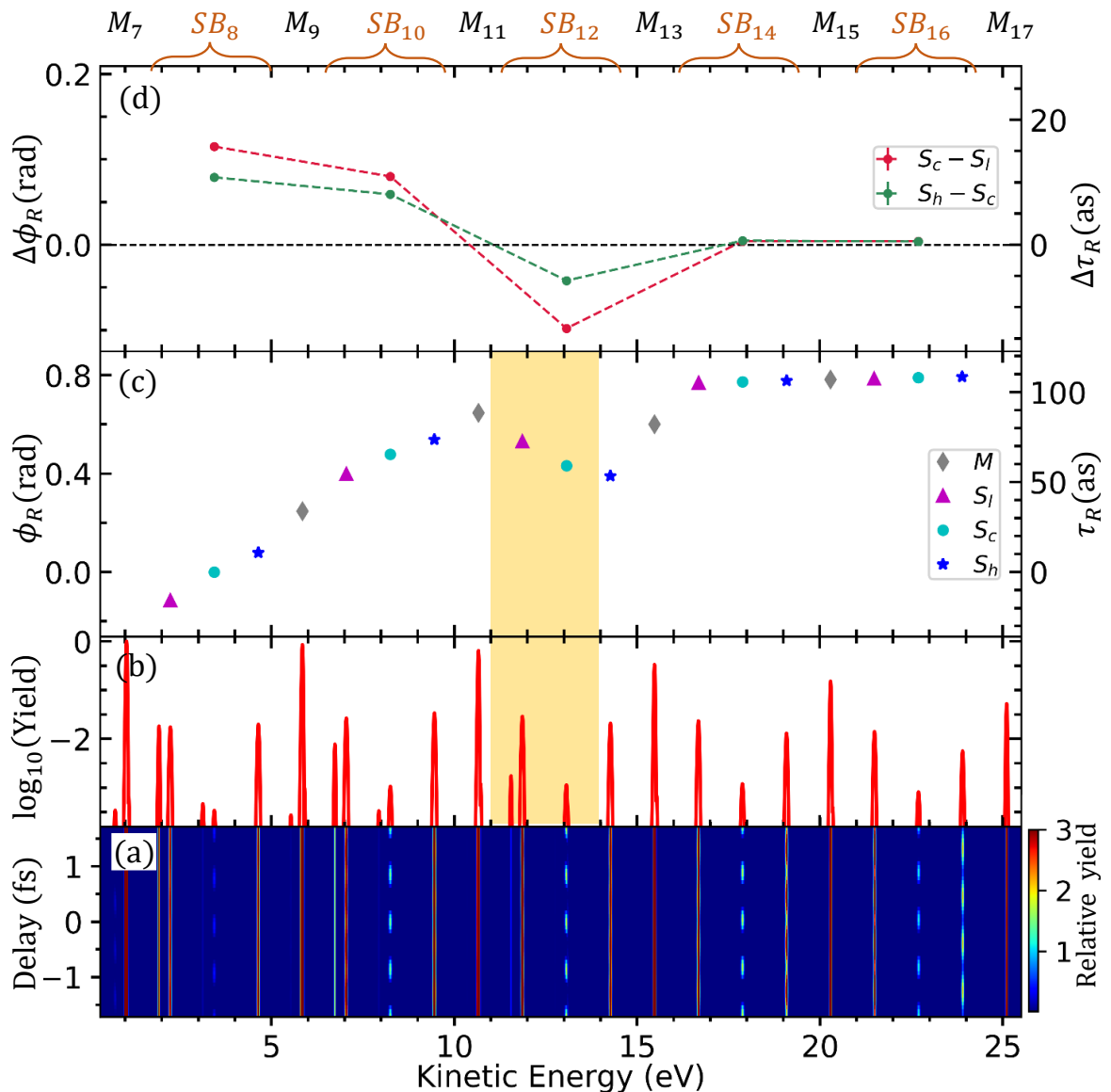


Figure 4.4. (a) Logarithmic colormap of the angle-integrated RABBITT trace, (b) Delay-integrated photoelectron spectrum normalized to its peak value, (c) Retrieved RABBITT phase of the sidebands obtained through fitting, and (d) Relative RABBITT phase of the lower and higher sidebands with respect to the RABBITT phase of the central sideband.

amplitude and phase of autoionized wave packets have also been measured using the Rainbow-RABBITT approach, in which the frequency of the harmonics is tuned across the autoionizing resonance [47, 52–54]. When the XUV photon energy is scanned across the resonance, the direct and autoionization paths compete, leading to rapid changes in both the photoelectron angular distribution and the yield oscillation phase in the resonant (or near-resonant) main band and the nearest sideband. In the 3-SB scheme, the phase in all three sidebands is linked. Therefore, even if the energy of only one main or sideband matches the energy of an autoionizing state, the impact on the phase is propagated to all three side-

bands. It is worth noting that the asymptotic approximation cannot be used in the case of autoionization.

Figure 4.4 displays the results obtained from an RMT simulation of 3-SB RABBITT in argon, using angle-integrated yields. It is important to note that the RMT calculation shown in this section is different from the one used in the paper. Specifically, the paper utilized a 10 fs XUV pulse containing six odd harmonics of 515 nm (i.e., H_7, H_9, \dots, H_{17}) with decreasing strength. On the other hand, the RMT calculation presented here utilized a Fourier-limited XUV pulse of 45-fs duration, comprising six odd harmonics of 515 nm, labeled as H_7, H_9, \dots, H_{17} , with equal strength. An XUV pulse intensity of 1×10^9 W/cm² and an IR pulse intensity of 3×10^{11} W/cm² were used, along with an IR pulse with a central wavelength of 1030 nm and a duration of 45 fs.

The delay between the two pulses was scanned over a range of one IR cycle in 50 steps. As the harmonic peaks are very narrow, the photoelectron peaks corresponding to $3s$ and $3p$ ionization are well resolved as they are separated by 0.3 eV from each other.

Figure 4.4(a) displays the angle-integrated RABBITT spectrum using a logarithmic colormap chosen to highlight the oscillations, (b) presents the delay-integrated photoelectron spectrum, normalized to its peak value, and (c) shows the RABBITT phase in the main band and sidebands obtained from the fitting process, with the trivial π phase removed from the lower and higher sidebands for better comparison. Finally, panel (d) illustrates the relative phase of the lower and higher sidebands with respect to the central sideband phase.

Except for group 12, where the autoionizing states lie (marked by the yellow shaded region), the phase difference decreases monotonically as the kinetic energy increases, as expected from the decomposition approximation. Since the exact position of the autoionizing states in the RMT-calculation has not been estimated, we do not know exactly which of the sidebands lies near these states.

The broad bandwidth of our harmonics spectrum and the limited resolution of the electron spectrometer make it difficult to observe the presence of autoionizing states in the experimental data. Nevertheless, by improving the spectrometer resolution and using narrow bandwidth XUV harmonics, one can study the effect of autoionizing resonances on the phase of the three sidebands. It is critical to ensure that the laser parameters remain stable during the measurement.

Chapter 5

Unpublished Results on Helium

In this chapter, we report the outcomes of 3-SB RABBITT experiments performed on helium, one of the simplest atoms after hydrogen. The ground state of helium has zero orbital and spin angular momentum, and the single-photon ionization induced by an XUV pulse results in the creation of a photoelectron in a well-defined p -state. The excitation of just a single orbital-angular-momentum channel during the ionization process simplifies the interpretation of the photoelectron interference patterns resulting from the interaction of the photoelectron with the IR photons. We begin by presenting the angle-integrated RABBITT results, followed by a discussion of angle-differential measurements at three different IR intensities. A key feature of this chapter is the investigation of the threshold sideband, which arises from a four-photon ionization process. We discuss the information that can be obtained from the RABBITT phases of this sideband, as well as the potential role of resonances in its formation.

5.1 Method

The experimental methodology is outlined in Publications I and III, and their associated appendices. In brief, the laser used in the experiment delivers 50 fs (FWHM) long IR pulses with a central wavelength of 1030 nm at a repetition rate of 49 kHz and a pulse energy of 1.2 mJ. The pulse is divided into two arms using a holey mirror, which reflects approximately 85% of the beam in the pump arm and allows the remainder to pass through into the probe arm. Within the pump arm, a BBO crystal is employed to produce the second harmonic (515 nm) of the laser pulse with an efficiency of 25-30%.

To generate the XUV pulses, the second harmonic beam was focused onto an argon gas jet with a backing pressure of 1.2 bar. The resulting XUV beam was transmitted through a 150 nm thick aluminum film and subsequently focused inside the ReMi onto a supersonic gas jet of argon. The XUV pulse ionizes the argon atoms and the resulting photoelectron

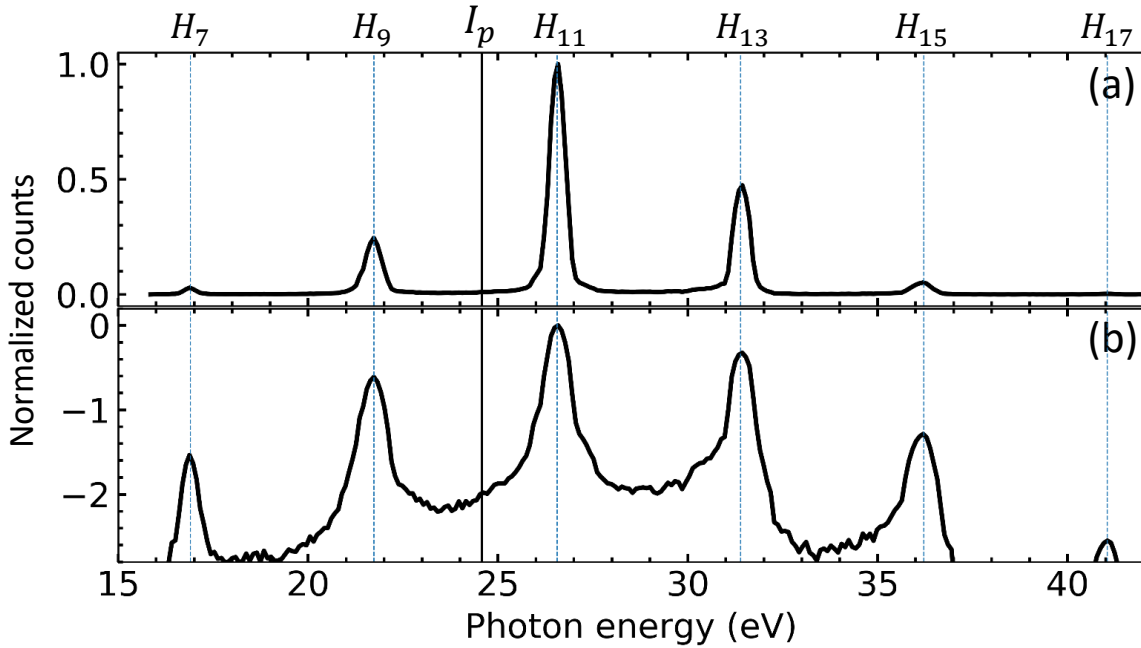


Figure 5.1. Reconstructed spectrum of the XUV pulse used in the RABBITT measurement, normalized to unity at the peak on linear (a) and (b) \log_{10} scales.

spectrum is recorded. To reconstruct the harmonic spectra after the aluminum filter, we normalized the photoelectron spectrum using the well-known ionization cross sections of the argon atom [55]. Figure 5.1 displays the reconstructed harmonic spectra, on both a linear (upper panel) and logarithmic scale (lower panel), which we utilized in generating the RABBITT traces in this chapter. Above the ionization threshold of helium, there are four harmonics, namely H_{11} , H_{13} , H_{15} , and H_{17} . Note that their strength decreases significantly with increasing photon energy. H_7 lies at the early transmission edge of the aluminum filter and is, therefore, severely dampened. The aluminum filter effectively removes all the harmonics below H_7 . It is important to note that the width of the harmonic peaks illustrated in the figure does not reflect the true bandwidth of the harmonics in the XUV. Rather, it is a convolution of the bandwidth of the harmonics, ionization cross-section, and energy resolution of the detector. The true width of the harmonics in the XUV spectral has not been determined. We adjusted the IR intensity in our measurements by utilizing an iris in the probe arm. We performed RABBITT measurements at three IR peak intensities: $I_1 \approx 5 \times 10^{11} \text{ W/cm}^2$, $I_2 \approx 7 \times 10^{11} \text{ W/cm}^2$, and $I_3 \approx 1.2 \times 10^{12} \text{ W/cm}^2$. The IR and XUV fields were linearly polarized parallel to each other and along the axis of the spectrometer. The XUV-IR temporal delay was scanned over a range equivalent to one and a half times the optical cycle of the IR pulse, which corresponds to a value of 5.15 fs. The delay was sampled at regular intervals of $T_0/60$, where $T_0=3.44 \text{ fs}$ is the period of the IR pulse. The XUV-IR light interferometer was actively stabilized throughout the experiment using the method described in Reference [56].

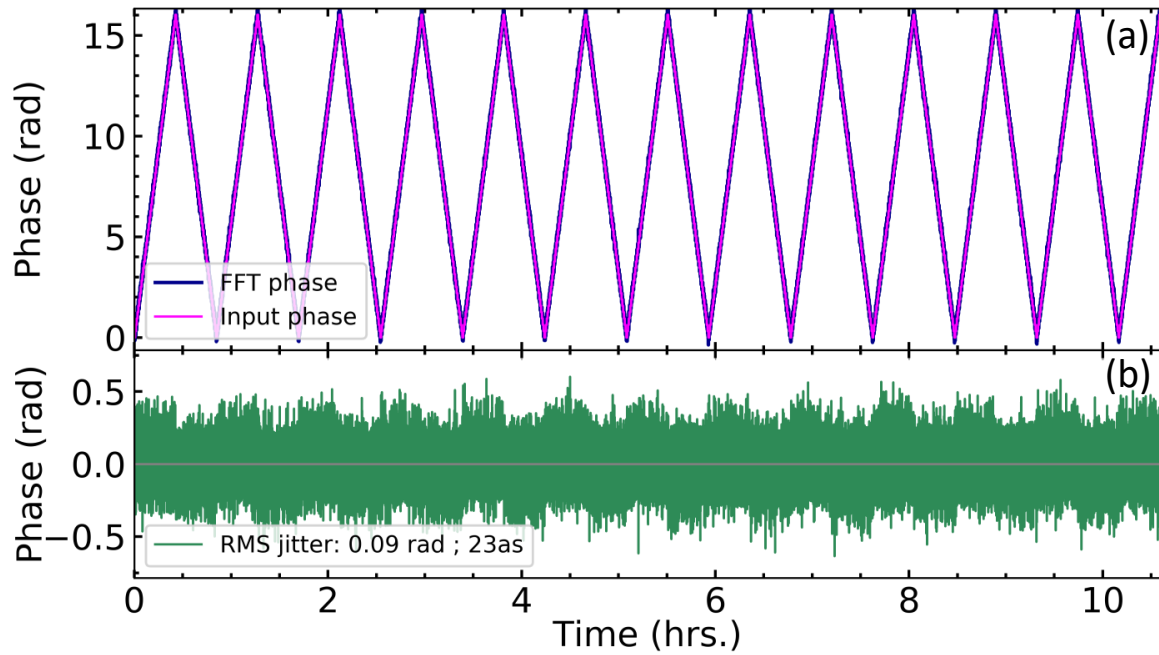


Figure 5.2. Stabilization of the interferometer over the duration of the scan.

Figure 5.2 illustrates the stability of the interferometer during the RABBITT measurement with probe intensity I_1 . The top panel shows the input phase (in pink) applied to the probe arm by moving the delay stage, and the retrieved phase (in dark blue) obtained by Fourier fringe analysis of the images captured on the camera. The bottom panel shows the difference between the input and retrieved phases. The root-mean-square (RMS) jitter throughout the entire measurement period is approximately 0.09 rad or equivalently 23 as. During the data analysis stage, it was discovered that the oscillation phase of a given sideband was shifting across different scan numbers implying the presence of a long-term drift in the interferometer with an approximate rate of 80 as/hr. To address this issue, the drift value was calculated for each iteration of the scanning process by tracking the oscillation phase of the sideband. Subsequently, the delay axis for each iteration was adjusted by shifting it according to the calculated drift value.

5.2 RABBITT Trace Analysis

5.2.1 Angle-integrated RABBITT

We first present the results from the angle-integrated RABBITT analysis, where we integrated the photoelectron signal over all emission angles. Figure 5.3 shows the results from three RABBITT measurements recorded at probe intensities I_1 (a), I_2 (b), and I_3 (c). In each case, the log-scale colormap in the lower panel shows the RABBITT trace obtained by subtracting the delay-integrated signal from the original trace to highlight the oscillations. The upper panel of Figure 5.3 displays the XUV-only photoelectron spectrum (gray line)

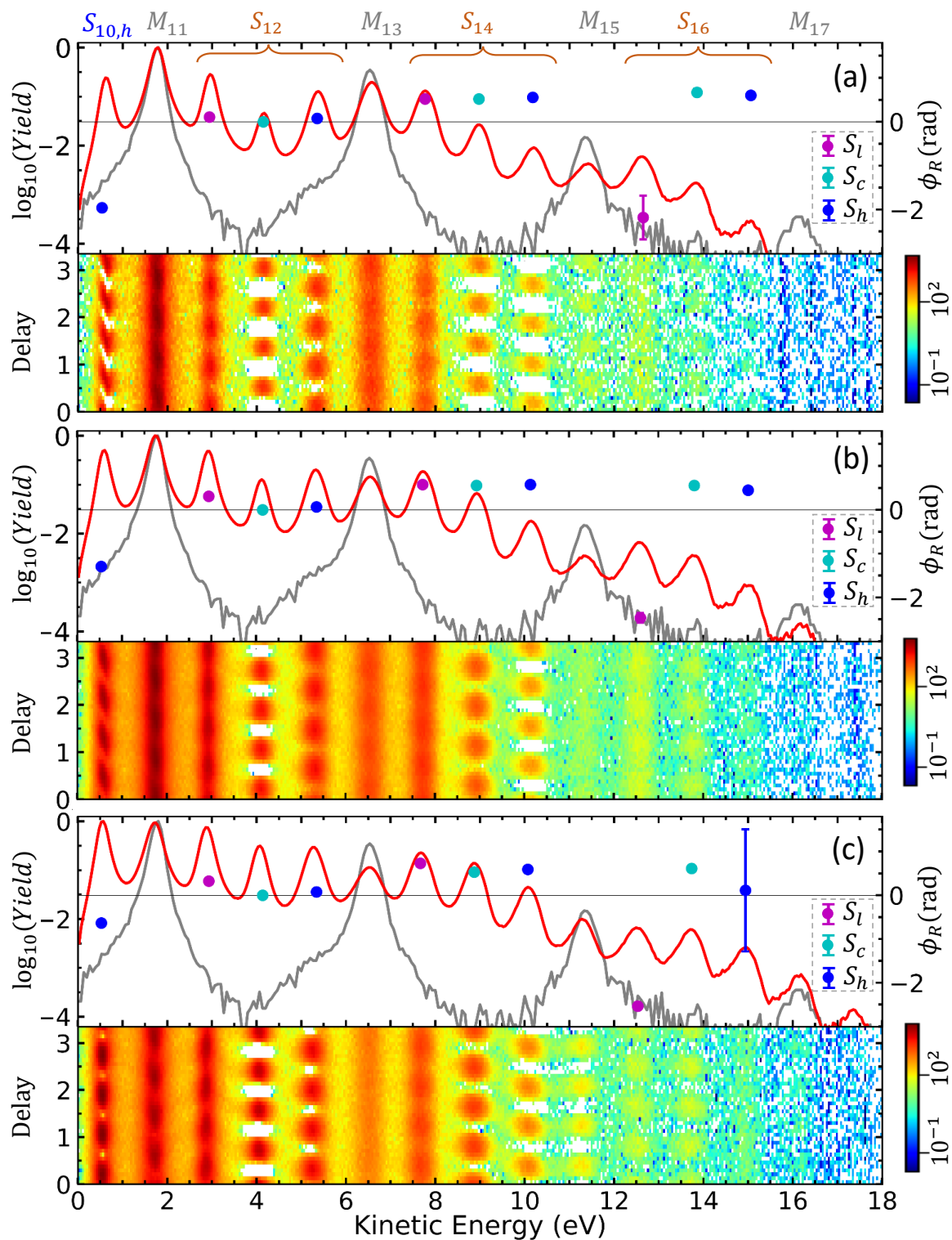


Figure 5.3. Results from the angle-integrated RABBITT measurements taken at peak IR intensities I_1 (a), I_2 (b), and I_3 (c). The logarithmic colormap in the lower panel displays the angle-integrated RABBITT traces, while the upper panel shows the XUV-only (gray line) and the delay-integrated photoelectron spectrum (red line) normalized to the peak value. The right y-axis shows the phases of the delay-dependent yield oscillations of the sidebands obtained from our fitting method, along with their fitting errors.

and the delay-integrated photoelectron spectrum (red line), both normalized to their peak values and plotted on a logarithmic scale.

Looking at the RABBITT traces, we see that the central sideband displays the clearest oscillation at all the applied IR intensities. This was expected since both the absorption and the emission paths that populate the central sideband are of the same order, making the interference stronger. In the lower and the higher sidebands, the two interfering terms are of different orders (2nd and 4th), and hence the contrast in the oscillation is not as good as compared to that in the central sideband. Also, the RABBITT traces demonstrate that the oscillation contrast is better for the higher sideband than for the lower sideband. This is due to the rapid decrease of the main peaks with increasing energy, which makes the amplitude of the two transition paths in the interference more balanced in case of the higher sideband compared to the lower sideband. In the case of the higher sideband of group 12 ($S_{12,h}$), for example, the upper main peak (M_{13}) is weaker than the lower main peak (M_{11}), resulting in the magnitude of a three-photon transition from the stronger lower main peak ($M_{11} + 3\omega$) becoming comparable to the magnitude of a one-photon transition from the weaker upper main peak ($M_{13} - \omega$). Hence the interference of these two terms leads to a strong delay-dependent oscillation. In contrast, for the lower sideband ($S_{12,l}$), the magnitude of a one-photon transition from the lower main peak ($M_{11} + \omega$) is much stronger than the magnitude of a three-photon transition from a weaker upper main peak ($M_{13} - 3\omega$), resulting in poor contrast of the oscillation. We also observe that even at the lowest applied IR intensity (I_1 , Fig. 5.3 (a)), the highest energy main peak M_{17} is almost entirely depleted, and it starts to get repopulated as the intensity is increased. The same observation can be made for the main peak M_{15} , which first depopulates as the IR intensity is increased and then repopulates on further increment. As for the 16th sideband group, we observe that the contrast in the lower sideband ($S_{16,l}$) is very poor at the lowest applied intensity, but it gradually improves as the IR intensity increases. On the other hand, the contrast of the oscillation in the higher sideband ($S_{16,h}$) deteriorates with increasing IR intensity.

When the kinetic energy or the IR intensity is increased, the continuum-continuum coupling becomes stronger, and it becomes crucial to also take into account the higher-order transitions. Such transitions result in multiple interference terms that can cause the total yield of the sidebands to vary with the XUV-IR temporal delay. Figure 5.4 shows many-order transition pathways leading to the lower and higher sidebands of group 16 and the interference schemes contributing to the oscillations of the yield. At the low IR intensity, the oscillation in the photoelectron yield of the lower sideband is predominantly influenced by the interference scheme T_A . However, since the upper main peak (M_{17}) is more than one order of magnitude smaller than the lower main peak (M_{15}), the higher-order transitions involving the main peaks from the lower energy side become significant.

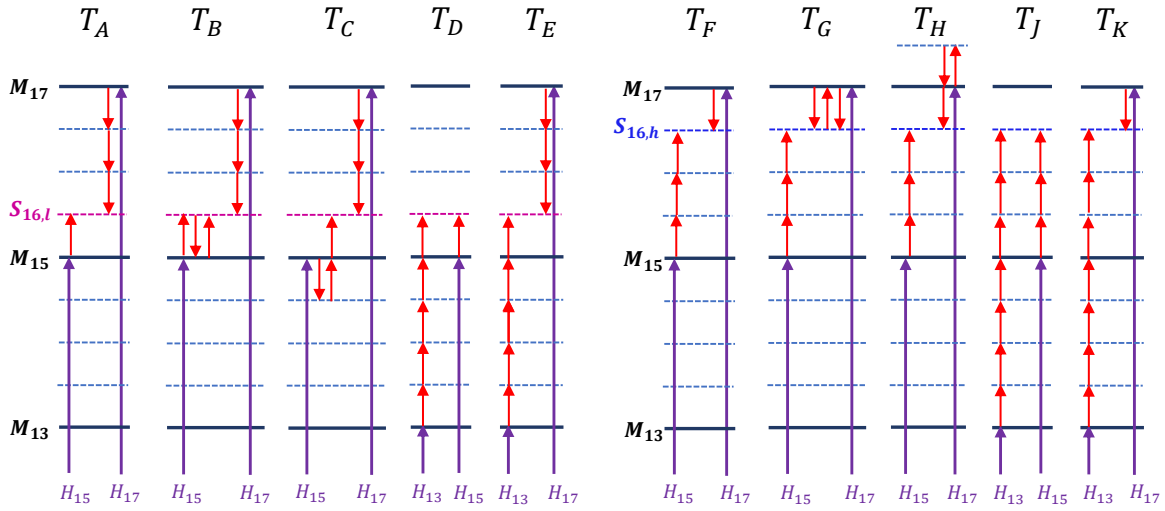


Figure 5.4. Energy diagram showing the many-order transitions to the lower and higher sideband in group 16. The oscillation of the total yield arises from the interference of two distinct transition paths involving different harmonics. Specifically, interference schemes T_A , T_B , T_C , T_D , T_F , T_G , T_H , and T_I produce oscillations at 4ω , while T_E and T_K result in an oscillation frequency of 8ω .

In addition, each dipole transition accumulates a phase shift of $\pi/2$. As shown in figure 5.4, the interference schemes T_B , T_C , and T_D involve a different number of photons compared to T_A . As a result, the oscillations that come from T_B , T_C , and T_D are shifted by π relative to the oscillation that comes from T_A . This causes a reduction in the oscillation contrast in the lower sideband, which can be seen in the RABBITT trace of Fig. 5.3 (a). With increased IR intensity T_D starts to dominate the remaining interference schemes, resulting in the reappearance of the oscillation in the lower sideband. Although the T_E scheme should produce an oscillation at 8ω , we could not resolve it in our measurements.

In the higher sideband ($S_{16,h}$) at lower intensities, the T_F interference scheme is dominant and thus determines the oscillation in the yield. However, as the intensity increases, the oscillations resulting from the interference schemes involving other higher-order transitions (T_G , T_H , and T_J) start to become comparable to the oscillation resulting from the lowest-order interference term (T_F), leading to the deterioration of the overall delay-dependent oscillation of the yield. The T_K scheme should produce oscillations at 8ω , but we also could not isolate this oscillation either.

In order to determine the phases of oscillation from each sideband, the photoelectron spectrum was first integrated within an energy window of 0.8 eV across the peak and then fitted to a cosine function of the form $A + B\cos(4\omega\tau - \phi_R)$. For the lower and higher sidebands, the trivial π phase was removed from the obtained phases. The retrieved phases of the oscillations obtained from the fitting process, along with their corresponding fitting

errors, are shown in the upper panel of Figure 5.3 and also listed in the Table 5.1. In Fig. 5.5(a), we plot the retrieved phase of the central sideband on the y-axis, and the corresponding kinetic energy on the x-axis, for the three RABBITT measurements.

Probe Intensity	SB 10	SB 12			SB 14				SB 16		
	S_h	S_l	S_c	S_h	S_l	S_c	S_h	S_l	S_c	S_h	
I_1	-1.96 ± 0.02	0.11 ± 0.02	0 ± 0.01	0.08 ± 0.02	0.52 ± 0.06	0.52 ± 0.01	0.55 ± 0.01	-2.18 ± 0.49	0.67 ± 0.08	0.60 ± 0.06	
I_2	-1.29 ± 0.01	0.31 ± 0.02	0 ± 0.01	0.07 ± 0.01	0.58 ± 0.04	0.56 ± 0.01	0.58 ± 0.01	-2.46 ± 0.11	0.56 ± 0.04	0.45 ± 0.07	
I_3	-0.64 ± 0.01	0.32 ± 0.02	0 ± 0.01	0.07 ± 0.01	0.73 ± 0.02	0.53 ± 0.11	0.59 ± 0.01	-2.53 ± 0.05	0.61 ± 0.03	0.11 ± 1.40	

Table 5.1. (a) Angle-integrated RABBITT phase (in radian) obtained from the fitting procedure from the measurements at three IR intensities.

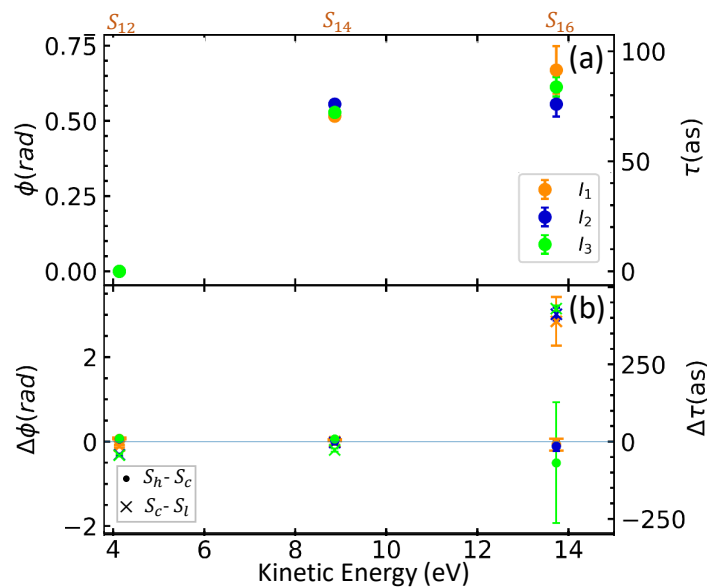


Figure 5.5. (a) The upper panel displays the central sideband (S_c) at various intensities, while the lower panel (b) illustrates the phase of the lower and higher sidebands relative to the central sideband.

As the absolute phase is unknown, the retrieved phases from the three measurements were shifted to align the first data point ($S_{12,c}$) at zero for comparison. The energy-dependent curve of the phase seems to slightly vary in the three scans, and it is challenging to determine the cause of this variation. It could be due to changes in the IR intensity, variations in the group-delay dispersion phase of the XUV pulse during the measurement, or a combination of both. Since the three measurements were conducted on different days, it cannot be guaranteed that the conditions in the HHG process were consistent throughout the three

measurements. The lower panel of Fig.5.5 displays the variation in the higher and lower sidebands relative to the central sideband at three IR intensities. The difference is less sensitive to the change in the XUV-phases. Within the group, the difference decreases going from group 12 to group 14, but it increases upon reaching group 16. Specifically, the lower sideband of group 16 exhibits almost a π change. This is because the contribution of the higher-order interference terms (T_B , T_C , and T_D) dominates over the lowest-order term (T_A). Since these higher order terms produce oscillations that are π out of phase with those arising from the lowest order term T_A , this results in the observed π change.

5.2.2 Under-threshold RABBITT

Now we focus on the 10th sideband group, where only the higher sideband ($S_{10,h}$) is detectable above threshold. This sideband can be excited through a two-photon process that involves absorption of the 11th harmonic from the XUV pulse and emission of an IR photon ($H_{11} - \omega$). However, in order to observe oscillations in the yield of this sideband, an additional path involving another harmonic is necessary. While a six-photon transition to $S_{10,h}$ can occur via absorption of the 13th harmonic from the XUV pulse and the subsequent emission of five IR photons, the strength of this transition is extremely weak.

Another pathway that can lead to $S_{10,h}$ involves four-photon ionization driven by the ninth harmonic from the XUV pulse and three IR photons ($H_9 + 3\omega$), as shown in Fig. 5.6. The type of RABBITT measurement where the first photoelectron peak corresponds to a sideband is commonly known as Under-threshold-RABBITT (uRABBITT). During the past few years, (uRABBITT) has gained significant interest due to the valuable information it can provide about the amplitude and phase of the bound-bound (real/virtual) transitions by analyzing the characteristics of the threshold sideband [57–62].

All of the above studies were conducted within the conventional 1-sideband RABBITT framework, where the population of the sideband via two-photon ionization (XUV+IR) is assisted by one of the XUV pulse harmonics being (near)-resonant with one of the discrete bound states. The oscillation phase of the yield as a function of detuning were investigated by tuning the harmonics in and out across the (anti) resonance, utilizing a narrow bandwidth and tunable central laser wavelength laser [60–62]. It has been estimated that the presence of a discrete resonance adds to the RABBITT phase a phase shift (ϕ_{res}) given as [59, 63]

$$\phi_{res} = \arctan \left[\frac{1}{\sqrt{\pi}} \frac{\Gamma}{\Delta} \right]. \quad (5.1)$$

Here Δ is the detuning from the resonance and Γ is the spectral width of the XUV field.

Figure 5.6 illustrates the energy levels of the Rydberg states of the field-free helium atom [64], along with the XUV and IR photon paths. If the transition encounters any resonance

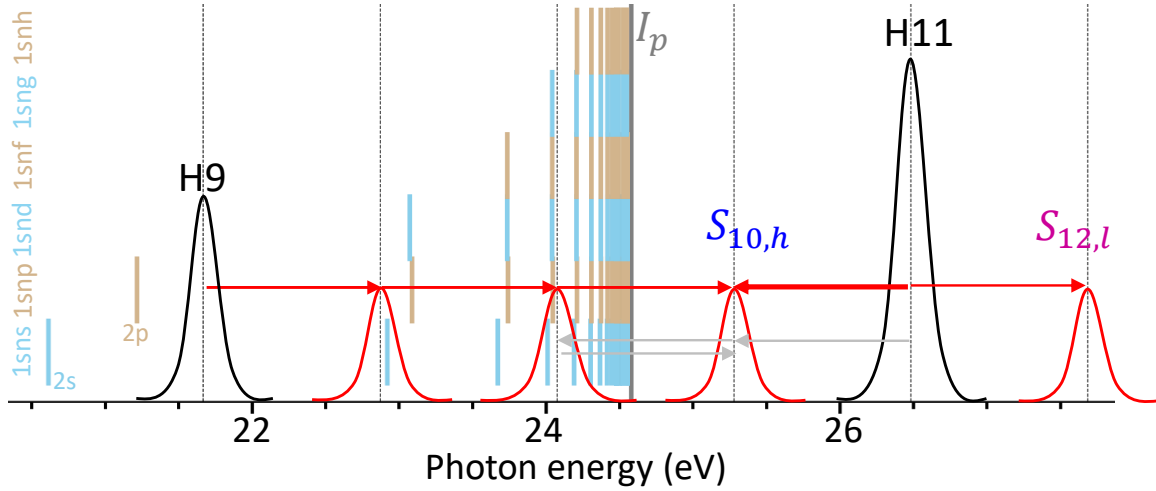


Figure 5.6. Energy level diagram showing the formation of the threshold sideband ($S_{10,h}$).

states below the threshold, the amplitude of this pathway can become very strong. Although the 9th harmonic is not resonant with any of the bound states, the $H_9 + 1\omega$ photon energy is close to the 1s3s level, and the 1s5p state is in resonance with $H_9 + 2\omega$. This four-photon ionization path ($H_9 + 3\omega$) interferes with the two-photon path that involves the absorption of the 11th harmonic and the emission of an IR photon ($H_{11} - \omega$) and leads to the delay-dependent oscillation in the yield. Interference between the four-photon ionization pathway driven by $H_9 + 3\omega$ and the two-photon pathway $H_{11} - \omega$ results in oscillations in the yield of $S_{10,h}$ as a function of the delay. The RABBITT traces shown in Figure 5.3 (a) indicate that the yield oscillation in $S_{10,h}$ is tilted, suggesting a strong phase variation as a function of energy across the peak. This tilt can also be seen in the RABBITT trace with the IR intensity I_2 shown in Figure 5.3 (b), but it disappears for the highest employed intensity I_3 , as shown in Figure 5.3 (c).

Figure 5.7 displays the angle-delay-integrated yield of $S_{10,h}$ for our three IR intensities. In each case, the yield of $S_{10,h}$ is normalized with respect to the highest value observed in the full photoelectron spectrum (PES). At the highest applied IR intensity (I_3), the photoelectron yield of $S_{10,h}$ is highest among the other peaks in the full PES. As the IR intensity increases, the peak position of $S_{10,h}$ in the kinetic energy distribution shifts towards the low-energy side due to the pondermotive shift. However, the measured bandwidth of the distribution remains approximately constant at around 0.25 eV. To obtain the phase variation as a function of energy, the angle-integrated photoelectron yields were binned into an energy window of 0.2 eV with an interval of 0.05 eV across the peak of $S_{10,h}$. Then, the delay-dependent photoelectron counts in each bin were fitted to a cosine function to retrieve the oscillation phase. The obtained phase variation as a function of energy is plotted on the right side in Figure 5.7, since the left panel shows the angle-integrated yield of $S_{10,h}$ and shares the same energy axis. At the lowest applied IR intensity, the phase across the peak

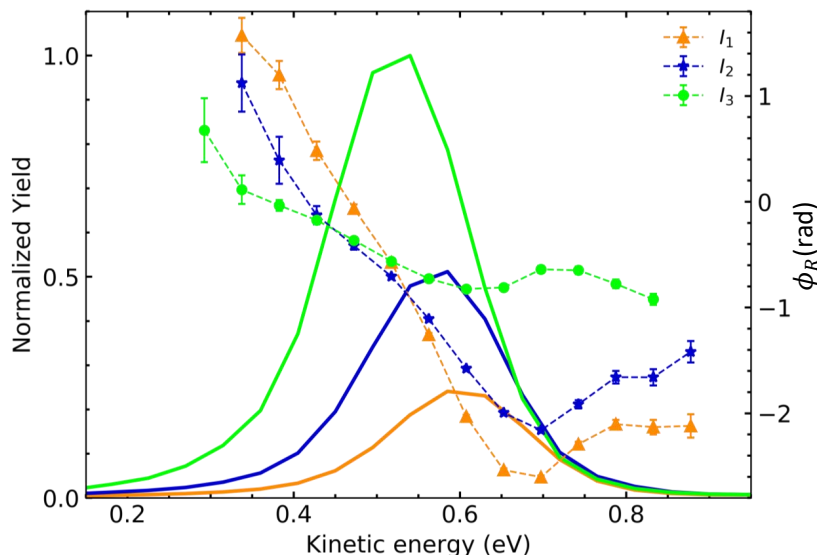


Figure 5.7. Variation in phase for the threshold sideband across the peak at different probe intensities.

initially decreases linearly at a rapid rate and then gradually begins to increase. As the IR intensity is increased, the rate of the phase change across the peak decreases, but the general behavior remains the same. This can be attributed to the intensity-dependent Stark shift of the $1s3s$ and $1s5p$ states resulting in the detuning of the resonances.

In our case, there are more than one intermediate resonant states getting excited in the four-photon ionization process. Estimating the phase variation as a function of detuning to these states is complicated and not carried out in this thesis.

5.2.3 Angle-resolved phase measurements

To examine the angle-dependence of the RABBITT phases, we analyzed the photoelectrons emitted at various angles relative to the spectrometer axis. This involved segregating the data into angle-differential data sets, which were generated by integrating the photoelectron yield over 10-degree angular windows at 5-degree intervals. The phase of the oscillation in each sideband was extracted from each angle-differential data set using the same method as outlined in the angle-integrated case. The photoelectron spectra from each sideband were integrated over a 0.6 eV energy window centered on the peak, and the resulting delay-dependent signal was fitted to a cosine function to obtain the phase.

Figures 5.8 and 5.9 illustrate the angle-dependence of the retrieved phases from the three sidebands in group 12 and group 14, respectively for different IR intensities: (a) I_1 , (b) I_2 , and (c) I_3 . For better comparison and the fact that we do not know the absolute phase, a common phase was added to the three sidebands of each group to shift the central sideband phase to zero at the first data point (5 deg) for each intensity. The statistical uncertainty of

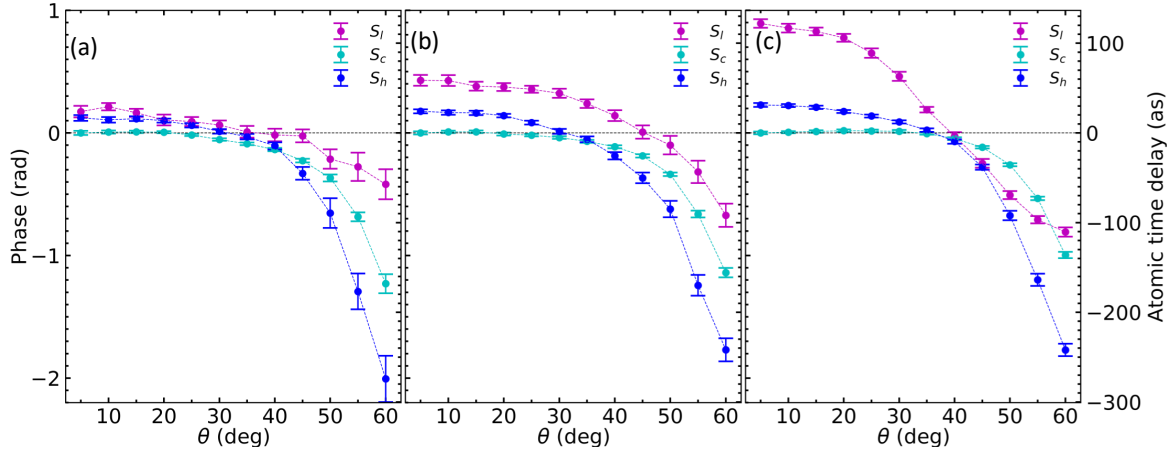


Figure 5.8. Angle-dependent phase retrieved from the 12th sideband group in the RABBITT scans, performed with IR intensities of I_1 (a), I_2 (b), and I_3 (c).

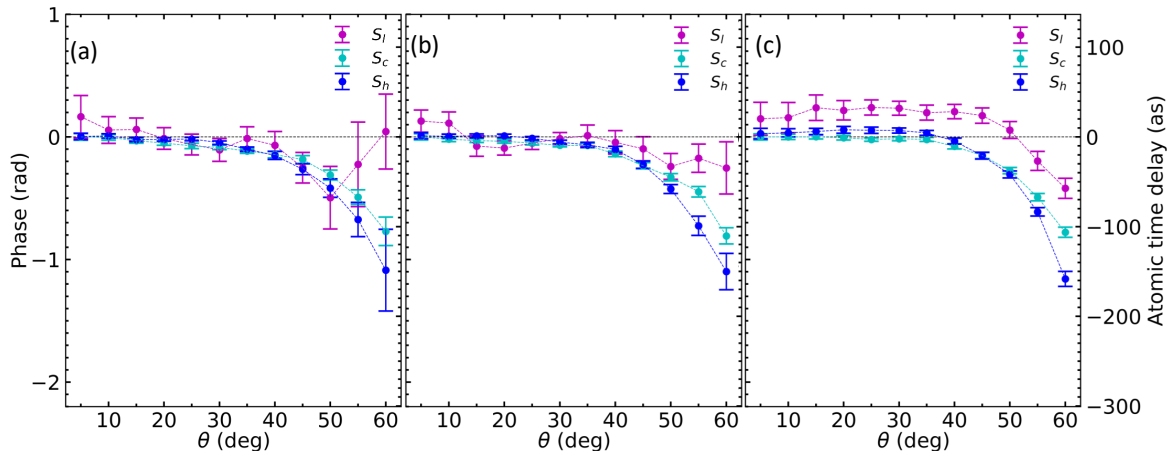


Figure 5.9. Angle-dependent phase retrieved from the 14th sideband group in the RABBITT scans, performed with IR intensities of I_1 (a), I_2 (b), and I_3 (c).

the data above 60 degrees was insufficient to reliably retrieve the oscillation phase. After analyzing the figure, it is evident that the angular dependence of the central sidebands in both group 12 and 14 remains similar for all three probe intensities. However, the angular dependence of the RABBITT phase in the higher sideband gradually changes with probe intensity, whereas the lower sideband shows the strongest variation.

The angle-dependence in the yield of the photoelectron signal or in the RABBITT phase arises due to the interference of various partial waves excited in the multi-photon transitions. The angular-momentum-resolved transition diagram for the lowest-order absorption and emission paths is shown in Fig. 5.10(a). We see that a three-photon transition to $S_{q,c}$ via absorption or emission of two probe photons ($H_{q\pm 1} \mp 2, \omega$) results in excitation of the p and f angular momentum states. In contrast, the two-photon transition to $S_{q,l}$ ($S_{q,h}$) creates a mixture of s and d states, while the four-photon transition to $S_{q,l}$ ($S_{q,h}$) excites s , d , and g states.

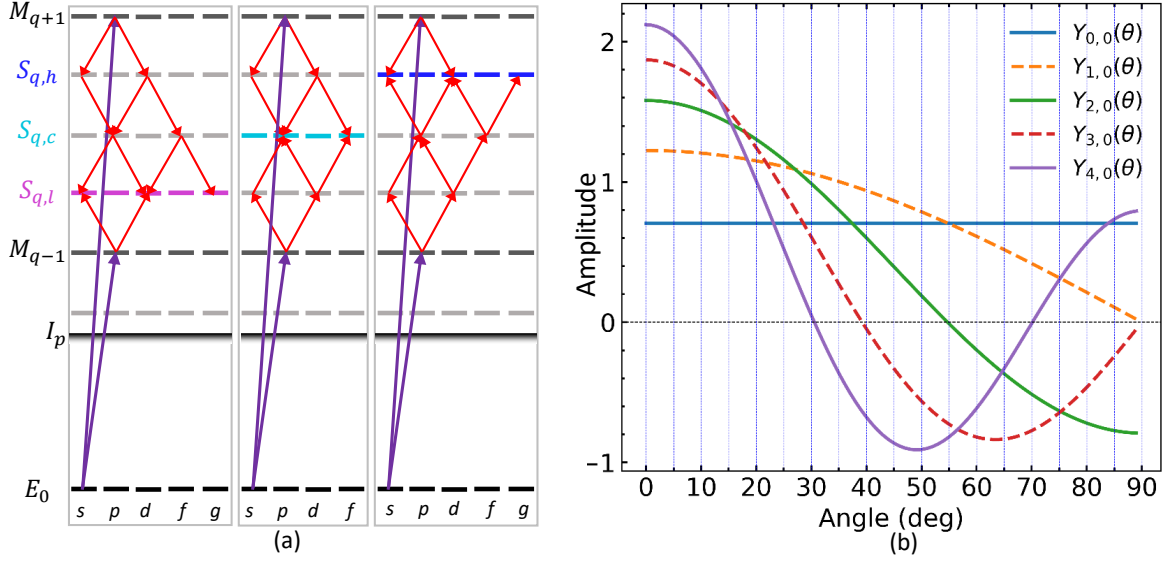


Figure 5.10. Transition diagram including various angular momentum channels (a) and Polar angle dependence of first few spherical harmonics (b)

In both the absorption and emission processes, there are multiple angular-momentum channels to form the sideband, and each channel from the absorption path will interfere with every channel from the emission path. Each interference will result in an oscillation in the yield as the delay of the XUV-IR pulses is varied. Each interference is characterized by an oscillation amplitude ($\mathcal{A}_{\ell,\ell'}$) and a phase ($\phi_R^{\ell\ell'}$). The overall oscillation in the signal is the resultant of all these channel-resolved oscillations and can be written as:

$$\begin{aligned}
 S_q(\tau, \theta) &\propto \sum_{\ell,\ell'} \alpha_\ell^a \alpha_{\ell'}^{e*} Y_{\ell,0}(\theta) Y_{\ell',0}^*(\theta) \cos(4\omega\tau - \Delta\phi_\Omega^q - \Delta\phi_{\ell\ell'}^{at}) \\
 &\propto \sum_{\ell,\ell'} \mathcal{A}_{\ell,\ell'}(\theta) \cos(4\omega\tau - \phi_R^{\ell\ell'}) \\
 &\propto I_1(\theta) \cos(4\omega\tau - \phi_R(\theta)).
 \end{aligned} \tag{5.2}$$

Here α^a and α^e are the transition amplitudes involving the XUV and IR fields and the matrix elements, while $\ell(\ell')$ denotes the final angular momentum of the sideband reached through the absorption (emission) path. $\Delta\phi_\Omega^q$ is the spectral phase difference of two neighboring harmonics.

The oscillation amplitude ($\mathcal{A}_{\ell,\ell'}$) of each interference is determined by the magnitude of the dipole transition matrix elements ($\alpha_\ell^a \alpha_{\ell'}^e$) and the spherical harmonics ($Y_{\ell,0} Y_{\ell',0}^*$) associated with the two angular momentum states of the sideband reached in the absorption and emission process. As the amplitude of the spherical harmonics varies with the polar angle, the oscillation amplitude also changes with the angle.

The atomic phase difference ($\Delta\phi_{\ell\ell'}^{at}$) is comprised of both the Wigner phase and the continuum-continuum transition phase. The Wigner phase contribution is identical in all

$\Delta\phi_{\ell\ell'}^{at}$ since the ionization process has only one angular momentum channel. However, as there are multiple angular channels available for continuum-continuum transitions, and the ϕ^{cc} value varies with the angular momentum, the resulting $\Delta\phi_{\ell\ell'}^{at}$ may differ for different interfering channels (absorption: ℓ and emission: ℓ').

Since the interference of two angular momentum channels leads to distinct oscillation phases ($\phi_R^{\ell\ell'}$) and angle-dependent oscillation amplitudes ($\mathcal{A}_{\ell,\ell'}(\theta)$), the overall oscillation phase retrieved from the experiment ($\phi_R(\theta)$) also varies with the emission angle.

The difference in ϕ^{cc} for different angular momentum values depends on the kinetic energy and is relatively small (less than $\pi/10$ for kinetic energy above 5 eV), as shown in Fig. 3.11. Consequently, the differences in $\Delta\phi_{\ell\ell'}^{at}$ (and thus in $\phi_R^{\ell,\ell'}$) for various interference terms are also generally very small. Therefore, the change in the oscillation amplitude ($\mathcal{A}_{\ell,\ell'}$), due to changes in the amplitude of the spherical harmonics with angle, leads to only a slight variation in the overall retrieved oscillation phase ϕ_R with angle. However, a substantial change in ϕ_R may occur when the electron emission angle approaches the node position of the spherical harmonics. In cross-channel interference, where $\ell \neq \ell'$, the product of the spherical harmonics $Y_{\ell,0}(\theta)Y_{\ell',0}(\theta)$ changes signs after their angular nodes (Fig. 5.10). This effect is equivalent to adding a π phase to the corresponding oscillation phase $\phi_R^{\ell\ell'}$. Depending on the relative weight of this cross-term interference compared to the other contributions, the overall retrieved phase (ϕ_R) may exhibit rapid variations near the node positions.

In Fig. 5.8(a), in the central sideband, the slow variation in the RABBITT phase below 40 deg is due to the angle-dependent oscillation amplitude ($\mathcal{A}_{\ell,\ell'}(\theta)$) changing the weight of the distinct oscillation phases ($\phi_R^{\ell\ell'}$) with a change in the emission angle. After 40 deg, the oscillation phase in the cross-channel interference ($p-f$) changes by π due to the sign change in the amplitude coefficient $Y_{3,0}(\theta)$.

The rapid variation in the RABBITT phase observed in the central sideband beyond 40 deg indicates that the ratio of the angle-dependent amplitudes of the cross-channel ($p-f$) interference to that of the same-channel interferences ($p-p$ and $f-f$) is increasing with the angle. This increasing ratio leads to a monotonic decrease in the overall RABBITT phase, which holds true for all three applied IR intensities.

For the lower sideband, a four-photon transition populates s , d , and g states, while a two-photon process populates s and d states. Based on the propensity rule for continuum-continuum transitions [41], the relative population of the g -state via three IR photon emission is very weak. Thus the π -jump in the oscillation phase in $s-g$ and $d-g$ cross-channel interference near 30 deg does not result in a significant variation of the RABBITT phase. We see a slight variation only after 50 deg, where the magnitude of the d -wave is reduced and approaches zero at 57 deg.

For the higher sideband, the three-photon absorption in the continuum creates a g -state with a significant weight. Thus, we see that the angle-dependence of the higher sideband starts to vary early following the node position of the g -wave around 30 deg.

Let us now compare the phases of the three sidebands at an electron detection angle of 5 deg, which corresponds to the photoelectrons collected over an angular range of 0 to 10 deg. At the lowest IR intensity, when higher-order interference terms can be neglected, the difference in the phases of the three sidebands arises due to the difference in the atomic phases $\Delta\phi_{\ell\ell'}^{at}$. This difference is caused by the dependence of the cc-phase (ϕ^{cc}) on the angular momentum channels, since the Wigner phase remains common and does not affect $\Delta\phi_{\ell\ell'}^{at}$. As the kinetic energy of the photoelectron increases, ϕ^{cc} becomes increasingly similar for the various angular momentum channels, resulting in a decreasing difference in $\Delta\phi_{\ell\ell'}^{at}$ of all three sidebands. Therefore, the overall phase of the three sidebands becomes similar at 5 deg.

This trend can be seen in Figures 5.8(a) and 5.9(b), where the phase difference between the central sideband and the higher sideband at 5 deg is smaller in the higher-energy group 14 than in the lower energy group 12. However, this behavior is not observed for the lower sideband, i.e. the phase difference between the lower and central sidebands at 5 deg does not decrease as we move from group 12 to group 14. Rather, in group 14, it appears to have increased even at the lowest applied intensity. Also the angle-dependent phase exhibits oscillations. This suggests a contribution from higher-order transitions, which can carry the spectral phase of far-away harmonics and/or have additional π phase shifts due to the involvement of different numbers of photons. When these higher-order transitions interfere with lower-order transitions, they can result in a different oscillation phase. Depending on the amplitude of this oscillation, it may alter the overall oscillation phase.

The oscillation in the RABBITT phase of the lower sideband with angle might also be explained by the presence of higher-order transitions. These transitions create higher angular momentum states. As a result, the cross-channel interference involving these transitions will exhibit several angular nodes. The oscillations associated with each channel may have different phases and amplitudes, which can vary with angle. This can cause an overall angular modulation in the observed RABBITT phase.

In group 12, as the intensity of the applied IR radiation increases, the lower sideband displays a strong variation as a function of angle. This behavior can be attributed to the increasing strength of six-photon transitions involving under-threshold harmonics (H_9) and Rydberg states. These transitions are enhanced due to resonances, resulting in the creation of higher angular momentum states and a strong angle-dependence of the phase. In contrast, group 14 exhibits a notable change in the angle dependence of the lower sideband as the applied IR intensity increases, albeit not as pronounced as that seen in group 12.

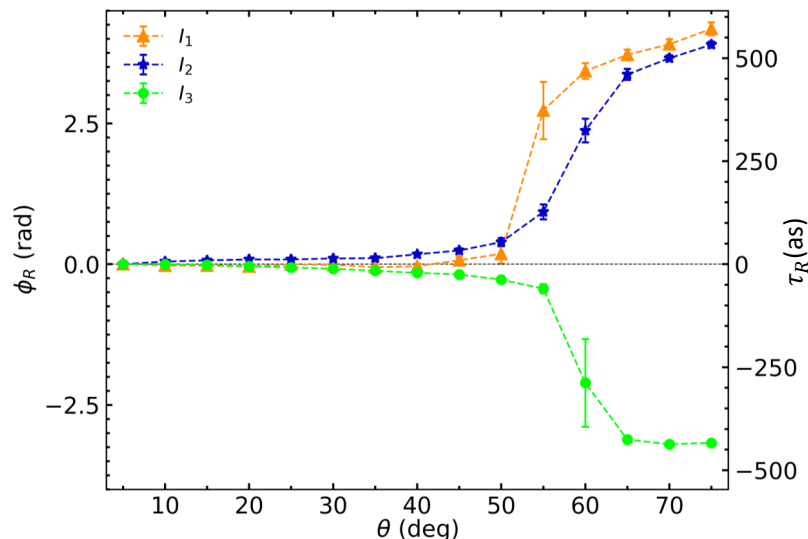


Figure 5.11. Angle-dependent RABBITT phase for the threshold sideband at different probe intensities.

Figure 5.11 displays the angle-dependence of the RABBITT phase in the threshold sideband ($S_{10,h}$). The data points were generated by integrating the photoelectron signal over a 0.6 eV energy window centered on the peak of $S_{10,h}$ and then binned into 10-degree angular windows at 5-degree intervals. At the lowest applied IR intensity (I_1), the phase experiences an abrupt change of almost π near 55 deg, which indicates the dominance of the $s-d$ cross-channel interference. As the IR intensity increases, this change becomes smoother, and at the highest applied IR intensity, the π -jump shifts towards the negative side, suggesting an additional π phase in the four-photon ionization path.

5.3 Summary and Outlook

In this chapter, we investigated various aspects of 3-SB RABBITT measurements on helium atoms performed at three different IR intensities. We first compared the angle-integrated RABBITT phases of the sideband triplet in three groups above threshold. We observed that the triplet of the first two groups (12 and 14) had similar phases, as expected from the decomposition approximation [42]. However, the sidebands in the 16th group showed some deviation due to the significant contribution of higher-order transitions. In addition, we investigated the threshold sideband, where a four-photon ionization process contributes an energy-dependent phase to the RABBITT phase. At the weakest applied dressing field, the four-photon-ionization path encounters at least two discrete resonances, resulting in a rapid change in the phase of the yield oscillation as a function of energy. However, as the intensity of the dressing field increases, the resonances are detuned due to the Stark shift of the states,

and the rate of phase variation as a function of kinetic energy decreases. By studying the angle-dependence of the yield oscillation phases, we could estimate which angular channels are most important in the formation of the three sidebands via the absorption and emission of IR photons.

As we look towards the future, there are several interesting avenues for further research. To begin with, it would be beneficial to generate a narrow bandwidth and tunable XUV-APT to study the RABBITT phase of the higher sideband of group 10, $S_{10,h}$, which involves four-photon ionization. This would allow us to better understand the underlying physical mechanisms involved. Another area of interest is the exploration of 3-SB RABBITT schemes in which two sidebands of the triplet are above threshold while the other one is below. These sidebands would have similar bound-bound and bound-continuum interactions (three-photon ionization), but different interactions in the continuum. Comparing the phases of these two groups would provide valuable insights into the ionization process.

To deepen our understanding of the complex dynamics that govern the ionization process in helium and other atomic systems, it will be important to further refine our experimental techniques. One important aspect is to push the cutoff of high harmonic generation (HHG), enabling us to generate a greater number of sideband groups. This expansion in the spectral range of the XUV will provide us with more data points to study the cc transitions at higher kinetic energy. Additionally, the availability of a tunable laser source would greatly facilitate the study of different energy levels and resonant conditions. Furthermore, as part of our future plans, we intend to compare our experimental findings with theoretical predictions derived from both SAE (Single Active Electron) and RMT calculations. The calculations will be performed by our collaborators.

Chapter 6

Discussion and Summary

This PhD research aimed to explore the dynamics of photon exchange between a quasi-free electron and a laser field in a photoionization process. The focus lies on the specific process, where an XUV pulse ionizes the system in the presence of a phase-locked IR pulse, and the resulting photoelectrons interact with the IR photons to undergo continuum-continuum transitions. The goal is to use a new technique called 3-SB RABBITT, which is an adaptation of the commonly used RABBITT technique (1-SB RABBITT) in attosecond metrology, to study the amplitude and phase of the outgoing electron wavepacket.

This thesis is based on the following three publications:

- Publication I: High-repetition rate attosecond beamline for multi-particle coincidence experiments.
- Publication II: Decomposition of the transition phase in multi-sideband schemes for reconstruction of attosecond beating by interference of two-photon transitions.
- Publication III: Multisideband interference structures observed via high-order photon-induced continuum-continuum transitions in argon.

Publication I details the attosecond pump-probe beam line setup at the MPIK in Heidelberg, which includes a high-repetition-rate and high-average-power IR laser source, an actively stabilized Mach-Zehnder interferometer, and a reaction microscope. The Mach-Zehnder configuration enables independent control of the pulse power, polarization, and frequency of the light sources in the pump and probe arms. However, this configuration also makes the alignment of the pump (XUV) and probe (IR) pulses more sensitive to thermal and mechanical disturbances. To address this issue, the interferometer is actively stabilized to reduce the temporal drift between the pump and probe pulses. The reaction microscope allows the coincident detection of charged fragments produced in photoionization and photodissociation, as well as the reconstruction of their full 3D momentum, making

it possible to analyze their angle-differential behavior. Furthermore, publication I presents significant results from pump-probe photo-dissociation experiments conducted on molecular hydrogen and argon dimers. The results showcase that the setup has high stability and precision, allowing it to perform kinematically complete measurements with attosecond accuracy.

In this thesis, we show and explain the results from 3-SB RABBITT measurements on argon and helium. Both the 1-SB and 3-SB RABBITT measurements involve ionizing the system with an XUV APT in the presence of an IR pulse, and then recording the resulting photoelectron spectra at varying temporal delays between the two pulses. As the delay between the pulses is varied, the photoelectron signal exhibits oscillations. The phases of these oscillations carry information about the dipole transition matrix elements that are involved in the creation of the photoelectron.

The direct photoionization by XUV APT in the 1-SB RABBITT setup produces discrete peaks in the photoelectron spectrum referred to as main peaks or main bands. These main peaks are spaced apart by twice the energy of the probe photon, and the presence of the probe photon causes an additional discrete peak to appear between the main peaks. This is called a sideband. On the other hand, in the 3-SB RABBITT setup, the main bands created directly by the XUV-APT are separated by four times the energy of the probe photon. Then, with the presence of the probe photon, three sidebands appear between every pair of main bands. In a 1-SB RABBITT measurement, a single transition in the continuum is sufficient to produce a delay-dependent oscillation in the photoelectron signal. Also, it is desirable to keep the IR field weak, so that only a single transition in the continuum can be assumed. The oscillation observed in the yield of the three sidebands in the 3-SB RABBITT scheme arises from the interference between quantum paths involving different numbers of transitions in the continuum. Publication II offers an in-depth analysis of the 3-SB RABBITT scheme and explores the valuable information that can be obtained through this method. The phase retrieved from the oscillation in the sideband yield reveals the intricate details of the multi-order interaction of photoelectrons in the continuum.

We built upon the commonly-used "asymptotic approximation" in RABBITT measurements, which splits the phase of the two-photon dipole transition matrix element into a Wigner phase associated with single-photon ionization and a continuum-continuum phase (ϕ^{cc}). To achieve this, we employed perturbation theory and substituted the intermediate and final states of the photoelectron with their corresponding asymptotic scattering states. Even when the photoelectron undergoes multiple transitions in the continuum, we demonstrated that the final phase of the electron wave packet can still be broken down into a single-photon ionization phase and a sequence of continuum-continuum coupling phases that correspond to each transition.

Our collaborators at Drake University in Des Moines (Iowa, USA) performed *ab initio* calculations of a 3-SB RABBITT scheme, first in atomic hydrogen and later also in argon, by solving the time-dependent Schrödinger equation. For atomic hydrogen, we analyzed the phases of the yield oscillations of the sidebands in detail and compared them with the analytical phase obtained using the decomposition approximation. The approximation predicts that the phase of the three sidebands between consecutive harmonics should be the same, but we observed deviations from this prediction in the simulation, mainly at the lowest kinetic energy. We attributed the discrepancy to the fact that the real cc-coupling phase depends on the angular momenta of the continuum states involved in the transitions. However, these angular momentum-dependent effects are not accounted for in the decomposition approximation, leading to the observed discrepancy.

Publication III reports the results of first-ever 3-SB RABBITT measurement in argon. We successfully observed the delay-dependent yield oscillation in all three sidebands and were able to retrieve the oscillation phases with good accuracy. This again shows the outstanding stability of the interferometer.

As anticipated, we observed that the oscillation phases retrieved from the three sidebands belonging to the same group tend to become more similar as the kinetic energy increases. Upon analyzing the oscillation phases as a function of the electron emission angle, it was found that the angle-dependence of the oscillation phase varied among the three sidebands of the same group. The lower and higher sidebands in the group have the same angular parity while the central sideband has the opposite parity. Despite having the same angular parity, the angle-dependence of the oscillation phase is still somewhat different in the lower and higher sidebands. The dependence of the RABBITT phase on the photoemission angle is strongly influenced by the amplitude and phase of the dipole transition matrix elements associated with the different quantum paths participating in the interference resulting in oscillations in the photoelectron yield. The total phase acquired by the electron wavepacket depends on the intermediate and final angular momentum states traversed in both the bound-continuum and continuum-continuum transitions.

The transition probability to specific angular-momentum states of the sidebands depends on two factors: a propensity rule, which favors an increase in angular momentum upon photon absorption and a decrease upon photon emission, and the number of possible ways in which the particular angular momentum state can be reached. The probability of transitioning to different final angular momentum states differs between the lower and higher sidebands due to the difference in the number of probe photons involved in their absorption and emission paths. Specifically, the lower sidebands involve absorption of one probe photon and emission of three probe photons, whereas the higher sideband involves absorption of three probe photons and emission of just one probe photon. As a result,

the transition probability ratios for the final angular-momentum states excited through absorption and emission paths differ between the lower and higher sidebands, leading to the observed difference in angle-dependence.

Furthermore, we observe significantly large deviations in the RABBITT phase among the three sidebands of the group located nearest to the ionization threshold and at the highest kinetic energy. These deviations are attributed to the increased contribution of higher-order transitions. Near the threshold, resonances with Rydberg states enhance the amplitude of higher-order transitions and alter the relation between the retrieved oscillation phases of the three sidebands of the group. In the higher-energy region, two factors contribute to the anomalies: the increased probability of continuum-continuum coupling and the unbalanced strength of the adjacent mainbands created in direct ionization. As the adjacent mainbands get depleted, the higher-order transitions originating from stronger lower-energy mainbands become significant and alter the retrieved oscillation phases of the three sidebands.

Based on theoretical data provided by our collaborators at Drake University, we discovered that the phases of the three sidebands within the autoionizing region exhibited significant variation within the group. However, due to technical limitations, we were unable to observe this phenomenon accurately in our experiment. It is important to note that the asymptotic or decomposition approximations are only applicable for a “flat” (no resonances) continuum, and a different interpretation is required for the oscillation phases of the sidebands in the autoionization region.

We performed three-sideband RABBITT measurements in helium using three different probe intensities. Given that the ground state of helium is an s -state, single-photon ionization induced by an XUV pulse selectively generates a well-defined p -state, simplifying the interpretation of the RABBITT phases of the three sidebands. Specifically, the contribution of the Wigner phase associated with the ionization by the XUV pulse remains constant in the RABBITT phase of all three sidebands. The differences in the RABBITT phase among the sidebands are then directly attributed to the varying contributions of the continuum-continuum transitions. In our helium measurements, we observed a similar behavior in the angle-integrated RABBITT phase as we did in our measurements on argon. Specifically, we observed a decrease in phase difference within the group as the kinetic energy increased. However, due to a limited number of detectable harmonics above the threshold, we were only able to compare three groups. In the highest kinetic energy group, the yield oscillation of the sidebands contained a significant contribution from transitions beyond lowest-order, resulting in a large change in the relative phase. As we increased the probe intensity, we observed that higher-order contributions dominated over the lowest-order transition in the yield oscillation. To explain the angle-dependent behavior of the RABBITT phases of the three sidebands in helium, we employed a similar approach to the one we used for argon.

One interesting aspect of the helium measurement was the lowest energy sideband, where two of the sidebands were below the ionization threshold. This sideband was formed by four-photon ionization and showed a rapid variation in phase with energy, which decreased as the probe intensity was increased.

We also employed a Few-Level-Model simulation to investigate the effect of different parameters on the retrieved oscillation phase and its angle-dependence. This included analyzing the impact of dipole transition amplitudes and phases, as well as probe intensity and XUV spectrum.

Looking ahead, there are several promising directions for future research. One possible avenue would be to develop a narrow bandwidth and tunable XUV-APT source, which could be used to investigate the relative RABBITT phases of the three sidebands in the auto-ionization region of argon, as well as the RABBITT phase of the threshold sideband in helium, which involves four-photon ionization. Another potential area of investigation would be to extend the 3-SB RABBITT technique to molecules, in order to study the role of multi-order continuum-continuum transitions. By pursuing these lines of inquiry, we hope to gain deeper insights into the underlying physical mechanisms at work in these systems.

Bibliography

- [1] T. H. Maiman. Stimulated optical radiation in Ruby. *Nature*, 187:493–494, 1960.
- [2] Hans W. Mocker and R. J. Collins. Mode competition and self-locking effects in a Q-switched ruby laser. *Applied Physics Letters*, 7:270–273, 2004.
- [3] Edmond B. Treacy. Compression of picosecond light pulses. *Physics Letters A*, 28:34–35, 1968.
- [4] Donna Strickland and Gerard Mourou. Compression of amplified chirped optical pulses. *Optics Communications*, 55:447–449, 1985.
- [5] A. McPherson, G. Gibson, H. Jara, U. Johann, T. S. Luk, I. A. McIntyre, K. Boyer, and C. K. Rhodes. Studies of multiphoton production of vacuum-ultraviolet radiation in the rare gases. *J. Opt. Soc. Am. B*, 4:595–601, 1987.
- [6] M Ferray, A L’Huillier, X F Li, L A Lompre, G Mainfray, and C Manus. Multiple-harmonic conversion of 1064 nm radiation in rare gases. *J. Phys. B: At. Mol. Opt. Phys.*, 21:L31, 1988.
- [7] P. M. Paul, E. S. Toma, P. Breger, G. Mullot, F. Augé, Ph. Balcou, H. G. Muller, and P. Agostini. Observation of a train of attosecond pulses from high harmonic generation. *Science*, 292:1689–1692, 2001.
- [8] M. Hentschel, R. Kienberger, Ch. Spielmann, G. A. Reider, N. Milosevic, T. Brabec, P. Corkum, U. Heinzmann, M. Drescher, and F. Krausz. Attosecond metrology. *Nature*, 414:509–513, 2001.
- [9] Thomas Gaumnitz, Arohi Jain, Yoann Pertot, Martin Huppert, Inga Jordan, Fernando Ardana-Lamas, and Hans Jakob Wörner. Streaking of 43-attosecond soft-x-ray pulses generated by a passively CEP-stable mid-infrared driver. *Opt. Express*, 25:27506–27518, 2017.

- [10] P Kruit and F H Read. Magnetic field paralleliser for 2π electron-spectrometer and electron-image magnifier. *Journal of Physics E: Scientific Instruments*, 16(4):313, apr 1983.
- [11] S Thorin. *Design and construction of a velocity map imaging spectrometer*. Master thesis, Lund University, 2004.
- [12] J Ullrich, R Moshhammer, A Dorn, R Dörner, L Ph H Schmidt, and H Schmidt-Böcking. Recoil-ion and electron momentum spectroscopy: reaction-microscopes. *Reports on Progress in Physics*, 66:1463, 2003.
- [13] H. G. Muller. Reconstruction of attosecond harmonic beating by interference of two-photon transitions. *Applied Physics B*, 74:s17–s21, 2002.
- [14] K. Klünder, J. M. Dahlström, M. Gisselbrecht, T. Fordell, M. Swoboda, D. Guénot, P. Johnsson, J. Caillat, J. Mauritsson, A. Maquet, R. Taïeb, and A. L’Huillier. Probing single-photon ionization on the attosecond time scale. *Phys. Rev. Lett.*, 106:143002, 2011.
- [15] S. Haessler, B. Fabre, J. Higuette, J. Caillat, T. Ruchon, P. Breger, B. Carré, E. Constant, A. Maquet, E. Mével, P. Salières, R. Taïeb, and Y. Mairesse. Phase-resolved attosecond near-threshold photoionization of molecular nitrogen. *Phys. Rev. A*, 80:011404, 2009.
- [16] Reto Locher, Luca Castiglioni, Matteo Lucchini, Michael Greif, Lukas Gallmann, Jürg Osterwalder, Matthias Hengsberger, and Ursula Keller. Energy-dependent photoemission delays from noble metal surfaces by attosecond interferometry. *Optica*, 2:405–410, 2015.
- [17] Caryn Palatchi, J M Dahlström, A S Kheifets, I A Ivanov, D M Canaday, P Agostini, and L F DiMauro. Atomic delay in helium, neon, argon and krypton*. *J. Phys. B: At. Mol. Opt. Phys.*, 47:245003, 2014.
- [18] Peter E. Powers and Joseph W. Haus. *Fundamentals of Nonlinear Optics*. CRC Press, 2019.
- [19] Tenio Popmintchev, Ming-Chang Chen, Paul Arpin, Margaret M. Murnane, and Henry C. Kapteyn. The attosecond nonlinear optics of bright coherent x-ray generation. *Nature Photonics*, 4(12):822–832, Dec 2010.
- [20] P. B. Corkum. Plasma perspective on strong field multiphoton ionization. *Phys. Rev. Lett.*, 71:1994–1997, 1993.

- [21] Jeffrey L. Krause, Kenneth J. Schafer, and Kenneth C. Kulander. High-order harmonic generation from atoms and ions in the high intensity regime. *Phys. Rev. Lett.*, 68:3535–3538, 1992.
- [22] Philippe Balcou, Pascal Salières, Anne L’Huillier, and Maciej Lewenstein. Generalized phase-matching conditions for high harmonics: The role of field-gradient forces. *Phys. Rev. A*, 55:3204–3210, 1997.
- [23] M Protopapas, C H Keitel, and P L Knight. Atomic physics with super-high intensity lasers. *Reports on Progress in Physics*, 60:389, 1997.
- [24] P. Agostini, F. Fabre, G. Mainfray, G. Petite, and N. K. Rahman. Free-free transitions following six-photon ionization of xenon atoms. *Phys. Rev. Lett.*, 42:1127–1130, 1979.
- [25] L. V. Keldysh. Ionization in the Field of a Strong Electromagnetic Wave. *J. Exp. Theor. Phys.*, 20:1307–1314, 1965.
- [26] M. V. Ammosov, N. B. Delone, and V. P. Krainov. *Tunnel ionization of complex atoms and atomic ions in electromagnetic field*. SPIE Society of Photo-Optical Instrumentation Engineers, United States, 1986.
- [27] Manoj Jain and Narkis Tzoar. X-ray absorption in atoms in the presence of an intense laser field. *Phys. Rev. A*, 15:147–153, 1977.
- [28] Aurelia Cionga, Viorica Florescu, Alfred Maquet, and Richard Taïeb. Target dressing effects in laser-assisted x-ray photoionization. *Phys. Rev. A*, 47:1830–1840, 1993.
- [29] J. Itatani, F. Quéré, G. L. Yudin, M. Yu. Ivanov, F. Krausz, and P. B. Corkum. Attosecond streak camera. *Phys. Rev. Lett.*, 88:173903, 2002.
- [30] M. Isinger, R. J. Squibb, D. Busto, S. Zhong, A. Harth, D. Kroon, S. Nandi, C. L. Arnold, M. Miranda, J. M. Dahlström, E. Lindroth, R. Feifel, M. Gisselbrecht, and A. L’Huillier. Photoionization in the time and frequency domain. *Science*, 358:893–896, 2017.
- [31] L. Argenti, Á. Jiménez-Galán, J. Caillat, R. Taïeb, A. Maquet, and F. Martín. Control of photoemission delay in resonant two-photon transitions. *Phys. Rev. A*, 95:043426, 2017.
- [32] J. Vos, L. Cattaneo, S. Patchkovskii, T. Zimmermann, C. Cirelli, M. Lucchini, A. Kheifets, A. S. Landsman, and U. Keller. Orientation-dependent stereo wigner

- time delay and electron localization in a small molecule. *Science*, 360:1326–1330, 2018.
- [33] J M Dahlström, A L’Huillier, and A Maquet. Introduction to attosecond delays in photoionization. *J. Phys. B: At. Mol. Opt. Phys.*, 45:183001, 2012.
- [34] L Eisenbud. PhD dissertation, Princeton University, 1948.
- [35] Eugene P. Wigner. Lower limit for the energy derivative of the scattering phase shift. *Phys. Rev.*, 98:145–147, 1955.
- [36] Felix T. Smith. Lifetime matrix in collision theory. *Phys. Rev.*, 118:349–356, 1960.
- [37] Jimmy Vinbladh, Jan Marcus Dahlström, and Eva Lindroth. Many-body calculations of two-photon, two-color matrix elements for attosecond delays. *Phys. Rev. A*, 100:043424, 2019.
- [38] Renate Pazourek, Stefan Nagele, and Joachim Burgdörfer. Attosecond chronoscopy of photoemission. *Rev. Mod. Phys.*, 87:765–802, 2015.
- [39] Sebastian Heuser, Álvaro Jiménez Galán, Claudio Cirelli, Carlos Marante, Mazyar Sabbar, Robert Boge, Matteo Lucchini, Lukas Gallmann, Igor Ivanov, Anatoli S. Kheifets, J. Marcus Dahlström, Eva Lindroth, Luca Argenti, Fernando Martín, and Ursula Keller. Angular dependence of photoemission time delay in helium. *Phys. Rev. A*, 94:063409, 2016.
- [40] Jaco Fuchs, Nicolas Douguet, Stefan Donsa, Fernando Martin, Joachim Burgdörfer, Luca Argenti, Laura Cattaneo, and Ursula Keller. Time delays from one-photon transitions in the continuum. *Optica*, 7:154–161, 2020.
- [41] Jasper Peschel, David Busto, Marius Plach, Mattias Bertolino, Maria Hoflund, Sylvain Maclot, Jimmy Vinbladh, Hampus Wikmark, Felipe Zapata, Eva Lindroth, Mathieu Gisselbrecht, Jan Marcus Dahlström, Anne L’Huillier, and Per Eng-Johnsson. Attosecond dynamics of multi-channel single-photon ionization. *Nature Communications*, 13:5205, 2022.
- [42] Divya Bharti, David Atri-Schuller, Gavin Menning, Kathryn R. Hamilton, Robert Moshhammer, Thomas Pfeifer, Nicolas Douguet, Klaus Bartschat, and Anne Harth. Decomposition of the transition phase in multi-sideband schemes for reconstruction of attosecond beating by interference of two-photon transitions. *Phys. Rev. A*, 103:022834, 2021.

- [43] Anne Harth, Nicolas Douguet, Klaus Bartschat, Robert Moshhammer, and Thomas Pfeifer. Extracting phase information on continuum-continuum couplings. *Phys. Rev. A*, 99:023410, 2019.
- [44] D. Bharti, H. Srinivas, F. Shobeiry, K. R. Hamilton, R. Moshhammer, T. Pfeifer, K. Bartschat, and A. Harth. Multisideband interference structures observed via high-order photon-induced continuum-continuum transitions in argon. *Phys. Rev. A*, 107:022801, 2023.
- [45] A. S. Davydov. *Quantum Mechanics*. Pergamon, 1965.
- [46] U. Fano. Propensity rules: An analytical approach. *Phys. Rev. A*, 32:617–618, 1985.
- [47] D Busto, L Barreau, M Isinger, M Turconi, C Alexandridi, A Harth, S Zhong, R J Squibb, D Kroon, S Plogmaker, M Miranda, Á Jiménez-Galán, L Argenti, C L Arnold, R Feifel, F Martín, M Gisselbrecht, A L’Huillier, and P Salières. Time–frequency representation of autoionization dynamics in helium. *J. Phys. B: At. Mol. Opt. Phys.*, 51:044002, 2018.
- [48] S. L. Sorensen, T. Åberg, J. Tulkki, E. Rachlew-Källne, G. Sundström, and M. Kirm. Argon 3s autoionization resonances. *Phys. Rev. A*, 50:1218–1230, 1994.
- [49] Christian Ott, Andreas Kaldun, Philipp Raith, Kristina Meyer, Martin Laux, Jörg Evers, Christoph H. Keitel, Chris H. Greene, and Thomas Pfeifer. Lorentz meets Fano in spectral line shapes: A universal phase and its laser control. *Science*, 340:716–720, 2013.
- [50] He Wang, Michael Chini, Shouyuan Chen, Chang-Hua Zhang, Feng He, Yan Cheng, Yi Wu, Uwe Thumm, and Zenghu Chang. Attosecond time-resolved autoionization of argon. *Phys. Rev. Lett.*, 105:143002, 2010.
- [51] Steve Gilbertson, Michael Chini, Ximao Feng, Sabih Khan, Yi Wu, and Zenghu Chang. Monitoring and controlling the electron dynamics in helium with isolated attosecond pulses. *Phys. Rev. Lett.*, 105:263003, 2010.
- [52] M. Kotur, D. Guénot, Á Jiménez-Galán, D. Kroon, E. W. Larsen, M. Louisy, S. Bengtsson, M. Miranda, J. Mauritsson, C. L. Arnold, S. E. Canton, M. Gisselbrecht, T. Carette, J. M. Dahlström, E. Lindroth, A. Maquet, L. Argenti, F. Martín, and A. L’Huillier. Spectral phase measurement of a Fano resonance using tunable attosecond pulses. *Nat. Commun.*, 7:10566, 2016.

- [53] Claudio Cirelli, Carlos Marante, Sebastian Heuser, C L M Petersson, Álvaro Jiménez Galán, Luca Argenti, Shiyang Zhong, David Busto, Marcus Isinger, Saikat Nandi, Sylvain Maclot, Linnea Rading, Per Johnsson, Mathieu Gisselbrecht, Matteo Lucchini, Lukas Gallmann, J Marcus Dahlström, Eva Lindroth, Anne L’Huillier, Fernando Martín, and Ursula Keller. Anisotropic photoemission time delays close to a Fano resonance. *Nat. Commun.*, 9:955, 2018.
- [54] V. Gruson, L. Barreau, Á. Jiménez-Galan, F. Risoud, J. Caillat, A. Maquet, B. Carré, F. Lepetit, J.-F. Hergott, T. Ruchon, L. Argenti, R. Taïeb, F. Martín, and P. Salières. Attosecond dynamics through a Fano resonance: Monitoring the birth of a photoelectron. *Science*, 354:734–738, 2016.
- [55] J.A.R. Samson and W.C. Stolte. Precision measurements of the total photoionization cross-sections of He, Ne, Ar, Kr, and Xe. *Journal of Electron Spectroscopy and Related Phenomena*, 123:265–276, 2002. Determination of cross-sections and momentum profiles of atoms, molecules and condensed matter.
- [56] Hemkumar Srinivas, Farshad Shobeiry, Divya Bharti, Thomas Pfeifer, Robert Moshhammer, and Anne Harth. High-repetition rate attosecond beamline for multiparticle coincidence experiments. *Opt. Express*, 30:13630–13646, 2022.
- [57] M. Swoboda, T. Fordell, K. Klünder, J. M. Dahlström, M. Miranda, C. Buth, K. J. Schafer, J. Mauritsson, A. L’Huillier, and M. Gisselbrecht. Phase measurement of resonant two-photon ionization in helium. *Phys. Rev. Lett.*, 104:103003, 2010.
- [58] D. M. Villeneuve, Paul Hockett, M. J. J. Vrakking, and Hiromichi Niikura. Coherent imaging of an attosecond electron wave packet. *Science*, 356:1150–1153, 2017.
- [59] Anatoli S. Kheifets and Alexander W. Bray. RABBITT phase transition across the ionization threshold. *Phys. Rev. A*, 103:L011101, 2021.
- [60] Alice Autuori, Dominique Platzer, Mariusz Lejman, Guillaume Gallician, Lucie Maëder, Antoine Covolo, Lea Bosse, Malay Dalui, David Bresteau, Jean-François Hergott, Olivier Tcherbakoff, Hugo J. B. Marroux, Vincent Loriot, Franck Lépine, Lionel Poisson, Richard Taïeb, Jérémie Caillat, and Pascal Salières. Anisotropic dynamics of two-photon ionization: An attosecond movie of photoemission. *Science Advances*, 8:7594, 2022.
- [61] L. Drescher, T. Witting, O. Kornilov, and M. J. J. Vrakking. Phase dependence of resonant and antiresonant two-photon excitations. *Phys. Rev. A*, 105:L011101, 2022.

- [62] L. Neoričić, D. Busto, H. Laurell, R. Weissenbilder, M. Ammitzböll, S. Luo, J. Peschel, H. Wikmark, J. Lahl, S. Maclot, R. J. Squibb, S. Zhong, P. Eng-Johnsson, C. L. Arnold, R. Feifel, M. Gisselbrecht, E. Lindroth, and A. L'Huillier. Resonant two-photon ionization of helium atoms studied by attosecond interferometry. *Frontiers in Physics*, 10, 2022.
- [63] Álvaro Jiménez-Galán, Luca Argenti, and Fernando Martín. Modulation of attosecond beating in resonant two-photon ionization. *Phys. Rev. Lett.*, 113:263001, 2014.
- [64] National Institute of Standards and Technology. Energy levels of Helium. NIST Atomic Spectra Database, 2021.
- [65] Steffen Hädrich, Arno Klenke, Armin Hoffmann, Tino Eidam, Thomas Gottschall, Jan Rothhardt, Jens Limpert, and Andreas Tünnermann. *Opt. Lett.*, 38(19):3866–3869, Oct 2013.
- [66] T.Y. Fan. Laser beam combining for high-power, high-radiance sources. *IEEE Journal of Selected Topics in Quantum Electronics*, 11(3):567–577, 2005.
- [67] Ram Gopal. *Electron Wave Packet Interferences in Ionization with Few-Cycle Laser Pulses and the Dissociative Photoionization of D₂ with Ultrashort Extreme Ultraviolet Pulses*. PhD dissertation, Ruperto-Carola University of Heidelberg, 2010.
- [68] Farshad Shobeiry. *Attosecond electron-nuclear dynamics in photodissociation of H₂ and D₂*. PhD dissertation, Ruperto-Carola University of Heidelberg, 2021.
- [69] Hemkumar Srinivas. *XUV-IR Pump-Probe measurements on Argon, Krypton and Nitrogen*. PhD dissertation, Ruperto-Carola University of Heidelberg, 2023.
- [70] Andreas Fischer. *Dissociative Photoionization of Molecular Hydrogen - A Joint Experimental and Theoretical Study of the Electron-Electron Correlations induced by XUV Photoionization and Nuclear Dynamics on IR-Laser Dressed Transition States*. PhD dissertation, Ruperto-Carola University of Heidelberg, 2015.
- [71] Daniel Fischer. *Mehr-Teilchen-Dynamik in der Einfach- und Doppelionisation von Helium durch geladene Projektile*. PhD dissertation, Ruperto-Carola University of Heidelberg, 2003.
- [72] Martin Dürr. *Electron Induced Break-up of Helium: Benchmark Experiments on a Dynamical Four-Body Coulomb System*. PhD dissertation, Ruperto-Carola University of Heidelberg, 2006.

Appendix A

Additional information on the Experimental Setup

This appendix provides an overview of the experimental setup employed in the study, which includes a femtosecond CPA laser, a hollow-core fiber system, a high-order harmonics generation unit, a Mach-Zehnder interferometer, and a reaction microscope. While most of the beamline information has been published in (Publication I), this section offers a brief discussion, highlighting details that were not previously covered.

A.1 Laser

The experimental laser system used in this study is a commercially-available high-power fiber laser from Active Fiber Systems GmbH, and its schematic is depicted in Fig. A.1. The system contains a Ytterbium-based fiber oscillator generating femtosecond pulses at around 1030 nm, which are then stretched to nanoseconds and passed through a waveshaper. The

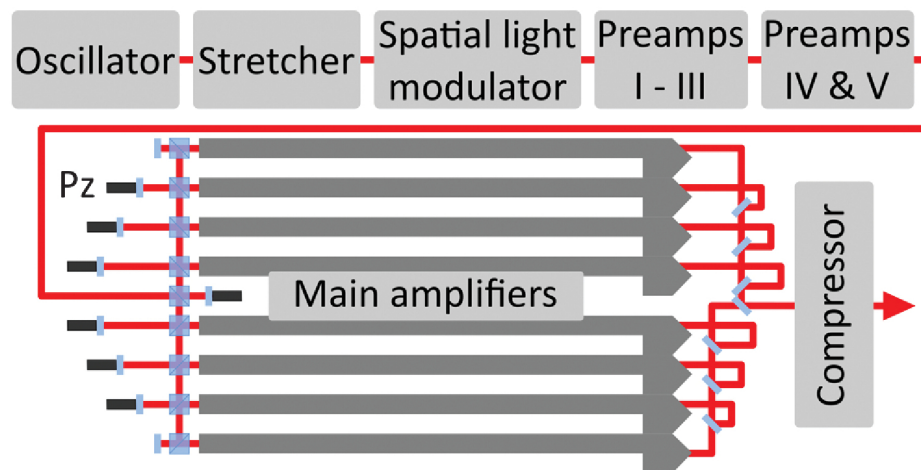


Figure A.1. Schematic of the CPA laser. [65]

waveshaper can be used to optimize the pulse compression at the output. The pulse is amplified using preamplifiers and evenly distributed among eight amplifier channels through polarizing beam splitters and half-wave plates. Each amplifier channel is pumped by a separate wavelength-stabilized fiber-coupled pump diode. The amplified output of each channel is coherently combined while maintaining their relative phases, resulting in constructive interference [66]. As a result, the system can produce high average power, high-repetition-rate pulses with high beam quality. Once the amplified pulses are combined coherently, they are passed through an acoustic-optic modulator (AOM) to select one of three available repetition rates: 50 kHz, 70 kHz, or 150 kHz. The selected pulses are then directed through a Treacy-type compressor [3], resulting in pulses that are 250 fs in duration with a pulse energy of 2 mJ. To achieve even shorter pulse duration, the CPA output is coupled into a 1.15-meter-long hollow-core fiber (HCF) with an inner diameter of 300 microns filled with argon gas at a pressure of 1-1.8 bar. As the pulse propagates through the HCF, it undergoes self-phase modulation (SPM), which broadens its spectrum. To compensate for the SPM-induced dispersion, the pulse is reflected multiple times off chirped mirrors that induce a group delay dispersion with an opposite sign to that caused by SPM in the HCF. As a result, the pulse is compressed in time, leading to a final pulse duration of 40 fs with a pulse energy of 1.2 mJ.

A.2 Interferometer

The interferometer is set up in a Mach-Zehnder configuration, where each arm has a length of 1.4 m A.2. The laser beam, which is *p*-polarized and parallel to the optical table, is split into two arms using a mirror (BS) with a central hole of either 4 mm or 3.5 mm, in a ratio of 80 : 20(85 : 15). The stronger beam is directed into the pump arm, while the remaining beam passes through the hole into the probe arm. The reflected donut beam then passes first through a planoconvex and then a planoconcave lens with focal lengths of 12 cm and -5 cm, respectively, separated by a distance of 5 cm. The slightly diverging beam then passes through a Beta Barium Borate (BBO) crystal of thickness 0.5 mm and width of 6 mm. The beam width at the BBO crystal is about 3 mm, which results in a second-harmonic generation (SHG) conversion efficiency of 25% – 30%. The fundamental beam is filtered out using a dichroic beam splitter (DBS), and the second harmonic beam is focused by a lens with a focal length of 12 cm to a spot size of 30 – 40 μm on a jet of noble gas inside a vacuum chamber. This leads to the generation of an XUV pulse train through high-harmonic generation (HHG). The gas nozzle has a diameter of 100 μm and is operated at a backing pressure of 0.8 – 1.5 bar with a chamber pressure of $1 - 8 \times 10^{-3}$ mbar.

The generated XUV beam is separated from the annular second harmonic using an ad-

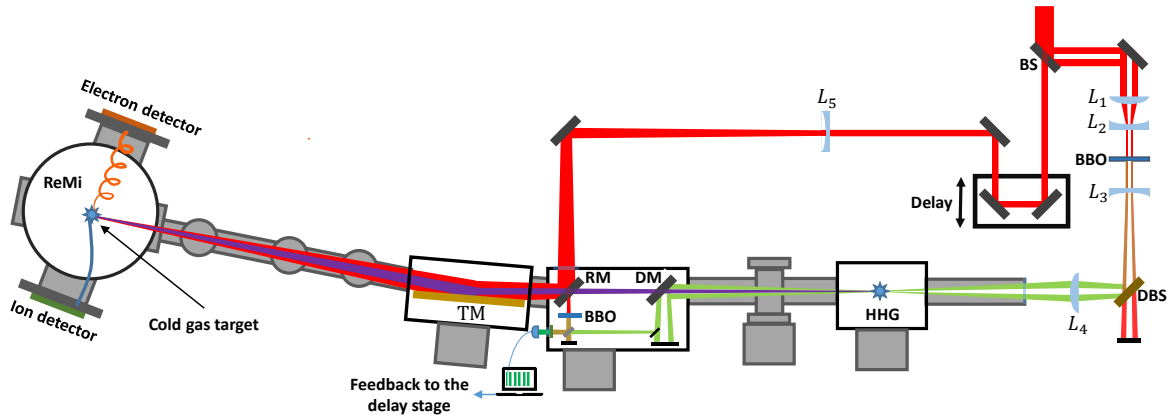


Figure A.2. Schematic of the interferometer. Legends: BS: Beam splitter; DBS: dichroic beam splitter; DM, Dump mirror; RM: Recombination mirror; TM: torroidal mirror; L_1 and L_4 : planoconvex lenses; L_2 , L_3 and L_5 : planoconcave lenses

ditional holey mirror (DM) with a central hole of 4 mm while the XUV beam with a smaller divergence than the driving pulse (second harmonic) passes through the hole. After the dumping mirror (DM), a metallic filter (aluminum, germanium, tin) mounted on a motorized wheel can be introduced to block the lower harmonic in the XUV beam. The XUV beam then passes uninterrupted through the hole of the recombination mirror (RM) that has two holes drilled at perpendicular direction.

The beam in the probe arm goes through a retro-reflector mounted on a piezoelectric-translation stage with a step resolution of 5 nm (P-629.1CL). A plano-concave lens with a focal length of -25 cm is placed in the probe arm so that the virtual focus of the probe beam is at the same distance from the recombination mirror as the focus of the high-harmonic generation (HHG) target. A $\lambda/2$ waveplate is used to rotate the polarization of the probe beam. A motorized mirror reflects the probe beam onto the recombination mirror. This allows a small part of the probe beam to pass through the hole for interferometer stabilization and the rest to be reflected and combine with the XUV beam. The recombined IR (probe) and XUV (pump) beam then make a grazing incidence at 8 degrees onto the toroidal mirror placed at $2f$ from the HHG target and then get focused inside a reaction microscope (ReMi) on a cold gas jet of gas. The toroid mirror is mounted on three motorized stages that are used to optimize the focus of the beam inside the ReMi. The toroidal chamber with pressure 1×10^{-7} mbar is connected to the main chamber of the ReMi having a typical pressure of 1×10^{-11} mbar through two differential pumping stages.

In order to find the temporal overlap between the two arms of the interferometer, the BBO crystal is rotated to have the least conversion of the second harmonic, the gas for the HHG conversion is cut off, and the pump arm is slightly misaligned to let the IR beam pass from the holes of the dump mirror and the recombination mirror. The recombined IR beams

from the pump and the probe arms are projected outside the ReMi by introducing a silver mirror in the beam path. This mirror must be removed during the experiment; otherwise it will introduce a huge amount of secondary electrons. The beams are focused on a camera, and the spatial and temporal overlap is ensured by obtaining the fringes. The intensity of the probe is adjusted by using an iris to yield the best contrast.

Stabilization

A small extension in the main interferometer is added to stabilize it actively. A plane mirror mounted on the translation stage reflects a small part of the second harmonic beam from the Dump mirror towards the second beamsplitter and rest of the second harmonic beam is dumped outside the chamber. The IR beam coming from the probe arm, which passes through the hole of the recombination mirror, is passed through another BBO crystal of 1mm thickness and then passes through the beam splitter (BS2). Another $\lambda/2$ waveplate is used to match the polarization of the two green beams from the pump and the probe arm. The recombined beams are then passed through a bandpass filter to remove the IR beam. The beam is then projected on the camera. First, the temporal overlap of the pump and the probe arms of the main interferometer is ensured by obtaining the fringes on the camera outside ReMi. Then the path length of the extended interferometer is adjusted to obtain fringes with good contrast. We move the piezoelectric stage and ensure the correlation in the movement of the fringes on both cameras. At the start of the experiment, the program moves the delay stage to one end of the scan range and records the fringe pattern at the camera. The phase of the fringe is retrieved by the Fourier transform and is taken as a reference phase. During the scan, the delay stage is moved at a fixed step size ($\Delta\tau$), and the reference phase is also adjusted accordingly. The camera captures 20 frames per second. The phase of the interference fringes from the current camera frame is compared with the reference phase, and the difference is used as feedback for the delay stage.

A.3 Reaction Microscope

The ReMi spectrometer used in this thesis was built over a decade ago, and more details about its construction and operation can be found in the following theses: [67–70]. To ensure some self-consistency, however, we here present a brief summary of details that were not discussed in Publication I.

A.3.1 Data acquisition and signal processing

The ReMi detector consists of a pair of Micro Channel Plates (MCP) arranged in a Chevron configuration and a Delay Line Anode (DLA). When a charged particle enters the MCP channel, it triggers an avalanche of electrons, causing a drop in the applied voltage and generating a negative voltage pulse that lasts for approximately 10 ns. The delay line anode consists of a flat insulating plate with two copper wires wound across opposite edges, forming a 2D grid. These positively biased wires detect the image of the charge cloud that exits from the rear end of the MCP stack. As this charge cloud travels to the two ends of the delay lines, it creates two signals from each wire.

The high-bandwidth fast amplifier amplifies both the MCP and DLA signals. To assign timing information independently of their pulse height, a constant-fraction-discriminator (CFD) is utilized, which produces a standard NIM output. A reference signal is also generated by a photodiode, which encodes the arrival time of the laser pulse at the target and is also sent to the CFD for creating a standard NIM output. The CFD signal is then digitized using a multi-hit Time-to-Digital Converter (TDC). The timing information of the signals from the MCP, DLA, and photodiode is stored for further analysis.

In order to calculate the complete momenta of the charged particles, both the time-of-flight (TOF) for each particle and its corresponding impact coordinates (x, y) on the detector are required. The time-of-flight is determined by calculating the time difference between the MCP signal and the photodetector signal. The hit position of the particle on the grid is determined by analyzing the time difference between two signals originating from the opposite ends of the DLA wire. Specifically,

$$x = v_{signal}(t_{x1} - t_{x2}); \quad y = v_{signal}(t_{y1} - t_{y2}). \quad (\text{A.1})$$

Here v_{signal} is the signal velocity in the copper wire.

A.3.2 Momentum reconstruction

Using the information of the TOF and the impact position on the detector, one can reconstruct the initial momentum vectors of the charged fragments. The longitudinal momentum of the charged particle, parallel to the spectrometer axis, can be reconstructed from its TOF (t) as follows:

$$p_{ion/e}^{long} = \frac{Ma}{t} - \frac{qUt}{2a}. \quad (\text{A.2})$$

Here M and q are the mass and charge of the charged particle, U is the applied voltage, and a ($=154.5$ mm) is the distance between the detector and the interaction volume. The transverse momentum for the ion is obtained as

$$p_{ion}^{trans} = \frac{M\sqrt{(x - x_0)^2 + (y - y_0)^2}}{t}. \quad (\text{A.3})$$

Here x_0 and y_0 are the centers of distribution of the position coordinate on the detector corresponding to zero transverse momentum. The two orthogonal components of the transverse momentum can be resolved as:

$$p_{ion}^x = \frac{(x - x_0)M}{t}; \quad p_{ion}^y = \frac{(y - y_0)M}{t}. \quad (\text{A.4})$$

Due to the magnetic field, the light electrons move in a helical path. This makes the reconstruction of their transverse momentum more complex compared to that of the heavy ions:

$$p_e^{trans} = \frac{eB\sqrt{(x - x_0)^2 + (y - y_0)^2}}{2|\sin(\omega_c t/2)|} \quad (\text{A.5})$$

Here B is the magnetic field and ω_c is the cyclotron frequency. Finally, p_x and p_y are calculated as

$$p_e^x = p_e^{trans} \cos\phi; \quad p_e^y = p_e^{trans} \sin\phi, \quad (\text{A.6})$$

where the azimuthal angle is calculated as

$$\phi_e = \arctan\left(\frac{y - y_0}{x - x_0}\right) - \frac{\omega_c t}{2}. \quad (\text{A.7})$$

A.3.3 Angular acceptance

Typically, the acceptance of a spectrometer is characterized by the maximum kinetic energy of a detected fragment over the full solid angle. There is no limit on the maximum kinetic energy of ions (electrons) that can be detected when emitted in the direction of the ion (electron) detector. However, the maximum kinetic energy of ions or electrons emitted in the opposite direction that can be extracted depends on the applied voltage, which can be determined as

$$E_{max}^{-z} = qU. \quad (\text{A.8})$$

For a spectrometer voltage of 50 V, E_{max}^{-z} is about 50 eV. This is larger than required for our experiment.

The detection of charged particles emitted in transverse directions is influenced by various factors, such as the length of the spectrometer, the MCP size, the electric and magnetic fields applied, and the charged particle's kinetic energy. The electric field guides the ions towards the ion MCP, whereas the confinement of the electrons primarily relies on the magnetic field. The maximum energy of the ion emitted in transverse direction that can be detected by the spectrometer is

$$E_{ion,max}^{trans} = \frac{qUR_{det}^2}{4a^2}. \quad (\text{A.9})$$

With the MCP plate radius set at $R_{det} = 40$ mm and an acceleration region length of $a = 154.5$ mm, the spectrometer can detect ions with a maximum transverse momentum of about 1.0 eV, which is more than sufficient for ions created in a single-photon ionization process.

For electron detection, the gyroradius should be smaller than half the MCP radius. The maximum energy of the electron emitted in transverse direction that can be detected by the spectrometer is

$$E_{e,max}^{trans} = \frac{(eR_{det}B)^2}{8M_e}. \quad (\text{A.10})$$

At an applied magnetic field of 10 Gauss, the maximum kinetic energy of the photoelectron that can be detected with full solid angle is approximately 35 eV.

A.3.4 Resolution

The resolution of the ReMi depends on various factors such as the strength and homogeneity of the electric and magnetic fields, the thermal velocity of the target beam, the size of the interaction volume, and the timing jitter in the digitizing electronics.

In the case of ions, the uncertainty in momentum is primarily influenced by the thermal velocity distribution of the target species. For helium, with a jet temperature of 1 K and a jet width of 1 mm, the momentum uncertainty in the jet direction is estimated to be $\Delta p_{therm}^y = 0.26$ atomic units (a.u.). In the transverse direction, the momentum uncertainties are approximately equal, with $\Delta p_{therm}^z \approx \Delta p_{therm}^x = 0.12$ a.u. [67, 71, 72]. Moreover, it is also affected by the uncertainty in determining the impact position on the detector and the time-of-flight. Specifically:

$$(\Delta p_z)^2 = (\Delta p_{therm}^z)^2 + \left(8.039 \times 10^{-3} \frac{\text{cm a.u. } qUM}{\text{eV ns } a} \delta t\right)^2 \quad (\text{A.11})$$

$$(\Delta p_x)^2 = (\Delta p_{therm}^x)^2 + \left(11.6 \times 10^{-3} \frac{\text{a.u.}}{\sqrt{\text{amu eV}}} \frac{\sqrt{qUM}}{2a} \delta r\right)^2 \quad (\text{A.12})$$

$$(\Delta p_y)^2 = (\Delta p_{therm}^y)^2 + \left(11.6 \times 10^{-3} \frac{\text{a.u.}}{\sqrt{\text{amu eV}}} \frac{qUM}{2a} \delta r\right)^2 \quad (\text{A.13})$$

For an applied voltage of 50 V, assuming a time-of-flight uncertainty of $\delta t \approx 1$ ns, and a position uncertainty of $\delta r \approx 1$ mm, the estimated momentum uncertainties are as follows:

$$\Delta p_z \approx 0.12 \text{ a.u. (spectrometer axis);} \quad (\text{A.14})$$

$$\Delta p_x \approx 0.54 \text{ a.u.;} \quad (\text{A.15})$$

$$\Delta p_y \approx 0.59 \text{ a.u. (jet direction).} \quad (\text{A.16})$$

Since the kinetic energy of the photoelectron is much larger than the thermal energy of the target species, the momentum uncertainty due to the thermal effect can be neglected for the electrons.

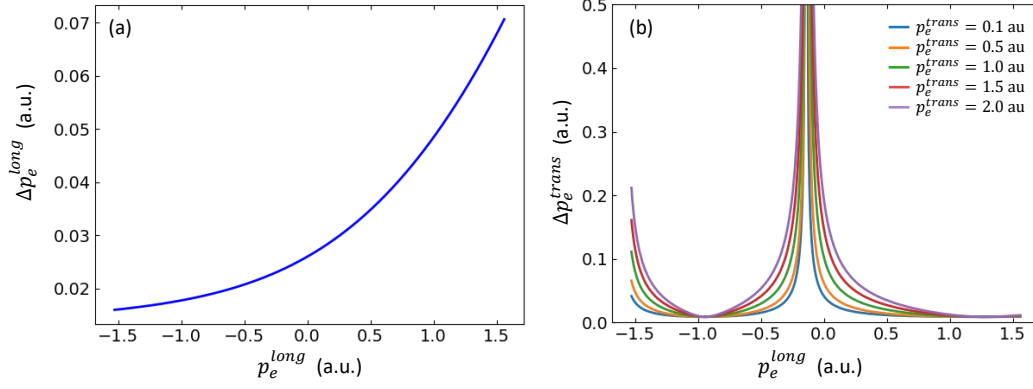


Figure A.3. Longitudinal (a) and transverse (b) momentum resolution of the electron spectrometer. $U = 50$ V ; $B=4.5$ Gauss

Next, the uncertainty in the longitudinal momentum of the electron is influenced by the uncertainty in the time-of-flight:

$$\Delta p^{long} = \frac{M_e a}{t^2} \delta t + \frac{qU}{2a} \delta t. \quad (\text{A.17})$$

As seen from Eq. (A.17), an increase in the time-of-flight leads to an improvement in the longitudinal momentum resolution. Finally, the transverse momentum resolution depends on both the position and the time-of-flight uncertainty:

$$\Delta p^{trans} = \frac{B}{2|\sin(\frac{1}{2}\omega t)|} \sqrt{(\Delta r)^2 + \left(\frac{r \omega \delta t}{2 \tan(\frac{1}{2}\omega t)}\right)^2}. \quad (\text{A.18})$$

The transverse component of the momentum resolution is periodic in nature and diverges at the magnetic node as can be seen in Fig. A.3.

Acknowledgements

Throughout my PhD journey, I have had the privilege of knowing and working with many people who have played an integral role in shaping my research work and experiences in general.

First and foremost, I would like to express my gratitude to my supervisors and mentors, Anne Harth and Thomas Pfeifer, for giving me the opportunity to work in their group and for providing me with constant guidance and supervision throughout my studies. Anne provided unwavering support during the entire time of my project and patiently listened to all of my problems. Her dedication and hard work were critical in advancing my research, and I feel very fortunate to have had the opportunity to work with her. Despite his busy schedule, Thomas was always available to discuss my research ideas and offer valuable feedback and suggestions to improve the quality of my work.

I would like to express my sincere appreciation to Robert Moshhammer for generously providing me with access to his lab and equipment. His expertise and critical thinking skills have been instrumental in enhancing my understanding of the research and its implications. I also express my gratitude to Klaus Bartschat, my collaborator, for his keen interest in my work and invaluable contributions to the theoretical aspects of my research. Additionally, I thank Kathryn Hamilton and Nicolas Douguet for carrying out the theoretical calculations that complemented my experimental data.

I am grateful to my colleagues Farshad and Hemkumar for their support during our time working together in the lab. Hemkumar's generous sharing of knowledge, coupled with our enjoyable discussions about physics, greatly contributed to my development as a researcher. I am also grateful to Claus-Dieter Schröter, Nikola Mollov, Alexander von der Dellen, and Christian Kaiser for their technical support in conducting my experiments.

Thanks to Denhi, Deepthy, Weiyu, David, Felix, and my all colleagues at MPIK for creating a joyful work environment. Even on depressive days when the lasers behaved badly or instruments malfunctioned, I could always talk to Weiyu and find something to laugh about.

It has been a privilege to work with such an amazing group of people, and I will always cherish the memories of our time together.

Finally, I want to thank my family for their endless support and patience.